Atomic and molecular oxygen collision processes over some crystalline solids

Víctor Morón Tejero

Universitat de Barcelona
Facultat de Química
Departament de Química Física
Programa de doctorat del bienni 2006-2008
(Química Teòrica i Computacional)

Atomic and molecular oxygen collision processes over some crystalline solids

Memòria que per a optar al grau de Doctor per la Universitat de Barcelona, presenta:

Víctor Morón Tejero

Directors:

Dr. Ramón Sayós Ortega
Departament de Química Física
Universitat de Barcelona

Dr. Pablo Gamallo Belmonte
Departament de Química Física
Universitat de Barcelona

Barcelona, Octubre de 2011

.

Agraïments

M'agradaria agrair a totes les persones que d'una manera o un altra han fet possible la realització d'aquesta tesi.

En primer lloc, agrair als meus directors de tesi Ramón Sayós i Pablo Gamallo per tot el que m'han ensenyat, el temps que han invertit i la paciència que han tingut, sobretot a la recta final de l'escriptura.

A tots els companys de feina dels que he après moltes coses, especialment als companys de *Bordeaux*: Cédric, Pascal i Ludo.

A la meva família, en especial als meus tius Rosa i Manolo, perquè formen part de mi.

Als meus amics, perquè d'una manera o d'un altra m'han ajudat a que els moments difícils no ho siguin tant.

Als companys de pis, perquè a més d'oferir-me amistat m'han acompanyat dia a dia tots els anys que ha durat la tesi.

Als companys de departament amb els que hem compartit els bons i mals moments durant la realització d'aquest treball.

I especialment als meus pares, que amb el seu recolzament incondicional m'han acompanyat des de que vaig nèixer fins arribar on avui em trobo.

Gràcies a tots els que heu estat al meu costat: *Ne marche pas devant moi, je ne suivrai peut-être pas. Ne marche pas derrière moi, je ne te guiderai peut-être pas. Marche juste à côté de moi et sois mon ami* (Albert Camus).

Contents

Chapter 1

Introduction

The analysis of a reaction system has been historically addressed in a phenomenological or macroscopic way, namely, by means of Thermodynamics, that is concerned with systems at equilibrium, and the Chemical Kinetics, that studies the influence of several macroscopic variables, such as temperature and pressure, on the rate of conversion of reactants to products. The information one can extract from these studies does not include a detailed knowledge of how the reactant molecules approach each other, which forces drive this process, the influence of their relative orientation on the final products, etc. With the aim of providing such information, in the last decades a new scientific discipline, the Molecular Reaction Dynamics, has acquired an increasing importance. In fact, three Nobel Prizes have been awarded to scientists working in this area, namely, those of 1986 (Polanyi, Lee, Hersbach), of 1991 (Marcus) and of 1999 (Zewail).

The study of the dynamics of a certain reactive process involves, in principle, the solution of the total Schrödinger equation for that system, i.e., for the electronic as well as the nuclear degrees of freedom. For a general system, the direct solution of this equation is clearly unreachable, so that some approximations must be introduced. The first approximation that is usually employed is that of Born and Oppenheimer, by means of which the movement of the electrons is separated from the movement of the nuclei. This separation leads to the key concept of Potential Energy Surfaces (PES), that is to say, the nuclei of the system can be regarded as if they evolved subject to an effective potential created by the electrons. A Potential Energy Surface is a function of the N nuclear degrees of freedom to be constructed by calculating the sum of the electronic and internuclear repulsion energies for each fixed nuclear configuration. In practice, the process is divided into three main steps: 1) calculation of the electronic wave function and energy for a set of nuclear configurations; 2) fit of the energies to a suitable analytical function; and 3) solution of the nuclear problem, either by a Classical, Quasiclassical, Semiclassical or Quantum methods.

1. INTRODUCTION

The calculation of the PES of a given reactive system involves the construction of the electronic wave function. This problem is the object of the Quantum Chemistry, that could be defined as the application of Quantum Mechanics to chemical problems. Quantum Chemistry derives from a theoretical model, which is basically that describing the forces that originate the chemical bond and that was initiated by Schrödinger and Dirac and further developed in the work by Heitler, London, Born, Oppenheimer, Mulliken, Pauling, Hartree, Fock, etc. Even though this model can in principle be applied to systems of arbitrary complexity, only for very simple systems exist an analytical solution. The practical application in these early years of Quantum Chemistry was subjected to strong simplifications leading to semiempirical models. It was not until the advent of electronic computers that it could be applied to systems of more than two or three atoms, reaching in some cases 'chemical accuracy' (i.e., errors within 1 Kcal·mol^{-1} in relative energies).

The aim of this work is to study the chemical processes that occur between gas phase atoms and molecules over a crystalline solid surface. The dynamics of the processes that occur over the thermal protection systems (TPS) of the space vehicles have a high industrial and economical interest and the knowledge about them is still scarce. These TPS are the responsible of the protection of the space vehicles which can store very important experimental information, expensive scientific instrumentation or even human lives. The failure of a TPS may imply the waste of many working time, the lost of high economical investment and a serious dead danger for the people involved, as it happened in the Columbia crash at 2003.

The TPS have to be able to resist the strong conditions when reentering the Earth's atmosphere at very high velocities, which can reach the Match 30 ($\sim$10,208 m/s). During the Earth reentry, there is a high heating on the vehicle surface due to the friction and the catalytic processes between the surface and the atmospheric gas (mainly formed by 78% of N_2, 21% of O_2 and 1% of Ar). Temperatures achieved are in the range of 500 - 1,900 K depending on the areas of the vehicle. The catalytic efficiency of such materials should be very low in order to minimize the heat flux transferred to the surface. Nowadays, a variety of materials are used as TPS such as silica tiles, reinforced carbon, nylon felt, ...

Computer fluid dynamics (CFD) simulations are usually carried out to predict the main aspects of the reentry aerothermodynamics. In these simulations two coefficients are required to include appropriately the wall catalytic effects: a) the atomic recombination coefficient γ and b) the chemical energy accommodation coefficient β. Although both coefficients are within the range $0 \leqslant \gamma, \beta \leqslant 1$, the lack of information about the real values does not allow the simulations to properly describe the catalytic contribution to the total heating process.

In order to improve the knowledge of the whole processes occurring over these materials, theoretical and computational chemistry can play an important role.

Thus, dynamical studies give us information about the way in which these processes take place from a microscopic point of view and in addition, about the role of the surface in the final products. Furthermore, the construction of kinetic models improves the available information about the γ and β coefficients for the different species that collide over these materials.

The structure of this thesis starts with an introduction to the theoretical methods used along the study: Density Functional Theory (DFT) applied to the modelization of solid materials, the methods used for the construction of analytical and interpolated Potential Energy Surfaces, some details about the quasiclassical trajectory method and about the construction of kinetic models. The most effort and consuming time issue were done for the construction of the different PES, and specially true for the interpolated one, which has required an adaptation to the specific systems involved, as well as the development of a new code from scratch.

The systems studied are divided in two parts. In both, the elementary processes occurring when atomic or molecular oxygen collide over two different solid surfaces are analysed. Oxygen is the second most abundant specie on Earth's atmosphere just behind molecular nitrogen. However, the lower molecular dissociation energy of oxygen suggests that its reactivity will play the main role. The first part of the results illustrates the study carried out over graphite surface, which is considered as a good approximation to the reinforced carbon material, widely used in TPS. An extensive DFT study of the several elementary processes is carried out and then used for the construction of two new PES. In addition, a dynamical study is carried out by using these two constructed PES. Among other information (i.e., reaction probabilities, angle scattering distributions, ...) an estimation of the γ coefficient is obtained by using a kinetic model. The second, extents the study realized in our research group about the interaction of oxygen over β-cristobalite, one of the main components of the silica tiles used as well in TPS. Thus, a dynamical study for some of the main elementary processes is presented using one of the available PES constructed previously. The dynamical and kinetic information is then used for constructing a kinetic model in order to obtain information of the overall elementary processes occurring at the same time and to estimate the γ and β coefficients.

Finally, the main conclusions of this work are summarized.

Chapter 2

Theoretical Background

2.1 Modelling periodic crystal structure

2.1.1 Bravais and reciprocal lattice

When defining an ideal material in solid state we talk about a single crystal formed by an ordered array of particles in all three-space dimensions in which, the cohesive force is strong enough to keep them around a given position. Thanks to this periodicity, crystalline structure plays an important role in the theoretical description and behaviour of solid properties. In this section, basic models for both, experimental and theoretical solid-state physics and chemistry are introduced.

The infinite repetition of an atom or a group of atoms gives a set of mathematical points called *lattice*, which can be classified in 14 different *Bravais lattices* depending on their spatial disposition. They can be constructed by an infinite translation over the space of a minimum structure, the *primitive* or *unit cell* defined itself by three primitive axes $\vec{a}_1$, $\vec{a}_2$ and $\vec{a}_3$. A specific Bravais lattice depends on the modulus and the angle between its primitive axes. Thus, any Bravais lattice can be constructed from a primitive cell by applying a translation vector $\vec{T}$,

$$\vec{T} = n_1\vec{a}_1 + n_2\vec{a}_2 + n_3\vec{a}_3 \tag{2.1}$$

where n_i are integers. Another primitive cell, named *Wigner-Seitz cell*, is defined by the volume delimited by the perpendicular planes to the lines drawn between all the closest neighbouring points.

Similarly to the direct lattice definition, a *reciprocal* lattice can be defined. Likewise direct lattice, reciprocal one is a Bravais lattice with an specific period-

icity defined by the translating vector,

$$\vec{G} = m_1\vec{b}_1 + m_2\vec{b}_2 + m_3\vec{b}_3 \tag{2.2}$$

where m_i are integers and $\vec{b}_1$, $\vec{b}_2$ and $\vec{b}_3$ correspond to the primitive vectors that form the reciprocal lattice. These vectors are simply related to the direct ones to allow a quick conversion between both lattices. Considering $\vec{a}_i$ as a direct lattice vector, and $\vec{b}_j$ as a reciprocal one, they fulfil the relation,

$$\vec{a}_i \cdot \vec{b}_j = 2\pi\delta_{ij} \tag{2.3}$$

since,

$$\vec{b}_1 = 2\pi\frac{\vec{a}_2 \times \vec{a}_3}{\vec{a}_1 \cdot (\vec{a}_2 \times \vec{a}_3)}; \quad \vec{b}_2 = 2\pi\frac{\vec{a}_3 \times \vec{a}_1}{\vec{a}_1 \cdot (\vec{a}_2 \times \vec{a}_3)}; \quad \vec{b}_3 = 2\pi\frac{\vec{a}_1 \times \vec{a}_2}{\vec{a}_1 \cdot (\vec{a}_2 \times \vec{a}_3)} \tag{2.4}$$

From equations 2.4 it is easy to demonstrate that any reciprocal vector is perpendicular to a direct lattice plane. Also, once a direct lattice is specified, there is only one possible reciprocal lattice; thus, the later is defined unequivocally and does not depend on the primitive vectors used. The equivalent Wigner-Seitz cell for a reciprocal lattice is called the *first Brillouin zone*.

A very useful notation employed for defining a set of atoms contained in a specific direction or in a specific plane is the *Miller indices*, [hkl] and (hkl), respectively. *Miller indices* for planes can be determined following a few simple rules:

- Find where the plane intercepts the primitive axes direction $\vec{a}_1$, $\vec{a}_2$ and $\vec{a}_3$.
- Take the reciprocals of these numbers and find the three integers that have the same ratio.
- In the case that a plane does not intercept one axis, the index is taken as 0.

2.1.2 Schrödinger equation applied to crystals

Schrödinger equation has to be solved for a solid system in a stationary state (ψ),

$$\hat{H} \cdot \psi(\vec{r}_1, \ldots, \vec{r}_n) = E \cdot \psi(\vec{r}_1, \ldots, \vec{r}_n) \tag{2.5}$$

where the Hamiltonian can be expressed as,

$$\begin{aligned}\hat{H} &= \hat{T}_e + \hat{T}_n + \hat{V}_{ee} + \hat{V}_{nn} + \hat{V}_{en} = \\ &= \sum_{i=1}^{N}\frac{-\hbar^2}{2m}\nabla^2(\vec{r}_i) + \sum_{\alpha=1}^{N_n}\frac{-\hbar^2}{2M_\alpha}\nabla^2(\vec{r}_\alpha)) + \sum_{i=1}^{N}\sum_{j>i}^{N}\frac{e^2}{4\pi\epsilon_0\vec{r}_{ij}} + \\ &+ \sum_{\alpha=1}^{N_n}\sum_{\beta>\alpha}^{N_n}\frac{e^2 Z_\alpha Z_\beta}{4\pi\epsilon_0\vec{r}_{\alpha\beta}} - \sum_{i=1}^{N}\sum_{\alpha=1}^{N_n}\frac{e^2 Z_\alpha}{4\pi\epsilon_0(\vec{r}_i - \vec{r}_\alpha)}\end{aligned} \tag{2.6}$$

where the $\hat{T}_e$ and $\hat{T}_n$ terms correspond to the kinetic energy of electrons and nuclei, respectively. $\hat{V}_{ee}$, $\hat{V}_{nn}$ and $\hat{V}_{en}$ terms are the potential interaction energy for electron-electron, nucleus-nucleus and electron-nucleus, respectively. $\vec{r}_i$ stands for electron i position vector, $\vec{r}_{ij} = \vec{r}_i - \vec{r}_j$ is the vector that specifies the relative position between electron i and j, $\vec{r}_\alpha$ defines the α nucleus position vector, $\vec{r}_{\alpha\beta}$ is the vector for the relative position between α and β nuclei, m is the electron mass and M_α the nucleus mass. Equation 2.6 can be simplified by taking into account the Born-Oppenheimer approximation. Thus, the electrons have an instantaneous response to slower nuclei motion since the bigger mass of the nuclei compared to the electron. According to this, nuclei can remain fixed at different $\vec{r}_\alpha$ positions whereas electronic states of the system can be obtained at these fixed nuclear positions. So, the electronic Hamiltonian can be then expressed as,

$$\hat{H}_e = \hat{T}_e + \hat{V}_{ee} + \hat{V}_{en} \tag{2.7}$$

Thus, if the field created over a single electron i in a specific space point $\vec{r}_i$ by other electrons is considered as $\Omega_i(\vec{r}_i)$, and the effective potential for this same electron i due to the fixed $\vec{r}_\alpha$ nuclei distribution is $v_i(\vec{r}_i)$, the single electron Hamiltonian in atomic units, has the form,

$$\hat{h}_i(\vec{r}_i) = \left[-\frac{1}{2}\nabla^2(\vec{r}_i) + \Omega_i(\vec{r}_i) + v_i(\vec{r}_i)\right] \tag{2.8}$$

so the electronic Hamiltonian can be reduced to a sum of single electron Hamiltonians,

$$\hat{H}_e = \sum_i \hat{h}_i(\vec{r}_i) \tag{2.9}$$

and the total energy can be expressed as a summation of all the energies per particle,

$$E_e = \sum_i \epsilon_i \tag{2.10}$$

On the other hand, valence electrons play the most important role in chemical reactivity while core electrons remain as spectators close to the nuclei. Consistently, electrons weakly attached to the nuclei must be considered while the core ones can be considered as a part of the ionic nuclei. The Hamiltonian can thus be expressed as,

$$\hat{H}_e \cong \hat{H}_e^V = \hat{T}_e^V + \hat{V}_{ee}^V + \hat{V}_{en}^V \tag{2.11}$$

where the V superscript accounts for valence electrons.

2.1.3 Bloch's Theorem

Bloch's theorem allows the application of periodicity in the Hamiltonian. This periodicity or translational symmetry of the Bravais lattice implies,

$$v(\vec{r}) = v(\vec{r} + \vec{T}) \tag{2.12}$$

where $\vec{T}$ is the Bravais lattice translation vector. Thus, Bloch's theorem specifies that solution functions of monoelectronic Schrödinger equation will take the form,

$$\psi_{\vec{k}}(\vec{r}) = e^{i\vec{k}\vec{r}} U_{\vec{k}}(\vec{r}) \tag{2.13}$$

called *Bloch functions*. These functions, are specified by a wave vector $\vec{k}$ and constructed by the product of a free electron wavefunction and a periodic function that ensures, obviously, the periodicity,

$$U_{\vec{k}}(\vec{r}) = U_{\vec{k}}(\vec{r} + \vec{T}) \tag{2.14}$$

From this theorem it can be deduced that:

- Eigenvalues of Schrödinger equation, E_e, depend on $\vec{k}$, since $\hat{H}_e$ and ψ are parametrised with it.
- $E_e(\vec{k})$ is quantised by the boundary condition but is in principle continuous. Moreover, it is an even function where $\vec{k} = (0, 0, 0)$ is an extreme value.
- $\vec{k}$ vectors can be always selected inside the first Brillouin zone.

Special attention has to be devoted to the last deduction. Thus, due to the symmetry properties of an infinite crystal, plane waves with wave vectors that do not differ by a reciprocal lattice vector ($\vec{G}$) do not couple, (i.e., $< \psi_{\vec{k}} | h(\vec{r}_i) | \psi_{\vec{k}'} >= 0$ for $\vec{k} \neq (\vec{k}' + \vec{G})$. Hence, the expansion of any wavefunction only contains plane waves that differ by reciprocal lattice vectors. To determine the total energy of a crystal, still a summation over the lowest eigenvalues has to be performed. For infinite periodic systems, this band structure energy in the total energy expression has to be replaced by an integral over the first Brillouin zone,

$$\sum_i \epsilon_i \rightarrow \sum_{bands_j} \frac{V}{(2\pi)^3} \int_{BZ} \epsilon_j d\vec{k} \tag{2.15}$$

where over all occupied energy bands has to be summed. Fortunately, this integral can be approximated by a sum over a finite set ok $\vec{k}$-points. In practice this means that one performs a number of calculations for different $\vec{k}$-points. The electron density ($\rho(\vec{r})$) in real space is also constructed by a Fourier transform over these $\vec{k}$-points. Finally the eigenenergies $\epsilon_j(\vec{k})$ at the different $\vec{k}$-points are summed up for the band structure term. The size of the Fourier coefficients matrix is determined by the number of plane waves in the expansion of wavefunctions. As a parameter characterizing the size of the plane wave basis set usually the kinetic energy of the highest Fourier component, the so-called cut-off energy is used.

$$\max_{\vec{G}} \frac{\hbar^2}{2m} |\vec{G} + \vec{k}|^2 = E_{cut-off} \tag{2.16}$$

In short, in the infinite solid models, the electron is supposed to behave as a free electron so, the wavefunction is just a *plane wave* ($e^{i\vec{k}\vec{r}}$) modulated by a function that contains information about the lattice periodicity ($U_{\vec{k}}(\vec{r})$). Thus, the total function is the above defined Bloch function 2.13. The number of plane waves that are necessary for defining the wavefunction are infinite, but this unphysical possibility is solved by working with a finite set of plane waves, whose kinetic energies are below a limit ($E_{cut-off}$).

2.2 Density Functional Theory

Due to the huge amount of atoms involved in crystalline systems, density functional theory (DFT) (1, 2) is widely used for their study since time consumption is much lower than by using *ab initio* post-HF methods, which are much more computationally expensive.

The basis of DFT is to work with electronic density (ρ) in order to determine the energetics of a system. The philosophy is different from *ab initio* calculations, where the wavefunction of the system is the initial statement for any calculation.

For a specific N-electronic system the ground electronic state is defined by,

$$\psi(\vec{x}_1, \vec{x}_2, \ldots, \vec{x}_N) \tag{2.17}$$

where N is the number of total electrons of the system and $\vec{x}_i(\vec{r}_i, \vec{s}_i)$ are the full set of spatial ($\vec{r}_i$) and spin ($\vec{s}_i$) coordinates for each electron. The probability of finding electron (1) between $\vec{x}_1$ and $\vec{x}_1 + d\vec{x}_1$, independently of where the others are found, is specified by,

$$\rho(\vec{x}_1) = N \int \psi(\vec{x}_1, \vec{x}_2, \ldots, \vec{x}_N)\psi^*(\vec{x}_1, \vec{x}_2, \ldots, \vec{x}_N)d\vec{x}_2 \ldots d\vec{x}_N \tag{2.18}$$

where $\rho(\vec{x}_1)$ is the *density function* for electron 1.

If equation 2.18 is integrated with respect to the spin coordinate of electron 1, the electronic density ($\rho(\vec{r}_1)$) is found,

$$\rho(\vec{r}_1) = \int \rho(\vec{x}_1)ds_1 = N \int \psi(\vec{x}_1, \vec{x}_2, \ldots, \vec{x}_N)\psi^*(\vec{x}_1, \vec{x}_2, \ldots, \vec{x}_N)ds_1 d\vec{x}_2 \ldots d\vec{x}_N \tag{2.19}$$

with the property that when $\vec{r}_1 \to \infty$, the electronic density tends to zero. Furthermore, electronic density is an experimentally measurable observable, from which energy can be calculated. Thus, the basic statement of DFT of working with a physical observable is fulfilled. To check this, it is a good choice to start supposing that ψ is normalised, so,

$$\int \rho(\vec{r})d\vec{r} = N \tag{2.20}$$

For this N-electronic system, N_α electrons have α spin and the remaining N_β electrons have β spin. So, it is possible to define the electron densities corresponding to the α and β electrons separately, $\rho^\alpha(\vec{r})$ and $\rho^\beta(\vec{r})$, respectively. The particular case of $\rho^\alpha(\vec{r}_1)$,

$$\rho^\alpha(\vec{r}_1) = N_\alpha \int \psi(\vec{x}_1, \vec{x}_2, \ldots, \vec{x}_N)\psi^*(\vec{x}_1, \vec{x}_2, \ldots, \vec{x}_N) ds_1 d\vec{x}_2 \ldots d\vec{x}_N \tag{2.21}$$

gives the probability of finding electron 1 with α spin between $\vec{r}_1$ and $\vec{r}_1 + d\vec{r}_1$.

The difference,

$$\rho^s(\vec{r}) = \rho^\alpha(\vec{r}) - \rho^\beta(\vec{r}) \tag{2.22}$$

constitutes the so-called spin density. A value of $\rho^s > 0$ indicates an α-density excess at point $\vec{r}$. Notice that in the density function (equation 2.18) the presence of other electrons in the system is not taken into account. To that end the *second order density function* ($\gamma_2(\vec{x}_1, \vec{x}_2)$) is used and gives the probability of finding electron 1 between $\vec{x}_1$ and $\vec{x}_1 + d\vec{x}_1$ and electron 2 between $\vec{x}_2$ and $\vec{x}_2 + d\vec{x}_2$, independently of where the others are found,

$$\gamma_2(\vec{x}_1, \vec{x}_2) = N(N-1) \int \psi(\vec{x}_1, \vec{x}_2, \ldots, \vec{x}_N)\psi^*(\vec{x}_1, \vec{x}_2, \ldots, \vec{x}_N) d\vec{x}_3 \ldots d\vec{x}_N \tag{2.23}$$

where $N(N-1)$ are the possible electron pairs that can be formed.

Integrating with respect to the spin variables, the two electron density or pair function is obtained,

$$\gamma_2(\vec{r}_1, \vec{r}_2) = \int \gamma_2(\vec{x}_1, \vec{x}_2) ds_1 ds_2 \tag{2.24}$$

which gives the probability of finding any two electrons, one between $\vec{r}_1$ and $\vec{r}_1 + d\vec{r}_1$ and the other between $\vec{r}_2$ and $\vec{r}_2 + d\vec{r}_2$, under any spin combination ($\alpha\alpha, \alpha\beta, \beta\alpha, \beta\beta$). In other words, the two electron density contains information about the correlated motion of two electrons. It is possible to define the exchange-correlation density ($\Gamma_{XC}(\vec{r}_1, \vec{r}_2)$) from,

$$\gamma_2(\vec{r}_1, \vec{r}_2) = \rho(\vec{r}_1)\rho(\vec{r}_2) + \Gamma_{XC}(\vec{r}_1, \vec{r}_2) \tag{2.25}$$

Considering electrons as uncorrelated independent particles, the term $\rho(\vec{r}_1)\rho(\vec{r}_2)$ is the two-electron density of finding an electron in $\vec{r}_1$ and another in $\vec{r}_2$. Consequently, the exchange-correlation density ($\Gamma_{XC}(\vec{r}_1, \vec{r}_2)$) represents the difference between the electron density of finding two electrons (one in $\vec{r}_1$ and other in $\vec{r}_2$) correlated or uncorrelated. Dividing equation 2.25 by $\rho(\vec{r}_1)$ leads to,

$$\frac{\gamma_2(\vec{r}_1, \vec{r}_2)}{\rho(\vec{r}_1)} = \rho(\vec{r}_2) + \rho_{XC}(\vec{r}_1, \vec{r}_2) \tag{2.26}$$

that results in the conditional electron density, which gives the two-electron density of finding one electron in $\vec{r}_2$ when there is already another one in $\vec{r}_1$. The term, $\rho_{XC}(\vec{r}_1, \vec{r}_2)$ is the so-called exchange-correlation or Fermi-Coulomb hole,

$$\rho_{XC}(\vec{r}_1, \vec{r}_2) = \frac{\Gamma_{XC}(\vec{r}_1, \vec{r}_2)}{\rho(\vec{r}_1)} \tag{2.27}$$

According to the last equations, the exchange-correlation hole is the correction term which must be added to the unconditional electronic density in order to obtain the conditional one, that defines the region around the electron in which the presence of others electrons is excluded to a greater or lesser degree.

Once, first and second order electron densities are known, electronic energy is known since as it is demonstrated below, it is a density functional.

Putting all together, and working in atomic units, the expected value for the system of N electrons and N_n nuclei can be expressed as[1],

$$E_{el} = \langle\psi|\hat{H}_{el}|\psi\rangle = \int_{\vec{r'}_1=\vec{r}_1} \left(-\frac{1}{2}\nabla^2(\vec{r}_1) + v_1(\vec{r}_1) \right) \rho_1(\vec{r}_1, \vec{r'}_1) d\vec{r}_1 + \frac{1}{2}\int\int \frac{\gamma_2(\vec{r}_1, \vec{r}_2)}{|\vec{r}_1 - \vec{r}_2|} d\vec{r}_1 d\vec{r}_2 \tag{2.28}$$

where the electronic single electron hamiltonian is defined by equation 2.8. Substituting equation 2.25 and 2.27 in the previous one, it is left with,

$$E_{el} = \int_{\vec{r'}_1=\vec{r}_1} \left(-\frac{1}{2}\nabla^2(\vec{r}_1) \right) \rho_1(\vec{r}_1, \vec{r'}_1) d\vec{r}_1 + \int v_1(\vec{r}_1)\rho(\vec{r}_1) d\vec{r}_1 + + \frac{1}{2}\int\int \frac{\rho(\vec{r}_1)\rho(\vec{r}_2)}{|\vec{r}_1 - \vec{r}_2|} d\vec{r}_1 d\vec{r}_2 + \frac{1}{2}\int\int \frac{\rho(\vec{r}_1)\rho_{XC}(\vec{r}_1, \vec{r}_2)}{|\vec{r}_1 - \vec{r}_2|} d\vec{r}_1 d\vec{r}_2 \tag{2.29}$$

where the terms are the kinetic energy of the electrons, the electron-nuclear potential energy, the Coulomb electronic repulsion and the electronic exchange-correlation energy, respectively. For the last term, it is possible to write,

$$W_{XC}[\rho] = \frac{1}{2}\int \rho(\vec{r}_1) \left[\int \frac{\rho_{XC}(\vec{r}_1, \vec{r}_2)}{|\vec{r}_1 - \vec{r}_2|} d\vec{r}_2 \right] d\vec{r}_1 = \int \rho(\vec{r}_1) v_{XC}(\vec{r}_1) d\vec{r}_1 \tag{2.30}$$

[1]In the particular case of a single electron system, the expected value of an operator $\hat{F}$ is given by $\langle F\rangle = \int \psi^*(\vec{x})\hat{F}\psi^*(\vec{x})d\vec{x}$. In the case of operators that contains only products or divisions, the expression resulting as a function of the electronic density is $\langle F\rangle = \int \hat{F}\rho(\vec{x})d\vec{x}$. In the case of operators that contain derivatives and other functions that impede the two functions ψ from being multiplied before applying the operator $\hat{F}$, we have,

$$\langle F\rangle = \int_{\vec{x'}=\vec{x}} \hat{F}\psi(\vec{x})\psi^*(\vec{x'})d\vec{x} = \int_{\vec{x'}=\vec{x}} \hat{F}\rho(\vec{x}, \vec{x'})d\vec{x}$$

where, first of all, $\hat{F}$ acts on the variable $\vec{x}$ and then, before proceeding onto the integration, the variable $\vec{x'}$ is transformed into $\vec{x}$, which is inidicated with $\vec{x'} = \vec{x}$ below the integration sign.

where W_{XC} is the exchange-correlation energy. Concretely, this term represents the interaction of $\rho(\vec{r}_1)$ with its exchange-correlation hole $\rho_{XC}(\vec{r}_1, \vec{r}_2)$. The electron interacts with an effective charge distribution corresponding to a positive electron, as follows from the sum rule. In short, equation 2.28 shows that it is possible to express the energy in terms of the first and second order density functions. Thus, the energy is a functional of the density.

It is worth noting that all the equations for single electron i contribution (i.e., to the energy and to the hamiltonian per particle terms: ϵ_i and $\hat{h}_i$, respectively) have a corresponding N-electronic one (E and $\hat{H}$, for total energy and hamiltonian, respectively).

2.2.1 The Hohenberg-Kohn theorems

DFT is based formally on two theorems stated by Hohenberg and Kohn:

- **FIRST THEOREM**: Any observable of a ground state, which is stationary and non-degenerate, can be calculated, exactly in theory, from the electronic density of the ground state. In other words, any observable can be written as a functional of the N-electron density of the ground state. For the cases where this theorem is valid,

$$E[\rho] = T[\rho] + V_{ee}[\rho] + v[\rho] \tag{2.31}$$

  where $T[\rho]$ and $V_{ee}[\rho]$ are universal functionals since they do not depend on the external potential ($v(\vec{r})$). They are usually encompassed within the Hohenberg-Kohn functional ($F_{HK}[\rho]$) with which,

$$E[\rho] = F_{HK}[\rho] + \int \rho(\vec{r}) v(\vec{r}) d\vec{r} \tag{2.32}$$

  where $E[\rho]$ indicates that, for a specific external potential $v(\vec{r})$, the energy is a functional of density.

- **SECOND THEOREM**: The N-electronic density of a non-degenerate ground state can be calculated, exactly in theory, determining the density that minimizes the energy of the ground state. This theorem provides the variational principle for $E[\rho]$. Thus, for a trial density, $\bar{\rho}(\vec{r})$ is fulfilled that

$$E[\bar{\rho}(\vec{r})] \geqslant E_0 \tag{2.33}$$

  where E_0 is the exact energy of the considered ground state. To demonstrate this equation it is necessary to apply the first Hohenberg-Kohn theorem to the trial density and to the exact one. According to this, it is left with,

$$E[\bar{\rho}(\vec{r})] = \left\langle \bar{\psi} | \hat{H} | \bar{\psi} \right\rangle \geqslant \left\langle \psi | \hat{H} | \psi \right\rangle = E_0 \tag{2.34}$$

where the inequality is a consequence of the variational principle. This principle assures that any trial density results in an energy greater or equal to the exact one for the ground state. Therefore, to obtain the exact density of the ground state, it is necessary to find the density that minimizes the energy according to,

$$\left[\frac{\delta E[\rho]}{\delta \rho}\right] = 0 \tag{2.35}$$

2.2.2 DFT fundamental equation

The second Hohenberg and Kohn theorem gives an important and basic tool to find the system energetics starting from the electronic density. The minimization of the energy functional respect to the electronic energy has to be done preserving the N-representability during the optimization process. This is done by introducing the restriction

$$\int \rho(\vec{r})d\vec{r} - N = 0 \tag{2.36}$$

by means of Lagrange undetermined multipliers method. For that, the following function is constructed,

$$E[\rho] - \mu\left(\int \rho(\vec{r})d\vec{r} - N\right) \tag{2.37}$$

where μ is the undefined Lagrange multiplier that has the meaning of a chemical potential (see (3) for further details). Next it is minimised,

$$\delta\left[E[\rho] - \mu\left(\int \rho(\vec{r})d\vec{r} - N\right)\right] = 0 \tag{2.38}$$

and proceeding from the definition of a functional differential it is left with,

$$\int \frac{\delta E[\rho]}{\delta \rho(\vec{r})}\delta\rho(\vec{r})d\vec{r} - \mu\int \delta\rho(\vec{r})d\vec{r} = 0 \tag{2.39}$$

and rearranging,

$$\int \left\{\frac{\delta E[\rho]}{\delta \rho(\vec{r})} - \mu\right\}\delta\rho(\vec{r})d\vec{r} = 0 \tag{2.40}$$

which gives the condition of constrained minimization and at the same time gives the expression for finding the minimum value of μ,

$$\mu = \frac{\delta E[\rho]}{\delta \rho(\vec{r})} = \frac{\delta F_{HK}[\rho]}{\delta \rho(\vec{r})} + v(\vec{r}) \tag{2.41}$$

This equation is the so-called fundamental equation of DFT. The Hohenberg-Kohn functional $F_{HK}[\rho]$ is the sum of terms that do not depend on the external potential.

$$F_{HK}[\rho] = T[\rho] + V_{ee}[\rho] \tag{2.42}$$

2.2.3 The Kohn-Sham method

Equation 2.41 gives an expression for the energy minimization for the ground state, but it is not possible to find the solution accurately. The problem that arises is that the exact expression relating F_{HK} with the density is unknown. In particular, the exact form of $T[\rho]$ is not known precisely enough. On the other hand, the kinetic energy is easily calculated if ψ is known. Proceeding from the expression of $T[\psi]$ for a single determinant function, Kohn and Sham proposed an ingenious method to calculate the energy from $\rho(\vec{r})$. For that purpose, they used a reference system of non interacting N-electrons that move under an external potential $v_s(\vec{r})$. This potential, when applied to the system, provides a wavefunction ψ, which has the same density as the real system. In this system, the electrons do not interact among themselves although there are Coulomb interactions with the nuclei. For such an ideal closed shell system, the HF method is exact, considering that without electron-electron interactions the orbital approximation leading to the HF equations provides the exact result. Here, the subscript "s" means that the variable is considered for a system that has the same density as that of the real system, but in which the electron-electron interactions are switched off.

The Hamiltonian for this such a system only contains the single-electron terms,

$$\hat{H} = \sum_{i=1}^{N} \hat{h}_s(\vec{r}_i) = \sum_{i=1}^{N} -\frac{1}{2}\nabla^2(\vec{r}_i) + \sum_{i=1}^{N} v_s(\vec{r}_i) \tag{2.43}$$

the exact wavefuntion of this system is the Slater determinant,

$$\psi = \frac{1}{\sqrt{N!}}|\chi_1\alpha(1)\chi_1\beta(2)\dots\chi_{N/2}\beta(N/2)| \tag{2.44}$$

where the crystal or molecule orbitals χ_i are obtained by solving the HF equations,

$$\left[-\frac{1}{2}\nabla^2(\vec{r}_i) + v_s(\vec{r}_i)\right]\chi_i = \epsilon_i\chi_i; \qquad \left\langle \chi_i \middle| \chi_j \right\rangle = \delta_{ij} \tag{2.45}$$

The exact density and the exact kinetic energy are, respectively,

$$\rho(\vec{r}) = \sum_{i=1}^{N_{OC}} |\chi_i(\vec{r}_i)|^2 \tag{2.46}$$

$$T_s[\rho] = \sum_{i=1}^{N_{OC}} \left\langle \chi_i \middle| -\frac{1}{2}\nabla^2(\vec{r}_i) \middle| \chi_i \right\rangle \tag{2.47}$$

where N_{OC} stands for the occupied number of orbitals (N/2 for a closed shell system).

The fundamental DFT equation can be written for this system as,

$$\frac{\delta E[\rho]}{\delta \rho(\vec{r})} = \frac{\delta T_s[\rho]}{\delta \rho(\vec{r})} + v_s(\vec{r}) = \mu \tag{2.48}$$

with,

$$E[\rho] = \sum_{i=1}^{N_{OC}} \epsilon_i = T_s[\rho] + \int \rho(\vec{r}) v_s(\vec{r}) d\vec{r} \tag{2.49}$$

Same equations could be written for a N-electron interacting system,

$$E[\rho] = T[\rho] + V_{ee}[\rho] + \int \rho(\vec{r}) v(\vec{r}) d\vec{r} \tag{2.50}$$

the exact kinetic energy for the real system $T[\rho]$ and that corresponding to the reference system $T_s[\rho]$ are different. The exact kinetic energy is reduced from equation 2.47 only in the case in which the HF solution is exact. The last equation can be rearranged as,

$$E[\rho] = T_s[\rho] + \int \rho(\vec{r}) v(\vec{r}) d\vec{r} + J[\rho] + (T[\rho] - T_s[\rho]) + (V_{ee}[\rho] - J[\rho]) \tag{2.51}$$

where as aforementioned, $T_s[\rho]$ is the kinetic energy of the electrons in a system with the same density that the real one, but in which the electron-electron interactions are not taken into account. $J[\rho]$ is the Coulomb repulsion,

$$J[\rho] = \frac{1}{2} \int \int \frac{\rho(\vec{r_1}) \rho(\vec{r_2})}{|\vec{r_1} - \vec{r_2}|} d\vec{r_1} d\vec{r_2} \tag{2.52}$$

It is possible to introduce the correlation kinetic energy $T_C[\rho]$ as the difference between the kinetic energy of the real system and that of the reference system,

$$T_C[\rho] = T[\rho] - T_s[\rho] \tag{2.53}$$

Moreover, the exchange-correlation energy $W_{XC}[\rho]$ of the N-electronic part is

$$W_{XC}[\rho] = V_{ee}[\rho] - J[\rho] \tag{2.54}$$

These last two contributions are mainly grouped in one simple term, $E_{XC}[\rho]$ which is the so-called total (or N-electron) exchange-correlation energy,

$$E_{XC}[\rho] = T_C[\rho] + W_{XC}[\rho] = (T[\rho] - T_s[\rho]) + (V_{ee}[\rho] - J[\rho]) \tag{2.55}$$

$E_{XC}[\rho]$ contains all the contributions to the energy, so it is not a simple expression. In particular, in $E_{XC}[\rho]$ the terms found are in the right side, the portion of kinetic

energy necessary to correct $T_s[\rho]$, and the correction made to the self-interaction introduced into the calculation of the electron repulsion based on equation 2.52. Taking into account equation 2.30 for single electron exchange correlation energy, the $E_{XC}[\rho]$ term for an N-electronic system is easily expressed as,

$$E_{XC}[\rho] = \int \rho(\vec{r}) v_{XC}(\vec{r}) d\vec{r} \tag{2.56}$$

so, applying equations 2.52, 2.54 and 2.55 to equation 2.51 the resulting total (or N-electronic) energy equation is

$$E[\rho] = T_s[\rho] + \int \rho(\vec{r}) v(\vec{r}) d\vec{r} + \frac{1}{2} \int \int \frac{\rho(\vec{r}_1)\rho(\vec{r}_2)}{|\vec{r}_1 - \vec{r}_2|} d\vec{r}_1 d\vec{r}_2 + E_{XC}[\rho] \tag{2.57}$$

Applying the fundamental equation of the DFT (equation 2.41) to the previous one leads to,

$$\frac{\delta E[\rho]}{\delta \rho(\vec{r})} = \frac{\delta T_s[\rho]}{\delta \rho(\vec{r})} + v(\vec{r}) + \int \frac{\rho(\vec{r}_2)}{|\vec{r}_1 - \vec{r}_2|} d\vec{r}_2 + \frac{\delta E_{XC}[\rho]}{\delta \rho(\vec{r})} = \mu \tag{2.58}$$

Defining the Coulomb potential as,

$$v_{cou}(\vec{r}) = v(\vec{r}) + \int \frac{\rho(\vec{r}_2)}{|\vec{r}_1 - \vec{r}_2|} d\vec{r}_2 \tag{2.59}$$

and the exchange-correlation potential following,

$$v_{XC}(\vec{r}) = \frac{\delta E_{XC}[\rho]}{\delta \rho(\vec{r})} \tag{2.60}$$

it is straightforward to get

$$\mu = \frac{\delta T_s[\rho]}{\delta \rho(\vec{r})} + (v_{cou}(\vec{r}) + v_{XC}(\vec{r})) = \frac{\delta T_s[\rho]}{\delta \rho(\vec{r})} + v_{eff}(\vec{r}) \tag{2.61}$$

Comparing the last two equations it is easy to conclude that the equation to solve for a system of interacting electrons is the same as for a system of electrons without interactions subjected to a potential $v_{eff}(\vec{r})$.

Consequently, the solution to the last equation is the same for equation 2.48, changing $v(\vec{r})$ for $v_{eff}(\vec{r})$. The equations to solve with,

$$v_{eff}(\vec{r}) = v(\vec{r}) + \int \frac{\rho(\vec{r}_2)}{|\vec{r}_1 - \vec{r}_2|} d\vec{r}_2 + v_{XC}(\vec{r}) \tag{2.62}$$

will therefore be,

$$\hat{h}_{KS}\chi_i(\vec{r}_i) = \epsilon_i \chi_i(\vec{r}_i); \quad \langle \chi_i | \chi_j \rangle = \delta_{ij} \tag{2.63}$$

where,

$$\hat{h}_{KS} = -\frac{1}{2}\nabla^2(\vec{r}) + v_{eff}(\vec{r}) \tag{2.64}$$

These equations are very similar to the HF equations. The χ_i orbitals, called Kohn-Sham orbitals, allow the immediate calculation of the electronic density proceeding from equation 2.46). Thus, the process to solve equations is equivalent to the method used for the Hartree-Fock method. Starting from an initial set of trial $\chi_i(\vec{r})$ molecular orbitals, the electronic density is calculated and the effective potential ($v_{eff}(\vec{r})$) is computed assuming some particular approach for the exchange-correlation term ($v_{XC}(\vec{r})$). Then, Khon-Sham equation is solved in order to find the eigenfunctions and the eigenvalues. The whole process is repeated until reaching the desired convergence.

It is important to stress that even if DFT method can contain all the electronic correlation energy, unlike Hartree-Fock methods, the expression for $v_{XC}(\vec{r})$ is not known, so the results will be always approximated. It can be said then that, the exact DFT method is a variational method but the fact of approximating the exchange-correlation energy does not allow the method to reach the exact energy of the system.

2.2.4 Exchange-correlation potential approaches

A good exchange-correlation potential is a basic aspect of the DFT. Equation 2.56 and 2.60 present the relationship existing between the exchange-correlation potential and the exchange-correlation energy. The equations,

$$E_{XC}[\rho] = \int \rho(\vec{r})\epsilon_{XC}[\rho]d\vec{r} = \int e_{XC}[\rho]d\vec{r} \tag{2.65}$$

$$v_{XC}(\vec{r}) = \frac{\delta(\rho(\vec{r})\epsilon_{XC}[\rho])}{\delta\rho(\vec{r})} = \frac{\delta e_{XC}[\rho]}{\delta\rho(\vec{r})} \tag{2.66}$$

relate the total exchange-correlation energy and potential with the exchange-correlation energy per particle (ϵ_{XC}) and with the exchange-correlation energy per unit volume (e_{XC}).

Two approximations are commonly used in order to compute the exchange-correlation potential $v_{XC}(\vec{r})$: the local density approach (LDA) and the generalised gradient approach (GGA).

Local Density Approach

In this approximation, the exchange-correlation energy ($E_{XC}[\rho]$) depends exclusively of the density,

$$E_{XC}^{LDA}[\rho] = \int \epsilon_{XC}^{LDA}[\rho]\rho(\vec{r})d\vec{r} \tag{2.67}$$

where the term $\epsilon_{XC}^{LDA}[\rho]$ is the exchange-correlation energy per particle. The contributions to the exchange and to the correlation are treated separately,

$$\epsilon_{XC}^{LDA}[\rho] = \epsilon_{X}^{LDA}[\rho] + \epsilon_{C}^{LDA}[\rho] \tag{2.68}$$

The homogeneous electron gas of constant density $\rho(\vec{r})$ is taken as a model for the part corresponding to the exchange,

$$\epsilon_{X}^{LDA}[\rho] = -\frac{9}{4}\alpha\left(\frac{3}{8\pi}\right)^{\frac{1}{3}}\rho^{\frac{1}{3}} \tag{2.69}$$

with $\alpha = 2/3$. For the correlation energy per particle ($\epsilon_C[\rho]$) there are several approaches available. Analytical expressions were proposed by Vosko, Wilk and Nusair (4) based on correlation energies calculated by means of Monte Carlo method. This approach is called local because it only depends on the electronic density value at each spatial point. This approximation works very well in systems in which the density is maintained approximately constant. It has been shown that good geometries, vibrational frequencies and charge densities are computed except in the nuclei surroundings. Nevertheless, it is not a good choice when weak bonds are present in the system.

Generalised Gradient Approach

GGA approach takes into account not only the spatial density at each point, but also the density gradients in order to improve the exchange-correlation energy per particle,

$$E_{XC}^{GGA}[\rho] = \int \epsilon_{XC}^{GGA}(\rho, \nabla\rho)\rho(\vec{r})d\vec{r} \tag{2.70}$$

and in the same manner as LDA approach, the contributions to the exchange and to the correlation energy are treated separately,

$$\epsilon_{XC}^{GGA}[\rho] = \epsilon_{X}^{GGA}[\rho, \nabla\rho] + \epsilon_{C}^{GGA}[\rho, \nabla\rho] \tag{2.71}$$

Geometries, vibrational frequencies and charge densities obtained within this approach improve the LDA results and give reliable thermochemical properties.

2.2.5 Pseudopotentials

As before mentioned, for chemical reactivity description purpose, valence electrons are much more important than the core ones, which are considered to stay unaltered when chemical processes are occurring. Pseudopotentials are based on this philosophy in order to lowering the computational cost of calculations. Thus, a pseudopotential can be described in two basic points:

- First, the core electrons are considered as a unique entity all together with the nuclei (*frozen core*), so only interaction between valence electrons and core has to be treated.

- Second, valence orbitals are replaced by *pseudofunctions* that obey the same behaviour from a minimum distance from the nuclei called the *core radius* (r_c) to longer distances. These pseudofunctions are responsible to represent the chemical bond.

A pseudopotential is constructed for each kind of atom in the system ensuring that Kohn-Sham eigenvalues for free electrons of isolated atoms are well reproduced. Electronic density has to be well described for distances higher than r_c.

The definition of r_c has to be done in order to ensure good portability of the pseudopotential and the computational cost. The same pseudopotential has to describe properly the atom interaction with the solid, liquid and/or gas phases of different compounds and has also to reproduce the atom scattering properties. For that purpose, the following condition has to be fulfilled,

$$\int_0^{r_c} |R_l^{ps}(r)|^2 r^2 dr = \int_0^{r_c} |R_l^{ae}(r)|^2 r^2 dr \tag{2.72}$$

where ps refers to the wave pseudofunction, ae stands for all electron orbitals and R for the radial part of the orbital l.

2.3 Methods for potential energy surfaces construction

A Potential Energy Surface (PES) is a function that describes the potential energy and its first derivatives for a specific system at any nuclear configuration for the ground or any electronic excited state. Thus, the PES construction (5, 6, 7, 8, 9, 10, 11, 12, 13) implies the calculation of many energies and derivatives of the system at several nuclear configurations. Then, interpolation or fitting methods are used in order to obtain the continuous and derivable representation function. The fitting of an analytical function is considered a global method meanwhile interpolation method uses local data to obtain the system information. In general, interpolation methods give an accurate description of the potential using much more data than analytical surfaces.

2.3.1 Analytical PES construction

The London-Eyring-Polanyi (LEP) function (14, 15) for $H + H_2 \rightarrow H_2 + H$ gas phase reaction, was derived from a valence bond approach as

$$V(r_1, r_2, r_3) = \sum_{i=1}^{3} Q_i(r_i) - \left[\frac{1}{2}\sum_{i<j}^{3}(U_i(r_i) - U_j(r_j))^2\right]^{\frac{1}{2}} \tag{2.73}$$

where i and j define the three interatomic distances ($1 \equiv AC, 2 \equiv BC, 3 \equiv AB$) of the system and Q_i and U_i are the Coulomb and exchange integrals, respectively, expressed for each pair of atoms (called here atom A and B) as,

$$Q_{AB}(r_3) = Q_3(r_3) = \left\langle \chi_A(1)\chi_B(2)\middle|\widehat{H}\middle|\chi_A(1)\chi_B(2)\right\rangle \tag{2.74}$$

$$U_{AB}(r_3) = U_3(r_3) = \left\langle \chi_A(1)\chi_B(2)\middle|\widehat{H}\middle|\chi_A(2)\chi_B(1)\right\rangle \tag{2.75}$$

where χ stands for the orbitals of each atom occupied by electron 1 or 2 and $\widehat{H}$ for the Hamiltonian of the system.

Afterwards, Sato introduced an adjustable parameter (Δ_i) in order to evaluate the orbital overlapping (16, 17) giving the final LEP-Sato (LEPS) expression as,

$$V(r_1, r_2, r_3) = \sum_{i=1}^{3}\left(\frac{Q_i(r_i)}{1+\Delta_i}\right) - \left[\frac{1}{2}\sum_{i<j}^{3}\left(\frac{U_i(r_i)}{1+\Delta_i} - \frac{U_j(r_j)}{1+\Delta_j}\right)^2\right]^{\frac{1}{2}} \tag{2.76}$$

For a general ABC system Q_i and U_i terms are estimated for each diatomic pair as,

$$Q_i(r_i) = \frac{D_i(r_i)}{4\big(1+\Delta_i\big)}\left[(3+\Delta_i)e^{-2\alpha_i(r_i - r_i^e)} - (2+6\Delta_i)e^{-\alpha_i(r_i - r_i^e)}\right] \tag{2.77}$$

$$U_i(r_i) = \frac{D_i(r_i)}{4\big(1+\Delta_i\big)}\left[(1+3\Delta_i)e^{-2\alpha_i(r_i - r_i^e)} - (6+2\Delta_i)e^{-\alpha_i(r_i - r_i^e)}\right] \tag{2.78}$$

where D_i, α_i and r_i^e are the well known Morse parameters (i.e., dissociation energy, Morse parameter and equilibrium distance).

For heterogeneous reactions (i.e., reactions over a surface) the potential energy is expressed as in equation 2.76, taking into account that two terms refer to the interaction of each atom (A and B) with the surface (s) and the third one refers to A and B atoms interaction (i.e. $1 \equiv As, 2 \equiv Bs$ and $3 \equiv AB$). Thus, the Q_i and U_i terms (i=1, 2) for the atom-surface interaction (Q_1, Q_2, U_1, U_2) must be X, Y and Z dependent, while for the diatomic molecule interaction (Q_3, U_3) the expressions must be r_3 dependent, as in equations 2.77 and 2.78 (figure 2.1).

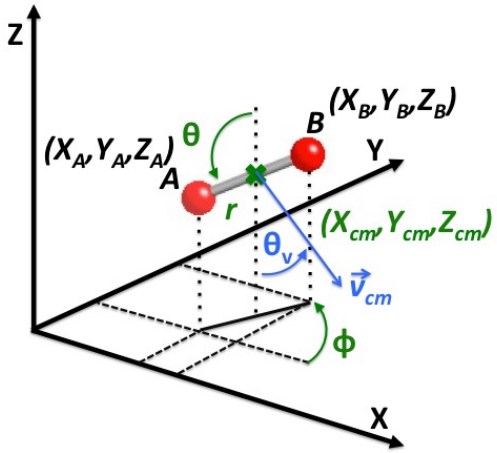

Figure 2.1: Sets of coordinates used to define the geometry of the two interacting atoms (A and B) over a solid surface. Internal coordinates (r, ϕ, θ, X_{cm}, Y_{cm}, Z_{cm}) (in green) and Cartesian coordinates (X_A,...,Z_B) (in black) are depicted.

In addition, in the heterogeneous treatment, it is important to ensure the periodicity of the surface. Thus, the Periodic LEPS model (PLEPS) (18, 19, 20) is introduced, where each Morse parameter for the atom-surface interaction (i.e., $i = 1, 2$) depends on X and Y coordinates by means of a Fourier expansion. The Fourier expansion depends not only on the total number of different sites used for the fit but also on the surface symmetry. For instance, the general expression of a Fourier expansion for two variables (u, v) takes the form,

$$P_j(u,v) = C_{00} + \sum_{n=1}^{\infty}\sum_{m=1}^{\infty}\left[C_{nm}cos\left(\frac{2n\pi u}{a} + \frac{2m\pi v}{b}\right) + S_{nm}sin\left(\frac{2n\pi u}{a} + \frac{2m\pi v}{b}\right)\right] \tag{2.79}$$

where a and b stand for the periods of the function and C_{00}, C_{nm} and S_{nm} are the Fourier coefficients which will be found by solving the system of equations for a set of sites for each P_j Morse parameter (e.g., $P_1 = D_1$). In addition, (u, v) represents the lattice coordinates for a given point of the surface.

An extension of the PLEPS model has been recently developed allowing to reach a good level of accuracy (Flexible PLEPS, FPLEPS) (20, 21, 22). For instance, in the case of the atom-surface system, a modified Morse potential is used instead of the classical Morse function in order to better describe the medium and short range interactions. Thus, the α_i Morse parameter (for $i = 1$ and 2) presents as well a Z dependence in order to describe both the attractive and

repulsive parts of the interaction potential of the atoms with the surface,

$$\alpha_i(X,Y,Z) = (1 - f_{s_{\alpha_i}}(Z)) \cdot \alpha_l(X,Y,Z) + f_{s_{\alpha_i}} \cdot \alpha_h(X,Y,Z) \tag{2.80}$$

where $f_{s_{\alpha_i}}$ is a switching function between the α_l and α_h functions, used for the repulsive (low Z values, Z_l) and attractive (high Z values, Z_h) parts, respectively, and obtained from the following equations that depend on α_0, α_1, $\alpha_0^{'}$ and $\alpha_1^{'}$ parameters obtained by the fitting procedure,

$$\alpha_h(X,Y,Z) = \alpha_0(X,Y) + \alpha_1(X,Y) \cdot Z \tag{2.81}$$

$$\alpha_l(X,Y,Z) = \alpha_0^{'}(X,Y) + \alpha_1^{'}(X,Y) \cdot Z \tag{2.82}$$

The expression for the switching function is,

$$f_{s_{\alpha_i}} = \frac{1}{2}\Big(1 + tanh(\varsigma \cdot Z - \zeta)\Big) \tag{2.83}$$

where ς and ζ are chosen to give a connection between repulsive and attractive part as smooth as possible.

Similarly, for the interaction between A and B atoms, $\alpha_3(r)$ is more flexible by using

$$\alpha_3(r_3) = \tilde{\alpha}_0 + \tilde{\alpha_1} \cdot r \tag{2.84}$$

which parameters are obtained from the molecular information (either experimental or DFT data).

For the specific case where only one atom is interacting with the surface, the general equation 2.76 for the potential can be simplified to,

$$V(X,Y,Z) = Q(X,Y,Z) \pm U(X,Y,Z) \tag{2.85}$$

where Q and U are calculated from equations 2.77 and 2.78 considering the X, Y and Z dependence of the Morse parameters. These two solutions correspond to a bound and to an unbound state. For the bound one, $(Q + U)$ a Morse-like potential is obtained,

$$V(X,Y,Z) = D_e(X,Y)\big(1 - e^{-\alpha(X,Y)(Z - Z_e(X,Y))}\big)^2 \tag{2.86}$$

so the resulting potential does not depend on the Sato parameter (Δ).

2.3.2 Interpolated PES construction

2.3.2.1 Corrugation Reducing Procedure

Within the rigid slab model for a system of one atom (A) interacting with a surface, the potential must be three dimensional ($V^{3D}(X_A, Y_A, Z_A)$), while for

describing the interaction of two atoms (A and B) with a surface must be six dimensional ($V^{6D}(X_A,\ Y_A,\ Z_A,\ X_B,\ Y_B,\ Z_B)$). In that case, the slab potential (V^{slab}) will be constant although the contribution could be added from DFT slab calculations or by using some empirical data (i.e., multidimensional PES). The potentials commonly used are for example pair potentials, where the electronic structure is replaced by a coefficient adjusted in such a way that some experimental structural properties of the solid are reproduced satisfactorily.

The Corrugation Reducing Procedure (CRP) has been used in many gas-surface systems (11, 23, 24). The corrugation term varies strongly with the atom or molecule position, so direct interpolation of the *ab initio* points (i.e., DFT) is not usually very satisfactory. The idea is to previously soften the data to be interpolated later. For the interaction of one atom (A) with the surface, a reference potential with the most of the atom-surface interaction is removed from the V^{3D} obtaining a softer function,

$$I^{3D}(X_A, Y_A, Z_A) = V^{3D}(X_A, Y_A, Z_A) - R^{3D}(X_A, Y_A, Z_A) \tag{2.87}$$

where ($X_A,\ Y_A,\ Z_A$) indicates the atom position over the surface and $R^{3D}(X_A,\ Y_A,\ Z_A)$ is usually expressed as a 1D pair potential summation,

$$R^{3D}(X_A, Y_A, Z_A) = \sum_{i=1}^{N} V^{1D}(r_i) \tag{2.88}$$

where r_i is the distance between the gas atom and an i atom from the surface, considering only the N closer surface atoms. Usually, V^{1D} is taken as the interaction potential of the gas atom with a particular surface atom direction, where the interaction is specially important and it is then interpolated by using cubic splines 1D (25, 26); thus, the $I^{3D}(X_A, Y_A, Z_A)$ function behaviour in (X, Y) is much softer. The 3D interpolation is done over the Z coordinate by using cubic splines and over X and Y with a Fourier expansion or cubic splines (26), in agreement with the cell symmetry. These methods ensure the first derivatives continuity. In addition, the spline function is defined at each interval as a third order polynomial and the derivatives are calculated analytically at each interval. Thus, the coherence between the interpolation and the derivatives is ensured.

Once the interpolation for I^{3D} is done, the V^{3D} potential can be obtained for any X_A, Y_A, Z_A configuration as,

$$V^{3D}(X_A, Y_A, Z_A) = I^{3D}(X_A, Y_A, Z_A) + \sum_{i=1}^{N} V^{1D}(r_i) \tag{2.89}$$

For the interaction of two atoms (A and B) with the surface the same criteria are used, thus,

$$\begin{aligned} I^{6D}(X_A, Y_A, Z_A, X_B, Y_B, Z_B) \;=\; & V^{6D}(X_A, Y_A, Z_A, X_B, Y_B, Z_B) + \\ & -R^{3D}(X_A, Y_A, Z_A) - R^{3D}(X_B, Y_B, Z_B) \end{aligned} \tag{2.90}$$

The average error (ΔE) done in the interpolation of N values can be computed by means of the root mean square deviation (RMSD),

$$\Delta E = \sqrt{\frac{1}{N}\sum_{i=1}^{N}(V^i_{interpolated} - V^i_{DFT})^2} \tag{2.91}$$

In most of the works where the CRP has been used, the interpolation was quite good, since the average error performed was ∼100 meV approximately.

2.3.2.2 Modified Shepard Interpolation Scheme in Cartesian coordinates for solid-gas interactions

The Modified Shepard Interpolation Scheme (MS) was firstly developed for gas phase reactions (27, 28) in order to obtain an automated way of constructing a PES. Due to its simplicity and good results, the method was quickly adapted for diatomic gas reactions over a surface (29, 30). The development was initially expressed in internal coordinates (i.e., internuclear distances) to simplify the expression of the system symmetry in gas phase. The implementation of the method for gas-surface interaction was also initially developed by using internal coordinates, but due to the specific symmetry requirements in the gas-surface systems some problems were found (i.e., translational symmetry was not properly described and both energy and first derivatives obtained for a configuration contained in the initial data were not satisfactorily reproduced). Thus, in order to solve these problems, a new development of the method was carried out by using Cartesian coordinates and implemented in the *surfMScoord*[1] code.

In order to obtain the interpolated energy for a specific geometrical configuration, weighted Taylor series around each of the available *ab initio* data points (N_{data}) were used,

$$V(\mathbf{X}) = \sum_{i=1}^{N_{data}} w^i(\mathbf{X}, \mathbf{X}^i) \cdot T^i(\mathbf{X}, \mathbf{X}^i) \tag{2.92}$$

where $\mathbf{X}$ stands for the configuration of the system where the energy wants to be known (i.e., $\mathbf{X} = (X_1, Y_1, Z_1, \ldots, Z_n)$ where n is the number of atoms) and $\mathbf{X}^i$ for the geometry of each *ab initio* point (DFT). $T^i(\mathbf{X}, \mathbf{X}^i)$ stands for the Taylor series developed around i evaluated at $\mathbf{X}$ and w^i for the normalised weight.

The weights are a probabilistic estimation of the accuracy of a given T^i term in describing the total interpolated energy. Obviously, the sum of all the weights

[1]The code was developed from scratch during the PhD, collaborating with Dr. Cédric Crespos from the University of Bordeaux I.

should give the unity. Thus, the normalised weight is,

$$w^i(\mathbf{X}, \mathbf{X}^i) = \frac{\nu^i(\mathbf{X}, \mathbf{X}^i)}{\sum_{i=1}^{N_{data}} \nu^i(\mathbf{X}, \mathbf{X}^i)} \tag{2.93}$$

where ν^i is the one-part primitive weight function,

$$\nu^i(\mathbf{X}, \mathbf{X}^i) = \frac{1}{d^p} \tag{2.94}$$

where d is the geometrical distance between both configurations (i.e., for one atom $((X_1 - X_1^i)^2 + (Y_1 - Y_1^i)^2 + \ldots + (Z_1 - Z_n^i)^2)^{1/2}$) and p is an adjustable parameter with values usually between 4 and 12. Thus, the closer $\mathbf{X}$ is to the configuration $\mathbf{X}^i$ the higher will be the primitive weight.

The Taylor expansion to the second order for the potential energy around the i point is calculated as,

$$\begin{aligned} T^i(\mathbf{X}, \mathbf{X}^i) &= V(\mathbf{X}^i) + \sum_{j=1}^{N_{coord}} (\mathbf{x}_j - \mathbf{x}_j^i) \left(\frac{\partial V(\mathbf{X})}{\partial \mathbf{x}_j} \right)_{\mathbf{X}=\mathbf{X}^i} + \\ &+ \frac{1}{2!} \sum_{j=1}^{N_{coord}} \sum_{l=1}^{N_{coord}} (\mathbf{x}_j - \mathbf{x}_j^i) \cdot (\mathbf{x}_l - \mathbf{x}_l^i) \left(\frac{\partial^2 V(\mathbf{X})}{\partial \mathbf{x}_j \partial \mathbf{x}_l} \right)_{\mathbf{X}=\mathbf{X}^i} \end{aligned} \tag{2.95}$$

where $\mathbf{x}_1 = X_1$, $\mathbf{x}_2 = Y_1$, $\ldots$, $\mathbf{x}_{N_{coord}} = Z_n$. Thus, the first and second derivatives are needed for each configuration belonging to the N_{data} *ab initio* points.

Analytical derivatives can be obtained easily by using the following expression,

$$\frac{\partial V(\mathbf{X})}{\partial \mathbf{x}_j} = \sum_{i=1}^{N_{data}} \left(\frac{\partial w^i(\mathbf{X}, \mathbf{X}^i)}{\partial \mathbf{x}_j} T^i(\mathbf{X}, \mathbf{X}^i) + w^i(\mathbf{X}, \mathbf{X}^i) \frac{\partial T^i(\mathbf{X}, \mathbf{X}^i)}{\partial \mathbf{x}_j} \right) \tag{2.96}$$

Thanks to the translational symmetry of gas-surface systems, only the unit cell is needed to describe the whole 2D surface. Thus, to take into account the periodic symmetry of the system, any configuration outside the unit cell will be well reproduced by looking for the equivalent one inside it. As the energy is calculated as a sum of Taylor expansions of the closest configurations in all the space directions, when the energy of a point next to the unit cell border is needed to be calculated, some of the configurations of the surrounding cells have to be taken into account. In the *surfMScoord* code, the total N_{data} configurations are formed by the central unit cell and a certain portion of the eight surrounding cells. In order to avoid an unnecessary high number N_{data}, the portion of the surrounding cells is selected by a single parameter (*outln*).

In many cases the whole unit cell can be generated by symmetry operations (i.e., σ mirror planes) starting from a minimum area. The use of these symmetry

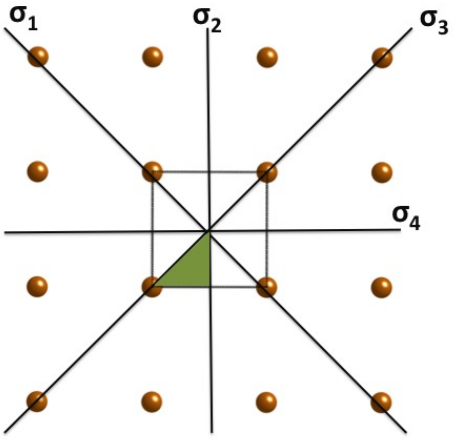

Figure 2.2: Minimum triangle (green) and symmetry planes of a generic cubic unit cell, which are used to produce the unit cell.

operations allows to minimize the number of configurations to be computed and the total computing time. As an example, in figure 2.2 the minimum triangle is used to generate the unit cell by using mirror planes.

To illustrate with some numbers the total N_{data} points used for performing the interpolation in the cubic system shown above, we consider 300 configurations inside the minimum triangle area. These 300 configurations will produce a total of 2,400 configurations inside the (1×1) unit cell (300×8). Moreover, if the whole eight surrounding cells were considered (3×3 supercell), a total of 21,600 configurations would be generated to describe the system, but if *outln* parameter is set to 0.5, N_{data} will be reduced to only 9,600.

These data reduction is very important to minimize the computing time for a single energy and first derivative interpolation. Nevertheless, experience shows that this reduction is not enough to compute trajectories in an acceptable time. Thus, a local data reduction was introduced considering that only the closer configurations are relevant for the interpolation. The concept of a tolerance weight (w_{tol}) was introduced considering that configurations with a normalised weight lower than the tolerance weight should not be considered. Depending on the system and the values of the tolerance weight, this restriction can reduce the total number of configurations in the summation 2.92 to less than 100, with a negligible effect on the energy and first derivatives calculation. Several tests done with the oxygen graphite system show that this procedure can reduce the computing time more than one order of magnitude.

One of the properties of the Modified Shepard interpolation is that the number of N_{data} *ab initio* points do not need to be calculated as a regular grid over the configuration space. This property allows to add configurations selectively in the areas where the dynamics is expected to be more important, avoiding the calculation of points where it is not necessary. Thus, the construction of the PES can be started from a small set of configurations and progressively grown automatically until convergence of some dynamical properties is reached. The general procedure is schematically described in figure 2.3 and can be splitted in two general processes:

1. a certain number of configurations are added to the initial set of *ab initio* configurations (N_{data}) used to describe the PES as follows:
   - a small batch of trajectories (i.e., $N_{small} = 10$) are carried out in order to store their configurations along time.
   - among the stored configurations (N_{store}) some of the most relevant ones are selected by means of some specific criterion.
   - the energy, first and second derivatives of the selected N_{add} configurations are computed using DFT and added, increasing the number of *ab initio* points to $N_{data} + N_{add}$.
   - the process is repeated several times (N) from the first step using the PES with the new data.
2. Once finished this previous loop, a bigger batch of trajectories (i.e., $N_{big} = 5,000$) is run and some dynamical properties of interest are calculated (i.e., reaction probabilities, polar scattering angles, ...). These properties are compared with the calculated ones in the previous loop. If convergence is reached between two consecutive loops the process is ended, otherwise the process is started again from the first step.

Two criteria are used to select the N_{add} (usually one or two) configurations to be added from the N_{store} points. One of them, considers that the best location to improve the PES accuracy would be to include the most dynamically important regions (just the zones where the main part of trajectories pass through), taking into account that there are not already many data points there. This criterion can be expressed using the h index for j configuration,

$$h^j = \frac{\sum_{m=1,m\neq j}^{N'_{store}} \nu^m(\mathbf{X}^j, \mathbf{X}^m)}{\sum_{i=1}^{N_{data}} \nu^i(\mathbf{X}^j, \mathbf{X}^i)} \tag{2.97}$$

where N'_{store} stands for the N_{store} configurations stored directly from the trajectory calculation plus all the symmetrically equivalent configurations inside the

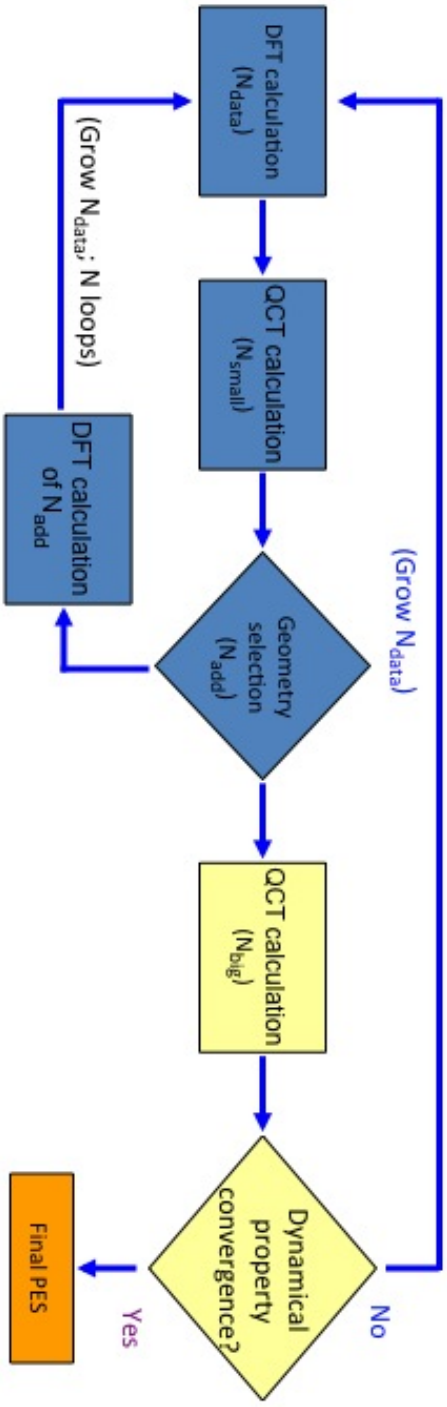

Figure 2.3: General flux diagram of the MS method used for PES construction.

unit cell and the surrounding ones. From N_{store} configuration we select the N_{add} ones that presents larger h_j indexes.

The second criterion estimates the uncertainty of each j configuration evaluating the variance associated as follows,

$$\sigma_j^2 = \sum_{i=1}^{N_{data}} w^i(\mathbf{X}^j, \mathbf{X}^i) \cdot \left[T^i(\mathbf{X}^j, \mathbf{X}^i) - V(\mathbf{X}^j)\right]^2 \tag{2.98}$$

Thus, if the Taylor series of the closest data points (with significant w^i) evaluate the configuration j very differently from the regular interpolation, this j configuration is considered as inaccurate and the σ_j^2 value will be large. Again, from the N_{store} configurations, the N_{add} ones that present larger σ_j^2 indexes are selected in order to improve the description of the interpolated points.

Both criteria are alternated for each loop.

2.4 Quasiclassical Trajectory Method

Classical dynamics allows the study of the interactions of atoms and molecules over a solid surface in a classical physics background during a period of time. At the end of this time, the physical properties of interest are studied (i.e., reaction probabilities, final energies, scattering angles,...). Although the computational cost is low, no quantum effects are taken into account in these simulations.

The nuclear motion for a N atom system along the time can be calculated solving the $3N$ Hamilton equations of motion (31),

$$\dot{q}_i = \frac{\partial H}{\partial p_i}, \qquad \dot{p}_i = -\frac{\partial H}{\partial q_i}, \qquad i = 1, 2, \ldots, 3N \tag{2.99}$$

where q_i are the generalised coordinates, p_i the linear momenta and H the classical Hamiltonian of the system, which is defined as,

$$H = \sum_{j=1}^{3N} \left(\frac{1}{2m_j} p_j^2\right) + V(q_1 \ldots q_{3N}) \tag{2.100}$$

where m_j is the mass of each implied atom. The last term in equation 2.100 stands for the interaction potential of the system, or in other words, for the PES.

Solving the coupled system of differential equations in a precise time t implies the knowledge of the system in the previous time step $t - \Delta t$. Among many others, the Beeman algorithm (32) integrates the system along time with a quick, accurate and simple way. The recursive method requires information about the trajectory in t and $t - \Delta t$ in order to get information at $t + \Delta t$.

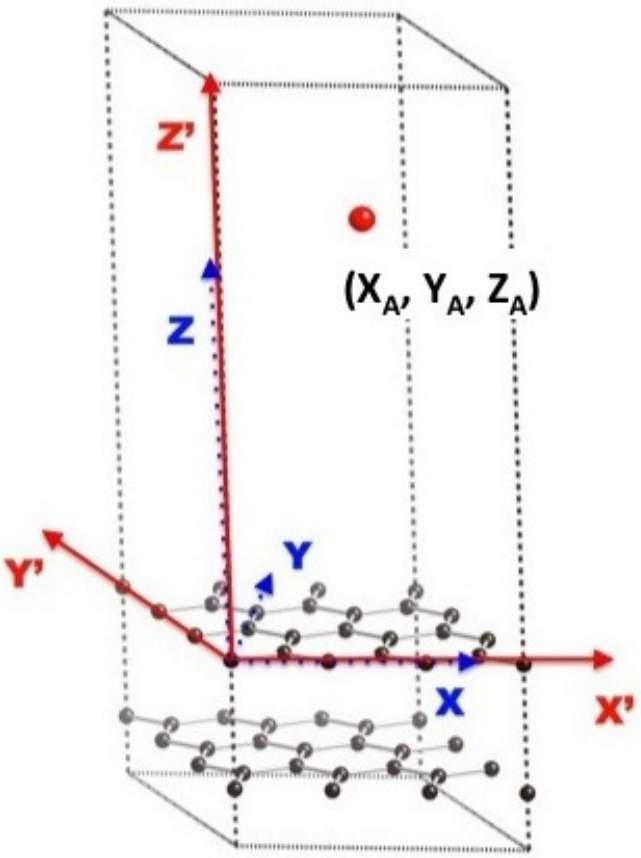

Figure 2.4: (X, Y, Z) orthogonal system of coordinates used in trajectory calculations over a solid surface (e.g., graphite) along with the oblique (X', Y', Z') coordinates.

For gas-surface dynamics assuming a rigid slab (i.e., solid without movement), the coordinate system is fixed and usually localised over a first layer atom of the solid (figure 2.4).

The initial (X, Y) position for the atom (X_A, Y_A) or the molecular center of mass (X_{cm}, Y_{cm}) are randomly selected inside the (1×1) unit cell by using random numbers (ξ_i) (33). These numbers are multiplied by the a and b cell parameters in order to obtain a randomly distribution of positions inside the unit cell by using the equations,

$$\begin{aligned} X_A &= a \cdot \xi_1 \\ Y_A &= b \cdot \xi_2 \end{aligned} \tag{2.101}$$

In figure 2.5, the initial positions for randomly atomic sampling of the unit cell are presented for 10,000 trajectories (N_T).

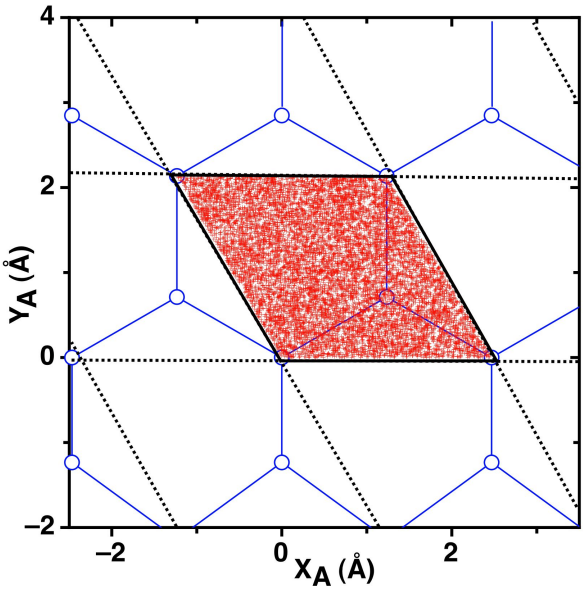

Figure 2.5: Random initial sampling of the atomic positions (X_A, Y_A) for 10,000 trajectories inside an (1×1) unit cell (e.g., graphite cell).

The initial Z_A for the atom or Z_{cm} for the molecule are selected large enough to ensure that there is no interaction with the surface. The initial velocity vector (θ_v) corresponding to a selected kinetic collision energy (E_{col}) for the atom or the molecular center of mass (figure 2.1) is selected between 0° and 90° whereas ϕ_v for off normal incidence is randomly selected between 0° and 360°.

In order to define the initial molecule geometry, the internuclear distance (r) is chosen between the corresponding inner (r_-) and outer (r_+) turning points for

a selected (v, j). Initial θ and ϕ angles (figure 2.1) are randomly selected between 0° and 360°. Furthermore, the angle η defining the orientation of $\vec{L}$ vector was randomly selected within 0° and 360°.

2.4.1 Generalised Langevin oscillator model

In a conservative system, the energy is conserved during the atomic or molecular collision. Nevertheless, it is desirable to include dissipation effects and surface temperature in the gas-surface dynamic simulations. Therefore, the substrate should not only act as a sink but also as a source from which energy can be transferred or received (heat bath), in order to model both thermalization and accommodation processes. A method for accomplishing the above is the Generalised Langevin Oscillator (GLO) model (34, 35, 36).

The surface motion can be represented in terms of a single 3D harmonic oscillator of mass m_s with coordinates $\vec{r}_s(X_s, Y_s, Z_s)$ and an associated 3×3 frequency matrix $\hat{\omega}_3$ (surface oscillator model). Then, the molecule-surface phonon coupling for an AB gas-rigid surface, whose 6D PES can be expressed using the Cartesian coordinates $\vec{r}_A(X_A, Y_A, Z_A)$ and $\vec{r}_B(X_B, Y_B, Z_B)$, is introduced by a space rigid shift $\vec{r}_s$ (X_s, Y_s, Z_s) of the 6D PES for the molecule in front of the rigid surface,

$$V(\vec{r}_A, \vec{r}_B; \vec{r}_s) = V^{6D}(\vec{r}_A - \vec{r}_s, \vec{r}_B - \vec{r}_s) \tag{2.102}$$

The GLO model adds dissipation and thermal fluctuation with the help of a ghost 3D oscillator with coordinates $\vec{r}_g(X_g, Y_g, Z_g)$ and associated 3×3 frequency matrix $\hat{\omega}_1$(figure 2.6).

The ghost and surface oscillators are coupled by a 3×3 frequency matrix ($\hat{\omega}_2$). Moreover, the ghost oscillator is subject to a viscous friction force with a damping matrix $\hat{\gamma}_g$ and to a fluctuation (random) force f_{rand} (Δt), whose one-time average value vanishes. The latter is obtained from a Gaussian white noise source and variance $(2k_B \cdot T_{surf} \cdot \gamma_g \cdot m_s/\Delta t)^{1/2}$, which will be generated for each integration step (Δt)

$$f_{rand}(\Delta t) = g_i\big(2 \cdot k_B \cdot T_{surf} \cdot \gamma_g \cdot m_s/\Delta t\big)^{1/2} \tag{2.103}$$

where g_i is a random number generated with a typical *gasdev* function (figure 2.7). This function is based on the polar form of the Box-Muller transformation that allows to transform uniformly distributed random variables to a new set of random variables with Gaussian (or Normal) distribution.

The 12 equations (i.e., 4×3) of motion to be integrated will be

$$\frac{d^2\vec{r}_A}{dt^2} = -\frac{1}{m_A}\vec{\nabla}_{\vec{r}_A} V^{6D}(\vec{r}_A - \vec{r}_s, \vec{r}_B - \vec{r}_s) \tag{2.104}$$

$$\frac{d^2\vec{r}_B}{dt^2} = -\frac{1}{m_B}\vec{\nabla}_{\vec{r}_B} V^{6D}(\vec{r}_A - \vec{r}_s, \vec{r}_B - \vec{r}_s) \tag{2.105}$$

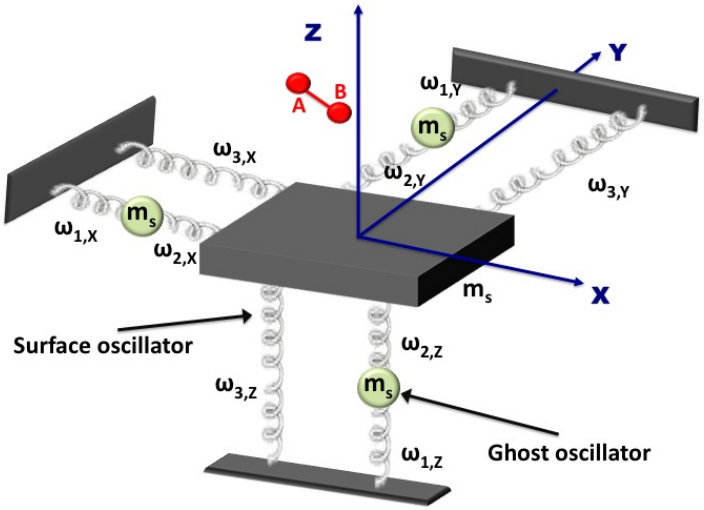

Figure 2.6: GLO model

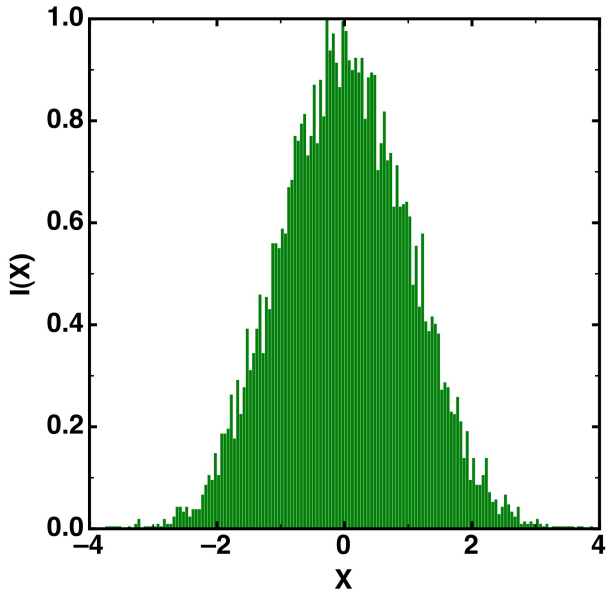

Figure 2.7: distribution of Gaussian random numbers (x) generated by using the *gasdev* function with an unit variance. 10000 calls are recorded and binned in Δx intervals of 0.05.

$$\frac{d^2\vec{r}_s}{dt^2} = -\frac{1}{m_s}\vec{\nabla}_{\vec{r}_s} V^{6D}(\vec{r}_A - \vec{r}_s, \vec{r}_B - \vec{r}_s) - \hat{\Omega}_p^2 \vec{r}_s + \hat{\Lambda}_0^{1/2}\hat{\omega}_0 \vec{r}_g \tag{2.106}$$

$$\frac{d^2\vec{r}_g}{dt^2} = -\hat{\omega}_0^2 \vec{r}_g + \hat{\Lambda}_0^{1/2}\hat{\omega}_0 \vec{r}_s - \hat{\gamma}_g \frac{d\vec{r}_g}{dt} + \frac{1}{m_s} f_{rand}(\Delta t) \tag{2.107}$$

Equations 2.104 and 2.105 will correspond to the accelerations of A and B atoms. Equation 2.106 describes the surface acceleration considering the rigid solid as a 3D oscillator of mass m_s.

Equation 2.107 concerns to the 3D ghost oscillator, including the friction (dissipation) and random (fluctuation) forces in the last two terms, which would represent the simplest Langevin equation for a free Brownian particle in absence of a potential (i.e., equation with only the last two terms). The friction and random forces are related through the second fluctuation-dissipation theorem, which qualitatively states that the energy dissipated must balance the energy introduced by the fluctuations in order to maintain the bath temperature. The frequency matrices ($\hat{\omega}_0$, $\hat{\Lambda}_0^{1/2}$, $\hat{\Omega}_p$) , which appear in these equations, are related with previous frequency matrices ($\hat{\omega}_1$, $\hat{\omega}_2$, $\hat{\omega}_3$) through the expressions:

$$\begin{aligned} &\Omega_{p,i}^2 = \omega_{2,i}^2 + \omega_{3,i}^2 \\ &\omega_{0,i}^2 = \omega_{1,i}^2 + \omega_{2,i}^2 \qquad (i = 1,2,3 \text{ for } x, y, z;\ \text{units of } \omega_{j,i} \text{ are time}^{-1}) \\ &\Lambda_{0,i}^{1/2}\omega_{0,i} = \omega_{2,i}^2 \end{aligned} \tag{2.108}$$

(see Appendix A for more details).

The surface oscillator (SO) model can be obtained from the GLO one removing equation 2.107 and the term related with $\vec{r}_g$ in equation 2.106, becoming the system conservative.

The initial coordinates ((X_g, Y_g, Z_g), (X_s, Y_s, Z_s)) and linear momenta ((p_{x_g}, p_{y_g}, p_{z_g}), (p_{x_s}, p_{y_s}, p_{z_s})) of ghost and surface particles, respectively, are generated using as well the *gasdev* function (see Appendix A for more details). The parameters of ($\hat{\omega}_0$, $\hat{\Lambda}_0^{1/2}$, $\hat{\Omega}_p$, $\hat{\gamma}_g$) matrices can be derived from knowledge of the surface and its vibrations. These can be chosen to reproduce experimental or computed information about the phonon spectral density ($\rho(\omega)$) of the solid. Moreover, some prescription for constructing the parameters matrices have been given by some authors (34, 35), based mainly on the bulk and surface Debye frequencies, or equivalently, the mass-weighted bulk and surface normal mean square displacements. Nevertheless, the sensitivity results to variations on these parameters are quite modest.

Usually, all matrices are assumed to have a diagonal form (i.e., uncorrelated friction and random forces) in the most recent studies (36, 37). Moreover, these latter studies confirm that the dynamical results are few sensitive to changes on these frequency values, even when those are modified by two orders of magnitude

(36, 37). Thus, for a Debye solid model,

$$\rho(\omega) = \frac{3}{\omega_D^3}\omega^2 \cdot \eta(\omega_D - \omega) \tag{2.109}$$

where $\eta(x)$ is an unit step function which cuts off the distribution for frequencies greater than the Debye frequency (ω_D), Ω_p or ω_0 can be estimated from

$$\Omega_p \approx \omega_0 \approx \frac{\omega_D}{\sqrt{3}} \tag{2.110}$$

The damping (friction) constants ($\hat{\gamma}_g$) are assumed to be isotropic too and can be chosen from the bulk or surface Debye frequencies of the solid by using (34, 38)

$$\gamma_{g,x} = \gamma_{g,y} = \gamma_{g,z} = \frac{\pi\omega_D}{6} \tag{2.111}$$

The mass (m_s) associated with the surface and ghost oscillators can be taken as an effective mass and will be similar (within a factor of 5 or so) to the mass of the real surface atoms (39). In fact, the incoming atom or molecule can interact with more than one surface atom (Armand effect (40)) during the collision due to the finite size of the projectile, which can justify even more the use of an effective mass.

The GLO procedure has been introduced in our *qctsurf* code using the FORTRAN subroutines from Fabio Busnengo, Antoine Salin and Ludovic Martin.

2.4.2 Product analysis

The reaction probabilities (P_i) and its statistical associated error (ΔP_i) are calculated as,

$$P_i = \frac{N_i}{N_T} \tag{2.112}$$

$$\Delta P_i = P_i\sqrt{\frac{N_T - N_i}{N_T \cdot N_i}} \tag{2.113}$$

where N_i are the reactive trajectories for process i and N_T correspond to the total number of calculated trajectories.

The product molecules (AB) formed or initially scattered in gas-solid elementary processes will have a final vibrorotational state ($v^{'}$, $j^{'}$). A quasiclassical approach allows to assign the quantum numbers.

The total energy for the molecules in gas phase (internal and translational energy (41)) can be expressed as,

$$E = E_{col}^{'} + E_{int}^{'} \tag{2.114}$$

The positions of the A and B molecule atoms ($\vec{r_i}$) and the linear momenta ($\vec{p_i}$) are known at the end of the trajectory and the center of mass position vector can be calculated as,

$$\vec{r}_{cm} = \frac{m_A \cdot \vec{r}_A + m_B \cdot \vec{r}_B}{M_{total}} \tag{2.115}$$

where $\vec{r}_A = (X_A, Y_A, Z_A)$ and $\vec{r}_B = (X_B, Y_B, Z_B)$ are the position vectors for each of the A and B atoms and M_{total} is the sum of the atomic masses. In a similar way, the velocity vector for the center of mass can be calculated,

$$\vec{v}_{cm} = \frac{m_A \cdot \vec{v}_A + m_B \cdot \vec{v}_B}{M_{total}} \tag{2.116}$$

In addition, the relative velocity vector of atom B respect to A is,

$$\vec{v}_R = \vec{v}_B - \vec{v}_A \tag{2.117}$$

and similarly, the relative position vector

$$\vec{r} = \vec{r}_B - \vec{r}_A \tag{2.118}$$

If the reduced mass of both atoms is introduced as,

$$\mu = \frac{m_A \cdot m_B}{m_A + m_B} \tag{2.119}$$

the translational energy of the molecule is obtained as the kinetic energy of the molecule in its center of mass

$$E'_{col} = \frac{1}{2} M_{total} \Big(v^2_{cm,X} + v^2_{cm,Y} + v^2_{cm,Z} \Big) \tag{2.120}$$

and the kinetic energy related to the internal movement,

$$E'_{kin(int)} = \frac{1}{2} \mu \Big(v^2_{R,X} + v^2_{R,Y} + v^2_{R,Z} \Big) \tag{2.121}$$

The total internal molecule energy for the AB molecule can be calculated as a sum of its kinetic energy (equation 2.120) and its potential energy,

$$E'_{int} = E'_{kin(int)} + V(r) \tag{2.122}$$

When the molecule is formed, the internuclear distance oscillates around the equilibrium (r_e) molecule distance. The amplitude of these oscillations is in general small, which allows to consider the development in Taylor series as,

$$V(r) \approx V(r_e) + \frac{1}{2!} \Big(\frac{d^2 V(r)}{dr^2} \Big)_{r=r_e} \cdot (r - r_e)^2 + \frac{1}{3!} \Big(\frac{d^3 V(r)}{dr^3} \Big)_{r=r_e} \cdot (r - r_e)^3 + \dots \tag{2.123}$$

where $V(r)$ at r_e corresponds to a minimum. Terms higher than order two can be neglected so the relative movement of the nuclei can be separated in a vibrational component equivalent to an harmonic oscillator movement

$$V(r) \approx V(r_e) + \frac{1}{2}\Big(\frac{d^2V(r)}{dr^2}\Big)_{r=r_e} \cdot (r - r_e)^2 \tag{2.124}$$

Thus, considering a rigid rotor model the internal energy can be expressed as (42)

$$E_{int}(v^{'}, j^{'}) = V(r_e) + \Big(v^{'} + \frac{1}{2}\Big)h\nu_e + j^{'}(j^{'}+1)hB_e \qquad v^{'} = 0, 1, 2, \ldots j^{'} = 0, 1, 2, \ldots \tag{2.125}$$

The last term depends on the quantum number which determines the modulus of the rotational angular momentum and stands for the energy associated to the rotational movement of the molecules, which has the same energy than the rigid rotor of two particles,

$$E_{rot} = j^{'}(j^{'}+1)hB_e \qquad j^{'} = 0, 1, 2, \ldots \tag{2.126}$$

being B_e the rotational constant of a rigid rotor in the equilibrium, calculated from the momentum of inertia of the molecule,

$$B_e = \frac{h}{8\pi^2 I_e} = \frac{h}{8\pi^2 \mu r_e^2} \tag{2.127}$$

and the vibrational energy corresponds to the harmonic oscillator energy

$$E_{vib} = \Big(v^{'} + \frac{1}{2}\Big)h\nu_e \qquad v^{'} = 0, 1, 2, \ldots \tag{2.128}$$

The rigid rotor oscillator approximation drives to good results when the internuclear distance is small and the molecular distortion, due to the centrifugal effect is also small. When these conditions are not accomplished or the accuracy needs to be improved, more terms should be added (42),

$$\begin{aligned} E_{int}(v^{'}, j^{'}) \;=\; & V(r_e) + \Big(v^{'} + \frac{1}{2}\Big)h\nu_e - \Big(v^{'} + \frac{1}{2}\Big)^2 h\nu_e X_e + j^{'}(j^{'}+1)hB_e - \\ & - j^{'}(j^{'}+1)\Big(v^{'} + \frac{1}{2}\Big)h\alpha_e - j^{'2}(j^{'}+1)^2 hD_e + Y_{00} \end{aligned} \tag{2.129}$$

where

- X_e is the anarmonicity constant.
- α_e is the vibration-rotation interaction constant. It is a measure of the coupling between the vibrational and the rotational motion.

- D_e is the centrifugal distortion constant and it is introduced in order to correct the rotational energy since the molecule is not a perfect rotor and can be distorted by the centrifugal effect when rotating.
- Y_{00} is related with the anharmonicity.

All these parameters are calculated from the potential energy function derivatives. The angular momentum of AB molecule is calculated from the vectorial product of the position vector and the relative velocity vector of the molecule,

$$\vec{J}_{AB} = \vec{r} \otimes \vec{p}_R = \mu \cdot (\vec{r} \otimes \vec{v}_R) \tag{2.130}$$

so each component can be obtained by solving

$$J_{AB,X} = \mu[(Y_B - Y_A) \cdot v_{R,Z} - (Z_B - Z_A) \cdot v_{R,Y}] \tag{2.131}$$
$$J_{AB,Y} = \mu[(Z_B - Z_A) \cdot v_{R,X} - (X_B - X_A) \cdot v_{R,Z}] \tag{2.132}$$
$$J_{AB,Z} = \mu[(X_B - X_A) \cdot v_{R,Y} - (Y_B - Y_A) \cdot v_{R,X}] \tag{2.133}$$

and the internal angular momenta modulus,

$$J_{AB} = \sqrt{J_{AB,X}^2 + J_{AB,Y}^2 + J_{AB,Z}^2} \tag{2.134}$$

The quantum rotational level ($j^{'}$) for the molecule can be calculated by assigning the closest integer (43) to the result of

$$j^{'} = \Big(-1 + \sqrt{1 + 4 \cdot J_{AB}^2/\hbar^2} \Big) \cdot \frac{1}{2} \tag{2.135}$$

The internal energy of the molecule is defined by means of the implicit equation (43),

$$\frac{1}{2} J_{v'} - \pi\hbar \Big(v^{'} + \frac{1}{2} \Big) = 0 \tag{2.136}$$

where

$$J_{v'} = 2 \int_{r_-}^{r_+} \Big[2\mu \Big(E_{int} - V(r) - \frac{J_{AB}^2}{2\mu r^2} \Big) \Big]^{1/2} dr \tag{2.137}$$

integrating the vibrational action during a complete period ($r_- \rightarrow r_+$). Finally, from equation 2.136 and 2.137,

$$v^{'} = -\frac{1}{2} + \frac{1}{\pi\hbar} \int_{r_-}^{r_+} \Big[2\mu \Big(E_{int} - V(r) - \frac{J_{AB}^2}{2\mu r^2} \Big) \Big]^{1/2} dr \tag{2.138}$$

where r_- and r_+ are the inner and outer points for the potential at the given internal energy (E_{int}). The solution is obtained numerically by means of Newton-Raphson iterative method. As for $j^{'}$, the final vibrational level ($v^{'}$) is assigned to the closest integer value.

2.4.3 Rate constants calculation

The rate constant for an elementary process can be derived from probability results of quasiclassical trajectories calculations. For instance, for the atomic adsorption reaction over a surface,

$$A_{(g)} + s \overset{k_{ad}}{\rightarrow} A_{ad} \tag{2.139}$$

the adsorption reaction velocity can be written as,

$$v_{ad} = k_{ad}[A_{(g)}][s] = Z_{A_{(g)}} \cdot P_{ad} \cdot \theta_s \tag{2.140}$$

where P_{ad} is the adsorption probability obtained from a quasiclassical trajectory calculation, θ_s stands for the fraction of free sites available for adsorption, calculated as $\theta_s = [s]/[s]_0$ and $Z_{A_{(g)}}$ can be calculated from,

$$Z_{A_{(g)}} = \frac{P_{A_{(g)}}}{(2\pi m_A k_B T)^{1/2}} = [A_{(g)}]\Big(\frac{k_B T}{2\pi m_a}\Big)^{1/2} \tag{2.141}$$

where $P_{A_{(g)}}$ is the pressure of A gas and m_A its mass. Thus, the rate constant for the adsorption reaction has units of m^3/s and is defined as,

$$k_{ad} = P_{ad}\Big(\frac{k_B T}{2\pi m_A}\Big)^{1/2} \cdot \frac{1}{[s]_0} \tag{2.142}$$

where the square term has the units of m/s and $[s]_0$ is the initial concentration of free sites ($sites/m^2$).

The rate constant for molecular adsorption over two surface sites can be similarly found. The molecular adsorption rate equation,

$$AB_{(g)} + 2s \overset{k_{ad}}{\rightarrow} AB_{ad} \tag{2.143}$$

can be expressed as

$$v_{ad} = k_{ad}[AB_{(g)}][s]^2 = Z_{AB_{(g)}} \cdot P_{ad} \cdot \theta_s^2 \tag{2.144}$$

Thus, the rate constant (m^5/s) for the molecular adsorption is found to be,

$$k_{ad} = P_{ad}\Big(\frac{k_B T}{2\pi m_{AB}}\Big)^{1/2} \frac{1}{[s]_0^2} \tag{2.145}$$

.

For an Eley-Rideal reaction, where one atom A from the gas phase reacts with a preadsorbed one B

$$A_{(g)} + B_{ad} \overset{k_{ER}}{\rightarrow} AB_{(g)} + s \tag{2.146}$$

The ER rate equation is expressed as

$$v_{ER} = k_{ER}[A_{(g)}][B_{ad}] = Z_{A_{(g)}} \cdot \theta_B \cdot P_{ER} \tag{2.147}$$

where the rate constant (m^3/s) is

$$k_{ER} = P_{ER}\Big(\frac{k_B T}{2\pi m_{AB}}\Big)^{1/2} \frac{1}{[s]_0} \tag{2.148}$$

The Langmuir-Hinshelwood process, in which two adsorbed atoms react to form the molecule in gas phase,

$$A_{ad} + B_{ad} \overset{k_{LH}}{\rightarrow} AB_{(g)} + 2s \tag{2.149}$$

has a rate equation as follows

$$v_{LH} = k_{LH}[A_{ad}][B_{ad}] = \nu_i[s]_0 \cdot P_{LH} \cdot \theta_A \cdot \theta_B \tag{2.150}$$

where

$$\nu_i = \frac{1}{\Delta}\Big(\frac{\pi k_B T}{2m_i}\Big)^{1/2} \tag{2.151}$$

Defining the mean distance between active sites as Δ. Thus, the LH rate constant is found to be

$$k_{LH} = P_{LH} \cdot \nu_i \frac{1}{[s]_0} \tag{2.152}$$

expressed in m^2/s.

2.5 Transition State Theory

For a generic elementary bimolecular gas phase reaction $A + B \rightarrow C + D$ (where A, B, C and D are either atoms or molecules) the reaction velocity is expressed as,

$$v = k(T)[A][B] \tag{2.153}$$

where $[A]$ and $[B]$ stand for the atom or molecules concentration in gas phase, with units of m^{-3}, $k(T)$ is the rate constant $(m^3 \cdot s^{-1})$, which depends on the temperature, and v the reaction velocity in $m^{-3} \cdot s^{-1}$.

From statistical point of view, the Transition State Theory (TST) (44, 45, 46) is the most used methodology, where the rate constant for the same elementary reaction can be calculated from

$$k(T) = \frac{k_B T}{h} \frac{Z^{\neq}}{Z_{A_{(g)}} Z_{B_{(g)}}} e^{-\Delta E_0^{\neq}/k_B T} \tag{2.154}$$

where $Z_{A_{(g)}}$ and $Z_{B_{(g)}}$ are the partition functions divided by the volume (V) of the reactants in gas phase and $Z^{\neq}$ is the partition function of the transition state (divided also by V), which connects reactants and products. $\Delta E_0^{\neq}$ is the energy barrier of the process taking into account the zero point energy correction.

For a particular gas-surface elementary process, for instance, atomic adsorption (equation 2.139), the rate contant derived has units of $m^3 \cdot s^{-1}$. In addition, the rate constant can be derived from the general expression presented in equation 2.154 considering the specific reactants and transition state. For atomic adsorption, the rate constant is expressed as,

$$k_{ad} = \frac{k_B T}{h} \frac{Z^{\neq}/S}{Z_{A_{(g)}} Z_s / S} e^{-\frac{\Delta E_{ad}^{0\neq}}{k_B T}} \tag{2.155}$$

where the partition function is divided by the volume (V) for gas phase species and by the site surface area (S) for adsorbed species. Thus, for the atomic partition function per unit volume in gas phase, only the three translational degrees of freedom are taken into account then,

$$Z_{A_{(g)}} = \frac{(2\pi m_A k_B T)^{3/2}}{h^3} \tag{2.156}$$

where m_A is the atomic mass. The partition function of a free site is $Z_s \approx 1$. For the transition state, only vibrational degrees of freedom are considered,

$$Z^{\neq} = \prod_{i=1}^{2} \left(\frac{1}{1 - e^{-hc\nu_i / k_B T}} \right) \tag{2.157}$$

where ν_i are the real i frequencies for the transition state, obtained from the *ab initio* (DFT) calculations or from the PES; in this particular case just two frequencies are needed since the third one is imaginary. In the case of the AB molecular adsorption, the transition state will have five frequencies instead of the two used for the atomic adsorption, but the expression will be equivalent to equation 2.157. The degrees of freedom for the gas phase homonuclear molecule are not only translational but also vibrational and rotational as well thus, the expression will be,

$$Z_{AB_{(g)}} = \frac{(2\pi m k_B T)^{3/2}}{h^3} \times \left(\frac{1}{1 - e^{hc\nu / k_B T}} \right) \times \left(\frac{8\pi^2 I k_B T}{h^2} \right) \tag{2.158}$$

and

$$k_{ad} = \frac{k_B T}{h} \cdot \frac{Z^{\neq}/S}{Z_{AB} \cdot (Z_s/S)^2} \cdot e^{-\frac{\Delta E_{0,ad}^{\neq}}{k_B T}} \tag{2.159}$$

For the ER elementary process (equation 2.146), the rate constant is defined considering the reactants and the transition state as well,

$$k_{ER} = \frac{k_B T}{h} \frac{Z^{\neq}/S}{Z_{A_{(g)}} Z_{B_{ad}}/S} e^{-\frac{\Delta E_{ER}^{0\neq}}{k_B T}} \tag{2.160}$$

where $Z_{A_{(g)}}$ will be calculated by using equation 2.156 and $Z_{B_{ad}}$ and $Z^{\neq}$ by using equation 2.157 considering three and two frequencies, respectively.

2.6 Microkinetic Models

Microkinetic models allow to describe all the heterogeneous processes involving a solid surface and a gas atom or a diatomic molecule, by modelling its elementary steps. First of all, the possible elementary steps of the system have to be defined. A simple model (47) can be considered assuming the following processes and their velocity expressions:

Chemisorption of atoms:

$$A_{(g)} + s \xrightarrow{k_{ad}} A_{ad} \tag{2.161}$$

$$v_{ad} = k_{ad}[A_{(g)}][s] \tag{2.162}$$

Dissociative molecular adsorption:

$$A_{2(g)} + 2s \xrightarrow{k_{diss}} A_{ad} + A_{ad} \tag{2.163}$$

$$v_{diss} = k_{diss}[A_{2(g)}][s]^2 \tag{2.164}$$

Eley-Rideal recombination:

$$A_{(g)} + A_{ad} \xrightarrow{k_{ER}} A_{2(g)} + s \tag{2.165}$$

$$v_{ER} = k_{ER}[A_{(g)}][A_{ad}] \tag{2.166}$$

Langmuir-Hinshelwood recombination:

$$A_{ad} + A_{ad} \xrightarrow{k_{LH}} A_{2(g)} + 2s \tag{2.167}$$

$$v_{LH} = k_{LH}[A_{ad}]^2 \tag{2.168}$$

Thermal atomic desorption:

$$A_{ad} \xrightarrow{k_{des}} A_{(g)} + s \tag{2.169}$$

$$v_{des} = k_{des}[A_{ad}] \tag{2.170}$$

Another processes could be added if they were relevant, (e.g., $A_{2(g)}+2s \rightarrow A_{2(ad)}$). The time evolution of the species involved in any of the previous reactions can be known along time, considering that all the processes are occurring at the same time. In addition, the coverage of the surface varies along time until a steady state is achieved,

$$\frac{d[A_{ad}]}{dt} = 0 \tag{2.171}$$

Applying this condition and considering all the elementary processes and their velocity expressions,

$$k_{ad}[A_{(g)}][s]+2k_{diss}[A_{2(g)}][s]^2-k_{ER}[A_{(g)}][A_{ad}]-2k_{LH}[A_{ad}]^2-k_{des}[A_{ad}] = 0 \tag{2.172}$$

where $[s] = [s]_0 - [A_{ad}]$ is the number of free sites per unit area, allowing the calculation of $[A_{ad}]$ for a given pressure and temperature.

For the aim of this work, two coefficients are calculated since they are needed for computer fluid dynamics (CFD) simulations. The atomic recombination coefficient γ (also called catalytic efficiency) (48, 49), and the chemical energy accommodation coefficient β (48, 49). Both are within the range $0 \leqslant \gamma, \beta \leqslant 1$ and are supposed to depend on temperature an total/partial pressures.

The atomic recombination coefficient γ is defined as (50),

$$\gamma = \frac{\text{flux of atoms recombining at surface}}{\text{flux of atoms impinging the surface}} \tag{2.173}$$

The number of consumed atoms per unit area and unit time can be derived from the expression of the molecules formed,

$$-\frac{d[A_{(g)}]}{dt} = 2 \cdot \frac{d[A_{2(g)}]}{dt} \tag{2.174}$$

Thus, the γ coefficient can be calculated as,

$$\gamma = \left\{2 \cdot (-k_{diss}[A_{2(g)}][s]^2 + k_{ER}[A_{(g)}][A_{ad}] + k_{LH}[A_{ad}]^2)\right\}/Z_A \tag{2.175}$$

where γ coefficient depends on temperature, partial pressures (P_A and P_{A_2}) and Z_A is calculated by using the Hertz-Knudsen equation,

$$Z_A = [A]\sqrt{\frac{k_B T}{2\pi m_A}} \tag{2.176}$$

The β coefficient, can be defined as the ratio between the energy released to the surface per atomic recombination and the maximum energy transferable. Which in this general case could be defined as,

$$\beta = \frac{\sum_i F_i Q_i}{Z_A \gamma (D_{A_2}/2)} \tag{2.177}$$

where D_{A_2} is the A_2 dissociation energy, F_i represents the atomic or molecular fluxes ($m^{-2} \cdot s^{-1}$) at the steady-state and Q_i are the energies per atom required or released in each process.

Chapter 3

O/O_2 mixtures over graphite (0001) surface

3.1 Introduction

Carbon-based materials have received considerable attention for their use in spacecraft components (e.g., reinforced carbon was used as a thermal protection system (TPS) in the nose of Space Shuttle) due to their light weight and high strength. In the low Earth orbits (LEO), 160 - 2,000 Km above Earth's surface, atomic oxygen is one of the main present species and can collide with the spacecraft surface at very high translational energies (i.e., about 4.5 ± 1.0 eV due to the orbital velocity of around 7.5 Km/s) producing an important etching, hence degrading any carbon-based TPS (51). Moreover, during hypersonic reentry flights into Earth's atmosphere (e.g., Space Shuttle) not only atomic oxygen but also molecular oxygen processes can be relevant to understand properly the huge heat transferred and the TPS behaviour under these extreme conditions (52). Therefore, a good understanding of all elementary processes involving atomic and molecular oxygen with carbon-based materials is essential for space technology. Thus, in principle, several heterogeneous processes could compete: a) O adsorption, b) O_2 dissociative or non-dissociative adsorption, c) O recombination via an Eley-Rideal (ER) mechanism (i.e., $O_{(g)}+O_{ad} \rightarrow O_{2(g)}$), d) O recombination via a Langmuir-Hinshelwood (LH) mechanism (i.e., $O_{ad}+O_{ad} \rightarrow O_{2(g)}$) and e) C etching producing CO or CO_2, where *ad* labels adsorbed species and *g* gas species. Another less important elementary processes could also be added.

There are abundant theoretical studies about the interaction of atomic and molecular oxygen with graphite (53, 54, 55, 56, 57), graphene (58, 59) and carbon nanotubes (54, 60, 61) covering different aspects but without giving a global approach about the O/O_2 reactivity over these carbon surfaces. They are mainly

concerned with adsorption studies over several type of surfaces (e.g., basal, zigzag, armchair,...) for different coverages. Thus, there was shown that atomic oxygen becomes mainly chemically adsorbed on a bridge position between two adjacent carbon atoms of graphite or graphene, forming an epoxy group, with adsorption energies in the range of 1.5 - 3.2 eV for a basal graphite surface depending on the oxygen coverages and the level of the calculations (53, 54, 55, 56). The molecular oxygen seems to be only physically adsorbed on basal graphite surfaces with a low adsorption energies of about 0.12±0.01 eV at 1 ML coverage as it has been shown using thermal desorption spectroscopy on highly oriented pyrolytic graphite (HOPG) (62). Common DFT studies are not accurate enough to provide reliable adsorption energies for O_2 over graphite (53, 54, 57), due to the importance of the missing van der Waals (vdW) contributions. Nevertheless, a suitable vdW treatment could be done for instance by adding pairwise interatomic C_6r^{-6} terms, where C_6 coefficients can be derived from ground-state electron density for molecules and solids (63). The inclusion of vdW interactions reproduces quite well the O_2 physisorption over graphite (64, 65). The interaction of O_2 with defective edge sites on graphite surfaces presents high adsorption energies (2.6 - 6.2 eV (57)) in a similar way as for atomic oxygen (4.5 - 5.7 eV (56)). Moreover, molecular oxygen adsorbs on edge graphite surfaces at 300°C and 1 atm of pressure (the perfect basal surface is hardly active (66)), being the energy barrier for O_2 dissociation larger and for CO formation lower when the oxygen surface coverage diminishes (67).

Characterization of the ER and LH reaction pathways is very important from a kinetic point of view. Only very recently, the migration (diffusion) barrier for O on a graphene sheet has been investigated (58), indicating an energy barrier of 0.58 eV at a coverage of 16.7%, which would imply a noticeable mobility of isolated adsorbed atoms.

Apart from the mentioned experimental studies about O_2 adsorption/desorption on graphite, there are as well a large number of experimental works concerned mainly with the interaction of hyperthermal atomic oxygen on HOPG surfaces, to understand the erosion and degradation of these surfaces under large collision energies (51, 68, 69), by forming CO and CO_2 gas species.

Thus, a study is done (70) including the main elementary processes involving O and O_2 over an initially clean graphite basal surface (0001) at the same DFT level, characterizing not only the minima but also the transition states (TS) at several oxygen coverages. These data are used in a proposed microkinetic model based on calculated thermal rate constants derived from Transition State Theory, which allows a kinetic study for different temperatures and total and partial pressures (i.e., several O/O_2 mixtures). We also determine the atomic oxygen recombination coefficient γ_O(T,P) ($0 \leqslant \gamma_O \leqslant 1$). γ_O values are necessary in standard computer fluid dynamics (CFD) simulations (52) of hypersonic flights in order to evaluate the aerodynamic heating. Furthermore, to understand the processes

from a microscopic point of view, a quasiclassical trajectory study is done for the main reactions (i.e., atomic collisions with a clean and oxygen preadsorbed surface and molecular collision with clean surface). Results obtained are compared with some available experimental results based on beam-surface scattering experiments at several conditions (71, 72) in order to evaluate the accuracy of dynamical calculations and explain more precisely the experimental observations.

3.2 Bulk graphite study

The main characteristic of ideal graphite bulk stands on the layered structure. On a singular layer, carbon atoms adopt a regular hexagonal ring distribution. Two consecutive layers share the same position for some carbon atoms while some other lay behind the hexagonal hollow. When this layer combination is repeated on space, the third layer carbon atoms lay at the same positions than the first one, an ABAB... graphite structure is obtained. Otherwise, if the third carbon layer stands in a different position than in the previous layers, an ABCABC... structure is obtained. For model simplicity, bulk and surface studies consider an ABAB structure. It will be seen further on the manuscript that this decision does not affect considerably on the properties studied.

Many experimental studies on graphite structure reveal very similar structural properties. The values obtained by Wickoff (73), for a $C6mc$ spatial group show a C-C distance of 1.418 Å and an interlayer distance of 3.348 Å. The unit cell parameters are $a = b = 2.456$ Å, $c = 6.696$ Å, $\alpha = 120°$ and $\beta = \gamma = 90°$ that are depicted in figure 3.1 along with an overview of their spatial repetition.

A previous DFT study of the optimised bulk structure was carried out by using similar conditions to those used in Incze et al. (55, 56) and Sha et al. (74). Thus, Vanderbilt ultrasoft (US) pseudopotentials were used taking into account the GGA approximation of Perdew-Wang 91 (75, 76) (PW91) using the VASP code (77, 78, 79, 80). A cut-off energy of 270 eV for the US pseudopotentials and a k-points mesh of 13×13×4 was used, although the Blöchl method was used for the partial band occupancies as it improves the results for semiconductor structures. Further calculations were carried out by using PAW pseudopotentials (81, 82) with PW91, PBE (83), and with the revised PBE algorithm (RPBE) (84). In order to obtain the optimal values of energy cut-off and the k-points mesh, some convergence tests using the optimised geometry obtained above were carried out. The energy convergence at different k-points meshes was firstly studied. The tolerance in the energy difference for an increasing number of k-points was stated at 0.001eV. For the PW91 case, a mesh of 14×14×4 (a total of 784 points) was needed for energy convergence. Despite a mesh of 16×16×3 (a total of 768 points) was enough for the PBE and RPBE functionals, one of 14×14×4 was used for all functionals in order to simplify calculations. For calculations of the system

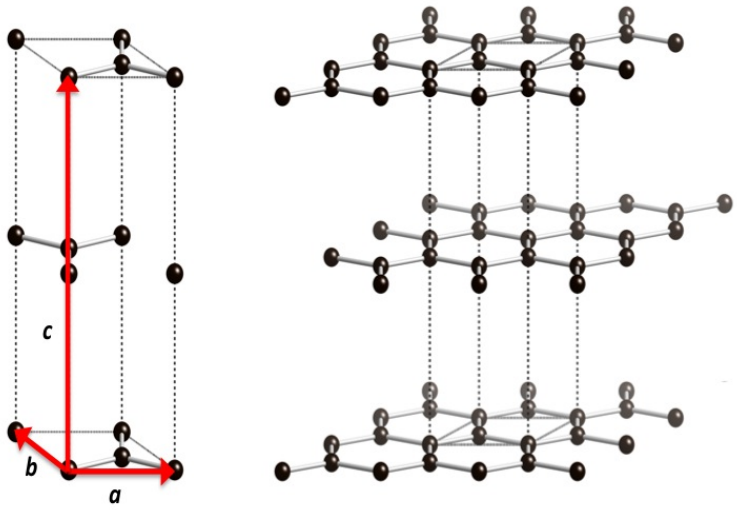

Figure 3.1: Unit cell representation with a, b and c cell parameters for graphite (0001) on the left. Spatial repetition of the unit cell in order to represent the solid.

using LDA approach, 16×16×3 k-points were needed. In table 3.1 the results for the energy convergence depending on the k-point mesh used are presented for the PW91 functional with PAW pseudopotentials. The energy convergence depending on the cut-off energy shows that for PW91, PBE and RPBE functionals an energy cut-off of 550 eV was enough, while 500 eV was the minimum energy cut-off for the LDA approximation.

The cohesive energy was calculated for the different functionals and approximations using the following formula,

$$E_{coh} = \frac{1}{N_C}\left(N_C E_{C(g)} - E_{bulk(eq.)}\right) \tag{3.1}$$

where N_C refers to the total number of carbon atoms in the unit cell, $E_{C(g)}$ stands for the free carbon atom energy (triplet state) and $E_{bulk(eq.)}$ for the total energy of the system at the optimal equilibrium configuration.

The results listed in table 3.2 show $a = b$ optimum parameters similar and close to the experimental value (73) where the relative errors are lower than 1%. On the other hand, optimised c parameter is overestimated in all cases. The value varies an amount of 20% and 15% from the experimental one by using RPBE and PW91 functionals, respectively. The common failure of GGA approach in predicting the c-axis lattice parameter and the small interlayer binding energy is well known. The inclusion of vdW interactions (85) in GGA and LDA calculations produces a good calculated interlayer binding energy, although the

Table 3.1: Total energy for the bulk of graphite depending on the k-points mesh (number of total k-points used in brackets) for the PW91 functional with PAW pseudopotentials at the PW91-US previously calculated geometry.

k-points mesh	Energy (eV)
9×9×3 (243)	-37.18360
9×9×4 (324)	-37.18172
10×10×3 (300)	-37.20919
10×10×4 (400)	-37.20921
12×12×3 (432)	-37.19607
12×12×4 (576)	-37.19504
14×14×3 (588)	-37.20478
14×14×4 (784)	-37.20479
16×16×3 (768)	-37.20389
16×16×4 (1024)	-37.20389

LDA description of c parameter is clearly closer to the experimental one. On the other hand, cohesive energies calculated using equation 3.1 are found to be much better described with the GGA approach. The value obtained with RPBE (7.516 eV/atom) is very close to the experimental one (7.371 eV/atom).

The isotropic bulk modulus (B_{iso}) is also presented in table 3.2 and its pressure derivative (B'_{iso}) obtained from volume changes with a constant c/a ratio, with several c values close to the experimental lattice parameter. B_{iso} and B'_{iso} are derived by means of a fit to the calculated pressure-volume data by using the third order Birch-Murnaghan equation of state (90). It can be seen that the calculated B_{iso} values are very similar and in good agreement with experimental ones, which were derived from the elastic constants of pyrolytic graphite (87, 88). The correct calculation of the usual bulk modulus (B_0) for highly anisotropic materials implies the use of an uni axial compression (91) instead of an uniform compression, which could produce values one order of magnitude larger than the experimental ones. Hence, the poor description of the c lattice parameter does not allow a proper calculation of B_o with the present DFT/GGA calculations. Calculated B'_{iso} are much lower than the experimental values estimated from the initial slopes of elastic constants with pressure at atmospheric pressure and 295 K (87) as shown in table 3.2.

In general, the conclusion that calculations by using GGA/RPBE give a reasonable good description of bulk graphite properties can be accepted, although

Table 3.2: Calculated and experimental lattice parameters, interatomic distances, cohesive energy, isotropic bulk modulus and its pressure derivative for graphite compound.

Method	$a = b$ (Å)	c (Å)	d_{C-C} (Å)	E_{coh} (eV/atom)[a]	B_{iso} (GPa)[a]	B'_{iso}
PW91	2.465	7.698	1.423	7.856	275.4	4.04
PBE	2.467	7.816	1.425	7.847	277.4	3.69
RPBE	2.467	8.022	1.425	7.516	270.3	4.29
LDA/CA[b]	2.441	6.64	–	8.903	–	–
PW91[b]	2.461	∼9.0	–	7.865	–	–
Exp.	2.456[c]	6.696[c]	1.418[c]	7.371±0.005[d]	318±11(0K)[e] 286±11(300K)[e]	13.6 (295 K)[f]

[a] *E_{coh}, B_{iso} and B'_{iso} were calculated by using the experimental c lattice value.*

[b] *LDA/Ceperley-Alder and GGA/Perdew-Wang 91 previous calculations with ultrasoft pseudopotentials(85).*

[c] *Experimental values(73).*

[d] *Experimental value (86) derived from $\Delta_f H^\circ$(0 K) for the process: $C(graphite) \rightarrow C(g, ideal)$.*

[e] *Experimental values(87, 88) obtained from elastic constants (C_{ij}) through the formula $B_{iso} = \frac{2}{9}(C_{11} + C_{12}) + \frac{4}{9}C_{13} + \frac{1}{9}C_{33}$, (89).*

[f] *Experimental value(87) obtained from the pressure derivative of the previous equation.*

it is necessary to use the experimental c lattice parameter. This fact does not represent a problem for the reliability of the atom or molecule-slab calculations in further studies, as it has been also assumed in similar previous theoretical studies (56).

3.3 DFT study of O/O_2 interaction with graphite

3.3.1 Adsorption and diffusion of oxygen

The adsorption of atomic oxygen on the basal (0001) graphite surface was studied, with a slab formed by one or two carbon layers. The results are almost identical regardless of the number of layers of the slab model, possibly due to the very weak interlayer interaction. This fact was also verified in previous O and K adsorption studies over graphite (53) by using 1, 2 or 3 layers. Even similar O/graphite studies have simulated the graphite surface as a single sheet of C atoms (54).

Three high-symmetry different sites have been considered (figure 3.2): on top of a surface C atom, which is either above another C atom (T1) or above an hexagon hollow of the second layer (T2), and over a bridge between the two nearest-neighbour carbon atoms (B). The hollow of the hexagonal ring of the first layer was also checked, but did not present significant adsorption in agreement with previous studies (55, 56). The atomic coverage effect was studied considering the adsorption of one O atom over three different unit cells: (1×1), (2×2) and (3×3), namely 50, 12.5 and 5.5% of coverage with respect to the C atoms (i.e., T1 and T2 sites). These coverages would be doubled taking into account only the most stable adsorption sites (i.e., true minima), which, in this case, correspond to the bridge (i.e., B) sites. When an O is over a bridge site, the closest free bridge sites become unavailable for another O adsorption because every C atom can make only four bonds. This coverage will be indicated throughout the text giving both values (i.e., % with respect to C or top sites and % with respect to bridge sites).

Table 3.3 presents the results for the atomic adsorption on T1, T2 and B sites for several oxygen coverages for a two-layer rigid slab. For T1 and T2 sites, the results obtained for both adsorption energies and geometrical variables are essentially matched. So, these top sites can be considered as almost identical instead of the different spatial symmetry. However, the adsorption energies for T1 and T2 sites are very small. The bridge site is the most stable one for all coverages. The analysis of its harmonic vibrational frequencies shown in table 3.3 reveals that it is a true minimum (i.e., all frequencies are positive). It is more stable for high O coverages, where O images are much closer (e.g., the minimum $d_{OO} = a = 2.467$ Å at 50% coverage) and can introduce an extra stabilization, in a similar way as was observed for O/graphene (58).

Table 3.3: Calculated properties for O adsorption over a basal (0001) graphite surface, without slab relaxation.

Coverage (%)[a]	**Site**[b]	E_{ad} (eV)	Z_O (Å)	d_{O-C} (Å)	ν_i (cm^{-1})[c] $\perp$	$\parallel$	
50/100	T1	-0.816	1.544	1.544	574.5	367.2i	374.2i
	T2	-0.811	1.509	1.509	571.0	407.6i	410.5i
	B	0.881	1.251	1.440	822.6	610.6	379.7
12.5/25	T1	0.281	1.556	1.556	542.7	89.0i	95.1i
	T2	0.308	1.554	1.554	583.2	196.1i	201.2i
	B	0.660	1.385	1.557	548.7	325.8	315.2
5.5/11.1	T1	0.0215	1.589	1.589	489.7	142.0	133.1
	T2	0.0679	1.584	1.584	526.8	151.7i	170.5i
	B	0.541	1.384	1.557	538.3	389.4	350.0

The slab geometry (two C layers) was fixed at its optimum geometry ($d_{C-C} = 1.425$ Å) derived in absence of O but with the interlayer distance (d_{12}) fixed to its experimental value (3.347 Å)).

[a] *The coverage was calculated with respect to the top sites (O/C %) or the bridge sites (O/bridge %) to facilitate the comparison with previous studies.*

[b] *In T1 and T2 sites, only the Z_O variable was optimised.*

[c] *Harmonic vibrational frequencies of the atomic adsorbate with respect to the rigid substrate. The first one corresponds to a perpendicular vibration and the other to parallel vibrations to the graphite surface.*

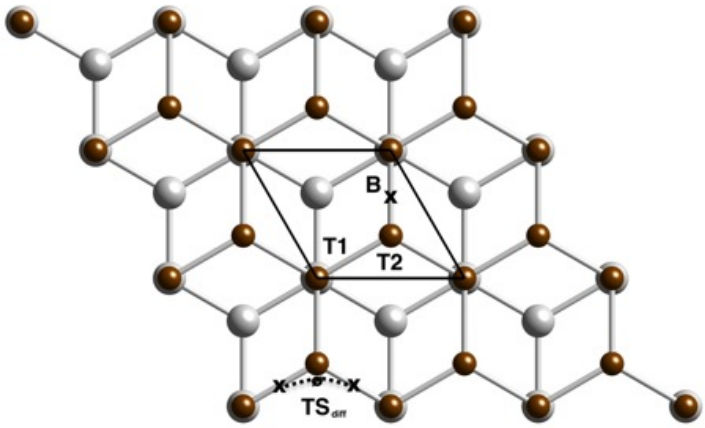

Figure 3.2: Top view of the graphite (0001) two-layer slab model with the different adsorption sites: bridge (B), on top a C with also a C below (T1) and on top a C without a C below (T2). The atoms of the second layer are plotted a bit larger and with light colour to be distinguished from first layer atoms. The transition state for O diffusion between two bridge adsorption sites is also shown. The *solid line* shows the (1×1) unit cell.

In all calculations, it was observed that the singlet state is the most stable for all sites in agreement with previous studies for O/graphite (54, 55, 56). In general, the present results are quite similar to the extensive study of Incze et al. (55, 56) by using GGA/PW91 with ultrasoft Vanderbilt type pseudopotentials, although they obtained large adsorption energies for bridge site (1.89 and 1.73 eV for 50 and 5.5% O/C coverages, respectively), within the rigid slab approximation.

T1 and T2 stationary points mainly present two imaginary frequencies, which seem to connect with the adsorption bridge minimum and with a diffusion transition state (see below for more details), although the slab relaxation can affect as well the character of these frequencies (e.g., reducing to one imaginary value for T1 site at 12.5/25% coverage).

In table 3.4 the effect of slab relaxation is summarised just over the bridge minimum site for several O coverages. This geometry relaxation corresponds to a stretching of C-C bond along with a reduction of both C-O bonds, with also a puckering of the two carbon atoms beneath the adsorbed atom. This behaviour is in good agreement with a similar DFT study by means of GGA/PW91 with ultrasoft pseudopotentials (54), which shows $d_{O-C} = 1.472$ Å and $d_{C-C} = 1.500$ Å, compared to the graphite $d_{O-C} = 1.420$ Å for a 5.5/11.1% coverage. However, a larger adsorption energy (1.91 eV) was calculated in that work. We observe as well that the slab relaxation implies that the adsorption energy tends to be larger

for low O coverages (table 3.4), conversely to the behaviour found for rigid slab (table 3.3).

Table 3.4: Calculated properties for O adsorption over a basal (0001) graphite surface, with slab relaxation.

Coverage	E_{ad}	Z_O	Z_C	d_{O-C}	d_{C-C}	ν_i $(cm^{-1})^c$		
(%)	(eV)	$(Å)^a$	$(Å)^a$	(Å)	(Å)	$\perp$	$\parallel$	
50/100	0.945	1.254	-[b]	1.437	1.432	830.7	617.8	400.7
12.5/25	1.283	1.532	0.246	1.482	1.472	652.4	411.3	337.2
5.5/11.1	1.255	1.547	0.267	1.478	1.479	655.2	438.1	337.0

The carbon atoms directly bound to oxygen adsorbed atom on B site were allowed to relax in all directions.

[a] *$Z = 0$ at the first layer formed by the C atoms without including the carbons underneath the O, which are at d_{C-C} separation.*

[b] *For the highest coverage (50/100%), the C relaxation implies that all the first layer is shifted upwards (i.e., d_{12} increases to 3.957 Å). For another coverages, d_{12} was kept fixed to its experimental value (3.347 Å).*

[c] *Harmonic vibrational frequencies of the atomic adsorbate with respect to the rigid substrate. The first one corresponds to a perpendicular vibration and the other to parallel vibrations to the graphite surface.*

The formation of this epoxide-like (COC) ring structure on bridge sites was observed in theoretical and experimental studies on graphene (59) and graphite (92, 93, 94) oxides. Thus, for symmetrical graphene epoxide, the calculated values, $d_{O-C} = 1.42 - 1.44$ Å and $d_{C-C} = 1.49 - 1.50$ Å ($d_{C-C} = 1.41$ for clean graphite) at high coverages show a similar trend as in the present work for oxygen over graphite. The epoxide groups enhance the wrinkling of carbon sheets (i.e., $Z_C = 0.25 - 0.27$ Å, table 3.4) in agreement with previous Monte Carlo studies on graphite oxide ($\langle Z_C \rangle = 0.33 \pm 0.04$ Å (94)). The oxidation of graphite increases also its interplanar spacing from 3.39 Å to 6.91 - 6.96 Å due to the expansion of the layers originated by the accommodation of various oxygen species in the interlayer zone, according to experiments (92, 93) and Monte Carlo simulations (94). In the present study, with only O and O_2 gas species, it is believed that sub-surface processes (e.g., O or O_2 penetration) will be negligible. For instance, in the centre of the hexagonal hollow, where O could seemingly enter into the sub-surface, the energy is very repulsive for O approach (e.g., for $Z_O = 1.91, 1.52$ and 1.12 Å the energy is 0.43, 1.51 and 4.52 eV with respect to O + slab asymp-

tote, respectively). Another possibility for O penetration into the slab could be through the same O bridge adsorption, although this would imply the breaking of the underlying C-C bond. This process seems to be infrequent as it has been shown in Monte Carlo simulations on graphite oxidation (94), where the use of only one C layer and the additional presence of hydrogen atoms in the gas phase could facilitate even more this penetration process in comparison with our two layer model that uses only pure oxygen atoms.

It was also observed a slight interlayer (d_{12}) enlargement for O adsorption at the highest coverage (50/100%, table 3.4), when slab was allowed to relax, but without O penetration into the slab. In fact, the interlayer distance was fixed to its experimental value in almost all calculations due to the poor description of vdW interaction with the present DFT approach.

A Bader's charge analysis of the epoxy groups shows an important charge transfer between the C atoms of the surface and the adsorbed oxygen (e.g., $q_O = -0.99$, $q_C = +0.41$, $+0.58$ at 50/100%). This arrangement of negatively charged oxygen atoms could avoid the nucleophilic attack on C atoms, explaining the relative chemical stability of the epoxide groups in graphite oxides, as it was earlier suggested (92).

In table 3.5 are summarised the properties of transition states for O adsorption and diffusion processes over the basal (0001) graphite surface at several coverages for rigid slab approximation. Adsorption process is clearly activated as it was also demonstrated for atomic hydrogen over graphene ($\Delta E^{\neq} \sim 0.14$ eV at low coverages (95)) or graphite ($\Delta E^{\neq} = 0.23$ eV at 12.5/25% coverage (74)). The main difference is that H is mainly adsorbed on top carbons while O prefers the bridge sites. In spite of H and O have different electronic properties, their open shell nature could justify the rather similar behaviour when reacting over the same substrate.

The energy barrier is larger for high O coverages, although slab relaxation tends to decrease this barrier as was observed for 12.5/25% coverage calculations. Usually, more exothermic reactions (i.e., atomic adsorption with slab relaxation) show lower energy barriers (i.e., early TS) in agreement with Hammond's Postulate. The slab relaxation modifies mainly the Z coordinate of both C atoms below the O adsorbed one, but the O-C distances are almost unchanged.

The analysis of the imaginary frequency in this transition state confirms that mainly the perpendicular movement of oxygen with respect to the surface (i.e., Z_O coordinate) corresponds to the adsorption process. This TS has mainly a triplet character due to its proximity to the O gas asymptote.

The diffusion of one adsorbed O over a bridge to the closest bridge is also an activated process that follows a path roughly shown in figure 3.2, with a TS mainly with a singlet character as in the adsorption minimum. The imaginary frequency involves mostly a parallel movement to the surface as could be expected for a diffusion process. The corresponding energy barrier decreases significantly

Table 3.5: Calculated properties of the transition states for O adsorption and diffusion processes over the basal (0001) graphite surface.

Process and coverage[a]	$\Delta E^{\neq}$	Z_O	d_{O-C}		ν_i $(\mathbf{cm}^{-1})^d$		
	(eV)[b]	(Å)[c]	(Å)[c]		$\perp$	$\parallel$	
$O_g + s \rightarrow O_{ad}$ *(adsorption)*							
50/100%	0.67(0.69)	1.755	1.878	1.910	535.4i	220.2	123.4
12.5/25%	0.31(0.32)	1.874	1.940	2.090	734.1i	103.8	47.5
	0.19(0.13[e])	2.060	1.863	1.918	112.1i	266.7	171.1
5.5/11%	0.28[f]	1.848	1.981	1.981	-	-	-
$O_{ad} + s' \rightarrow O_{ad'} + s$ *(diffusion)*							
50/100%	1.43(1.49)	1.425	1.955		675.1	611.7i	306.4
12.5/25%	0.38(0.42)	1.533	1.555		549.7	188.6i	113.0
	0.73(0.70)[e]	1.718	1.421		709.6	157.3	101.7i
5.5/11.1%	0.47(0.51)	1.585	1.588		519.9	169.8	97.8i

The slab geometry (two C layers) was fixed at its optimum geometry ($d_{C-C} = 1.425$ Å) derived in absence of O but with the interlayer distance (d_{12}) fixed to its experimental value (3.347 Å).

[a] *s or s′ correspond to C-C bridge sites.*

[b] *Energy barriers with respect to reactants (including zero point energy between parentheses).*

[c] *The transition state for adsorption is practically over the C-C bridge site and for diffusion is between two non-adjacent C atoms (figure 3.2).*

[d] *Harmonic vibrational frequencies of the atomic adsorbate with respect to the rigid substrate.*

[e] *In this case, the carbon atoms directly bound to oxygen adsorbed atom were allowed to relax in all directions (i.e., $Z_C = 0.314$ and 0.297 Å for adsorption and diffusion TS, respectively).*

[f] *This TS was derived approximately from the crossing between the singlet and triplet states.*

when the coverage is reduced, likewise as for the adsorption process (table 3.5). However, the slab relaxation increases considerably this energy barrier from 0.38 to 0.73 eV at 12.5/25% as could be expected because the adsorption energy of adatom changed from 0.66 to 1.28 eV due to C relaxation in Z direction. Therefore, the adatom should diffuse quickly over the graphite surface only at high temperatures, which is also in agreement with previous values derived for O over graphite ($\Delta E^{\neq} \geqslant 0.36$eV at 3.12% (53)) or graphene ($\Delta E^{\neq} = 0.58$ eV at 16.7% (58)).

Although DFT calculations do not reveal any physisorption minimum, curves calculated over a specific site for several Z_O distances show the existence of a physisorption minimum in the entrance valley. Thus, in order to evaluate the possible stabilization of this minimum over a bridge site, the empirical dispersion energy based on $C_6 \cdot r^{-6}$ terms was added (96). The dispersion correction to the DFT energy is defined as,

$$E_{disp} = -s_6 \sum_{i=1}^{N_{at}-1} \sum_{j=i+1}^{N_{at}} \frac{C_6^{ij}}{r_{ij}^6} f_{dmp}(r_{ij}) \tag{3.2}$$

where N_{at} stands for the number of atoms in the system, C_6^{ij} denotes the dispersion coefficient for atom pair ij, s_6 is a global scaling factor taken as 0.75 for PBE functionals, and r_{ij} is the interatomic distance between i and j atoms. f_{dmp} is a dumping function used to avoid near-singularities for small internuclear distances, and takes the form of,

$$f_{dmp}(r_{ij}) = \frac{1}{1 + e^{-d(r_{ij}/r_r - 1)}} \tag{3.3}$$

where r_r is the sum of atomic vdW radii and d the threshold distance for energy cut-off ($d \geqslant 20$Å). The graphite slab used for the calculations was a two layers model formed by 64 carbon atoms (4×3 supercell), locating the oxygen atom approximately in the middle of the supercell to make sure that all relevant O-C interactions were properly included.

The curves obtained for the adsorption over a top or a bridge site show similar minima (figure 3.3a and 3.3b, respectively). The most stable minimum calculated corresponds to $Z_O = 2.731$ Å over a bridge site and a stabilization energy of $E_{ad} = 0.124$ eV, while over a top site, the stabilization energy is smaller, $E_{ad} = 0.117$ eV for a distance between the surface and the oxygen atom of $Z_O = 2.769$ Å.

3.3.2 Molecular adsorption

With the present DFT approach the adsorption of molecular oxygen on the basal surface of graphite was also studied. Thus, perpendicular and parallel initial configurations with the center of mass over the different adsorption sites (figure 3.2)

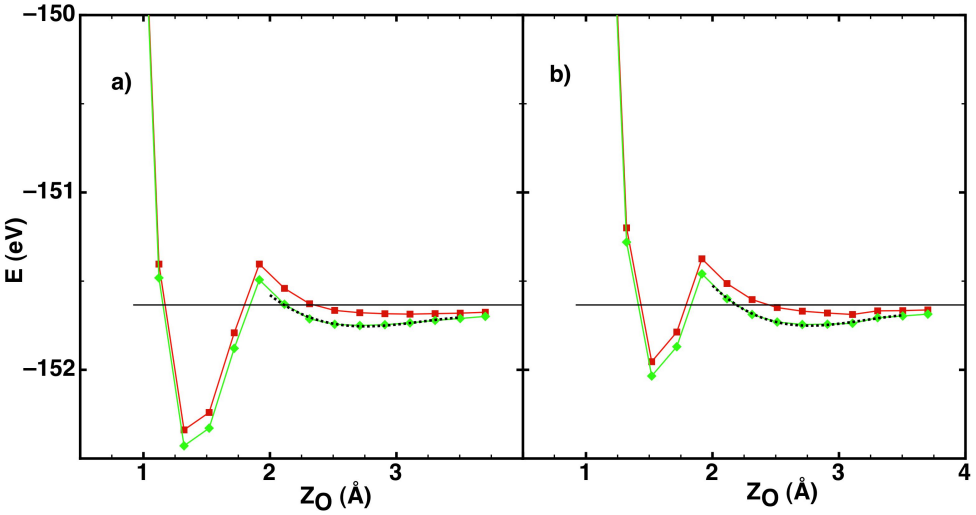

Figure 3.3: DFT calculated curves for atomic oxygen over a) bridge site and b) top site at different surface distances (Z_O) in red, the dispersion corrected ones in green and the fitted curve for each physisorption minima in a dotted black line. The value of the asymptote is plotted with a black line.

were considered, optimizing all degrees of freedom including also the slab relaxation by using a 2×2 unit cell. There were found very low adsorption energies ($E_{ad} \leqslant 0.01$ eV) at long distances of the center of mass from the surface (Z_{cm}= 3.70 - 3.75 Å) with O-O bond distances of 1.238 Å, slightly larger compared to those for the free molecule of 1.235 Å. These results are quite similar to previous studies that used either a cluster ($E_{ad} = 0.011$ eV, $Z_{cm} = 4.212$ Å, $d_{OO} = 1.167$ compared with 1.166 Å in $O_{2(g)}$ (57)) or slab model ($E_{ad} = 0.039$ eV, $Z_{cm} = 3.362$ Å, $d_{OO} = 1.238$ Å compared with 1.237 Å in $O_{2(g)}$ (54)) over graphite, which also showed that triplet state was more stable than the singlet one. The quality of the DFT spin description of this system would not possibly explain these energy differences because it was also observed a clear and reasonable spin polarization involving mostly the gas and some of the first layer slab atoms in another very similar studies (e.g., O and N over β-cristobalite (97) or over α-alumina (98)). Those could be rather originated by the DFT limitations to describe the vdW interactions, whose importance has also been postulated in some previous experimental and theoretical studies for O_2 with carbon SWNT bundles or graphite (64, 65), as it was explained above (section 3.3.1). Therefore, a better DFT description should be necessary to account for the small experimental physisorption energy (0.12 ± 0.01 eV at 1 ML coverage (62)). For this reason, the empirical dispersion energy correction to the DFT calculated energies was included as for the atomic oxygen adsorption (previous subsection, equations 3.2 and 3.3). Op-

timised configurations for O_2 molecule parallel to the surface at several distances (Z_{cm}) were used to calculate the curve plotted in figure 3.4. The inclusion of the

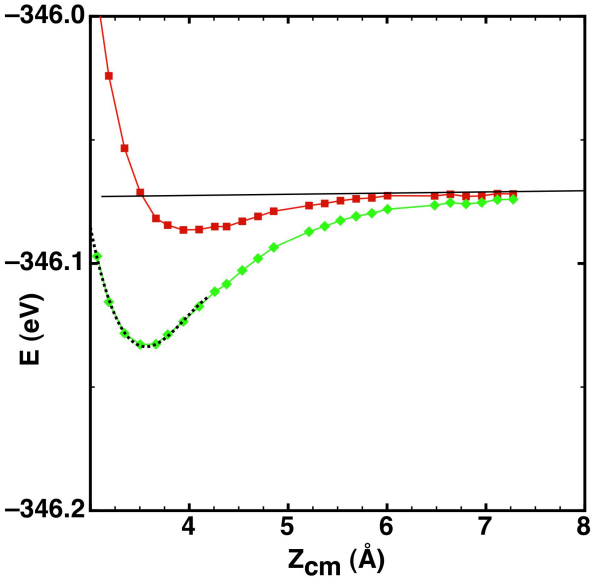

Figure 3.4: DFT calculated curves for the molecular oxygen over bridge site (red) at different surface distances. The dispersion corrected ones in green and the fitted curve for the physisorption minimum in a dotted black line. The value of the asymptote is plotted with a black line.

dispersion energy stabilizes more the vdW minimum, which is finally located at $Z_{cm} = 3.548$ Å, $r = 1.240$ Å and $E_{ad} = 0.060$ eV, with a slightly larger r distance compared to the free molecule bound distance of 1.235 Å. These results are similar to those found on bibliography (62) and quite close to the experimental physisorption energy of 0.12 ± 0.01 eV although were calculated for a much lower coverage.

3.3.3 Recombination reactions of atomic oxygen

The minimum energy reaction paths (MEP) for ER and LH processes were calculated by means of the climbing Nudge Elastic Band (NEB) method (99, 100), using at least 6 images. For instance, for ER reaction, the first image was the adsorbed atom of oxygen over a bridge along with the $O_{(g)}$ above it, but well separated from the surface. The final image was the O_2 molecule in a perpendicular configuration far from the surface. It was checked that the final stationary points had the lowest energies and that they properly correspond to ER or LH processes, being therefore independent of the MEP. Moreover, as the construction of

the analytical and interpolated PES was planned for O/graphite and O_2/graphite or O/O-graphite dynamical studies, additional grids of points were calculated at different geometries over the unit cell, whose energies were in complete agreement with the proposed stationary points.

Atomic recombination processes (i.e., ER and LH reactions) over the basal (0001) graphite surface were found to be activated processes although their energy barriers considerably decrease when the coverage is increased, as can be seen in table 3.6.

The ER transition state corresponds to a perpendicular O-O orientation over the bridge site (figure 3.5), being the imaginary frequency also a perpendicular movement that gives place to $O_{2(g)}$. Contrarily, the LH transition state presents a parallel configuration with a similar O-O distance as for ER TS (e.g., for a 2×2 unit cell); in this case, the imaginary frequency has a mixture of both parallel and perpendicular movements, as could be expected. There is not experimental information to compare with these energy barriers. However, a similar DFT study with H over graphite (0001) surface for a 12.5/25% coverage shows that at this low coverage, the ER energy barrier would be equally very low ($\leqslant$ 0.05 eV), as could be observed from cross-section vs. incident energy plots of quantum scattering calculations (74). However, the authors assumed a puckering of the C atom below the adsorbed H on top ($Z = 0.36$ Å), which possibly reduces more this ER energy barrier. Conversely, the relaxation of the slab in the present study could increase this energy barrier for O as occurred for the diffusion process, because the adsorbed oxygen atom tends to become more stable after slab relaxation. This effect could also be expected for LH reaction, although the slab relaxation effect should be checked with additional calculations.

The LH reaction is expected to be by far, less important than ER (or hot atom) reaction as can be concluded from the large differences in their energy barriers. This fact has also been previously found for O recombination over β-cristobalite (101) and will be confirmed in the next section.

3.3.4 CO etching processes

Experimental results (51, 71) show an important formation of CO molecules when hot atomic oxygen impinges the graphite surface, among other species as CO_2. Although the process will not be included in the microkinetic model, an estimation is computed for the energy necessary to take out a carbon atom from the surface to form a gas phase CO molecule leaving a vacant in the graphite surface.

Figure 3.6 shows the energetic profile for the CO formation from a perfect graphite surface and an oxygen atom approaching to the surface at X_O and Y_O corresponding to the top site. The DFT calculations were done as in previous calculations (i.e., RPBE functional, 11×11×1 k-points mesh,...) using a (2×2) supercell. It has to be considered as a first approximation that the graphite

Table 3.6: Calculated properties of the transition states for Eley-Rideal (ER) and Langmuir-Hinshelwood (LH) processes involving O atoms over the basal (0001) graphite surface.

Process and coverage[a]	$\Delta E^{\neq}$	Z_O		d_{O-C}		d_{O-O}	ν_i (cm^{-1}) [d]					
	(eV)[b]	(Å)[c]		d_a, d_b [c](Å)		(Å)	$\perp$	$\parallel$				
$O_{(g)} + O_{ad} \rightarrow O_2$+s *(ER reaction)*												
50/100%	1.11 (1.06)	1.525	3.235	1.685	1.682	1.711	962.4i	246.7	339.7	152.8	124.2	63.5
12.5/25%	0.10 (0.076)	1.499	3.492	1.647	1.672	2.024	527.9i	209.5	301.8	268.4	87.7i	33.9
$O_{ad} + O_{ad} \rightarrow O_{2(g)}$+s *(LH reaction)*												
25/50%	1.91 (1.87)	1.569	1.570	1.609	1.610	1.736	611.6i	496.8	397.4	330.0	256.2	196.0
11.1/22.2%	1.28[e]	1.600	1.600	1.625	1.622	1.774	–					

The slab geometry (two C layers) was fixed at its optimum geometry ($d_{C-C} = 1.425$ Å) derived in absence of O but with the interlayer distance (d_{12}) fixed to its experimental value (3.347 Å).

[a] *s corresponds to C-C bridge sites. For LH reaction, coverages are necessarily doubled with respect to ER or adsorption processes when using the same unit cell.*

[b] *Energy barriers with respect to reactants (including zero point energy between parentheses).*

[c] *The transition state for ER and LH reaction are depicted in figure 3.5. <OCCO dihedral is 24.7° at 25/50% and 16.8° at 11.1/22.2% for LH TS.*

[d] *Harmonic vibrational frequencies of the atomic adsorbate with respect to the rigid substrate. Approximately, the two first correspond to perpendicular and the other to parallel vibrations with respect to the graphite surface for the ER reaction. In the case of LH reaction the imaginary frequency shows a mixture of parallel and perpendicular movements.*

[e] *This TS was derived approximately from some grids of points.*

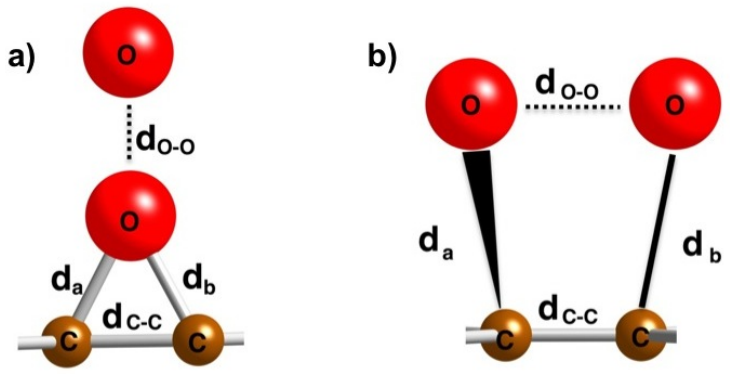

Figure 3.5: Geometries corresponding to the transition states for: a) ER reaction and b) LH reaction, labelling the different interatomic distances.

surface is not relaxed when the oxygen is pulling up the carbon atom from the surface. This relaxation could imply a reduction in the energy barrier and the asymptote. However, the current calculation gives a threshold to the barrier that should be considered for this kind of process. The calculated energy necessary to form the CO molecule from adsorbed O atom is found to be 4.362 eV (endothermicity) through a barrier of 5.362 eV. The C-O distance for the transition state was found to be 1.159 Å (slightly larger than the calculated for the CO molecule in gas phase, 1.143 Å). Specifications for the transition state can be found in table 3.7, where the imaginary frequency shows mainly a perpendicular movement of both atoms respect the surface. The calculated $\Delta E_{etching}$ (3.608 eV) from $O_{(g)}$ to form $CO_{(g)}$ is close to the experimental value of 4.2 - 4.5 eV (102). It is worth noting that the total process implies: first the adsorption of the atom through the calculated adsorption barrier and then the abstraction of the CO described here. This second process is much more endothermic.

The initial collision energies at the temperatures used for the microkinetic model presented are considerably lower than the calculated barrier for the etching (i.e., if T=1,300 K, the mean kinetic energy for the atoms will be 0.17 eV). Thus, the etching process is not expected to play an important role in the global representation and thus, will not be considered. However, this is not true for the initial conditions used in the experiments done by Paci et al. (71), where the hyperthermal distribution of colliding oxygen atoms presents a maximum at 5.22 eV. In that case, the etching of the graphite surface should be considered for the dynamical simulations but PES has not been constructed yet taking into account this specific process.

Table 3.7: Calculated properties of the transition state for the CO formation from an O adsorbed over a C atom of the surface.

$\Delta E^{\neq}$ (eV)	5.362
Z_O (Å)	2.979
Z_C (Å)	1.820
d_{O-C} (Å)	1.159

	$\perp$	$\parallel$	
ν_i (cm^{-1})	228.8i	479.7	101.3
	3935.8	477.1	74.3

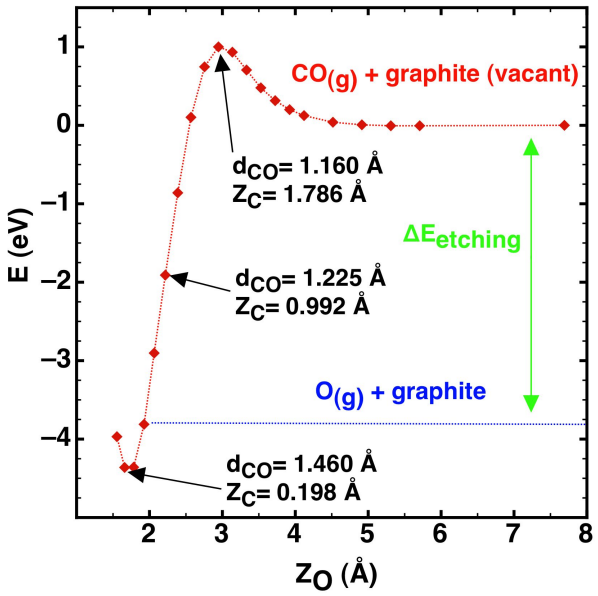

Figure 3.6: Energetic diagram for the etching process of a carbon atom from the graphite surface by an incoming oxygen atom. Slab was considered rigid excepting the reacting C atom.

3.4 Microkinetic model for O/O_2 mixtures reacting over graphite

A microkinetic model is proposed to estimate the overall effect of all studied heterogeneous processes involving different O/O_2 mixtures over a graphite (0001) surface. Six surface elementary processes were included:

Chemisorption (k_1) and desorption (k_{-1}) of oxygen atom:

$$O_{(g)} + s \underset{k_{-1}}{\overset{k_1}{\rightleftharpoons}} O_{ad} \tag{3.4}$$

Langmuir-Hinshelwood reaction (k_2) and dissociative molecular adsorption (k_{-2})

$$O_{ad} + O_{ad} \underset{k_{-2}}{\overset{k_2}{\rightleftharpoons}} O_{2(g)} + 2s \tag{3.5}$$

Eley-Rideal reaction (k_3) and another dissociative molecular adsorption channel (k_{-3})

$$O_{(g)} + O_{ad} \underset{k_{-3}}{\overset{k_3}{\rightleftharpoons}} O_{2(g)} + s \tag{3.6}$$

where s indicates a free site over the surface. Despite the elementary processes were listed using direct and reverse notation, both type of processes can be produced simultaneously and almost independently (i.e., 2/-2 or 3/-3) for the several O/O_2 initial reactant's mixtures.

Non-dissociative molecular adsorption is not taken into account because the almost negligible above-mentioned O_2 physisorption. The O_2 dissociation can produce several final products (e.g., O_{ad} + O_{ad}, $O_{(g)} + O_{ad}$, ...). The diffusion processes (e.g., $O_{ad} + s \rightarrow O'_{ad} + s'$, for instance between two bridge sites) will not have a global contribution to the final atomic coverage because its reverse process would cancel the direct one ($v_{dif} = v_{-dif}$). However, diffusion could enhance the approach of two adatoms to adjacent bridges separated only with a C-C bond, which could increase the LH probability. Atomic diffusion should be included in kinetic Monte Carlo simulations, where non-uniform atomic coverages can occur. Nevertheless, in the present simple model, with an uniform coverage assumption is not possible to include the diffusion over the surface.

For each elementary step, the rate constant was derived from the standard Transition State Theory (46) (TST) by equations presented in section 2.5 where the partition functions of reactants and transition state are needed. Thus, accurate DFT calculations for these specific geometries are required.

The DFT data for rigid slab and low coverage (i.e., 12.5/25% for one adsorbed atom processes or 11.1/22.2% for LH reaction) were used in order to derive the

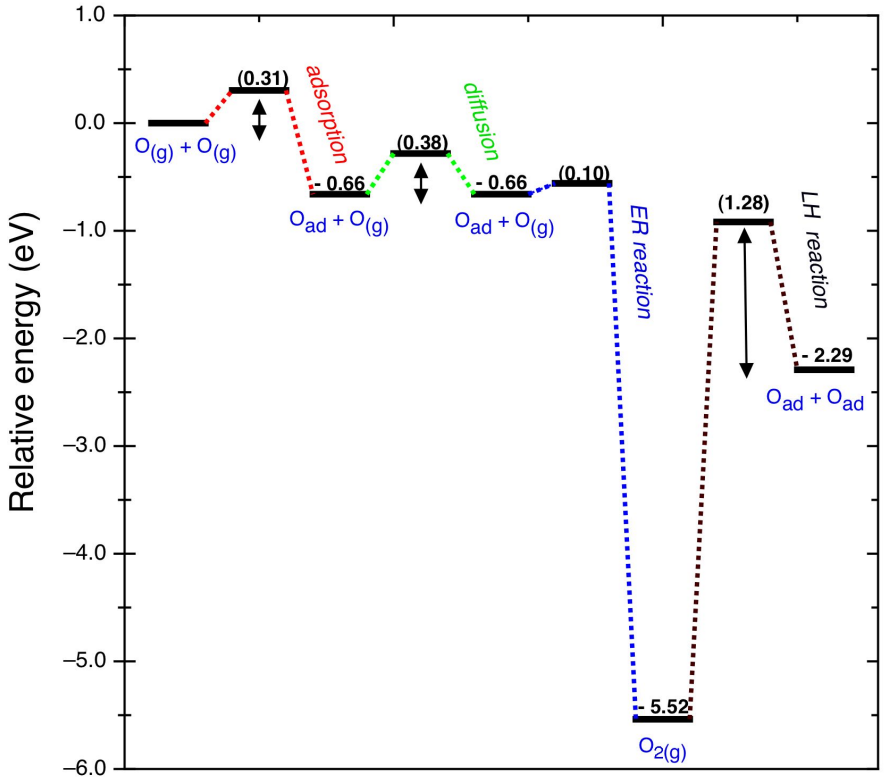

Figure 3.7: Energy diagram for several O heterogeneous elementary processes over a graphite (0001) surface for a 12.5/25% coverage (11.1/22.2% for LH reaction). Values between parentheses give the energy barriers without ZPE with respect to the closest reactants. O_2 dissociation energy can change in approximately ±0.1 eV due to a small size consistency problem in the asymptotes (i.e., $O(^3P)$+$O(^3P)$+slab calculated as supermolecule or as fragments addition.

different thermal rate constants. The energy diagram for the overall processes considered in the model is plotted in figure 3.7. The initial surface density of free sites $[s]_0$ was taken as $1.90 \cdot 10^{19}$ bridge sites/m^2. Figure 3.8 shows the calculated TST rate constants within the 400 - 2,000K range of temperature. It

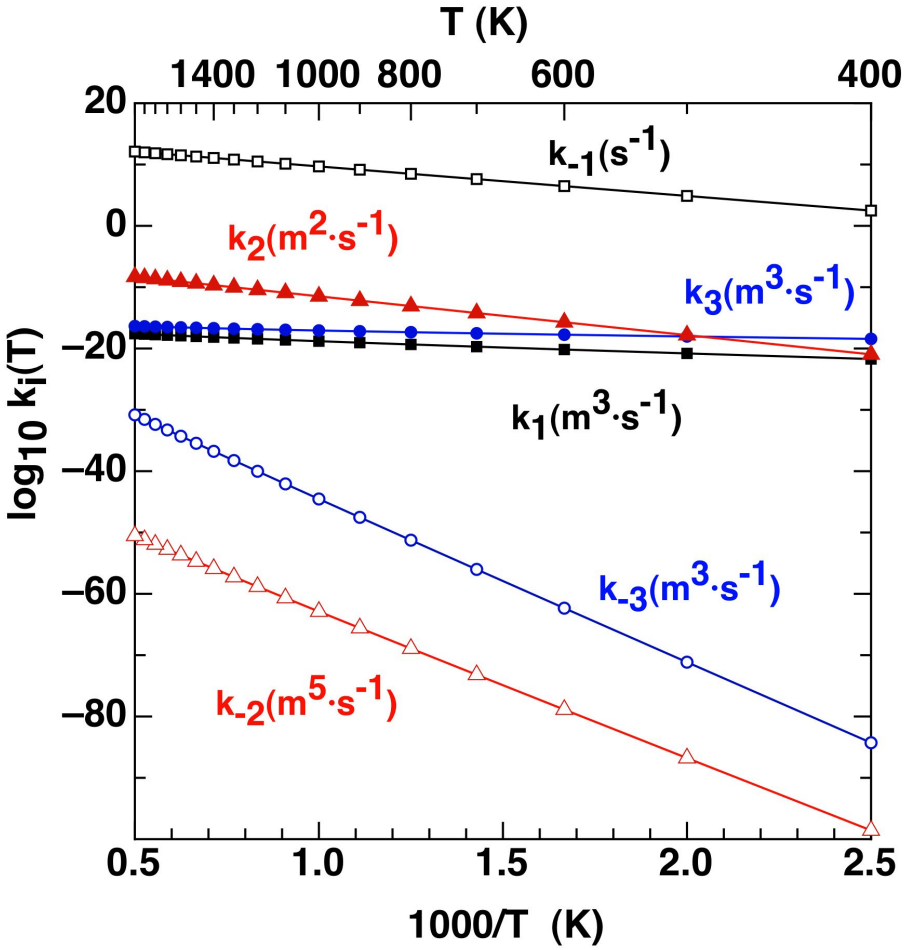

Figure 3.8: Calculated TST thermal rate constants for the different heterogeneous processes involved in the proposed microkinetic model, based on DFT data for a 12.5/25% coverage (11.1/22.2% for LH reaction). Only k_i with same units could be compared directly. Points are connected with a line to guide the view.

is evident that there are large differences in rate constants, so it is expected that they will play an important influence on the global kinetics of the system once the concentrations are included.

Certainly, during reentry (e.g., of Space Shuttle) there are several regimes depending on the altitude and the velocity of the vehicle: a) chemical and thermal

equilibrium, b) chemical non-equilibrium with thermal equilibrium and c) chemical and thermal non-equilibrium inside the shock layer (52). Near the surface (in the boundary layer), a lot of kinetic models assume thermal equilibrium with chemical non-equilibrium (47, 48). Therefore a canonical ensemble approach was considered as suitable for the description of the regime.

From the differential equation for adsorbed atomic oxygen ($d[O_{ad}]/dt$) can be developed the expression in terms of the atomic surface coverage (θ_O), which takes the form,

$$\begin{aligned}\frac{d\theta_O}{dt} &= \theta_O^2\left(\frac{2}{3}k_{-2}[O_2][s]_0 - 2\frac{2}{3}k_2[s]_0\right) - \\ &\quad -\theta_O\left(\big(k_1+k_3\big)[O] + 2\frac{2}{3}k_{-2}[O_2][s]_0 + k_{-3}[O_2] + k_{-1}\right) + \\ &\quad +\left(k_1[O] + \frac{2}{3}k_{-2}[O_2][s]_0 + k_{-3}[O_2]\right) \end{aligned} \tag{3.7}$$

where the 2/3 factor takes into account that only for LH reaction (or its reverse) two adsorbed atoms (or two free sites) not in adjacent bridges and separated only with a C-C bond are able to react (e.g., 4 from 6 possibilities in a 2×2 supercell). The numerical integration of this differential equation for a constant flux of an O/O_2 mixture impinging over the surface allows to obatin the time evolution of θ_O.

The O and O_2 partial pressures were introduced through the [O] and [O_2] concentrations (e.g., $[O] = P_O/RT$). In fact, these pressures were kept constant in the model (i.e., [O]≈[O]$_0$ and [O_2]≈[O_2]$_0$) because the reactivity is very low and moreover, in several experiments with the aim of determining γ_0 coefficients, the initial concentrations of gas are maintained constant during time (103, 104).

It is worth noting that a steady-state (ss) is reached rapidly for different initial conditions (i.e., P_O, P_{O_2} and T) with a final low atomic coverage in all studied cases (figure 3.9). In figure 3.10 the θ_O is plotted at several temperatures for two representative partial pressures although another combinations were also explored. Thus, very low values of a final steady-state atomic surface coverage ($\theta_O < 10^{-3}$) are observed between 300 and 1,000 K for both mixtures, with larger values for the higher O partial pressure as could be expected. This chemisorption of atomic oxygen on the (0001) graphite surface was also revealed experimentally (66), with a low level of adsorption on the basal surface, mainly enhanced by the concentration of defect sites (67). Moreover, these low final θ_O values support as well the use of the DFT data for low coverage in the calculated rate constants.

The shape of θ_O as a function of the temperature shows a maximum at different temperatures (i.e., 400 and 500 K), which depends basically on the initial P_O value

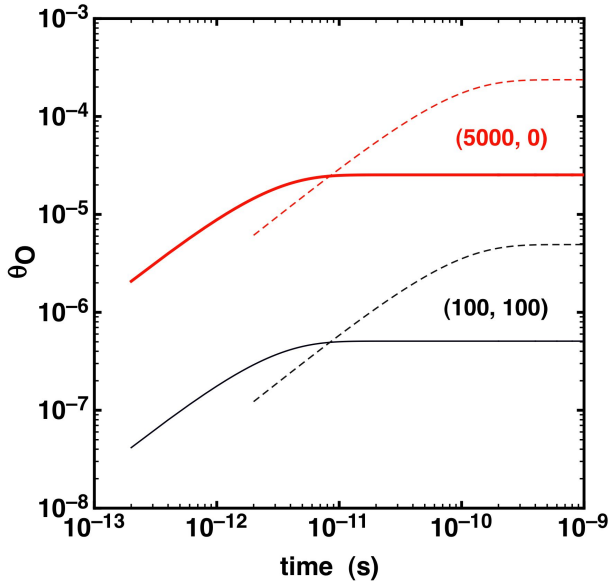

Figure 3.9: Atomic surface coverage time evolution for two O/O_2 initial mixtures: (100, 100 Pa) and (5000, 0 Pa) at 700 K (dashed line) and 900 K (solid line).

as could be expected because at high temperatures the desorption becomes the most important process.

The atomic oxygen recombination coefficient was also estimated from the following equation,

$$\gamma_O = \frac{k_1[O](1-\theta_{O(ss)})[s]_0 + k_3[O]\theta_{O(ss)}[s]_0 - k_{-1}\theta_{O(ss)}[s]_0}{Z_O} \tag{3.8}$$

which includes only the processes that directly involve atomic oxygen, namely adsorption, ER and desorption, once achieved the steady-state ($\theta_{O(ss)}$), and where Z_O is the number of O collisions per unit area and unit time with a planar surface (equation 2.176).

The γ_O coefficient shown in figure 3.10 almost matches the shape of the θ_O plot. An analysis of the three contributions establishes clearly that at low temperatures adsorption and ER reaction are the most important processes with similar contributions, while at high temperatures the rates for adsorption and desorption processes are counterbalanced (i.e., $v_1 = v_{-1}$), and γ_0 finally decreases as a consequence of the lower $\theta_{O(ss)}$ values. Although the final steady-state coverage depends as well on LH process (see equation 3.7), in the present case its contribution is really small due to its low rate constant.

The comparison of the $\gamma_O(T)$ shape over graphite with respect to other materials (e.g., metals (105), alumina (103), silica (104),...) is similar but with lower

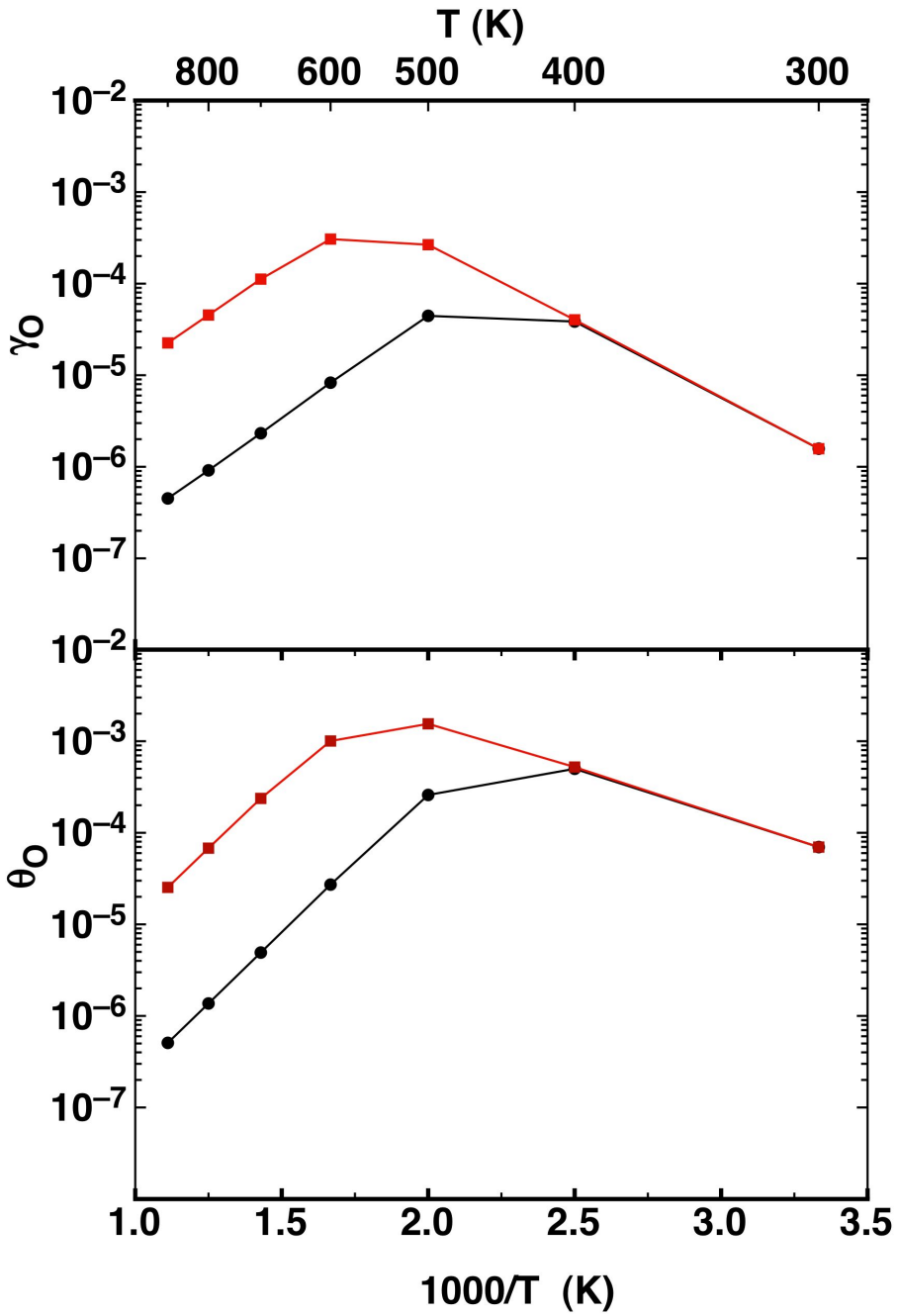

Figure 3.10: Atomic surface coverage and γ_O coefficient in front of the temperature for two O/O_2 initial mixtures: in black circles (100, 100 Pa) and red squares (5,000, 0 Pa).

values. Moreover, the γ_O decline is produced at lower temperature for graphite, possibly as a consequence of its lower desorption energy. The introduction of new rate constants based on DFT data with slab relaxation and/or higher coverages does not produce very important changes with respect to the present results as was checked with some additional calculations, possibly because the very low γ_O values.

The effect of introducing molecular oxygen (i.e., $P_{O_2} \neq 0$) in the initial flux is negligible in all the temperature range explored (300-1,000 K) for both γ_O and θ_O. This is supported by the large energy barriers associated with the two dissociative molecular processes (i.e., very small k_{-2} and k_{-3}).

The very low γ_O coefficients and the large melting point of the graphite (4,800±100 K at a pressure of 10 - 100 MPa (106)) could seemingly indicate that carbon-based materials should be a good proposal to be used as TPS for atmospheres containing oxygen. Nevertheless, the oxidative etching of graphite, forming $CO_{(g)}$ and also $CO_{2(g)}$, can degrade this material and would prevent its use even at moderate temperatures. In fact, several experimental studies (67, 102, 107) have shown that O_2 (or O) oxidation can produce finally $CO_{(g)}$ (a highly endothermic process, 4.2 - 4.5 eV (102)). Although this carbon etching is mainly enhanced by the presence of defect sites, at temperatures higher than 1,148 K also occurs in basal plane carbon atoms (106); HOPG samples at 298 - 493 K exposed to pulsed hyperthermal beams containing atomic and molecular oxygen yield an important and spatially anisotropic etching (69). For this reason, calculations were only made with the proposed microkinetic model up to 1,000 K. Therefore, at higher temperatures, the etching and other surface processes should be included, as for instance:

$$O_{(g)} + graphite \rightarrow CO_{(g)} + graphite \text{ (vacant)} \tag{3.9}$$

$$O_{2(g)} + graphite \rightarrow CO_{2(g)} + graphite \text{ (vacant)} \tag{3.10}$$

In spite of the fact that this kind of microkinetic models are frequently used to simulate the heterogeneous chemical kinetics of dissociated air impinging different kind of surfaces (47, 108) with good agreement in comparison with available experimental data (e.g., total heat flux to the surface, γ coefficients, ...), more sophisticated Monte Carlo simulations (e.g., N over silica (105), H over graphite (109)) can also be performed including, for instance, different types of Eley-Rideal mechanisms or the coverage effect through the time evolution of the system.

3.5 PES construction for O/O_2 over graphite system

One of the aims of this work is to study the dynamics of the atomic and molecular oxygen interacting with a basal graphite surface. For this reason, fundamental potential energy surfaces for O/O_2 over graphite surface were constructed from DFT data. In the case of the atomic oxygen over graphite, two methods were used to obtain two different potential energy surfaces: an analytical one by means of the Flexible Periodic London-Eyring-Polanyi-Sato (FPLEPS) method and an interpolated one by using the Modified Shepard (MS) method. In general, the description of the system by means of an interpolated surface is in principle considered more accurate than using an analytical one since a higher number of geometrical configurations are included in the first method and the energies of these configurations are perfectly matched. According to this, analytical surfaces are cheaper and easier to construct in the sense that just a small set of DFT data is needed to describe the system. In this work, just a small set of DFT points was used for the FPLEPS fit whereas a broad set was used for the MS interpolation. The general trends of both methods were described in section 2.3, so just some particularities for the systems of interest are presented here. DFT calculations were carried out in the same conditions as the adsorption study of section 3.3.1, (i.e., the GGA/RPBE functional by means of the VASP code with 11×11×1 k-points).

3.5.1 Atomic oxygen over graphite PES

3.5.1.1 Unit cell and symmetry considerations

The complete 2D (X, Y) description of the surface of graphite is achieved by considering just the minimum triangle area inside the unit cell, as shown in figure 3.11. According to this, equivalent configurations to those inside the minimum triangle can be extended to the whole surface through basic symmetry operations (i.e., translations, rotations, ...). Thus, in order to study the interaction of atomic oxygen with the entire graphite surface is enough with getting the energy associated with several DFT configurations, that means to calculate at different X_O, Y_O, Z_O coordinates of the impinging atom just only inside this minimum triangle area. For the case of FPLEPS fitting, just a reduced set of DFT points at six selected sites (i.e., X_O, Y_O), namely T1, T2, B, H, T1H and T2H (hereafter high-symmetry sites) at different Z_O values were enough. Figure 3.12a plots the location of the high-symmetry sites inside the minimum triangle area whereas table 3.8 shows their X_O, Y_O coordinates. A 2×2 supercell (coverage of 12.5/25%) was used for the calculations in order to avoid as much as possible the interaction

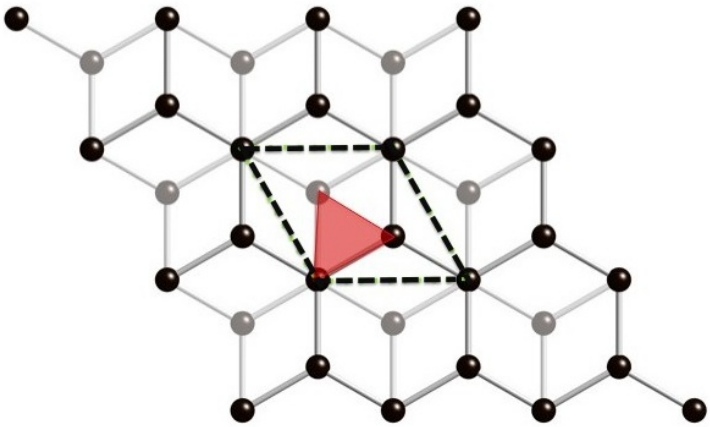

Figure 3.11: Graphite slab top view. The unit cell is shown with black dotted lines and the minimum triangle needed to define the whole solid surface by symmetry operations is shown in red.

with atoms of surrounding cells.

Table 3.8: Cartesian coordinates for the six high-symmetry sites used for the FPLEPS fitting.

Site	X_O (Å)	Y_O (Å)
T1	0.000	0.000
T2	1.234	0.712
B	0.617	0.356
H	0.000	1.424
T1H	0.000	0.712
T2H	0.617	1.068

For each high-symmetry site a total of sixteen Z_O values in the range of 0.2 Å $\leqslant Z_O \leqslant$ 3.1 Å were considered. Thus, a total of 96 DFT data were used for obtaining the FPLEPS PES. For the case of MS interpolation a total of 465 DFT points at different geometries (X_O, Y_O, Z_O) were considered as it can be seen in figure 3.12b. Of all these configurations, only 399 were obtained from a regular grid over the minimum triangle area at Z_O distances in the range of 0.9 Å $\leqslant Z_O \leqslant$ 3.7 Å, whereas 66 configurations were added during the surface

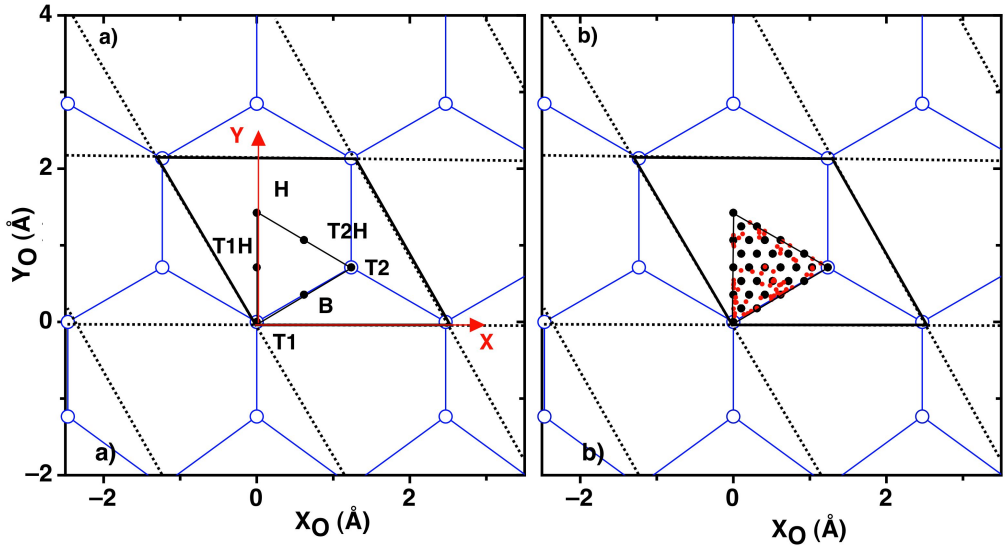

Figure 3.12: X_O, Y_O distribution of DFT points (black dots) used for a) FPLEPS and b) MS PESs. For MS the red points are extra geometries added during the growing process.

growing process. It was observed that very repulsive configurations ($Z_O \leqslant 0.9$ eV) give a non negligible effect on the interpolated energy at points close to this distance. Thus, configurations for lower Z_O values were not included in the interpolation. On the other hand, a deeper study of asymptote for the system at longer distances than 3.1 Å showed the existence of a physisorption minimum. For this reason, configurations between 3.1 Å$\leqslant Z_O \leqslant$ 3.7 Å were also added for the MS interpolation.

Second derivatives for the points (X_i, X_j) needed for the MS interpolation were calculated by using the finite difference method (110) expressed as,

$$\frac{\partial^2 V}{\partial X_i \partial X_j} = \frac{\left(\partial V/\partial X_i\right)_{X_j+\Delta} - \left(\partial V/\partial X_i\right)_{X_j-\Delta}}{2 \cdot \Delta_{X_j}} \tag{3.11}$$

where Δ is a small displacement in the X_j direction. After several convergence tests, Δ was taken as 0.05 Å.

3.5.1.2 Analytical FPLEPS PES

The specific FPLEPS expression used for the interaction potential of the oxygen atom with the surface is expressed as in equation 2.85. In previous studies, the FPLEPS (20, 21, 22) model was applied for the interaction of atom/molecule with

metallic surfaces, where the atom/molecule potential could be described with a modified Morse type potential. Since the oxygen adsorption on graphite shows a more complicated picture with the presence of barriers along the adsorption path (figures 3.13a-f), the good description of these barriers requires the introduction of small modifications in the FPLEPS model. Thus, a switching function to the atom/surface potential was added as follows,

$$U'_{Os}(X_O, Y_O, Z_O) = U_{Os}(X_O, Y_O, Z_O) + \frac{1}{2} f_{s_O}(X_O, Y_O, Z_O) \quad (3.12)$$

$$Q'_{Os}(X_O, Y_O, Z_O) = Q_{Os}(X_O, Y_O, Z_O) + \frac{1}{2} f_{s_O}(X_O, Y_O, Z_O) \quad (3.13)$$

where the switching function has the form of,

$$f_{s_O}(X_O, Y_O, Z_O) = \lambda(X_O, Y_O) \cdot \left(1 + \tanh\left(\vartheta(X_O, Y_O) \cdot Z_O + \chi(X_O, Y_O) \right) \right) \quad (3.14)$$

where $\vartheta(X_O, Y_O)$ and $\chi(X_O, Y_O)$ are taken as follows:

$$\vartheta(X_O, Y_O) = \frac{7}{Z_l(X_O, Y_O) - Z_h(X_O, Y_O)} \quad (3.15)$$

$$\chi(X_O, Y_O) = -3.5 - Z_h(X_O, Y_O) \cdot \vartheta(X_O, Y_O) \quad (3.16)$$

Thus, $f_{s_O}(X_O, Y_O, Z_O)$ varies between 0 at $Z_O = Z_l$ and 2λ at $Z_O = Z_h$ where λ, Z_l and Z_h, are obtained from the fit of the DFT data. Knowing that the height and position of these barriers are significantly shifted from one site to another, it is necessary to introduce an explicit dependence of the switching function parameters (Z_l, Z_h and λ) with the X_O and Y_O coordinates as done for the Morse parameters Δ_{Os}, α_{Os} and $Z_{e,Os}$. It is worth noting that the periodic dependence of α_{Os} is taken into account through the parameters α_0, α_1, α'_0 and α'_1 which are also periodic functions of (X_O, Y_O). This dependence of the parameters with (X_O, Y_O) is attained by using a Fourier expansion, which will be introduced below. The advantage of adding the f_{s_O} function is to well describe the entrance barriers found with DFT calculations.

The Coulomb and exchange integrals (U_{Os} and Q_{Os}) of equations 3.12 and 3.13, respectively, have the of equations 2.78 and 2.77, respectively, presented in section 2.3.1. Furthermore, for the accurate description of the attractive and repulsive branches, the switching function presented in equation 2.83 takes the form,

$$f_{s_{\alpha O}} = \frac{1}{2}\Big(1 + \tanh(35 \cdot Z_O - 52.5)\Big) \quad (3.17)$$

According to this, $\alpha_{Os} = \alpha_l$ (equation 2.81) for values of $Z_O < 1.2$ Å (for the repulsive branch) and $\alpha_{Os} = \alpha_h$ (equation 2.82) for values of $Z_O > 1.66$ Å (for the attractive branch).

The fitting is performed independently at each high-symmetry site considered (T1, T2, B, H, T1H and T2H). The values obtained with this fit are listed in table 3.9. These parameters reproduce perfectly the DFT curves at each high symmetry site, as it can be seen in figure 3.13.

Table 3.9: Value of the parameters P_j at each high-symmetry sites obtained from fitting the DFT data in FPLEPS surface.

		T1	**T2**	**H**	**T2H**	**B**	**T1H**
D_{Os} **(eV)**	P_1	6.345	6.370	3.795	2.916	4.860	3.038
$Z_{e,Os}$ **(Å)**	P_2	1.492	1.491	1.736	1.454	1.348	1.448
α_0 **(Å^{-1})**	P_3	-1.791	-1.791	-0.208	-0.537	-1.732	-0.432
α_1 **(Å^{-2})**	P_4	2.376	2.376	1.029	1.670	2.137	1.576
$\alpha_0^{'}$ **(Å^{-1})**	P_5	2.375	2.360	0.649	1.315	1.655	1.318
$\alpha_1^{'}$ **(Å^{-2})**	P_6	-0.752	-0.736	0.370	0.262	-0.084	0.246
Z_l **(Å)**	P_7	0.800	0.800	0.460	0.550	0.790	0.510
Z_h **(Å)**	P_8	3.110	3.110	3.980	3.270	3.140	3.310
λ **(eV)**	P_9	3.250	3.250	2.590	1.80	2.150	1.900

As mentioned above, to get the values for the parameters at any X_O, Y_O coordinates, a Fourier series as a function of vectors of the reciprocal lattice is used. Thus, for each parameter (i.e.,D_{Os}, $Z_{e,Os}$, α_0, α_1, $\alpha_0^{'}$, $\alpha_1^{'}$, Z_l, Z_h and λ) a fifth order expansion is used, since 6 high-symmetry sites were considered,

$$
\begin{aligned}
P_j(X_O,Y_O) = C_{j0} &+ C_{j1}\left(\cos\left(\frac{2\pi}{a}(u_O+v_O)\right)+\cos\left(\frac{2\pi}{a}u_O\right)+\cos\left(\frac{2\pi}{a}v_O\right)\right)+\\
&+C_{j2}\left(\sin\left(\frac{2\pi}{a}(u_O+v_O)\right)-\sin\left(\frac{2\pi}{a}u_O\right)-\sin\left(\frac{2\pi}{a}v_O\right)\right)+\\
&+C_{j3}\left(\cos\left(\frac{2\pi}{a}(2u_O+v_O)\right)+cos\left(\frac{2\pi}{a}(u_O+2v_O)\right)+\cos\left(\frac{2\pi}{a}(u_O-v_O)\right)\right)+\\
&+C_{j4}\left(\cos\left(\frac{4\pi}{a}(u_O+v_O)\right)+cos\left(\frac{4\pi}{a}u_O\right)+\cos\left(\frac{4\pi}{a}v_O\right)\right)+\\
&+C_{j5}\left(\sin\left(\frac{4\pi}{a}(u_O+v_O)\right)-\sin\left(\frac{4\pi}{a}u_O\right)-\sin\left(\frac{4\pi}{a}v_O\right)\right) \qquad (3.18)
\end{aligned}
$$

where a is the cell parameter ($a = b = 2.468$ Å) P_j stands for each parameter (i.e., $P_1 \equiv D_{Os}$,...; as shown in table 3.13) and where u_O and v_O are the components of

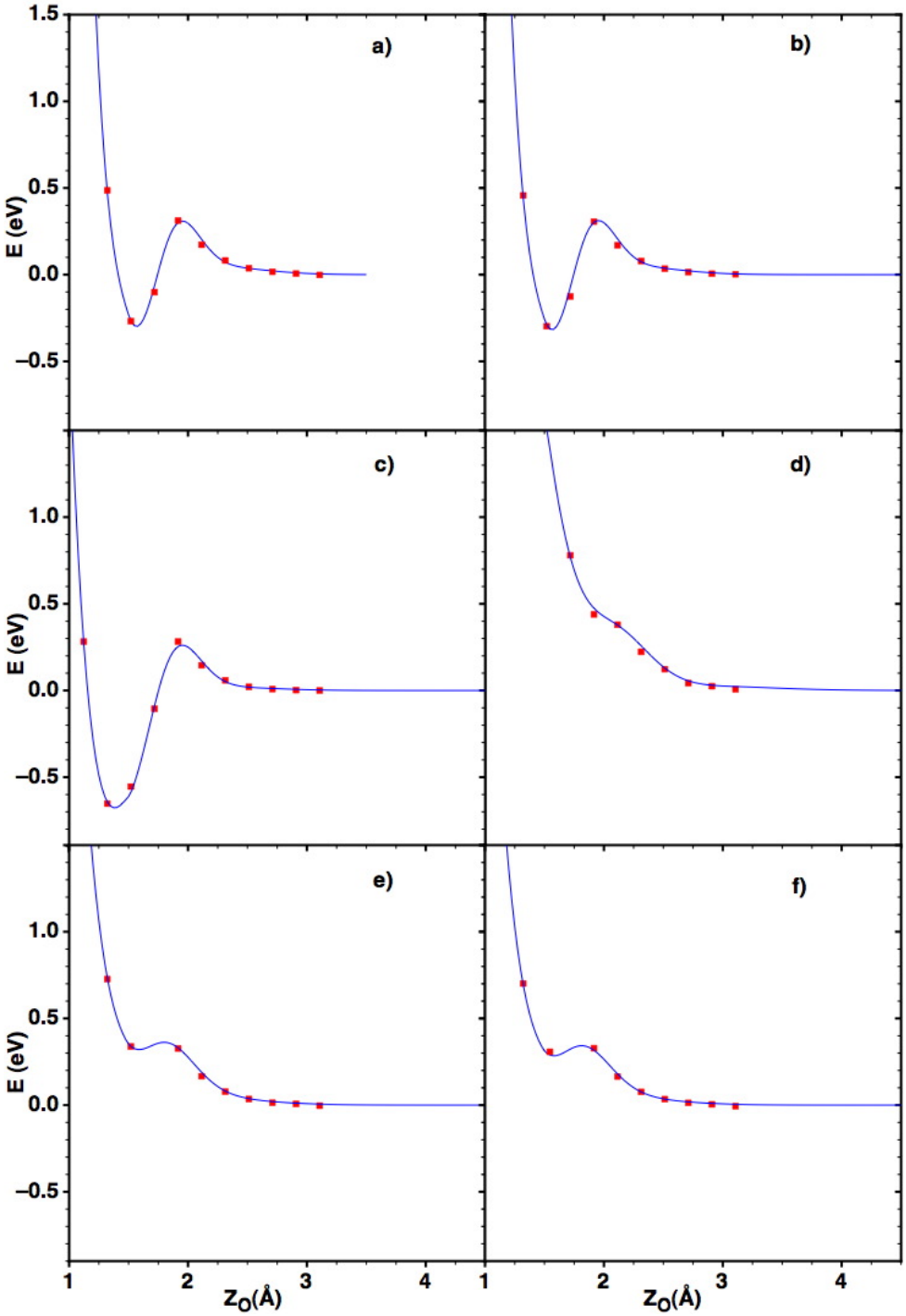

Figure 3.13: DFT calculated data (red points) and FPLEPS fitting (blue lines) for the six high-symmetry sites over graphite: a) T1, b) T2, c) B, d) H, e) T1H and f) T2H. Zero of energies is considered at O+graphite asymptote.

the lattice vectors of the rombohedric cell (although for simplicity α cell parameter was 60° instead of 120°)

$$u_O = X_O - \frac{Y_O}{\sqrt{3}}, \qquad v_O = \frac{2}{\sqrt{3}} Y_O \tag{3.19}$$

For each of the parameters, a system formed by 6 equations and 6 variables is constructed with the Fourier expansion over each of the high-symmetry sites. The solution of the system allows to obtain the Fourier coefficients listed in table 3.10.

Table 3.10: Fourier coefficients for each of the parameters P_j obtained by solving the system of equations.

		$\mathbf{C}_{j0}$	$\mathbf{C}_{j1}$	$\mathbf{C}_{j2}$	$\mathbf{C}_{j3}$	$\mathbf{C}_{j4}$	$\mathbf{C}_{j5}$
D_{Os} **(eV)**	P_1	4.079	0.383	0.635	0.475	-0.102	0.139
$Z_{e,Os}$ **(Å)**	P_2	1.456	$-2.942\cdot10^{-2}$	$-4.980\cdot10^{-2}$	$3.917\cdot10^{-2}$	$2.639\cdot10^{-3}$	$-2.464\cdot10^{-3}$
α_0 **(Å^{-1})**	P_3	-0.991	-0.223	-0.416	$-9.075\cdot10^{-2}$	$4.686\cdot10^{-2}$	-0.111
α_1 **(Å^{-2})**	P_4	1.828	0.143	0.275	$3.317\cdot10^{-2}$	$6.333\cdot10^{-3}$	$1.617\cdot10^{-2}$
$\alpha_0^{'}$ **(Å^{-1})**	P_5	1.521	0.174	0.296	$9.133\cdot10^{-2}$	$1.978\cdot10^{-2}$	$-3.368\cdot10^{-2}$
$\alpha_1^{'}$ **(Å^{-2})**	P_6	$1.283\cdot10^{-2}$	-0.125	-0.207	-0.129	$-1.444\cdot10^{-3}$	$5.581\cdot10^{-3}$
Z_l **(Å)**	P_7	0.634	$4.500\cdot10^{-2}$	$8.949\cdot10^{-2}$	$1.750\cdot10^{-2}$	$-7.222\cdot10^{-3}$	$2.406\cdot10^{-2}$
Z_h **(Å)**	P_8	3.280	$-8.000\cdot10^{-2}$	-0.150	$4.000\cdot10^{-2}$	$-1.667\cdot10^{-2}$	$1.732\cdot10^{-2}$
λ **(eV)**	P_9	2.220	$9.250\cdot10^{-2}$	0.131	0.270	$-1.917\cdot10^{-2}$	$4.330\cdot10^{-3}$

It is worth noting that the Fourier series used ensures the 2D periodicity of the FPLEPS surface. In order to use the Fourier expansion presented in equation 3.18, it is necessary to determine the Fourier coefficients. This determination is equivalent to solve a system of linear equations (n is the number of unknown Fourier coefficients):

$$CS(n,n) \cdot C(n) = P(n) \tag{3.20}$$

where, $C(n)$ is the Fourier coefficients matrix, $CS(n,n)$ is the cosine and sine terms matrix and $P(n)$ is the matrix with the parameter values over the high-symmetry sites. The resolution of the system is performed by using a LU decomposition which decomposes the $CS(n,n)$ matrix as the product of a lower triangular matrix (L matrix) and an upper triangular matrix (U matrix): $CS = L \cdot U$. Therefore, it can be considered $CS \cdot C = (L \cdot U) \cdot C = P$ that can be solved easily considering the two following steps:

1. Another matrix B, can be defined as $B = U \cdot C$, so the equation to be solved is $LB = P$. As the L matrix is triangular, the determination of the B matrix is straighforward.

2. Afterwards, it is solved $U \cdot C = B$. As the U matrix is triangular, the Fourier coefficients matrix (C) can be finally reached.

When the value of the parameters over the high-symmetry sites (the P matrix) are constant, the resolution of the system, that is the determination of the Fourier coefficients is done only once.

Analytical derivatives were also obtained for the FPLEPS surface in order to integrate Hamilton's equation of motion.

3.5.1.3 Interpolated MS PES

The specific expression for the interaction description by MS interpolation scheme is,

$$V(X_O, Y_O, Z_O) = \sum_{i=1}^{N_{data}} w_i(X_O, Y_O, Z_O) \cdot T_i(X_O, Y_O, Z_O) \tag{3.21}$$

where i refers to each of the DFT data used in the interpolation, T_i is a Taylor expansion and w_i is the weight associated with i configuration. The total number of *ab initio* data (N_{data}) used is the sum over all the 465 DFT points calculated inside the minimum triangle area and all the equivalent configurations inside the (1×1) unit cell obtained by using symmetry operations. Considering the unit cell and the half of the surrounding ones (*outln* parameter set to 0.5), a total of 9,156 configurations were used, of which 2,289 were inside of the initial unit cell. The normalised weight w_i for a specific T_i is defined as,

$$w_i = \frac{\nu_i(X_O - X_i, Y_O - Y_i, Z_O - Z_i)}{\sum_{j=1}^{N_{data}} \nu_j(X_O - X_j, Y_O - Y_j, Z_O - Z_j)} \tag{3.22}$$

The primitive weight ν_i for each configuration is calculated considering a simple form depending on the distance between the interpolated point (X_O, Y_O, Z_O) and a specific i configuration (X_i, Y_i, Z_i) as,

$$\nu_i(X_O - X_i, Y_O - Y_i, Z_O - Z_i) = \frac{1}{\left(\sqrt{(X_O - X_i)^2 + (Y_O - Y_i)^2 + (Z_O - Z_i)^2}\right)^p} \tag{3.23}$$

The selection of parameter p was tested for different values within the range $4 \leqslant p \leqslant 12$ and checking the energy conservation during the trajectory, obtaining an optimal value of $p = 8$. Using the same checking procedure, a threshold or a tolerance for the normalised weight (w_i) was stated at $w_{tol} = 1 \cdot 10^{-8}$. Thus, configurations with a weight smaller than this limit ($w_i \leqslant w_{tol}$) were not considered in the potential energy summatorium (equation 3.21). Obviously considering a

smaller limit gives very small differences on the interpolated points (in all checked cases lower than 0.0001 eV).

In order to describe the asymptotic behaviour, a switching function is used (f_{ass}) for Z_O higher than 3.7 Å ($Z_1 = 3.7$ Å) with the form of,

$$f_{ass} = \frac{Z_O}{Z_O^{Z_1^{0.97\cdot(Z_O - Z_1)}}} \tag{3.24}$$

where the value 0.97 is selected in a way that when Z_O tends to Z_1 the derivatives of the function f_{ass} tend to the derivatives of the interpolated function in Z_1, ensuring a soft connection. The potential is then calculated as,

$$V(X_O, Y_O, Z_O) = (V(X_O, Y_O, Z_O = 3.7\text{Å}) - V_{ass}) \cdot f_{ass} + V_{ass} \tag{3.25}$$

where V_{ass} is the asymptotic value (-151.6343 eV) corresponding to O + slab.

For the automated growing of the number of configurations (i) for the MS surface interpolation, the two criteria mentioned in section 2.3.2.2 were used (equations 2.97 and 2.98). Applying these criteria, the surface was grown in 66 points for three initial collision energies ($E_{col} = 0.3, 1.0$ and 3.0 eV) for the trajectory calculations.

3.5.1.4 Characterization of FPLEPS and MS PES

Previously to the dynamical study, a preliminary characterization and comparison between the two PES developed for the atomic oxygen interaction with graphite is presented.

In order to have a first evaluation of the accuracy of the FPLEPS surface, it was calculated the Root Mean Square Deviation (RMSD, equation 2.91) between several DFT calculated energies and the ones obtained with the fit at the same geometry. Very repulsive configurations were not used for the RMSD calculation since the absolute value of the energy for these points is very high and the total RMSD increased considerably. Furthermore, at the initial collision energies used for dynamical calculations these configurations will not be accessible. Thus, a total of 64 configurations between 1.1 Å $\leqslant Z_O \leqslant$ 3.1 Å, used for constructing the FPLEPS, were included to obtain the RMSD, giving a value of 0.0348 eV. Furthermore, the energies of the DFT configurations used for the MS interpolation, were also compared with the fitted energies. In that case, not only repulsive configurations were rejected but also the configurations introduced in the fitting. A total number of 328 configurations were used, giving a RMSD of 0.0954 eV. With those results, it can be said that the FPLEPS surface is very accurate for the system in the tested region.

For comparing FPLEPS and MS surfaces, several curves for the interaction of the oxygen atom at different surface distances (Z_O) at a fixed position over the surface (X_O, Y_O) are plotted in figure 3.14.

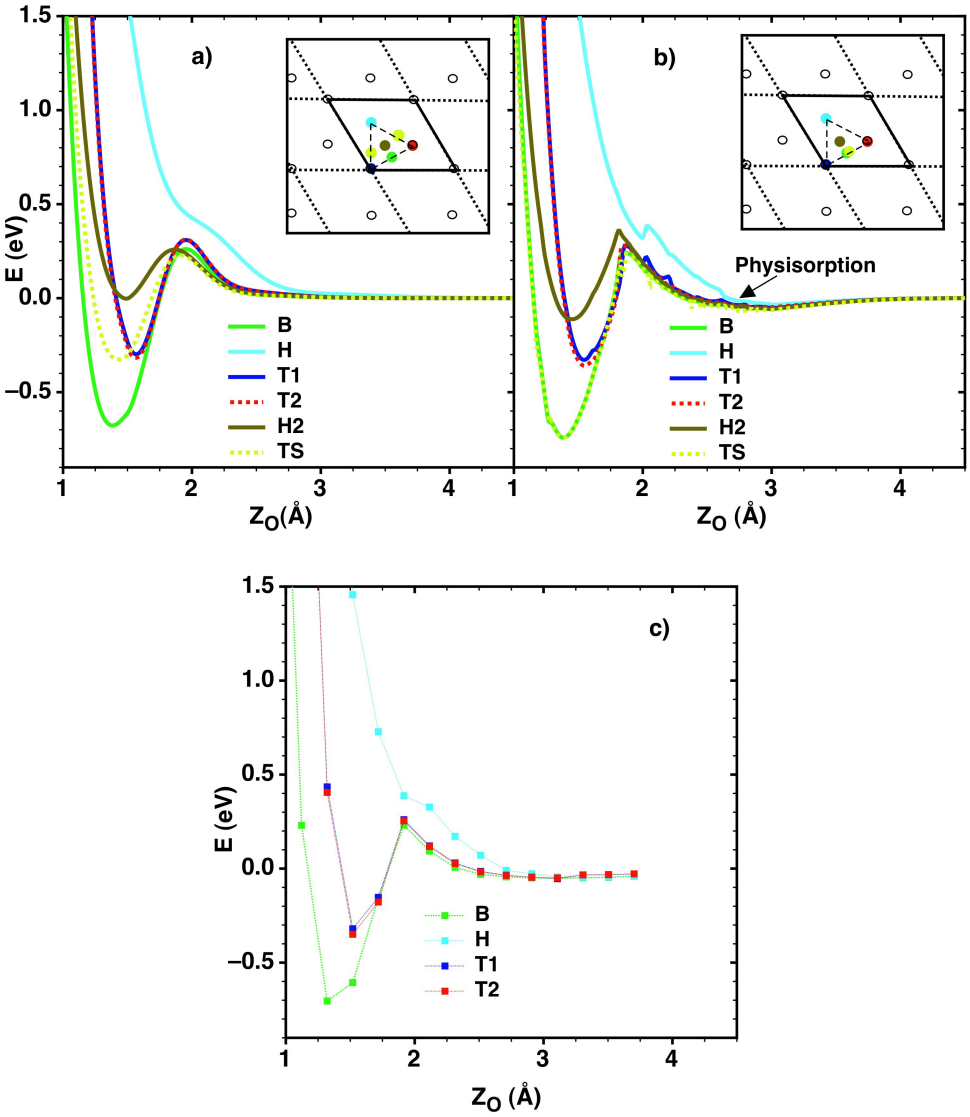

Figure 3.14: Oxygen atom interaction energy at different surface distances (Z_O) for a given X_O and Y_O position over the graphite surface for a) FPLEPS, b) MS and c) for calculated DFT data. Curves named as TS are calculated at the X_O and Y_O where the minimum barrier was found.

Curves were calculated over four high-symmetry sites (B, T1, T2 and H) according to figure 3.12 and over two intermediate points: the one in the middle of the minimum triangle area (H2) and one over the point (TS) where the minimum barrier was found at each PES. The energy values found for each curve calculated over the high-symmetry points at the minimum and the barrier are listed in table 3.11.

Table 3.11: Calculated properties for atomic O adsorption over a basal (0001) graphite surface, without slab relaxation. Zero of energies were considered at $O_{(g)}$ + *Slab* as a supermolecule.

		B	**T1**	**T2**	**H2**	**TS**
FPLEPS	$\mathbf{E}_{min}$ **(eV)**	-0.677	-0.298	-0.317	-0.003	-0.326
	Z_{Omin} **(Å)**	1.384	1.567	1.564	~ 1.49	~ 1.43
	$\mathbf{E}^{\neq}$ **(eV)**	0.261	0.309	0.312	0.259	0.227
	$Z_O^{\neq}$ **(Å)**	1.95	1.95	1.95	1.87	1.91
MS	$\mathbf{E}_{min}$ **(eV)**	-0.742	-0.347	-0.363	-0.112	-0.742
	Z_{Omin} **(Å)**	1.384	1.549	1.547	~ 1.45	~ 1.31
	$\mathbf{E}^{\neq}$ **(eV)**	0.241	0.281	0.279	0.359	0.237
	Z_O **(Å)**	1.86	1.87	1.85	1.82	1.87
DFT	$\mathbf{E}_{min}$ **(eV)**	-0.660	-0.281	-0.308	–	–
	Z_{Omin} **(Å)**	1.385	1.556	1.554	–	–
	$\mathbf{E}^{\neq}$ **(eV)**	0.310	~ 0.31	~ 0.31	–	–
	Z_O **(Å)**	1.874	~ 1.90	~ 1.90	–	–

It is important to note that the absolute energy used as the asymptote for the adsorption study presented in section 3.3.1 and within FPLEPS surface, differs slightly from the one used in MS PES. In all cases, the zero of energies was obtained for a supermolecule calculation considering the oxygen atom far away from the surface although the absolute value for the MS PES was 0.052 eV higher. This new asymptote for the MS was considered after a deeper study at longer distances. The asymptote was taken as the higher absolute energy from several calculations of the oxygen atom at a distance of 5 and 6 Å from the surface at several X_O and Y_O configurations. The asymptote used for the adsorption study and within the FPLEPS surface was calculated averaging the energy of several X_O and Y_O configurations at a distance of 3.1 Å. Thus, the physisorption minima observed for MS curves in figure 3.14 at distances close to 3 Å is not reproduced

in the FPLEPS curves. The 0.052 eV energy difference in the asymptote has to be taken into account when, for example, the results of table 3.11 are compared.

The computed minimum adsorption energies for three high-symmetry sites with FPLEPS and MS surfaces are very close to the calculated ones listed in table 3.3 at the same coverage (12.5/25%). The highest difference between calculated adsorption energies and PES description is found for the bridge minimum for the MS PES, which is not only due to the reference asymptote difference but also due to the bad description of the first and second derivatives around the calculated minimum. The first derivatives in a Taylor series define the slope whereas the second derivatives define the curvature; thus, a bad description in these first or second derivatives for a specific point, as the bridge minimum, leads to a bad description of the area around the point. On the other hand, the optimised distances of oxygen atom from the surface are similar in all computed minima. In that case, the value of the distance does not depend on the asymptote assignment and it can be seen in the close values obtained for both PES. Actually, bridge minimum Z_O distance is the same for both surfaces and very close to the DFT one. Furthermore, top minima are also consistent with the values found in previous adsorption calculations (see table 3.3); although some discrepancies arise from the different surface used. Regarding to the MS physisorption minimum, it is found at distances around 2.75 Å with an stabilization energy lower than 0.06 eV, although vdW contribution is missing (see section 3.3.1).

Calculated barriers over the three high-symmetry sites considered are slightly lower for the MS surface compared to the FPLEPS ones, mainly because of the asymptote definition. On the other hand, the barrier found for the H2 site is found 0.1 eV smaller for FPLEPS surface than for MS one, probably as an artefact of the less accuracy of the fitted surface, since less DFT data were used. It is worth noting that the minimum barrier for the FPLEPS surface appear to be a bit lower than the barrier over the bridge site for the same surface, which seems to be an artefact of the fitting procedure due to the lack of DFT points used in this area. This fact is not observed in the MS surface, where the lowest barrier found (TS) lays in the bridge surroundings, as could be expected. The TS curve was calculated at different Z_O distances from the surface, fixing the position X_O and Y_O, where the minimum barrier was found. For the FPLEPS, this barrier is found close to the T1 in an area where no DFT points were added. As before mentioned, TS curve for MS is almost coincident with the bridge curve for the same surface, which indicates that actually the MEP is close to the adsorption minimum.

Several energy contour plots at three fixed distances of the oxygen atom to the surface at different X_O and Y_O values are presented in figures 3.15a-f in order to give a complete analysis and comparison between both surfaces. In general, good agreement between both representations is found. MS potential energy surface shows wiggly equipotential lines for the effect of the low accuracy in the second

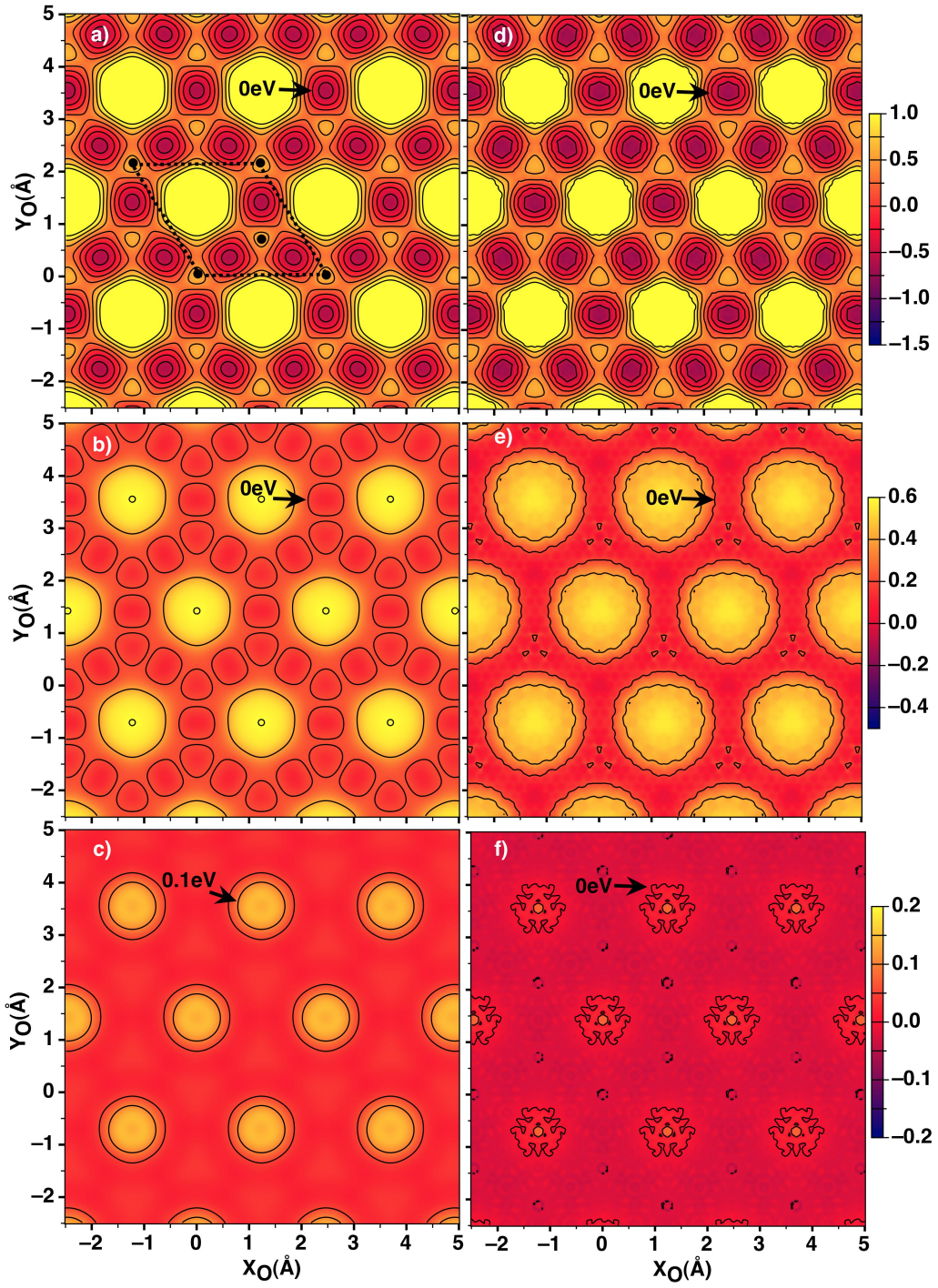

Figure 3.15: Energy contour plots for fixed Z_O along X_O and Y_O oxygen coordinates over graphite surface for FPLEPS at a) 1.30 Å, b) 1.80 Å, and c) 2.50 Å and for MS at d) 1.30 Å e) 1.80 Å and f) 2.50 Å. The energy separation between lines is 0.25 eV for a) and d), 0.2 eV for b) and e) and 0.05 eV for c) and f).

derivatives calculation, as discussed in section 2.3.

The energy contour plots for a Z_O close to the adsorption minimum (figure 3.15a and 3.15d for FPLEPS and MS PES, respectively) show that the central area of the hexagon (close to the hollow site) is quite repulsive. This fact avoids the penetration of the atom in the graphite bulk. The most stable adsorption minimum is found on the Bridge site, above the C-C bond. Furthermore, top sites (T1 and T2) are shown to be more repulsive at this surface distance than the surrounding areas, so the adsorption will be clearly directed to the absolute minimum on bridge site.

Contour plots drawn in figures 3.15b and 3.15e show the energy at a fixed Z_O of 1.80 Å, close to the barrier distances. Although the energetic differences are more clear in these plots due to the smaller scale, the central area of the hexagon is still repulsive and the areas around the bridge and top sites are found to have lower barriers for both surfaces. For the plots at a distance of 2.5 Å a basic difference between the two surfaces is shown. MS surface describes a small stabilization due to the small physisorption minimum, while in FPLEPS surface this minimum is not observed. As it has been told before, this fact is due to the deeper study of the asymptote for the MS surface that was not carried out at the moment of constructing the FPLEPS. Even though, the trend is similar in both plots, where the hexagonal hollow is more repulsive than areas close to the bridge and top sites.

3.5.2 Two oxygen atoms over graphite PES

The interaction of two oxygen atoms with the graphite surface was studied from two points of view. First, the processes associated with the interaction of an impinging O_2 molecule with the surface (this basically leads to molecular scattering and dissociation of the molecule where either both oxygen atoms end in the gas phase or with one or both oxygen atoms being chemisorbed over the surface). And second, the processes related with the interaction of an oxygen atom with an oxygen-precovered surface. In that case, not only processes as adsorption and reflection of the impinging atom or desorption of the preadsorbed atom are studied, but also the Eley-Rideal reaction, which is very important in heterogeneous reactivity. For these reasons, an FPLEPS analytical surface was initially constructed considering a preadsorbed oxygen atom, namely O_A, interacting with an incoming oxygen atom (hereafter O_B). Since the most stable atomic adsorption site was the bridge one for the atomic constructed PES as well as for DFT data, the configurations included into the PES fitting procedure consider also an O_A atom fixed to the DFT calculated bridge minimum for a 3×3 supercell (i.e., a 11.1% of coverage considering bridge sites). Working with such a big supercell increases considerably the number of atoms to be included in DFT calculations, and consequently the computing time but, this was necessary in order to avoid

interactions between adsorbed atoms in contiguous cells. A picture showing the parameters used to define the geometry of the system is found in figure 2.1. To ensure a proper description of the interaction of the incident O_B atom with the preadsorbed one, configurations at different ϕ angles (i.e., $\phi = 30°$, $60°$, $90°$ and $120°$) were calculated for several impact parameters (figure 3.16) in the range of 0.0 Å $\leqslant b \leqslant$ 3.0 Å and considering O_B atom at Z_{O_B} values between 1.1 Å and 3.1 Å. For the analytical fit, a total of 563 geometrical configurations were used at the different before mentioned conditions.

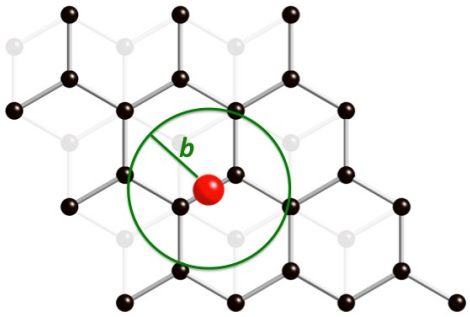

Figure 3.16: Definition of the impact parameter b.

The FPLEPS expression for the two incoming oxygen atoms case is expressed as in equation 2.76 considering that Coulomb and exchange integrals are expressed in the same manner than in equations 2.77 and 2.78, respectively. A term to improve the entrance valley shape for the ER reaction is added with the form,

$$\sum_{i=1}^{2} G_i(\phi) \tag{3.26}$$

where each $G_i(\phi, b, Z_{cm})$ takes the form of a Gaussian function,

$$G_i(\phi, b, Z_{cm}) = A_i(\phi) \cdot e^{-\left[\left(\frac{(b-b_i(\phi))^2}{\sigma_i(\phi)}\right)+\left(\frac{(Z_{cm}-Z_{cm,i}(\phi))^2}{\sigma_{cm,i}(\phi)}\right)\right]} \qquad i = 1, 2 \tag{3.27}$$

where,

$$Z_{cm} = \frac{(Z_{O_A}+Z_{O_B})}{2}, \quad b = \sqrt{(X_{O_B} - X_{O_A})^2 + (Y_{O_B} - Y_{O_A})^2} \tag{3.28}$$

where Z_{cm} refers to the molecule center of mass, and b to the impact parameter. The other parameters used in equation 3.27 (i.e., A_i, $b_i(\phi)$, $Z_{cm,i}(\phi)$, $\sigma_i(\phi)$ and

$\sigma_{cm,i}(\phi)$) define the height, the position and the width of the function and are found by fitting the DFT data available.

From now on, the Sato and Gaussian parameters are used in the FPLEPS to fit the DFT data within the ER area entrance channel. The parameters used for the molecular terms ($Q_{O_AO_B}, U_{O_AO_B}$) and for the Sato Δ_{Os} parameter for the atomic interaction with the surface require to include the ϕ dependence. The function defining this dependence must accomplish,

$$f(\phi) = f(-\phi) \quad \text{and} \quad f(\phi) = f(\pi + \phi) \tag{3.29}$$

which corresponds to the periodicity of the surface when atom O_A is adsorbed over a bridge site (the function would be different if the adsorbed atom were over another site like the T1). $P_j(\phi)$ function used for the j parameter calculation is defined as follows,

$$P_j(\phi) = B_{j0} + B_{j1}\cos(2\phi) + B_{j2}\cos(4\phi) + B_{j3}\cos(6\phi) \tag{3.30}$$

These B_{ij} parameters are obtained by solving the equation system listed below,

$$\begin{aligned}
B_{j0}(\phi) &= \frac{1}{6}\Big(P_j(\phi=30^\circ) + 2P_j(\phi=60^\circ) + 2P_j(\phi=90^\circ) + P_j(\phi=120^\circ)\Big) \\
B_{j1}(\phi) &= \frac{1}{3}\Big(P_j(\phi=30^\circ) + P_j(\phi=60^\circ) - P_j(\phi=90^\circ) - P_j(\phi=120^\circ)\Big) \\
B_{j2}(\phi) &= \frac{1}{3}\Big(P_j(\phi=30^\circ) - P_j(\phi=60^\circ) - P_j(\phi=90^\circ) + P_j(\phi=120^\circ)\Big) \\
B_{j3}(\phi) &= \frac{1}{6}\Big(P_j(\phi=30^\circ) - 2P_j(\phi=60^\circ) + 2P_j(\phi=90^\circ) - P_j(\phi=120^\circ)\Big)
\end{aligned} \tag{3.31}$$

where $P_j(\phi)$ are obtained from the fitting of the ER DFT data. The parameters $P_j(\phi)$ obtained by the DFT data fit are found in table 3.12. First and second rows parameters found in the table correspond to Sato parameters, and the rest are associated with the Gaussian functions defined above (equation 3.27). Furthermore, in table 3.13 the B_{ji} coefficients obtained by solving the system of equations for $P_j(\phi)$ are listed.

The ϕ dependence used in the FPLEPS model produces an artefact in the potential at $b = 0$ since the ϕ angle is not well defined at this value. Thus, in order to obtain a correct representation for this impact parameter, it was necessary to include a switching function for the two Sato parameters as,

$$\Delta'_{O_AO_B}(\phi) = (1 - f_{s_b}) \cdot \xi_1 + f_{s_b} \cdot \Delta_{O_AO_B}(\phi) \tag{3.32}$$

$$\Delta'_{Os}(\phi) = (1 - f_{s_b}) \cdot \xi_2 + f_{s_b} \cdot \Delta_{Os}(\phi) \tag{3.33}$$

Table 3.12: $P_j(\phi)$ parameters obtained by fitting DFT data for the FPLEPS surface.

		$\phi = 30°$	$\phi = 60°$	$\phi = 90°$	$\phi = 120°$
$\Delta_{O_AO_B}(\phi)$ (eV)	P_1	-0.10	0.01	-0.27	0.01
$\Delta_{Os}(\phi)$ (eV)	P_2	-0.13	-0.16	-0.13	-0.35
$A_1(\phi)$ (eV)	P_3	-1.97	-0.80	-0.41	2.24
$b_1(\phi)$ (Å)	P_4	1.07	1.05	1.11	1.53
$\sigma_1(\phi)$ (Å)	P_5	0.17	0.08	0.17	0.20
$Z_{cm,1}(\phi)$ (Å)	P_6	1.72	1.73	1.98	1.27
$\sigma_{cm,1}(\phi)$ (Å)	P_7	0.06	0.02	0.09	0.13
$A_2(\phi)$ (eV)	P_8	0.85	1.33	0.92	0.38
$b_2(\phi)$ (Å)	P_9	2.26	1.64	1.64	1.69
$\sigma_2(\phi)$ (Å)	P_{10}	0.22	0.09	0.13	0.50
$Z_{cm,2}(\phi)$ (Å)	P_{11}	1.39	1.43	1.36	1.26
$\sigma_{cm,2}(\phi)$ (Å)	P_{12}	0.06	0.02	0.02	0.04

Table 3.13: B_{ij} coefficients for each $P_j(\phi)$ function.

		B_{j0}	B_{j1}	B_{j2}	B_{j3}
$\Delta_{O_AO_B}(\phi)$(eV)	P_1	-0.10	$5.67{\cdot}10^{-2}$	$5.67{\cdot}10^{-2}$	-0.11
$\Delta_{Os}(\phi)$ (eV)	P_2	-0.18	$6.33{\cdot}10^{-2}$	$-6.33{\cdot}10^{-2}$	$4.67{\cdot}10^{-2}$
$A_1(\phi)$ (eV)	P_3	-0.36	-1.53	0.49	-0.57
$b_1(\phi)$ (Å)	P_4	1.15	-0.17	0.15	$-5.37{\cdot}10^{-2}$
$\sigma_1(\phi)$ (Å)	P_5	0.15	$-4.00{\cdot}10^{-2}$	$4.00{\cdot}10^{-2}$	$2.50{\cdot}10^{-2}$
$Z_{cm,1}(\phi)$ (Å)	P_6	1.74	$6.67{\cdot}10^{-2}$	-0.24	0.16
$\sigma_{cm,1}(\phi)$ (Å)	P_7	$6.83{\cdot}10^{-2}$	$-4.67{\cdot}10^{-2}$	$2.67{\cdot}10^{-2}$	$1.17{\cdot}10^{-2}$
$A_2(\phi)$ (eV)	P_8	0.96	0.29	-0.34	$-5.83{\cdot}10^{-2}$
$b_2(\phi)$ (Å)	P_9	1.98	-0.25	0.63	$-9.83{\cdot}10^{-2}$
$\sigma_2(\phi)$ (Å)	P_{10}	0.19	-0.11	0.17	$-3.33{\cdot}10^{-2}$
$Z_{cm,2}(\phi)$ (Å)	P_{11}	1.37	$6.67{\cdot}10^{-2}$	$-4.67{\cdot}10^{-2}$	$-1.67{\cdot}10^{-3}$
$\sigma_{cm,2}(\phi)$ (Å)	P_{12}	$3.00{\cdot}10^{-2}$	$6.67{\cdot}10^{-3}$	$2.00{\cdot}10^{-2}$	$3.33{\cdot}10^{-3}$

where ξ_i is the value of the Sato parameter at $b = 0$. The switching function used is,

$$f_{s_b} = \frac{1}{2}\Big(1 + \tanh(\varpi_2 \cdot b + \kappa_2)\Big) \tag{3.34}$$

where ϖ_2 and κ_2 are chosen in order to give a connection as smooth as possible. Furthermore, in order to obtain a good behaviour of the PES at $b = 0$ compared with the DFT data, the Sato parameters at $b = 0$ (ξ_i) are obtained as,

$$\xi_i = (1 - f_{is_{b2}}) \cdot l_i + f_{is_{b2}} \cdot m_i \qquad i = 1, 2 \tag{3.35}$$

where l_i and m_i correspond to the values you have to switch. For ξ_1 the values to switch are related with $P_1 \equiv \Delta_{O_AO_B}$ and the values varies from 0.010 eV to -0.158 eV. For ξ_2 the values to switch are related with $P_2 \equiv \Delta_{Os}$ and the values change from -0.250 eV to -0.133 eV. The switching function used have the form,

$$f_{1s_{b2}} = \frac{1}{2}\Big(1 + \tanh(\varpi_3 \cdot r + \kappa_3)\Big) \tag{3.36}$$

$$f_{2s_{b2}} = \frac{1}{2}\Big(1 + \tanh(\varpi_3 \cdot Z_{Os} + \kappa_3)\Big) \tag{3.37}$$

where ϖ_3 and κ_3 are chosen to the smoothest connection. The parameters used for the correct description at $b = 0$ are listed in table 3.14.

Table 3.14: Values for the parameters used in Sato switching functions for the correct description of b impact parameter at 0.

κ_2 (adim.)	-3.5
κ_3 (adim.)	$-3.5 - 1.48\varpi_3$
ϖ_2 (Å^{-1})	20
ϖ_3 (Å^{-1})	76.923
l_1 (eV)	0.010
l_2 (eV)	-0.350
m_1 (eV)	-0.158
m_2 (eV)	-0.113

Parameters used in equation 2.77, 2.78 and 2.84 for the molecular term ($\Delta_{O_AO_B}$, $\widetilde{\alpha}_0$, $\widetilde{\alpha}_1$, r^e), are obtained from the gas phase O_2 potential determined from coupled cluster calculations (111), which are in good agreement with experimental results (i.e., $D_{O_2(exp)} = 5.210$ eV and $r^e_{OAO_B(exp)}$=1.219 Å (112)) and are listed in table 3.15.

Table 3.15: Parameters obtained from the gas phase O_2 Morse fitting used in equations 2.77, 2.78 and 2.84.

D_{O_2} (eV)	5.219
$\widetilde{\alpha}_0$ (Å^{-1})	1.541
$\widetilde{\alpha}_1$ (Å^{-1})	0.956
r^e (Å)	1.219

As mentioned in section 2.3.1 several parameters from the atom/surface term, presented in previous equations (Δ_{Os}, Z^e_{Os}, α_0, α_1, $\alpha_0^{'}$, $\alpha_1^{'}$, Z_l, Z_h, λ) depend on (X_O, Y_O) coordinates and are periodic through a Fourier expansion, which depends on the crystal surface symmetry. These parameters at each high-symmetry site were already calculated for the atomic FPLEPS and can be found in table 3.9. Furthermore, the Fourier coefficients that allow to compute the parameters at any (X_O, Y_O) coordinates are found in table 3.10.

The behaviour of the fitted surface was checked at different conditions. Firstly, the description of the atomic adsorption at two different bridge sites far enough from each other is plotted in figure 3.17 in order to confirm as negligible the interaction between them. The graph shows a perfect concordance with the results obtained for the atomic FPLEPS surface; one atom adsorption energy is reproduced along with the adsorption barrier for each of the independent atoms. Thus, the minimum observed for O_{ad} + O_{ad} is at 1.35 eV. Furthermore, the energetic of the surface when one of the oxygen atoms is over a bridge site and the other over the contiguous one at several Z_{O_A} and Z_{O_B} values is plotted in figure 3.18a. The distance between two contiguous bridge sites is of 1.214 Å, very close to the equilibrium distance for the O_2 molecule used in the FPLEPS (1.219 Å). Thus, the energetics of the O_2 molecule approaching to the surface can be considered approximately when $Z_{O_A} = Z_{O_B}$. It can be observed in figure 3.18a that at long distances from the surface, the energy is lower than -5 eV (see the diagonal of the graph), in concordance with the O_2 gas dissociation energy of 5.219 eV (used in the FPLEPS fit). For shorter distances the interaction becomes repulsive, which indicates that the adsorption of two atoms on consecutive bridge sites is unfavourable. In the picture can be also seen (i.e., long Z_{O_A} and short Z_{O_B} distances) that the surface reproduces as well the adsorption energy of a single oxygen atom on a bridge site when the other is at long surface distances. For the approaching of one O atom to the surface when the other one is already preadsorbed, it is observed that to form the O_2 molecule (Eley-Rideal process), a transition state with a lower barrier is obtained. In figure 3.18b the energetics of the approaching for both atoms over the same bridge site is also plotted. The

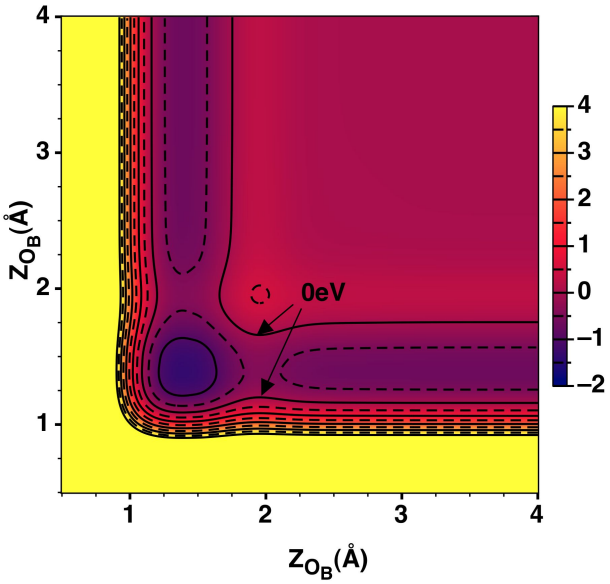

Figure 3.17: Energy contour plots for fixed X_{O_A}, Y_{O_A} and X_{O_B}, Y_{O_B} over two distant bridge sites assuring that the interaction between atom A and B is negligible. The energetic separation between lines is 0.5 eV and the zero of energies is at $O_{(g)} + O_{(g)} + slab$.

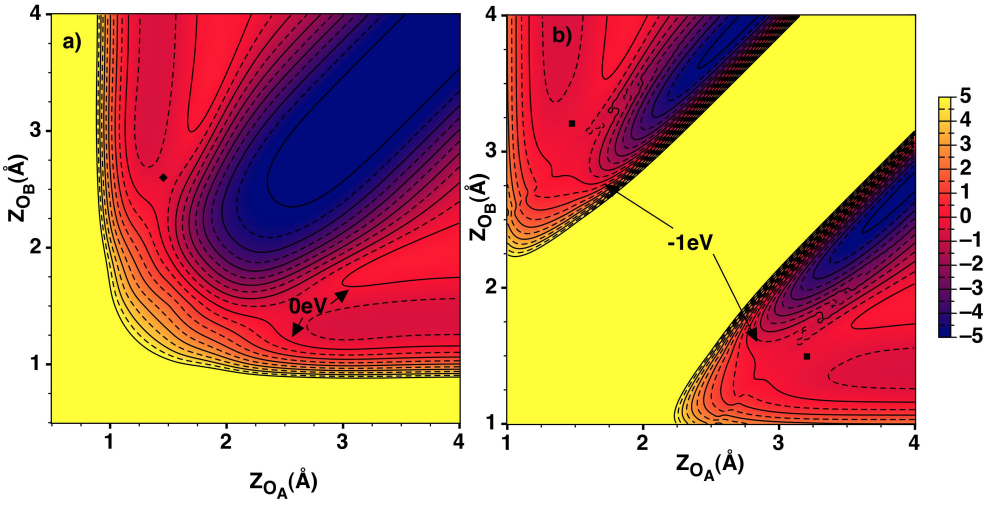

Figure 3.18: Energy contour plots for fixed X_{O_A}, Y_{O_A} and X_{O_B}, Y_{O_B} a) over consecutive bridges at a distance of 1.214 Å and b) both atoms over the same bridge (perpendicular configuration) where the approximate TS (for ER reaction) is indicated by a black square. The energetic separation between lines is 0.5 eV.

very repulsive yellow area drawn corresponds to configurations where the atoms are very close to each other or very close to the surface. On the other hand, the stabilised blue area corresponds to the formation of the O_2 molecule perpendicular to the surface. When for example one atom is adsorbed O_{ad} and the other is at long distances, the atomic adsorption energy is well reproduced. Equally to the previous plot, a transition state with a low barrier is observed for the O_2 formation via Eley-Rideal reaction considering this specific configuration.

In order to analyse the transition state for the Eley-Rideal process, different plots were made for a grid of X_O and Y_O, keeping fix the Z_O for the incoming O atom and the coordinates of the other atom fixed to the optimum adsorption minimum in the FPLEPS surface (i.e.,X_{O_A} = 0.627 Å, Y_{O_A} = 0.362 Å and Z_{O_A} = 1.384 Å). Plots presented in figure 3.19a and 3.19b show the more stable X_{O_B} and Y_{O_B} positions for the approximation of the oxygen atom on gas phase to the preadsorbed atom on the surface at Z_{O_B} = 2.5 and 3.0 Å, respectively. It can

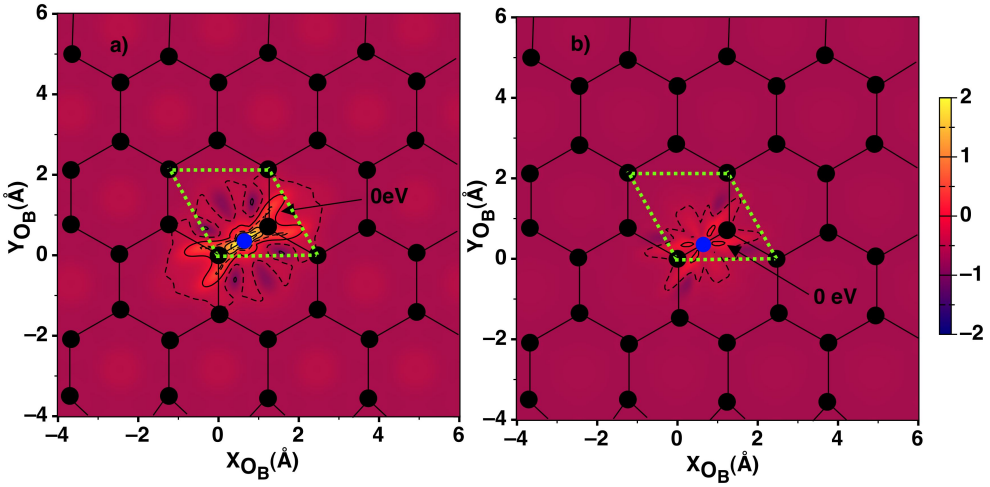

Figure 3.19: Energy contour plots for fixed preadsorbed O_A (X_{O_A} = 0.627$\AA$, Y_{O_A} =0.362 Å, Z_{O_A}=1.384 Å) on the bridge minimum site (represented by a blue circle) for a grid of the incoming O_B atom (X_{O_B}, Y_{O_B}) at a) Z_{O_B} = 2.5 Å and b) Z_{O_B} = 3.0 Å. The energetic separation between lines is 0.5 eV.

be seen that at 3.0 Å the most stable approximation area is over the contiguous bridge sites while at a closer distance of 2.5 Å, areas close to the hexagonal hollow are also accessible. Thus, in order to find a threshold for the ER reaction some calculations were carried out taking into account these specific positions. Due to the small value of the barrier no full optimization for this TS structure was possible, but several calculations reveal that a TS could exist when O atom is approaching to the surface near the hollow area. The geometric parameters found for the TS are listed in table 3.16 and lead to a low barrier of 0.112 eV. The

analysis of second derivatives at this point show an imaginary frequency, which ensured the existence of a transition state although further dynamical results will show the possible existence of a lower one, which was not found in the exhaustive analysis of the present potential energy surface.

Table 3.16: Geometric parameters for the Eley-Rideal transition state. C_1 and C_2 are the closest carbon atoms to both of the oxygen atoms.

Z_{O_A} (Å)	1.345
Z_{O_B} (Å)	3.05
r (Å)	2.053
$\Delta E^{\neq}$ (eV)	0.112
dO_AC_1 (Å)	1.519
dO_AC_1 (Å)	1.524
dO_BC_2 (Å)	3.331
dO_BC_2 (Å)	3.324

The analytical surface obtained by fitting the DFT data (mainly for ER configurations) was tested by comparing with additional DFT data in order to check the accuracy of this PES. Thus, new molecular DFT configurations were calculated with the O_2 molecule center of mass fixed over the bridge site at several Z_{cm} values between 1.3 Å and 5.0 Å. The internuclear distance (r) was varied in the range 1.15 Å $\leqslant r \leqslant$ 3.0 Å. A total of 654 calculated configurations were compared with the FPLEPS analytical energy discarding the same points that have a repulsion energy higher than 3.0 eV. The RMSD obtained was 0.773 eV. It was also calculated the RMSD for some of the configurations used in the PES fitting. For that purpose, as it was done before, only configurations with a repulsion energy lower than 3.0 eV were taken into account. Thus, a total of 332 points were used, giving a RMSD of 0.701 eV. These results, if compared with RMSD for the atomic FPLEPS, could seem not very good. Nevertheless, the configurations used here are allowed to be much more repulsive than in the atomic case.

Contour plots of the energy for the oxygen molecule at the equilibrium distance $r^e = 1.219$ Å for a grid in X_{cm} and Y_{cm} are plotted in figure 3.20 for $\phi = 30°$ and 120° for parallel configurations of the molecule respect the surface ($\theta = 90°$ (figure 2.1) at three Z_{cm} distances of 1.8, 2.4 and 3.5 Å. To simplify the comprehension, asymptote used for these plots has been considered zero for the O_2 molecule in gas phase at a long distance from the surface. The interaction at the closest distances of the molecule to the surface is repulsive. It can be observed for distances of 1.8 Å that the ϕ orientation of the molecule has a big effect on

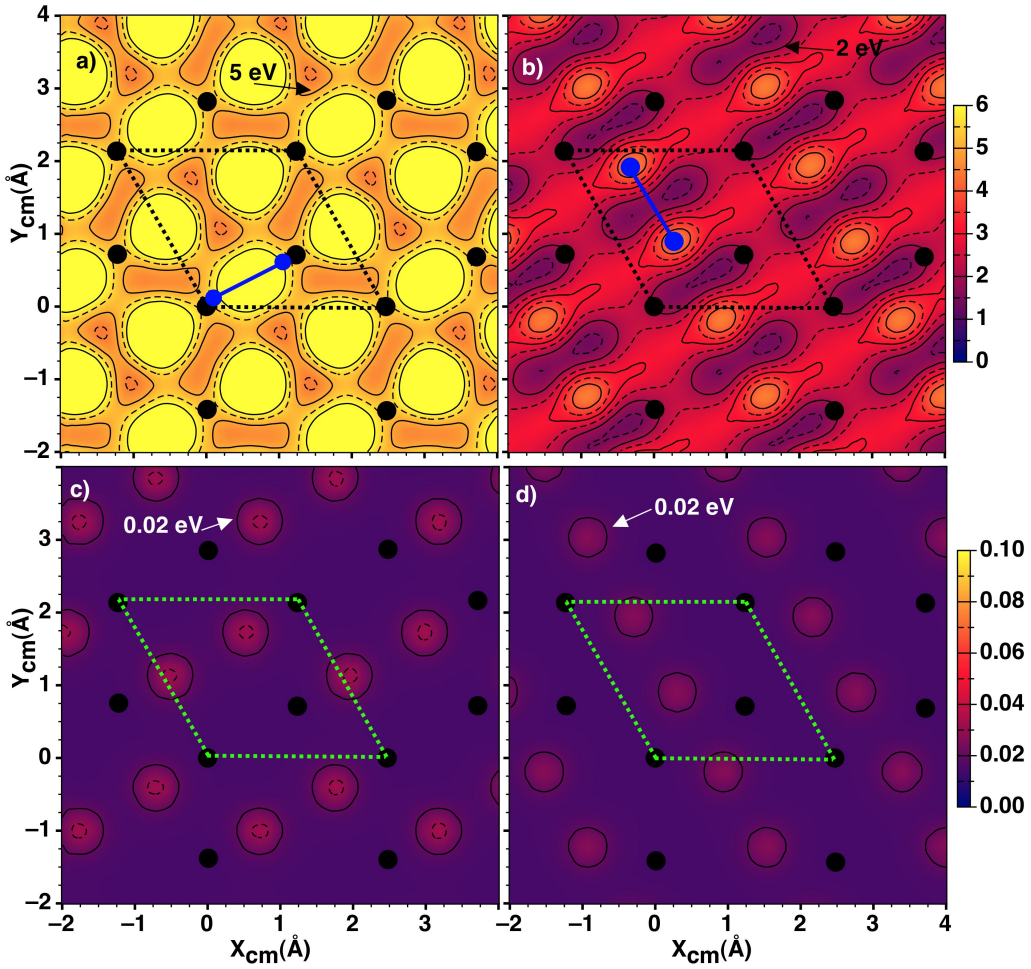

Figure 3.20: Energy contour plots for the molecule at the equilibrium r^e interatomic distance of 1.219 Å for a (X_{cm}, Y_{cm}) grid at a) $\phi = 30°$ and $Z_{cm} = 1.8$ Å, b) $\phi = 120°$ and $Z_{cm} = 1.8$ Å, c) $\phi = 30°$ and $Z_{cm} = 3.5$ Å and d) $\phi = 120°$ and $Z_{cm} = 3.5$ Å. The energetic separation between lines is 0.5 eV for a) and b) and 0.01 eV for c) and d).

the energy. In general, for $\phi = 30°$ the configurations are much more repulsive than for $\phi = 120°$ ones. No physisorption minimum is observed as the DFT calculations predict. Although a better vdW description of the interaction (section 3.3.2) could produce a small physisorption minimum that has not been included here.

The energetics of the molecule at different orientations (θ, ϕ) and surface distances (Z_{O_A}, Z_{O_B}) point out that molecular adsorption is not an important process in that system (section 3.3.2 and figure 3.20). On the other hand, molecular dissociation energetics was explored fixing the molecular centre of mass over the bridge site for $\phi = 0°$ and $90°$ for parallel configurations ($\theta = 90°$). In figure 3.21 the energy variation along r internuclear distance and Z_{cm} is plotted. The zero reference energy is taken here as the two atoms in gas phase at long surface distances, thus, the minimum observed in figure 3.21a at short Z_{cm} distances for $r \approx 2.5$ Å corresponds to the adsorption of two oxygen atoms over two independent bridge sites (notice that the distance between two non consecutive bridge sites is 2.468 Å). The dissociation process ($O_{2(g)} \rightarrow O_{ad} + O_{ad}$) observed at this specific configuration has a high activation energy associated with a transition state. Although no transition state was found analysing the PES, from the figure a threshold is observed at $\Delta E^{\neq} = 5.657$ (with an endothermicity of 3.865 eV) eV for $\phi = 0°$, $\theta = 90°$ at $r = 1.75$ Å and $Z_{cm} = 1.65$ Å. At $\phi = 90°$ and $\theta = 90°$ the behaviour is very similar to that presented before. The only significant difference is found at short surface distances since the PES does not present any adsorption minimum. Obviously, the dissociation could present different energetic profiles from the bridge site if different Z_{cm} is fixed at other coordinates (X_{cm}, Y_{cm}) over the surface.

3.6 QCT study of oxygen interaction with graphite

3.6.1 Atomic oxygen QCT collision study

3.6.1.1 Computational details

A dynamical study of the adsorption and reflection of atomic oxygen over (0001) graphite surface was done by means of the quasiclassical trajectory method. Several initial collision energies between 0.05 eV $\leqslant E_{col} \leqslant$ 3.0 eV were considered for both FPLEPS and MS surfaces at two incident angles, $\theta_v = 0°$ and $45°$, for the initial velocity vector $\vec{v}$ (figure 3.22). All these conditions were firstly explored assuming rigid slab model without the effect of the surface temperature and with the surface temperature effect via a Generalised Langevin Oscillator (GLO) model (section 2.4.1). Surface temperatures (T_{surf}) considered were in the range of 100 K $\leqslant T_{surf} \leqslant$ 1,300 K. In addition, thermal initial conditions

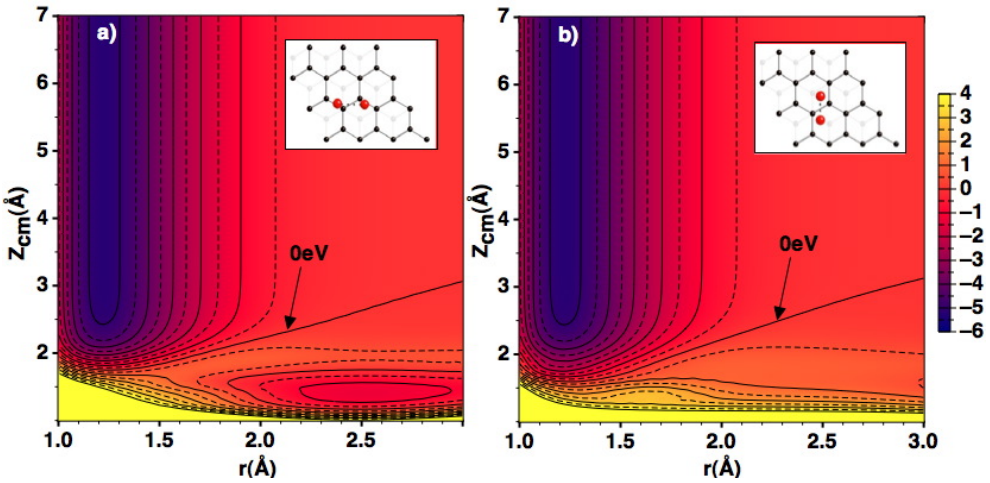

Figure 3.21: Energy contour plots for fixed X_{cm}=0.627 , Y_{cm} =0.362 Å at several Z_{cm} and r at a) $\phi = 0°$ and b) $\phi = 90°$ and $\theta = 90°$. The energetic separation between lines is 0.5 eV. Zero of energy at $O_{(g)} + O_{(g)} + slab$.

for O atom (T_g) were also investigated for a temperature range between 300 K $\leqslant T_g \leqslant$ 1,500 K for initial $\theta_v = 0°$ and 45° approaching angles. Finally, a hyperthermal atom distribution at $T_{surf} = 503$ K was also studied in order to compare directly with the experimental study of Paci et al. (71).

Initial incoming oxygen position (X_O, Y_O) is randomly selected along the (1×1) unit cell meanwhile initial Z_O position is set to 6.5 Å, where the interaction with the surface is negligible. Quasiclassical trajectories were calculated with *qctsurf* program developed in our group, which integrates the Hamilton's equations with the Beeman algorithm. The time step used for both surfaces was $5 \cdot 10^{-17}$ s which ensures a total energy conservation along the trajectories lower than 10^{-4} - 10^{-5} eV when GLO bath was not used. Total integration time was set to a maximum of $1.5 \cdot 10^{-12}$ s, long enough to ensure a proper interaction of the oxygen atom with the surface.

In order to classify the trajectories in one of the two possible exit channels (adsorption or reflection) the following criteria were taken into account. For a trajectory to be considered as reflection, Z_O coordinate must be higher than 7.1 Å and the direction of the velocity vector must be pointing to the vacuum. On the other hand, for a trajectory to be considered as adsorption, the Z_O of the incoming atom should be lower than 2.2 Å and the number of total rebounds with the surface have to be more than 8. In figure 3.23 a specific Z_O evolution along time for an adsorption trajectory is represented in order to facilitate the comprehension of the rebounds over the surface. It has also checked that the adsorption probability is not dependent when varying both the threshold distance

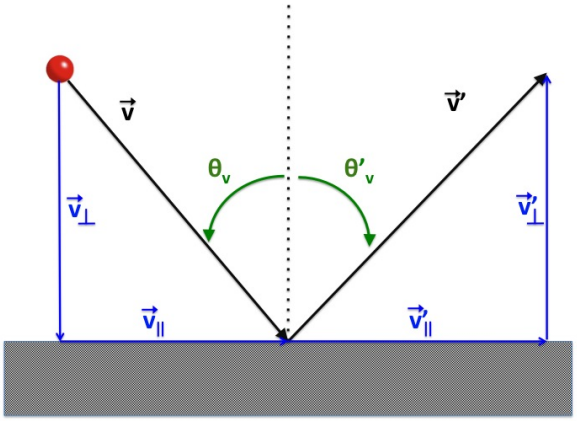

Figure 3.22: Initial and final velocity angles (θ_v and $\theta_v^{'}$, respectively) definition for scattered atoms along with their perpendicular ($\perp$) and parallel ($\|$) components.

of the atom to the surface and the total number of rebounds. For the MS surface physisorption is also observed, so these trajectories were classified separately from the chemisorption. In that case, the trajectory was integrated a longer time and was considered as physisorbed if the distance to the surface was in the range where the vdW minimum was observed (2.2 - 4.1 Å). For adsorption probabilities, physisorption and chemisorption were summed together.

The minimum number of total trajectories (N_T) calculated for each condition was at least of 10,000 which, for example, leads to a maximum error of 1.65% for the adsorption probability with FPLEPS PES at $E_{col} = 0.325$ eV, normal incidence ($\theta_v = 0°$) and without surface temperature effects.

To account for energy exchange and dissipation, a generalised Langevin model (GLO) is used for atomic or molecule oxygen colliding with a clean graphite (0001) surface. Initially, as oscillator frequencies ($\omega_{i,x}$, $i = 1, 2, 3$) were used the values derived from bulk (T_D) or surface ($T_{s,D} \approx T_D/\sqrt{2}$) Debye temperatures of graphite (i.e., $T_{s,D} = 350$ K (113) and $T_D = 423.6$ K (114) , 393.9 K (115)) by means of equations 2.108 and 2.110 listed in the theoretical background. Thus, values close to $1{\cdot}10^{-3}$ for ω_D and to $5{\cdot}10^{-4}$ for ω_i, in atomic units of time^{-1}, were reported. These values were used as guess frequencies to fit the experimental mean-square of perpendicular displacement of graphite surface atoms as a function of the surface temperature (116), as shown in figure 3.24.

The agreement with experimental data is quite good for surface temperatures over 150 K. The optimal parameters are: $\omega_{i,x} = \omega_{i,y} = 1 \cdot 10^{-3}$ and $\omega_{i,z} = 3.4{\cdot}10^{-4}$ a.u. for i = 1,2,3). The optimum $\omega_{i,z}$ value is also close to the maximum (i.e., $5.8{\cdot}10^{-4}$ a.u.) of the frequency distribution relative to lattice vibrations perpendicular to the basal plane of graphite (116).

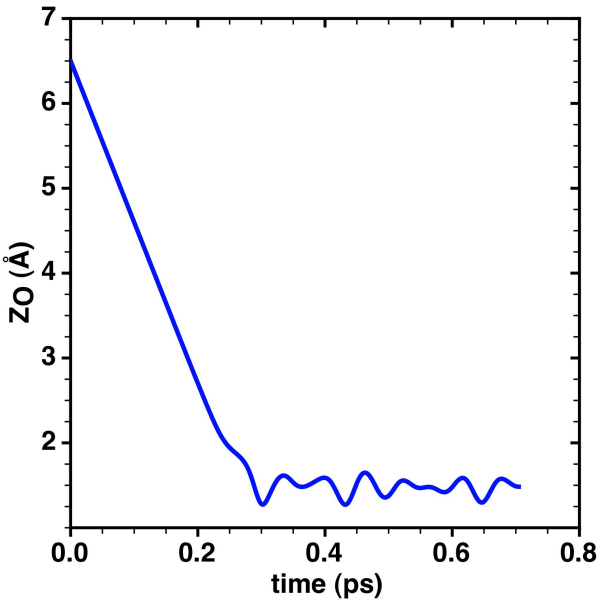

Figure 3.23: Z_O evolution along time for a specific adsorption trajectory, where a total of 8 rebounds on the surface are observed.

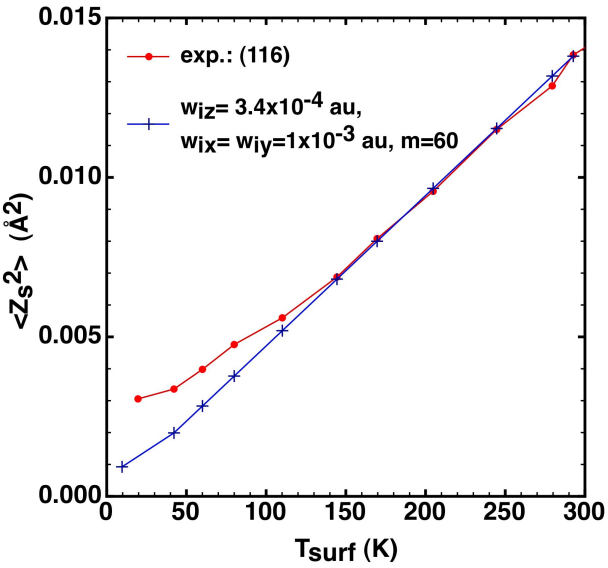

Figure 3.24: Experimental and calculated (GLO model) mean-square perpendicular displacement of graphite surface atoms as a function of the surface temperature.

It was checked that changes on the effective m_s mass (e.g., from 12 (one atom) to 60 amu (5 atoms of the unit cell)) produce negligible effects on the quality of the fit of $\langle Z_s^2 \rangle$ in figure 3.24. Thus, it was added an extra and previous QCT calculation to select m_s along with ($\gamma_{g,x}$, $\gamma_{g,y}$, $\gamma_{g,z}$) parameters for the GLO model. 30,000 trajectories were calculated for hyperthermal O atom ($\langle E_{col} \rangle$ = 5.2 eV) colliding at off-normal incidence ($\theta_v = 45°$) over highly oriented pyrolytic graphite (HOPG) with a surface temperature of 503 K (71). The final values m_s = 60 amu and $\gamma_{g,x} = \gamma_{g,y} = \gamma_{g,z}$ $4.0{\cdot}10^{-4}$ (units of time^{-1}) parameters were able to reproduce the experimental peak near 60° of the polar angular distribution (θ_v') of the scattered O, although QCT distribution was broader than the experimental one.

The final GLO parameters are able to describe the above-mentioned experimental distributions although another combination of those could also be acceptable.

It was also verified that the average total energy of the GLO system at a given surface temperature corresponds to the expected value of $3Nk_BT_{surf}$ with N=2 (surface and ghost particles). Moreover, kinetic and potential (referred to the minimum) energy averages were also coincident as virial theorem states.

3.6.1.2 Dynamical study for FPLEPS surface

• Without surface temperature

Adsorption and reflection probabilities were calculated at different initial conditions of E_{col} and θ_v. In a first study, surface temperature was not taken into account. Thus, for each incident angle (θ_v), E_{col} was varied in the range of 0.1 to 2.0 eV.

Results plotted in figure 3.25 show that reflection is by far more important than atomic adsorption at all energies and incident θ_v angles explored. Dynamical results for normal incidence, show a threshold for the adsorption at an energy around 0.20 eV. Below this energy adsorption is not observed. The threshold values are in agreement with the lowest energy barrier found in the PES (table 3.11). However, the barrier height depends on the X_O and Y_O position of the incoming atom. Thus, when the atom overcomes the barrier to the potential well ($Z_O < 2.0$ Å) part of the perpendicular kinetic energy, which is the effective energy for surpassing the barrier, is transformed into parallel energy making more difficult to the atom to return back to the gas phase producing that the atom remains adsorbed. Furthermore, even if the initial angular momentum for the atom is zero when θ_v= 0°, it is not necessary conserved along the trajectory. Thus, a variation on the effective centrifugal potential while the atom is close to the surface, will produce an increase of the barrier (the centrifugal contribution to the potential is always positive) favouring even more the trapping.

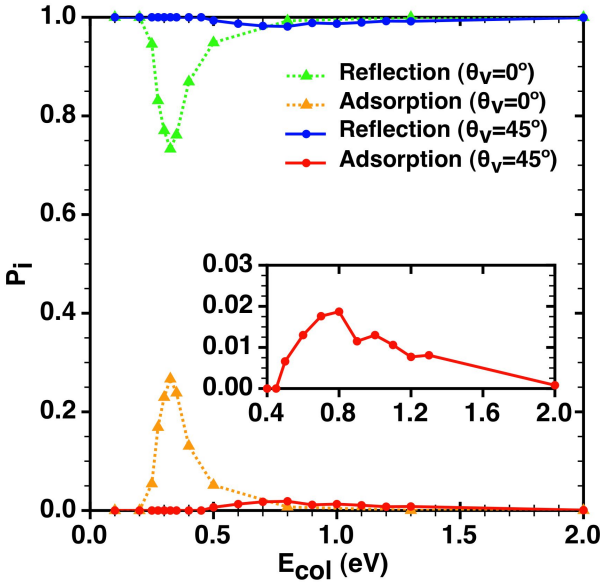

Figure 3.25: Oxygen adsorption and reflection probabilities (P_i) as a function of collision energy at initial $\theta_v = 0°$ and 45° for a rigid slab with the FPLEPS surface. In the inset, a detail of the adsorption probability for $\theta_v = 45°$ is also plotted.

If E_{col} is slightly increased, the adsorption probability also increases. This happens until a maximum value that is reached at around 0.325 eV. The increase of the probability within this small energy range is also explained by the small changes of the energy values produced at different X_O, Y_O coordinates (table 3.11). The incoming atom at these collision energies is able to overcome not only the minimum adsorption barrier but also higher energy barriers found in other X_O and Y_O regions of the surface. Again, when the incoming atom is on the potential well, the conversion of perpendicular effective kinetic energy into parallel one and the modification of the barrier by the effective centrifugal potential favours the trapping of the atom. On the other hand, at higher E_{col} the trapping is not possible. This explains the decrease of the adsorption probability for $E_{col} >$ 0.325 eV.

For off normal incidence it is observed a clear increase of the reflection at all energies with a small maximum in the adsorption probability for a collision energy of 0.8 eV as it can be seen in the inset image in figure 3.25. In that case, the threshold for the adsorption is found at 0.5 eV. This can be explained since the effective perpendicular energy is lower when increasing the angle of incidence,

$$E_{\perp} = E_{col} \cdot cos^2(\theta_v) \tag{3.38}$$

For instance, when $E_{col} = 0.5$ eV and $\theta_v = 45°$, the initial effective perpendicular

energy is 0.25 eV, which is almost coincident with the threshold observed for normal incidence. This fact explains the shift of the adsorption probability at higher values of E_{col} when compared with normal incidence. Furthermore, the adsorption probabilities are lower at all energies compared with the case of normal incidence, which could be explained since the effective centrifugal potential for the atom presents larger barriers (this fact makes also the effective minimum shallower).

Energy scaling (i.e., total or normal) can be studied when results at different θ_v are available. For this purpose, probabilities at several θ_v are plotted versus the E'_{col} where

$$E'_{col} = E_{col} cos^n(\theta_v) \tag{3.39}$$

and n is selected in such a way that the probabilities at different angles lay in the same curve or line. If n= 2, parallel energy scaling is observed and when n= 0 it is said that total energy scaling is obtained. For the oxygen graphite system none of the n values between 0 and 2 accomplish the condition, although as it can be seen in figure 3.26 and as it was explained before, the thresholds and the maximum of the probability position are coincident at both θ_v angles (for n = 2). Thus, a clear dependence on the perpendicular collision energy is observed. However, a deeper study should be done since a complex behaviour is expected. For instance some parallel momentum accommodation (117) or a dependence on the initial collision energy (118) could also be present. Thus, there is a clear

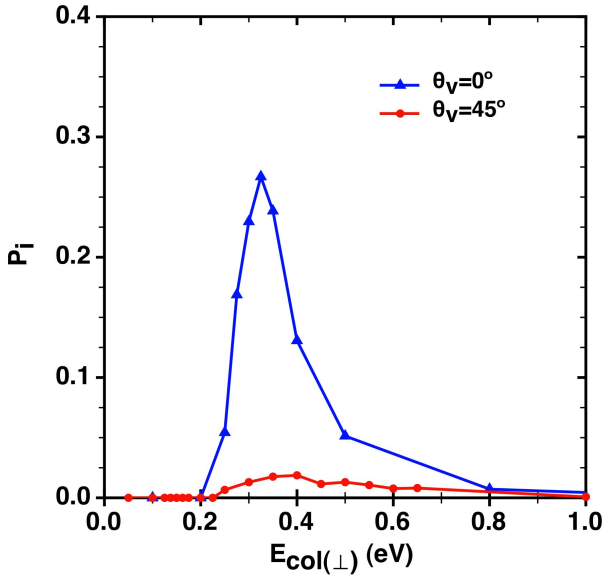

Figure 3.26: Adsorption probabilities as a function of perpendicular initial collision energy for two incident angles (θ_v).

breakdown of the typical energy scaling limits in this system.

The initial position of the trajectories that finally produce adsorption and reflection for a normal incidence trajectory calculation at $E_{col} = 0.3$ eV (close to the maximum of 0.325 eV of figure 3.26) are presented in figure 3.27a along with the final position of the adsorbed atoms (figure 3.27b). It can be observed

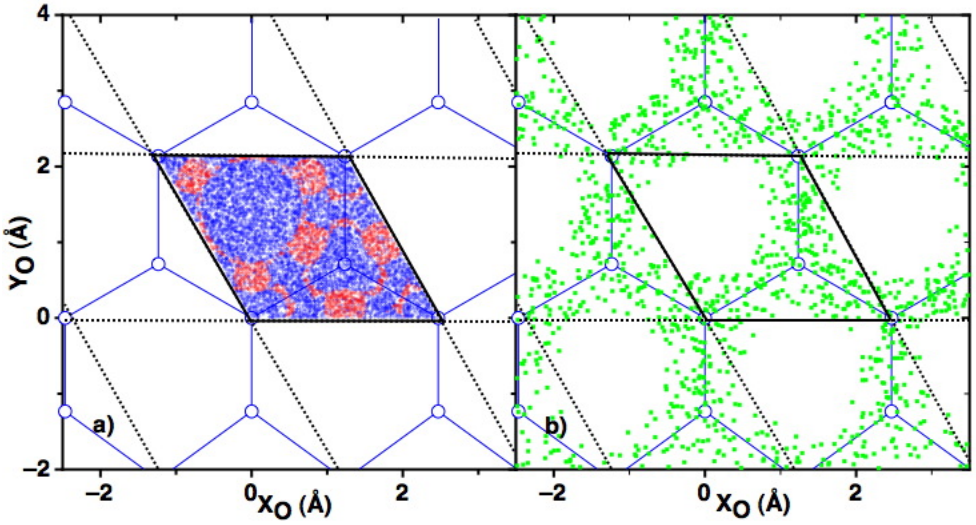

Figure 3.27: a) Initial X_O and Y_O position for adsorbed (red) and reflected (blue) trajectories and b) final position for adsorbed (green) trajectories for normal incidence at $E_{col} = 0.3$ eV.

favourable initial positions for the finally adsorbed trajectories mainly above the area where the minimum barrier for the FPLEPS adsorption was found (figure 3.11a) and close to the C-C bridge sites. Final adsorbed atoms lay on bridge sites and their surroundings, where the stabilization is favoured whereas adsorption trajectories are not observed over the repulsive hexagonal hollow area, which clearly enhances the reflection together with C top sites. It is worth noting that trajectories initially started over the unit cell can finally produce adsorption on the bridges of adjacent cells. This could be explained considering that oxygen atoms can diffuse (e.g., with some rebounds) over the graphite surface before becoming adsorbed.

The analysis of the polar scattering angle for the reflected trajectories (θ_v') is presented in figure 3.28 for trajectories at initial $\theta_v = 0°$ and 45°. To make possible comparison between different initial conditions, the distributions are normalised to the unit area. Thus, the sum of the amplitude of each data bin multiplied by its intensity is normalised to the unit, although the graphs are depicted joining intensity points for each bin with a straight line. For low perpendicular $E_\perp$ collision energies ($E_{col} = 0.25$ eV at normal incidence and $E_{col} = 0.25, 0.5$ eV

for $\theta_v = 45°$) elastic reflection is observed. Thus, for normal incidence (figure

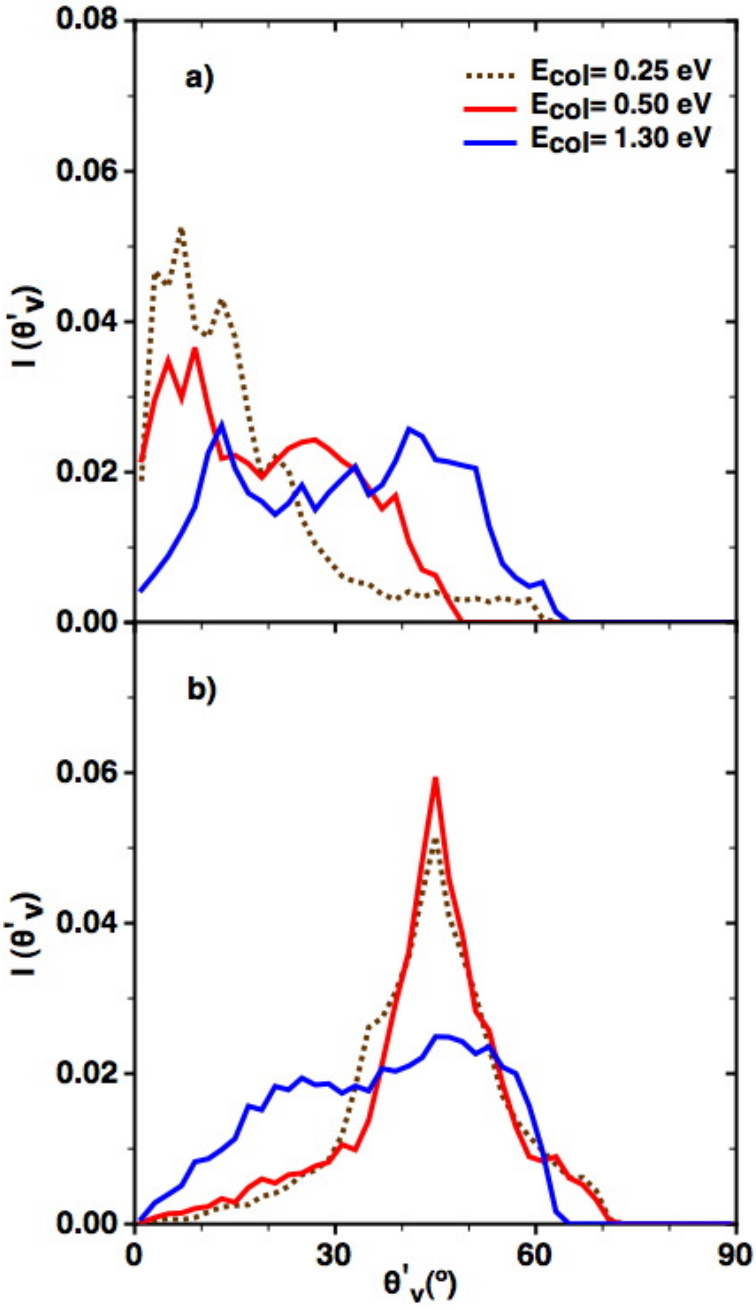

Figure 3.28: Polar scattering angle distribution for $E_{col} = 0.25, 0.5, 1.3$ eV and a) $\theta_v = 0°$ and b) $\theta_v = 45°$ for the FPLEPS surface without temperature effects.

3.28a), scattering angles close to the normal ($\theta_v' \approx 0°$) are obtained, while for

off normal incidence a maximum probability of the scattering angle equivalent to the incident velocity angle is observed ($\theta_v^{'} \approx 45°$). Note that $\theta_v^{'}$ and θ_v are the minimum angle between velocity vector and the positive Z-axis (figure 3.22). At higher collision energies, the final scattering angle distributions are broader. To illustrate this behaviour of the scattering angle it is appropriate to analize the minimum distance to the surface just before that the trajectory is reflected. The mean values of the corresponding Z_{min} at each collision energy for normal incidence are listed in table 3.17 and the distribution of Z_{min} is plotted in figure 3.29. A bimodal distribution is observed centered around 1.2 Å and 2.0 Å, being the peak at 1.2 Å more important for high collision energies. At lower collision energies (e.g., $E_{col} = 0.25$ eV), the reflection follows mainly the MEP because the Z_{min} is practically the value corresponding to the TS (table 3.11). When the energy is increased the system can evolve through configurations far from the MEP and the atom interacts at distances closer to the surface ($Z_{min} \approx 1.2$ Å) where the potential is more repulsive. This can explain that inelastic trajectories are scattered with a wider range of scattering angles ($\theta_v^{'}$).

Table 3.17: Mean value of the $\langle Z_{min} \rangle$ for the oxygen atom along reflected trajectories for a batch of 10,000 trajectories at several initial collision energies, with $\theta_v = 0°$.

E_{col} (eV)	$\langle Z_{min} \rangle$ (Å)
0.25	1.973
0.30	1.664
0.50	1.262
0.80	1.205
1.30	1.167

• With surface temperature

The effect of the surface temperature was added by using the GLO model presented in section 2.4.1. Trajectory calculations within a surface temperature range of 100 - 1,300 K were carried out at different collision energies in the range of 0.05 eV $\leqslant E_{col} \leqslant$ 3.0 eV for two initial incident angles ($\theta_v = 0°$ and 45°).

The probabilities for the reflection and adsorption processes of oxygen atom over graphite at a surface temperature of 100 K and 900 K for different initial collision energies are presented in figure 3.30. Adsorption probabilities show higher values than without considering surface temperature at the same energies

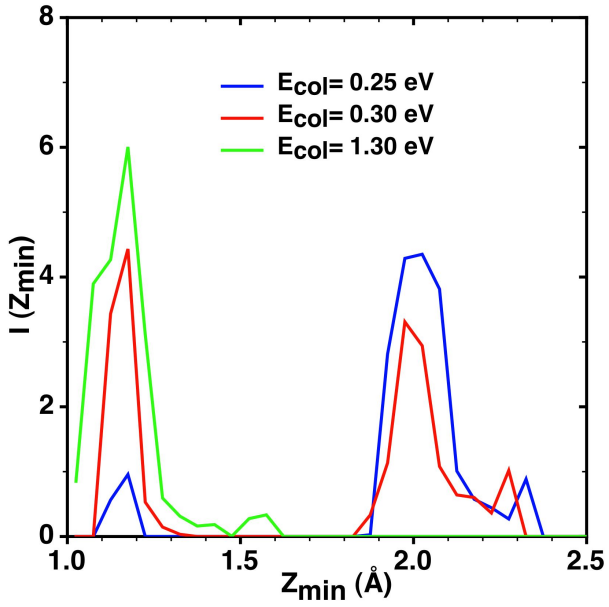

Figure 3.29: Z_{min} distribution of the reflection trajectories with normal incidence at three initial collision energies.

for both incident angles (figure 3.25). For low energies, adsorption is the main process observed, overcoming the reflection probability, i.e. for normal incidence at energies between 0.3 and 0.8 eV. This fact was not observed for calculations without including surface temperature. Although the explanations given for the system without including surface temperature are valid in that case too, the model for taking the surface temperature into account allows the gas atoms to exchange energy with the surface adding some extra phenomena to explain the adsorption. As will be seen later in the text, generally the surface takes energy from the atom reducing its kinetic energy. This loss of kinetic energy favours the trapping of the atom into the adsorption potential well. Moreover, adsorption process is observed to occur at lower initial collision energies than in the case of a slab without temperature effect. This is specially true for higher energies as 900 K, where adsorption is already observed with more than an 18% of probability, when the collision energy is 0.2 eV. For slab with no temperature effects, adsorption was not observed until an energy of 0.25 eV with approximately just a fourth of the probability observed at 900 K. Thus, the thermal bath is not only giving extra stabilization by exchanging energy with atoms, but also is allowing atoms with smaller collision energy to overcome the barrier as the bath can provide some extra energy to the oxygen atoms. The effect of energy exchange between oxygen and the surface is more important as the surface temperature is increased. Thus, although including the temperature increases the adsorption probability for

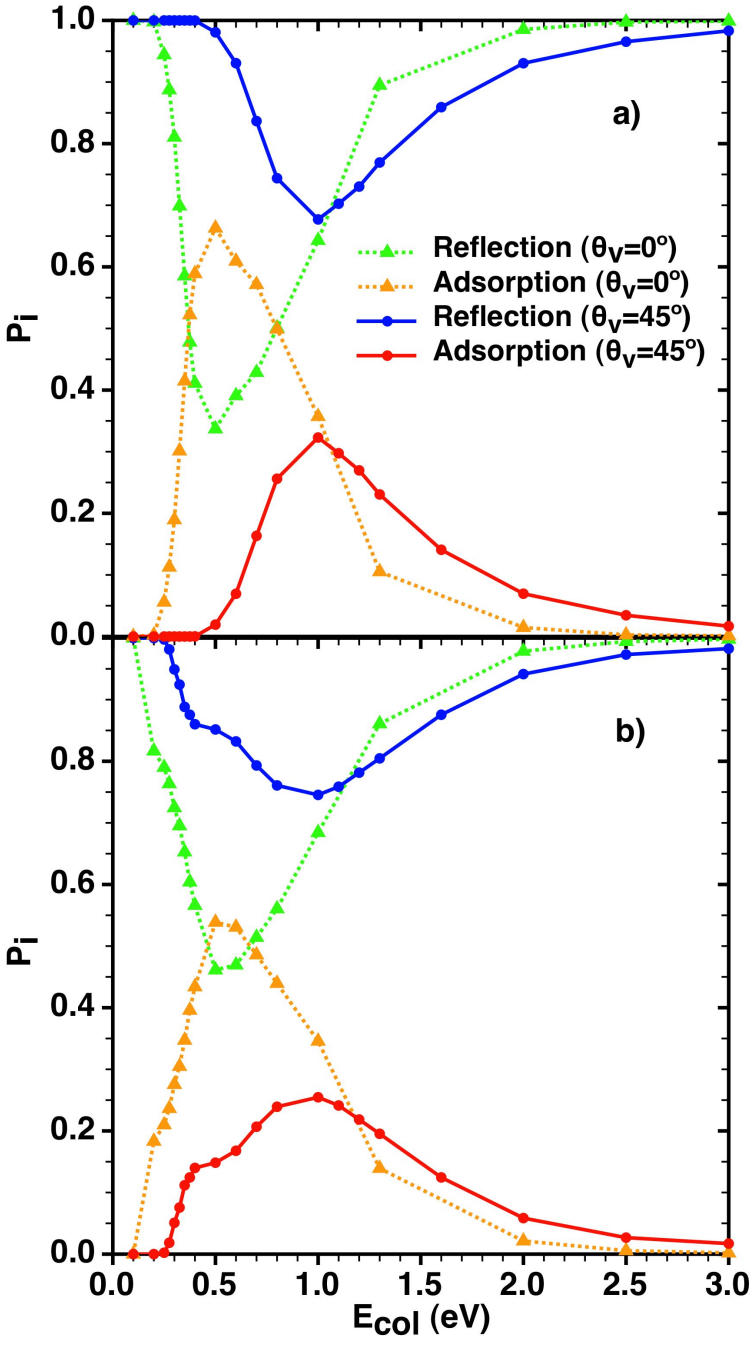

Figure 3.30: Oxygen adsorption and reflection probabilities (P_i) as a function of initial collision energy at initial $\theta_v = 0°$ and 45° at two surface temperatures a) $T_{surf} = 100$ K and b) $T_{surf} = 900$ K with the FPLEPS surface.

the above-mentioned extra stabilization, an increase in the surface temperature enhances the atomic reflection due to the increment of desorption, as it would be expected. The maximum probability for the adsorption at T_{surf} =100 K for normal incidence is 66.3% while at 900 K is 53.8%. This maximum is observed at 0.5 eV while for rigid slab was observed at 0.325 eV, which proves again the effect of the energy exchange with the surface which allows the stabilization of more energetic collisions. The behaviour for $\theta_v = 45°$ is similar to that observed with the model without surface temperature.

An analysis of normal incidence trajectories considering a surface temperature of 300 K is done in figure 3.31. Thus, initial position of the adsorbed and reflected atoms at $E_{col} = 0.3, 0.5$ and 1.2 eV are shown in figure 3.31a, b and c, respectively. In addition, the final position for the adsorbed trajectories is plotted in figure 3.31d, e and f for the same E_{col} values, respectively. Comparing with the same results obtained for a slab with no temperature effects (figure 3.27), adsorbed atoms tend to finally stay closer around the bridge region. The atom can diminish its energy (i.e., decreasing its potential or kinetic energy) getting closer to the real adsorption minimum. Furthermore, it can be observed how the concentration of finally adsorbed atoms is decreasing rapidly when moving away from the central unit cell bridges. This fact proves that diffusion in this system will be smaller than the observed in the rigid slab, specially at lower energies.

Reflected atoms at low collision energy (i.e., $E_{col} = 0.3$ and 0.5 eV) are provided from two sets of initial positions. Trajectories starting close to the hexagonal hollow yield mainly to reflection as could be expected. On the other hand, a big amount of trajectories started above the adsorption sites (tops and bridges) produce reflection as well, mainly at $E_{col} = 0.3$ eV. This is more difficult to explain, as the value for the adsorption barrier in this area is not the lowest but is not specially high (0.261 eV) compared for example with the barrier over T1 and T2 (0.309 eV and 0.312 eV, respectively). The X_O and Y_O time evolution for some reflected trajectories, that start over the bridge site, is plotted in figure 3.32; this shows the tendency of the oxygen atom to gain kinetic energy in the X and Y directions. This movement parallel to the surface is not favouring the adsorption, specially for these trajectories, started over the bridge site and its surroundings which are, in many cases, driven to the repulsive hollow area, giving reflection processes. When analysing the minimum approximation distance (Z_{min}) of the impinging atom to the surface along the trajectories it is observed two different patterns, similarly as for calculations without including surface temperature effects (figure 3.29). Z_{min} distribution for reflected trajectories is shown in figure 3.33a. The distribution shows two maxima centered at very different distances, one around the 1.2 Å, once the barrier is overcomed, and another around the 2.0 Å, near the barrier position, as in the case of a surface with no temperature effects (figure 3.29). Initial positions for reflected trajectories depending on the Z_{min} to the surface are plotted in figure 3.33b. It can be observed that atoms

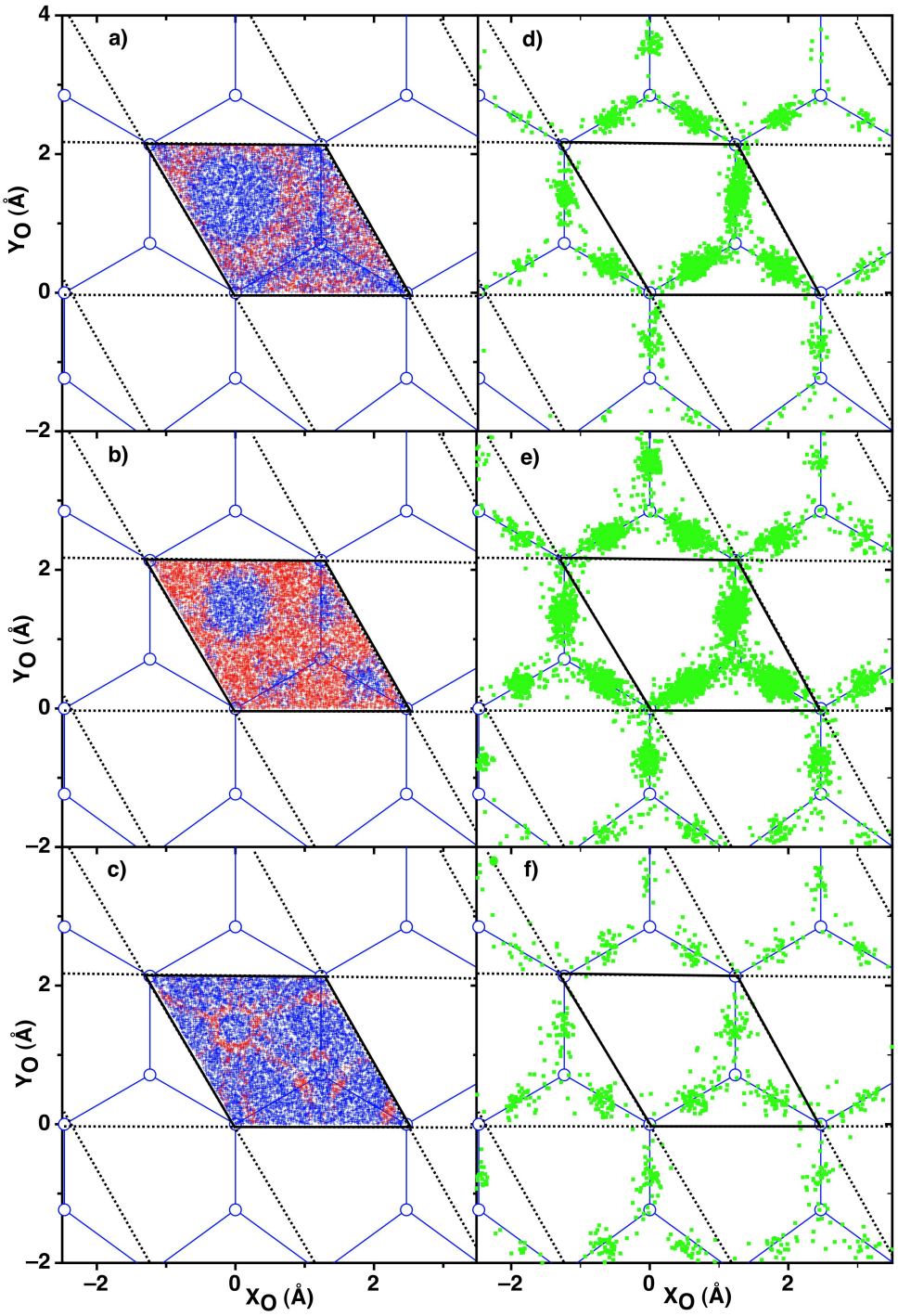

Figure 3.31: Initial X_O and Y_O position for adsorbed (red) and reflected (blue) trajectories (left panels) and final position for adsorbed trajectories (right panels, in green) at normal incidence ($\theta_v = 0°$) for a), d) $E_{col} = 0.3$ eV, b), e) $E_{col} = 0.5$ eV and c), f) $E_{col} = 1.3$ eV at $T_{surf} = 300$ K.

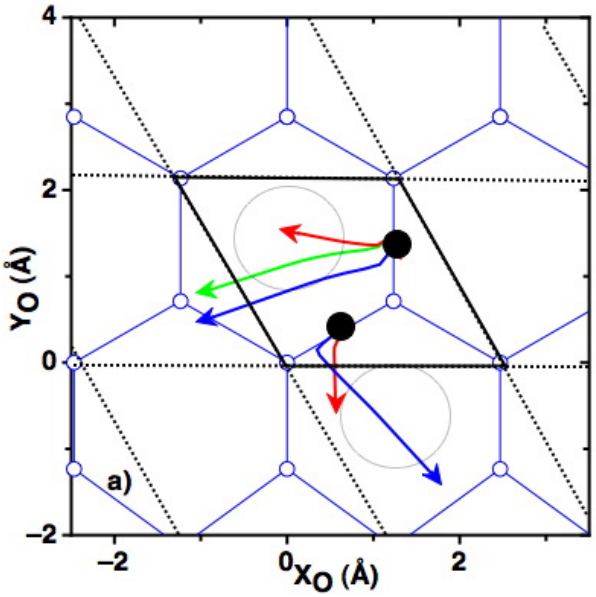

Figure 3.32: X_O and Y_O trajectory time evolution for five selected reflected trajectories at normal incidence and E_{col}= 0.3 eV starting over the bridge site. The repulsive hollow area is represented on the graph by a grey circle. The black circle shows the initial position and the arrows show the trajectory evolution.

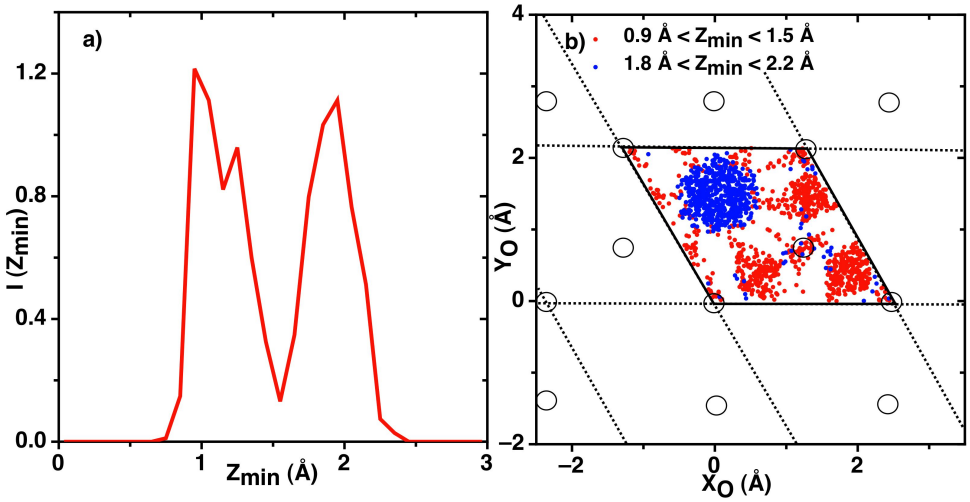

Figure 3.33: a) Z_{min} distribution of the reflected trajectories with normal incidence at 0.5 eV and b) initial position of the reflected trajectories achiving Z_{min} vales within the intervals of 0.9 Å $\leqslant Z_{min} \leqslant$ 1.5 Å and 1.8 Å $\leqslant Z_{min} \leqslant$ 2.2 Å.

initially above the hollow site are reflected at large distances (1.8 Å $\leqslant Z_{min} \leqslant$ 2.2 Å) due to the direct interaction with the potential wall found at this area (highly repulsive) while trajectories starting on bridge site and its surroundings achieve shorter surface distancies (0.9 Å $\leqslant Z_{min} \leqslant$ 1.5 Å) and reflection is caused by nuclear repulsion at shorter distances.

The main conclusions obtained by considering initial and final incoming atom position of trajectories at a lower energy, can be applied to higher ones. In that case, the total amount of reflected trajectories is much higher and the initial area where the atoms are reflected expands on the entire space. The effect of gaining kinetic energy on parallel direction to the surface enhances the reflection of trajectories when starting close to the bridge site. The opposite effect is observed when trajectories start close to the repulsive hollow area. In this case, oxygen atom is driven from the repulsive area directly to the adsorption minimum over bridge site, favouring the adsorption over the surface.

Polar scattering distribution ($\theta_v^{'}$) of reflected atoms was studied for $E_{col} = 0.25, 0.5$ and 1.3 eV at $\theta_v = 0°$ and 45° for low and high surface temperatures ($T_{surf} = 300$ K and $T_{surf} = 900$ K, respectively). When surface temperature is considered the behaviour observed in figure 3.34 does not differ substantially from the one observed for a surface without temperature effects in figure 3.28. Thus, elastic reflection is mainly observed at low collision energies while the distribution is wider at higher collision energies. The only small difference that could be mentioned is the tendency for off normal incidence at $E_{col} = 0.5$ eV to give a peak slightly shifted to higher values due to the possibility of energy exchange between impinging atoms and surface. The distributions obtained for both temperatures do not show any remarkable difference.

When the thermal bath is introduced the energy exchange between the impinging atom and the surface is possible. In figure 3.35 the distribution of the difference between the final and initial collision energies ($\Delta E_{col} = E_{col}^{'} - E_{col}$) is plotted for three different initial collision energies ($E_{col} = 0.25, 0.50$ and 1.30 eV) and normal incidence. The energy exchange is in general from the atom to the surface (negative values) and becomes more important as the initial collision energy increases. Furthermore, it can be observed for a small number of trajectories a positive energy exchange, which means that in some cases, the surface is giving energy to the impinging atom. This effect increases as temperature does as it could be expected and it is more important for low initial collision energies. As before mentioned, this positive exchange of energy allows that trajectories starting at an energy not high enough to overcome the energy adsorption barrier get finally adsorbed.

Batches of trajectories were also run considering a quasithermal gas temperature with a Boltzmann distribution at the same surface temperature ($T_{surf} = T_O = T$) for $\theta_v = 0°$ and 45°. Results plotted in figure 3.36, show very low adsorption probabilities as the initial collision energies for such temperatures are

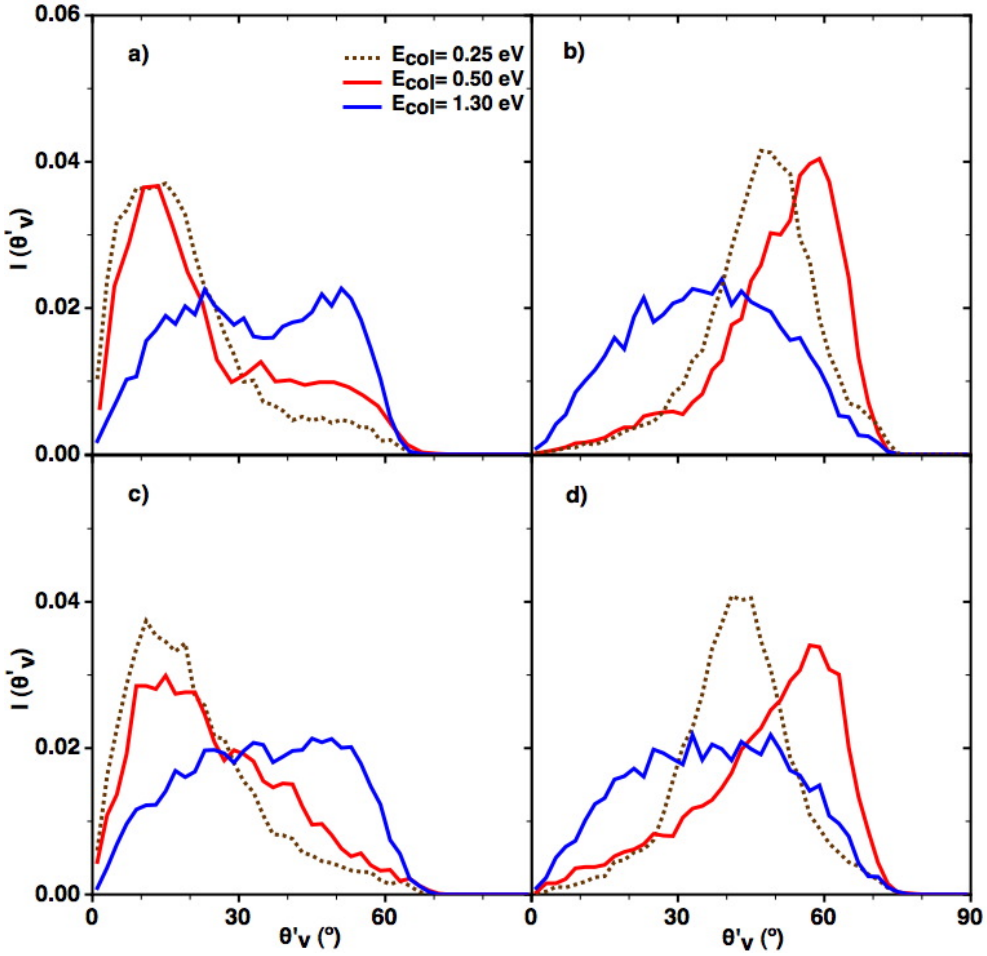

Figure 3.34: Polar scattering angle distribution for $E_{col} = 0.25, 0.5, 1.3$ eV for a) $\theta_v = 0°$ and $T_{surf} = 300K$, b) $\theta_v = 45°$ and $T_{surf} = 300K$, c) $\theta_v = 0°$ and $T_{surf} = 900K$ and d) $\theta_v = 45°$ and $T_{surf} = 900K$ with FPLEPS surface.

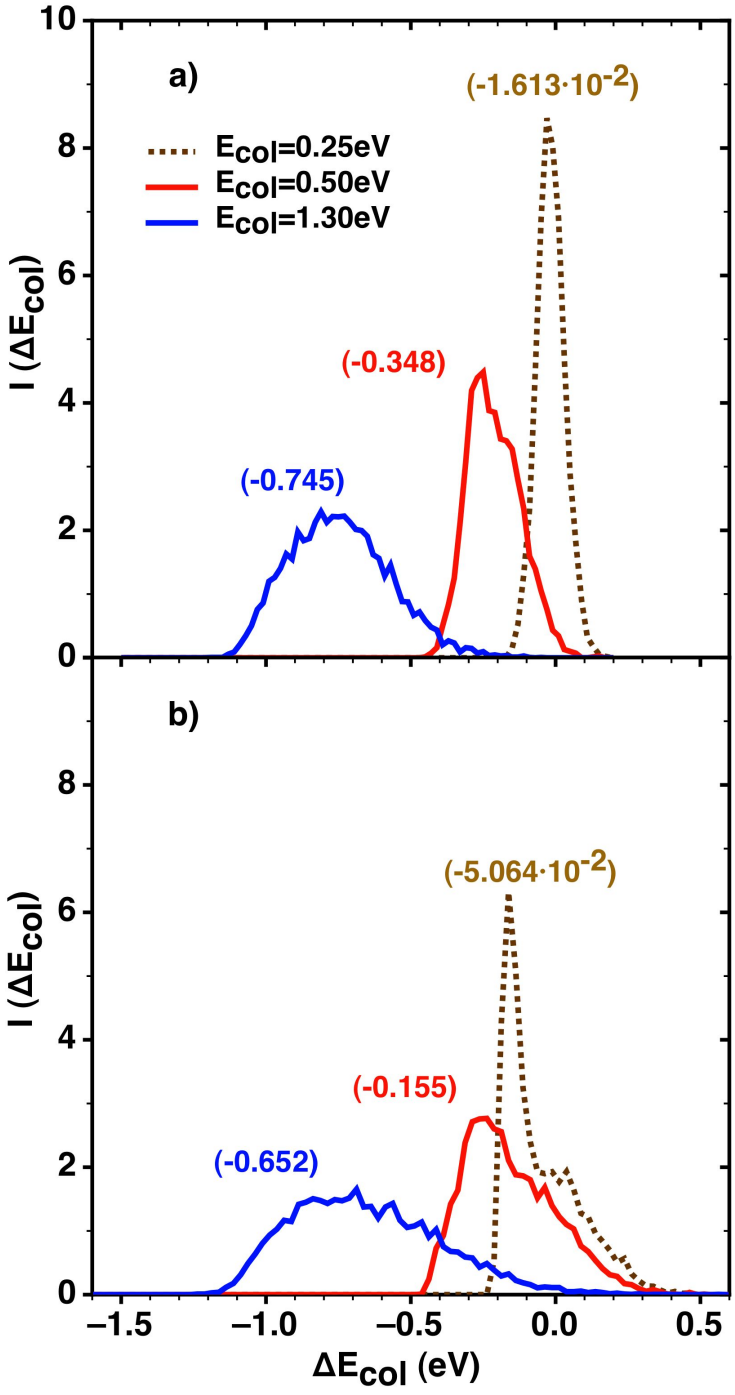

Figure 3.35: Energy exchange (ΔE_{col}) for reflected trajectories at initial $E_{col} = 0.25, 0.5$ and 1.3 eV and $\theta_v = 0°$ at a) $T_{surf} = 300$ K and b) $T_{surf} = 900$ K. Between parentheses are given the mean values ($\langle E_{col} \rangle$) in eV.

in general very low (i.e. $\langle E_{col} \rangle = 0.19$ eV for $T = 1,500$ K). Thus, the general

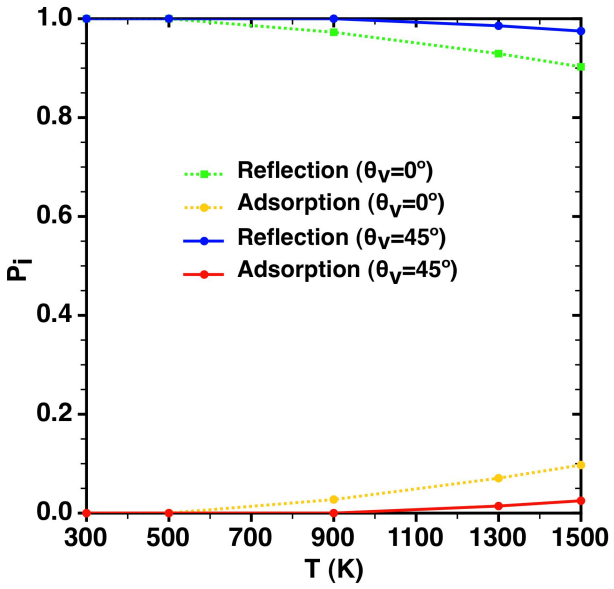

Figure 3.36: Adsorption and reflection probabilities for and impinging oxygen atom at different temperatures for initial $\theta_v = 0°$ and 45°.

trend of the studied properties (i.e., probabilities, polar scattering angles,...) is expected to be close to the one found at low initial collision energies (figure 3.30 and 3.37). When temperature is increased at normal incidence it is observed a small tendency of giving slightly wider distributions, which is also observed for off normal incindence.

Concerning to the energy exchange of the atom with the surface (figures 3.37c and d), it can be said that the behaviour is similar to the one observed at E_{col}=0.25 eV for state specific calculations. This fact occurs because the mean initial collision energy for these temperatures is very low. For instance, the mean value of $\langle E_{col} \rangle$ for a thermal distribution for the atomic oxygen at 1,500 K is 0.194 eV. When the temperature increases, there is more available energy to exchange between the impinging atom and the surface, hence becoming the distributions wider.

Finally, a simulation of experimental conditions of Paci et al. (71) was carried out. A Pulsed beam of hyperthermal O and O_2 was used for surface scattering experiments with HOPG at 503 K. A batch of 30,000 trajectories are calculated emulating the initial experimental population (figure 3.38). Both, experimental and theoretical results for the final scattering angle are presented in figure 3.39 where the maximum was normalised to one to compare with experimental distribution. The peak observed for the polar scattering angle distribution is located

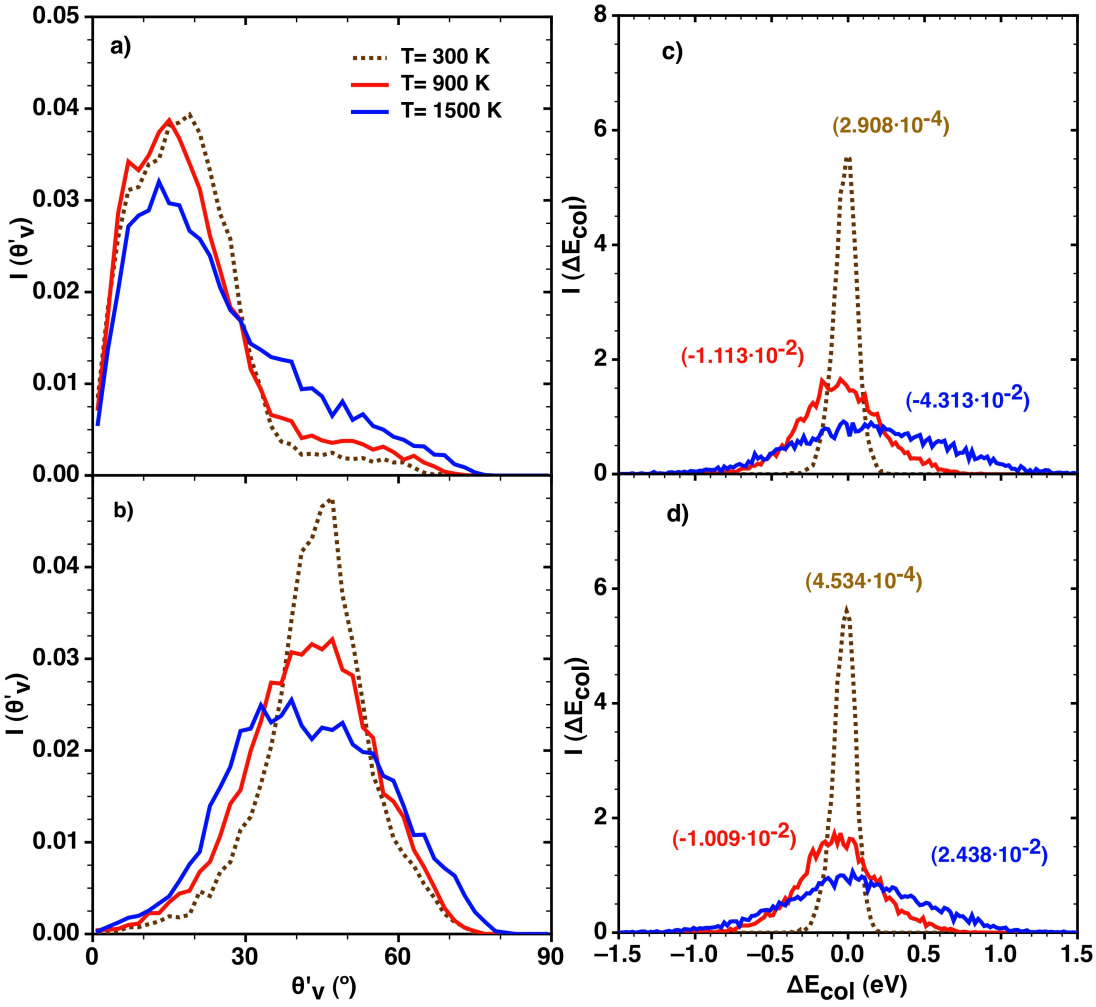

Figure 3.37: Polar scattering angle (left panels) and energy exchange distributions (right panels) of reflected atoms for trajectories at three different temperatures and a) and c) $\theta_v = 0°$ and b) and d) $\theta_v = 45°$ with FPLEPS surface. Between parentheses are given the mean values ($\langle E_{col} \rangle$) in eV.

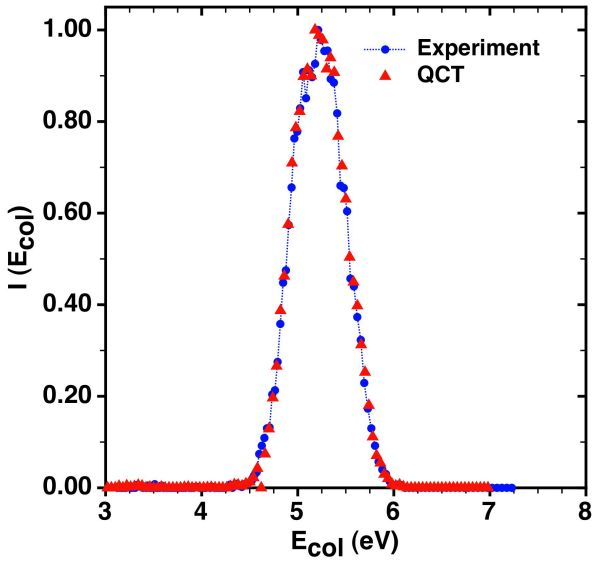

Figure 3.38: Experimental hyperthermal distribution of atomic oxygen (71) in blue and the simulated by QCT calculations in red.

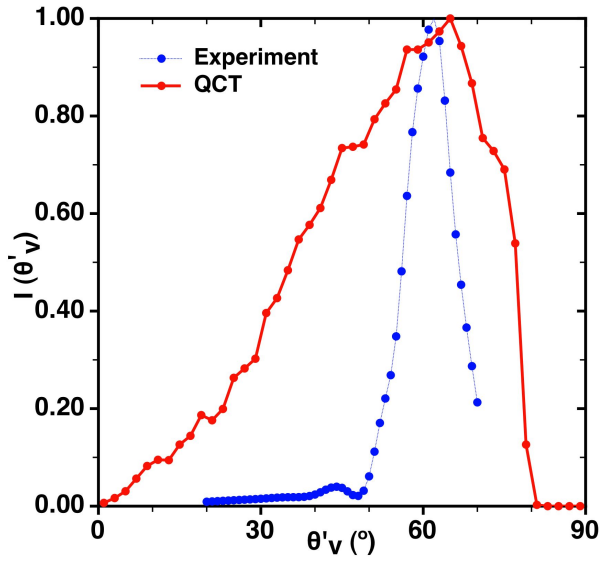

Figure 3.39: Theoretical and experimental (71) polar scattering angle distributions of reflected atomic oxygen for a hot (hyperthermal) beam with an incident angle of $\theta_v = 45°$ and $T_{surf} = 503$ K, using the FPLEPS PES.

very close to the experimental one ($\theta_v^{'} = 62°$). This result could be expected since one of the criteria used for selecting the mass of the ghost atom used in the GLO model was the comparison of these experimental and theoretical distributions. Nevertheless, experimental results show a much narrower distribution than theoretical one. However, in the experiment both O and O_2 are in the same beam. This fact, suggests that incident O atoms could also react directly with preadsorbed O to produce O_2 (Eley-Rideal mechanism), scattering from the surface with another distribution. Thus, a part of the incoming atoms would not be scattered and this fact could modify also the final angular distribution. Moreover, some important formation of both CO and CO_2 molecules is reported in the experimental study. In the present theoretical study all atoms are necessary reflected. Therefore, the O atoms that directly participate in O_2 and/or CO/CO_2 formation would change the initial O distribution that are finally reflected. It is worth noting that the theoretical results in that case, give a correct general trend compared with the experimental data available, but are not able to reproduce them with high accuracy, possibly because our PES should introduce another reacting processes (i.e., CO formation). Moreover, the study of scattered O in a surface precovered with O will show the effect on the final polar angle scattering distribution when comparing with a clean surface study.

3.6.1.3 Dynamical study for MS surface

An equivalent dynamical study to that done for the FPLEPS surface was carried out by using the MS interpolated surface. Thus, firstly, adsorption and reflection probabilities at different initial conditions of E_{col} and θ_v without including surface temperature were carried out.

•Without surface temperature

Reaction probabilities at $\theta_v = 0°$ and $45°$ for initial collision energies in the range between 0.05 eV $\leqslant E_{col} \leqslant$ 2.0 eV are plotted in figure 3.40. The main process observed for both initial incident angles is reflection. For both, normal and off normal incidence, a maximum in the adsorption probability is observed at similar energies than for the FPLEPS surface with no temperature effects, and explanations given there, are also valid here. On the other hand, important differences on probabilities are found at very low energies. This is due to the physisorption minimum described for the MS surface, which was not introduced in FPLEPS. The adsorption probability contains the sum of the physisorption and chemisorption contributions. In this case, physisorption only appears at low energies while chemisorption is shown at high ones. Moreover, physisorption decreases rapidly when initial collision energy is increased. Physisorption probabilities for off normal incidence are much more important.

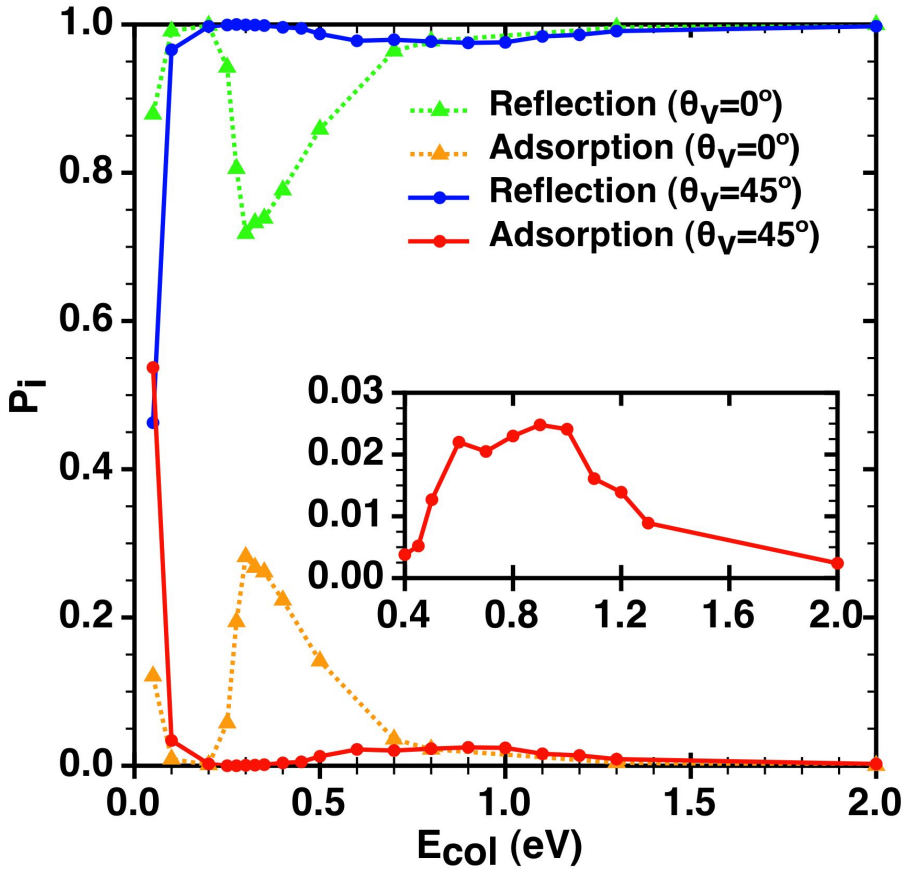

Figure 3.40: Oxygen adsorption and reflection probabilities as a function of collision energy at initial $\theta_v = 0°and45°$ for a slab without surface temperature over the MS PES. In the inset, a detail of the adsorption probability for $\theta_v = 45°$ is also plotted.

Initial positions for the finally adsorbed and reflected atoms for normal incidence trajectory calculations at $E_{col} = 0.3$ eV are plotted in figure 3.41. The

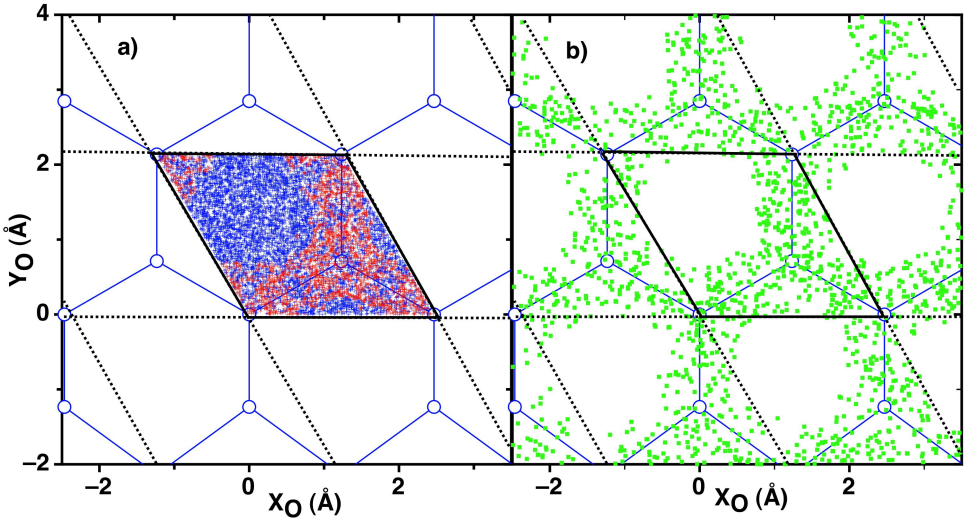

Figure 3.41: a) Initial X_O and Y_O position for adsorbed (red) and reflected (blue) trajectories and b) final position for adsorbed (green) trajectories for normal incidence at $E_{col} = 0.3$ eV.

area that favours the adsorption of the atom is initially around the bridge and top sites where the barriers are lower. In general, there is no adsorption when the trajectory is started around the repulsive zone of the hexagonal hollow site. This result differs a bit respect the one obtained with the FPLEPS, where the initial position for adsorption was concentrated mainly between top and hollow sites (T1H and T2H, figure 3.12). However, in both PES, final adsorbed trajectories are found stabilised on the bridge sites and their surrounding areas and no adsorbed atoms are found over the repulsive hollow area.

Distributions of the polar scattering angle for $E_{col} = 0.25, 0.50$ and 1.3 eV at $\theta_v = 0°$ and 45° are plotted in figure 3.42. Results are comparable to the ones obtained for the FPLEPS surface. The only small difference is found in the polar scattering distribution of the trajectories at E_{col}= 0.5 eV. This is probably due to the small minimum observed in the hollow site at a surface distance of 2.0 Å and at 0.5 eV (figure 3.14). As it was observed before, the range of scattered angles (θ_v') obtained for the reflected atoms increases with collision energy as the atom can reach shorter Z_O distances with a stronger interaction. This effect can be specially observed for normal incidence when collision energy increases from 0.25 eV to 0.50 eV and from the latter to 1.3 eV. At $\theta_v = 45°$ and $E_{col} = 1.30$ eV a wide range of scattered angles of atoms is observed, although the peak for elastic scattering at around 45° is still present. On the other hand, the scattering

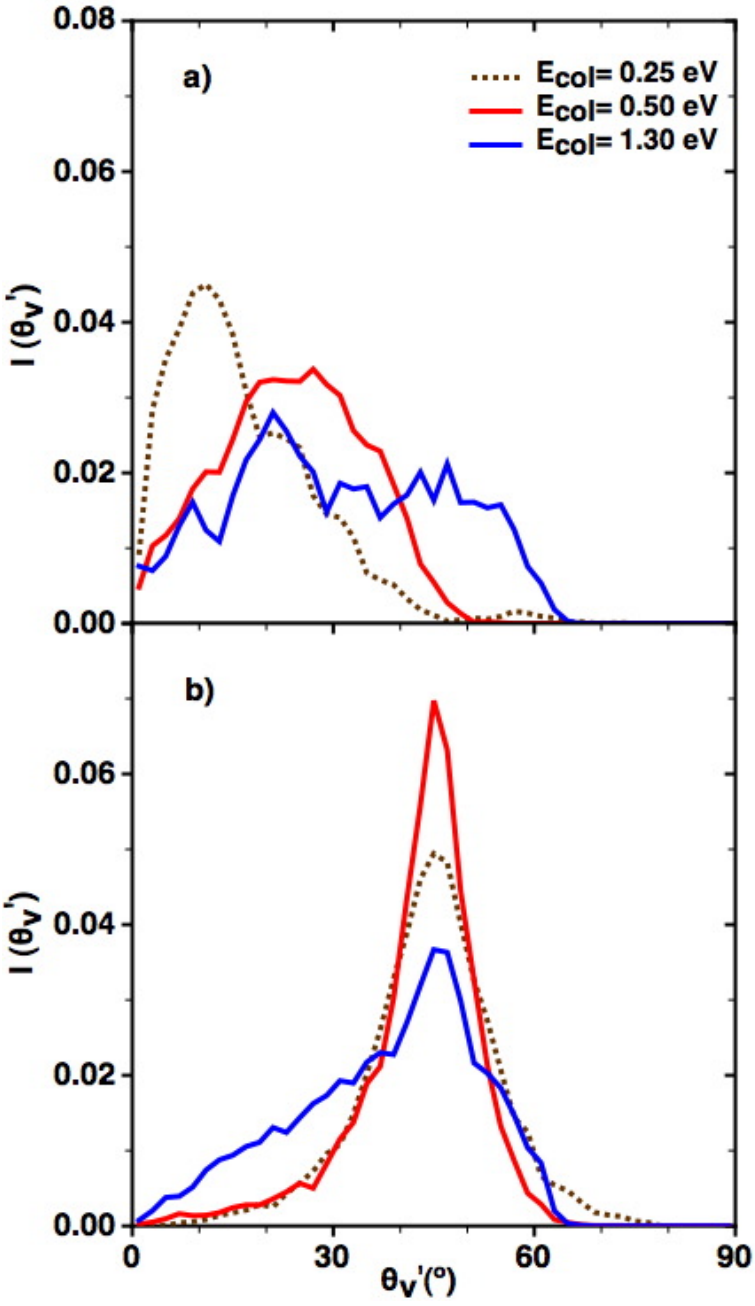

Figure 3.42: Polar scattering angle distribution for $E_{col} = 0.25, 0.5, 1.3$ eV at a) $\theta_v = 0°$ and b) $\theta_v = 45°$ for rigid slab with the MS surface.

of atomic oxygen at low energies at θ_v' gives specular reflection, which is lost gradually when increasing the initial collision energy.

•With surface temperature

Surface temperature was added for the dynamical study with the MS surface as for the previous PES. The trends observed for the FPLEPS surface are also observed here (figure 3.43) with the same arguments used previously. The main difference between the two surfaces is due to the physisorption minimum. The adsorption probability at 100 K presents two maxima. Each of them corresponds to a chemisorption at high collision energies whereas to a physisorption for low energies. In figure 3.44 the contribution of chemisorption and physisorption to the total probability is plotted for normal incidence at 100 K. For E_{col} higher than 0.5 eV, the adsorption probability is due to chemisorption; at collision energies lower than 0.2 eV is due mainly to physisorption, while a mixture of both contributions gives the total adsorption at intermediate E_{col}. Physisorption strongly depends on surface temperature. At low surface temperature (T_{surf} =100 K) adsorption probability increases considerably as the initial collision energy decreases. On the other hand, at higher temperature (T_{surf} = 500 K) the adsorption probability does not increase as initial collision energy decrease. This different behaviour can be explained if energy exchange between the surface and the oxygen atom is considered. The energy transferred from the surface to the atom at 900 K is enough to overcome the physisorption well and release the oxygen back to the gas phase, while at 100 K the energetic exchange would not be enough for the desorption process to occur. The effect of the temperature in the energy exchange between surface and oxygen atom will be discussed below.

Initial positions for finally adsorbed and reflected atoms at normal incidence for T_{surf} = 300 K at initial $E_{col} = 0.3, 0.5$ and 1.3 eV are plotted in figure 3.45. Reflected trajectories at the collision energy of 0.3 and 0.5 eV (figure 3.45a and b) are found mainly on the hexagonal hollow area. The domain of this area is bigger than for the FPLEPS equivalent results. It is easy to explain if it is considered that reflection probability for MS at this collision energy and surface temperature is higher than for FPLEPS at same conditions. On the other hand, reflected atoms whose trajectories started around the bridge site lead to smaller reflection than in the case of the FPLEPS surface. The tendency to reflection for the trajectories started over this site is more diffuse along the space than in FPLEPS. When the initial collision energy is increased, adsorption trajectories are started around the same areas obtained for the FPLEPS. Thus, close to the repulsive hollow site, trajectories are redirected to the bridge sites favouring the adsorption, while trajectories starting over the bridge sites and their surroundings, again tend to give reflection processes due to the tendency of the surface to displace the atom towards the repulsive hollow site. Final adsorbed atoms, clearly finish around

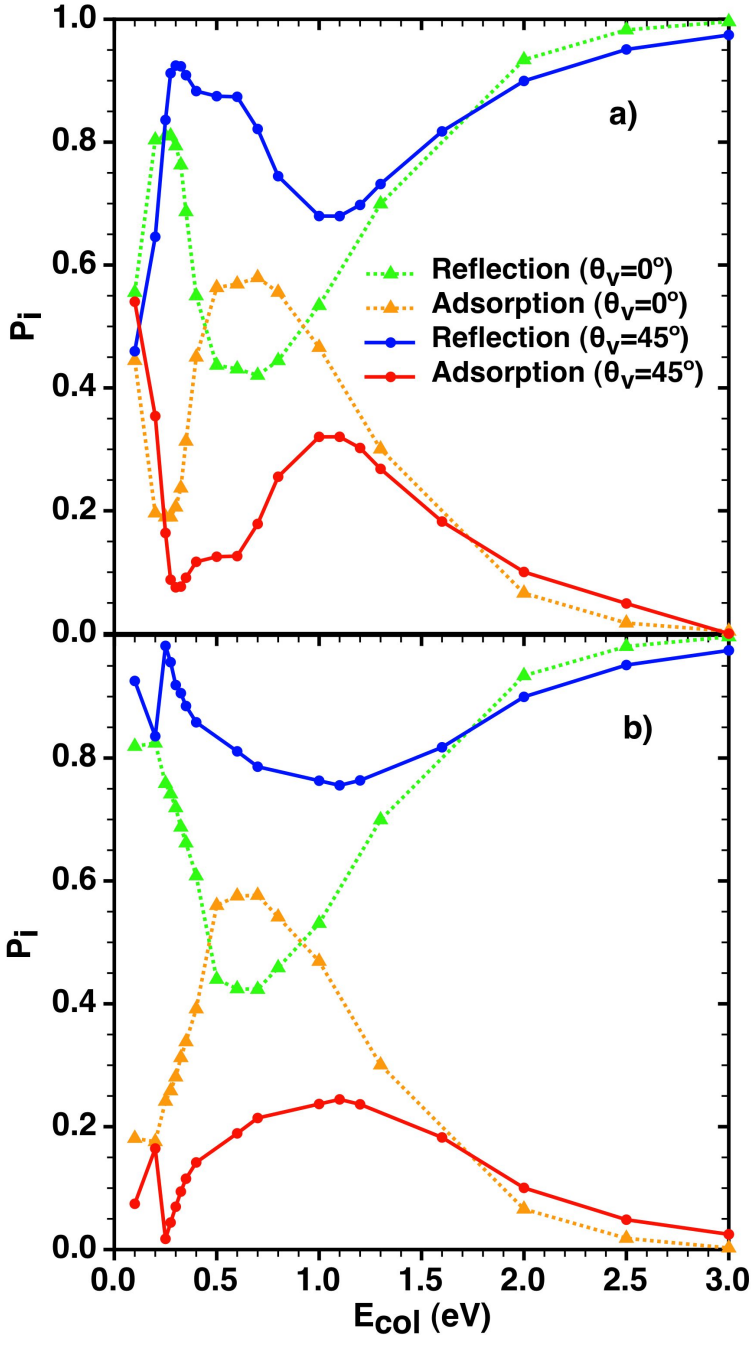

Figure 3.43: Oxygen adsorption and reflection probabilities as a function of initial collision energy at initial $\theta_v = 0°$ and 45° at a) $T_{surf} = 100$ K and b) $T_{surf} = 900$ K) with the MS surface.

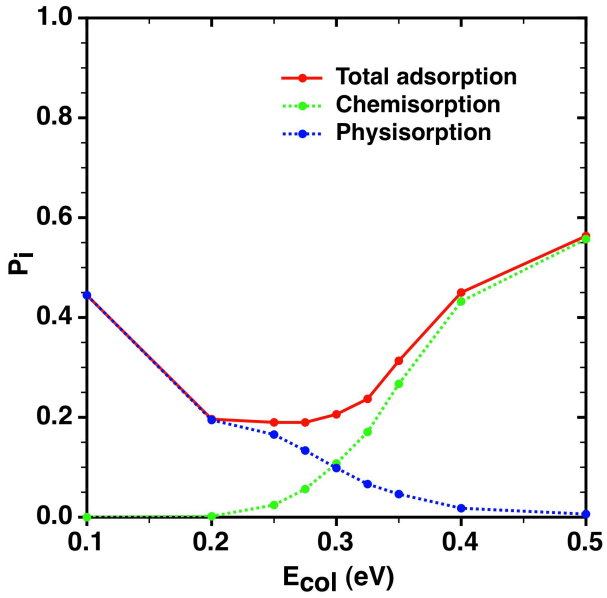

Figure 3.44: Contribution of chemisorption and physisorption to the total adsorption probability for normal incidence at $T_{surf} = 100$ K.

the bridge sites since energy is dissipated to the surface, giving to the atom the opportunity to be finally stabilised at the minimum well. The concentration of final trajectories over the different bridge sites along the surface shows again the effect of diffusion. Some of the atoms get adsorbed on bridge sites, that are not located neither on the sampled unit cell nor immediately close to this cell. This fact means that these atoms diffuse over the surface to bridge sites located further in space, although the total number of atoms arriving to these sites decreases clearly with the distance from the initial sampled cell.

Polar scattering angle distribution is presented in figure 3.46 at two surface temperatures for $\theta_v = 0°$ and $45°$. The distributions show similarities with FPLEPS results, although some small differences are found. For instance, the distributions for the lowest energy (0.25 eV) at normal incidence for both temperatures show a peak at low angles. If compared with previous results, the peak is a bit wider and slightly shifted to higher angles. The minimum observed in the hollow site, which could be accessible if the atom gains enough energy from the surface, could be the responsible for this small change. As observed previously, the amplitude of the polar scattering angle distribution increases with collision energy. The behaviour observed for off normal incidence is quite comparable with the observed in calculations with no surface temperature with MS surface and with the FPLEPS results. The double peak observed at initial collision energy of 0.5 eV, which was not observed before, could be produced by the hollow

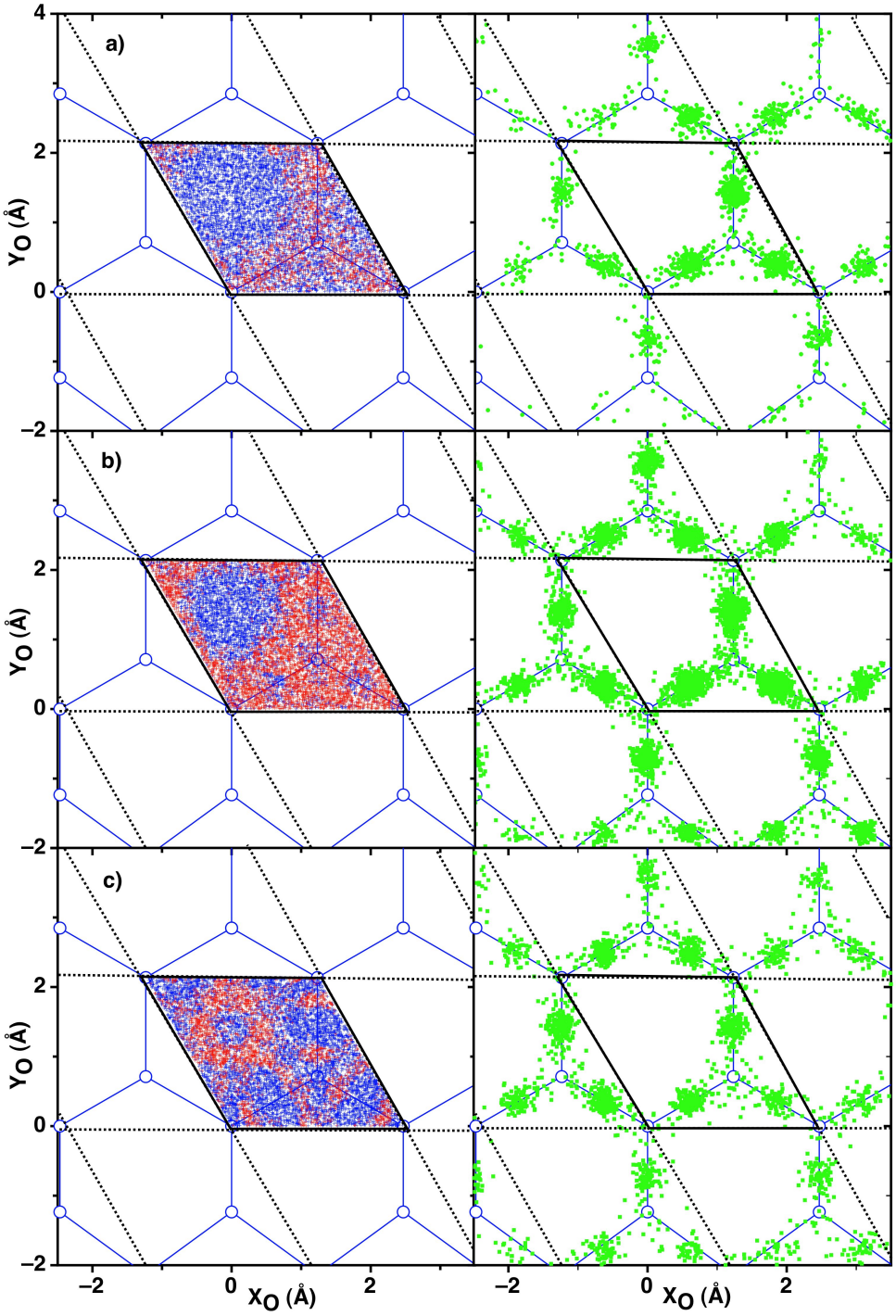

Figure 3.45: Initial X_O and Y_O position for adsorbed (red) and reflected (blue) trajectories and final position for adsorbed (green) trajectories at normal incidence at T_{surf}= 300 K for a) E_{col} = 0.3 eV, b) E_{col} = 0.5 eV and c) E_{col} = 1.3 eV for the MS PES.

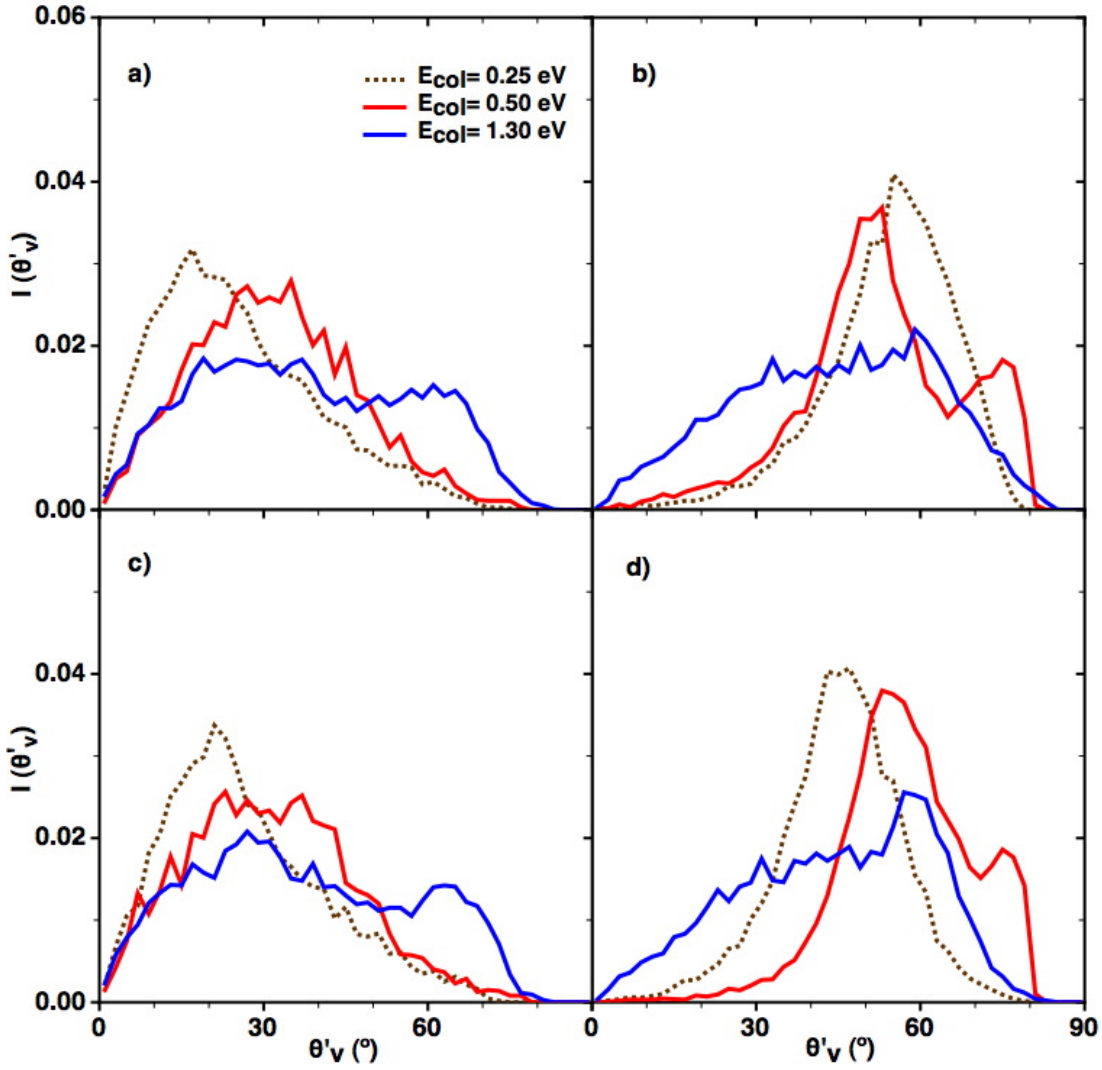

Figure 3.46: Polar scattering angle distributions for $E_{col} = 0.25, 0.5, 1.3$ eV at a) $\theta_v = 0°$ and $T_{surf} = 300$ K, b) $\theta_v = 45°$ and $T_{surf} = 300$ K, c) $\theta_v = 0°$ and $T_{surf} = 900$ K and d) $\theta_v = 45°$ and $T_{surf} = 900$ K with MS surface.

minimum, but none of the analysis carried out gave a clear explanation to this fact.

Distribution for the exchange energy (ΔE_{col}) is plotted for three different initial energies (E_{col} = 0.25, 0.50 and 1.3 eV) for normal incidence in figure 3.47. In general, it is observed a negative energy exchange of the oxygen with the surface, which means that the oxygen collision energy decreases giving part of it to the surface. This is also observed for atoms at an initial collision energy of 0.25 eV although there is an important fraction of those gaining some energy from the surface, reflected in the positive values of the ΔE distributions. This is specially true for the lowest collision energy at the higher temperature (figure 3.47b) where an amount of 0.5 eV can be transferred from the surface to the impinging atom. As was mentioned before, this extra energy transferred to the atom could be the responsible for the decreasing probability of physisorption when surface temperature is increased. At these higher temperatures, the energy gained by the reflected atom can be high enough to minimize the effect of the physisorption well, being the atom released back to the gas phase.

QCT calculations at thermal conditions ($T_{surf} = T_O$) for temperatures between 300 - 1,300 K for $\theta_v = 0°$ and 45° are also performed. As it was said for the FPLEPS thermal study, the initial collision energy achieved by the atom at these temperatures is in general very low, so the results should be similar to those obtained for the state specific case at low energies. The adsorption and reflection probabilities at different temperatures are presented in figure 3.48. At lowest temperature, the probability of adsorption is very similar to the reflection one for normal incidence and a little bit higher for off normal incidence. When increasing temperature, a decrease in the adsorption probability is observed until a temperature of 1,300 K, when adsorption increases again. In contrast with FPLEPS results, the huge adsorption probability observed at low temperatures is due to the physisorption well, which is favoured at off normal incidence. When increasing temperature, the physisorption process will decrease for two reasons: firstly because the initial collision energy is higher, so oxygen atoms have too much energy to be stabilised around the physisorption well, and secondly, because the increase in surface temperature allows an energetic exchange from the surface to the oxygen atom, which gives to the atom energy enough to go back to the gas phase. On the other hand, when temperature is high enough, some of the atoms have enough energy to overcome the adsorption barrier and lead to chemisorption. Thus, the increase in adsorption probability from 1,300 K to 1,500 K is produced for the small increment in the chemisorption process.

Scattering polar angle distributions presented in figure 3.49 show different behaviour than the previous results (figure 3.37). This is specially evident for the scattering angle distribution observed at T = 300 K where the initial collision energies are very low. The amplitude of the distribution shows no specific tendence for any particular angle because of the interaction of these low energy

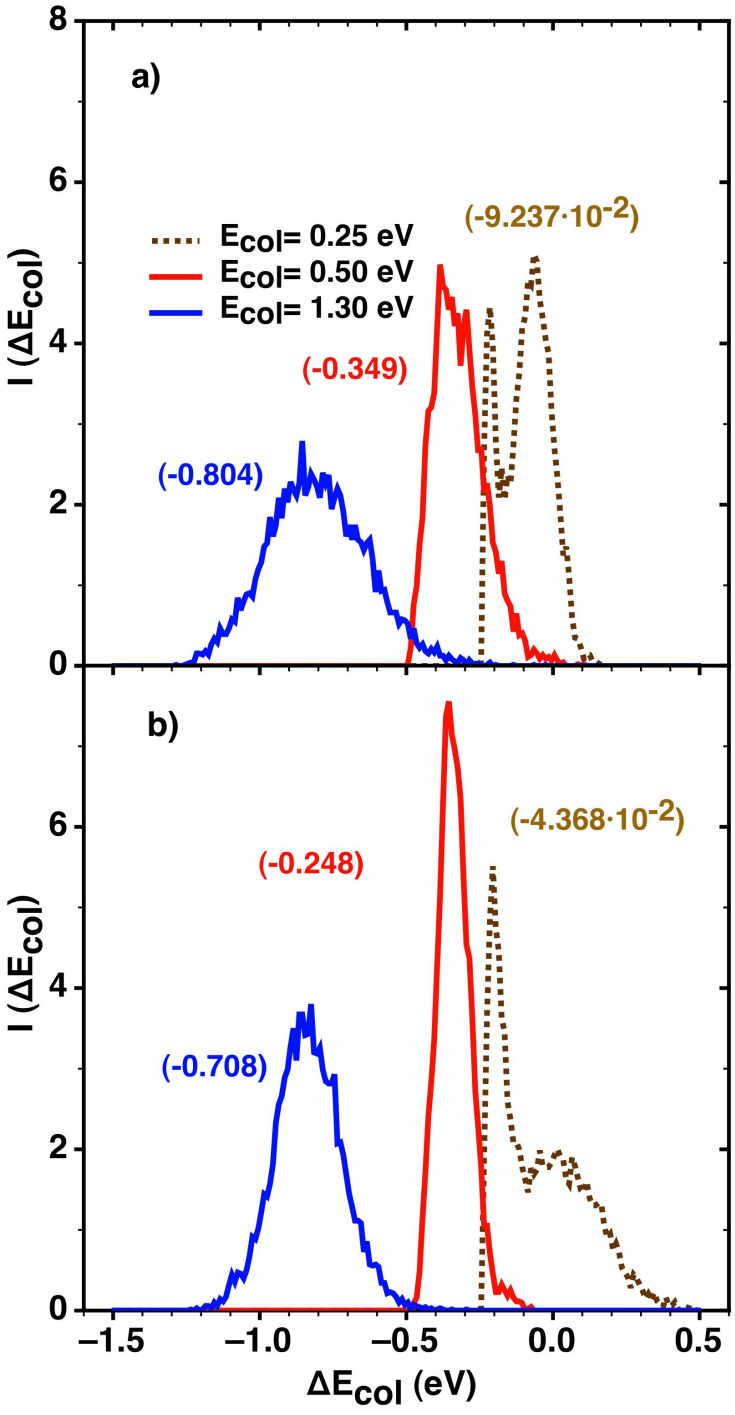

Figure 3.47: Energy exchange (ΔE_{col}) for reflected trajectories at initial E_{col} = 0.25, 0.5 and 1.3 eV and $\theta_v = 0°$ at a) T_{surf} = 300 K and b) T_{surf} = 900 K for MS surface. Between parantheses are given the mean values of $\langle E_{col} \rangle$ in eV.

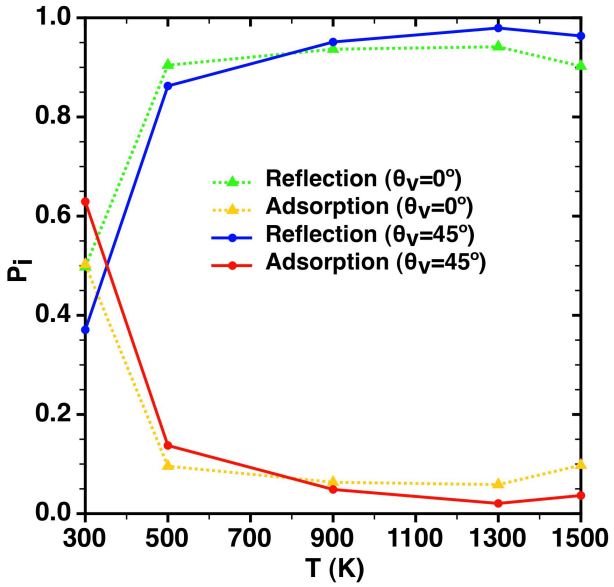

Figure 3.48: Adsorption and reflection probabilities for the atomic oxygen and the surface at different temperatures for initial $\theta_v = 0°$ and 45° impinging angles.

atoms with the physisorption well. It can be observed how the effect of the interaction with the physisorption well is less important for higher energies as the atom has in general higher initial collision energy. On the other hand, the energy transferred is also perfectly comparable with the FPLEPS results. Thus, when increasing temperature, the exchange of energy between the atom and the surface is higher because of the higher initial collision energies and the surface temperature, although mean values are close to 0, indicating both types of energy transfers.

Experimental conditions of Paci et al. (71) were also simulated with the MS surface as was also discussed in previous section. Figure 3.50 shows the calculated scattering angle distribution compared with the experimental one. A batch of 30,000 trajectories were calculated emulating the initial experimental population of the experiment with a hot oxygen beam impinging the surface at $\theta_v = 45°$ and $T_{surf} = 503$ K. The peak observed for the scattering angles distribution is situated around $\theta_v' = 65°$ for the theoretical results and at $\theta_v' = 62°$ for the experimental ones. As for the FPLEPS simulation, peaks are very close, although experimental results show a narrower distribution. The FPLEPS and MS results are similar and the explanation in previous section is valid also here.

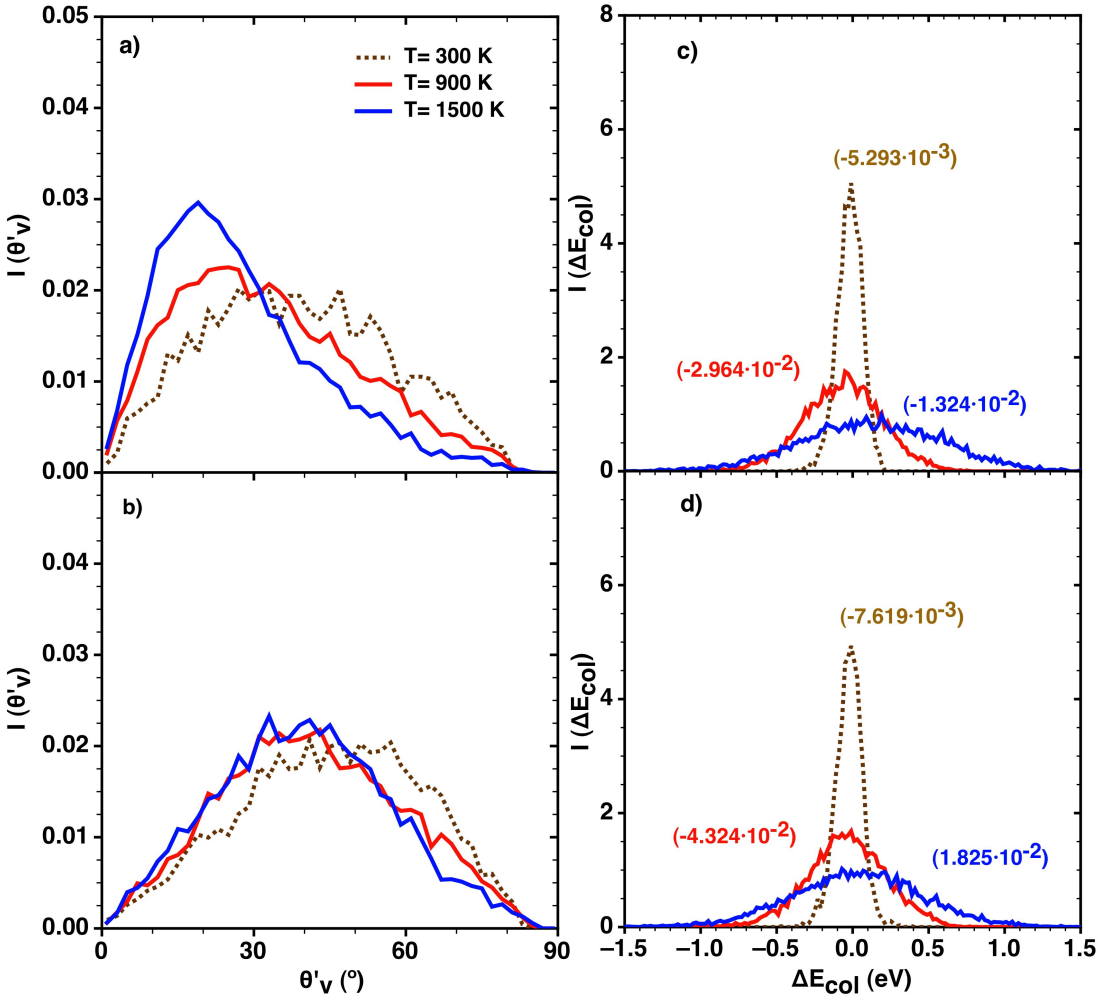

Figure 3.49: Polar scattering angle (left panels) and energy exchange distributions (right panels) of reflected atoms for trajectories at three different temperatures at a), c) $\theta_v = 0°$ and b), d) $\theta_v = 45°$ with MS surface. Mean values (between parentheses) of ΔE_{col} are given in eV.

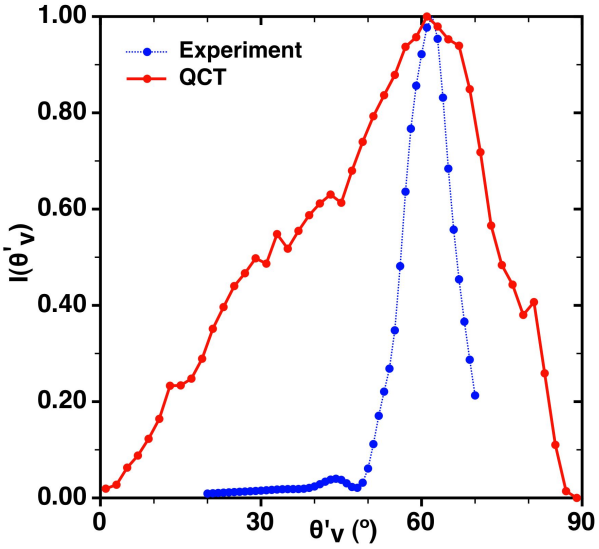

Figure 3.50: Theoretical and experimental (71) distribution of polar scattering angle of reflected atomic oxygen for a hot (hyperthermal) beam with incident angle $\theta_v = 45°$ and $T_{surf} = 503$ K using the MS surface.

3.6.1.4 Summary and comparison of dynamical results

Two different potential energy surfaces for the interaction of atomic oxygen over graphite (0001) surface have been constructed: the FPLEPS surface, based on a reduced set of DFT data over high-symmetry sites, and the MS one that uses the interpolation scheme of Shepard, based on a large set of DFT data. Quasiclassical trajectory method has been applied to the study with both PES in order to get adsorption and reflection probabilities as a function of collision energy and surface temperature and for two different incident angles ($\theta_v = 0°$ and $45°$). In addition, scattering angle distributions and energy exchanged (Δ_{col}) between the incoming atom and the surface has been investigated at three collision energies ($E_{col} = 0.25, 0.5$ and 1.3 eV) with several surface temperatures. Moreover, some quasithermal and hyperthermal studies have been done in order to reach scattering angle distribution at some particular conditions for comparing with experimental data available.

In general, the results obtained by using the two PES are in agreement in practically all the conditions explored. Nevertheless, some discrepancies are obtained at very low collision energies due to the presence of a physisorption minimum in MS surface that was not reproduced in FPLEPS one. The description of the system by means of interpolated surfaces is considered more accurate than analytical ones since a big amount of geometry information is included in order to describe the system; it is worth noting that MS surface matches the DFT or *ab*

initio information whereas the FPLEPS one is obatined by fitting, so an associated root mean square deviation respect to DFT or *ab initio* data is associated with it.

The polar scattering peak for hyperthermal conditions is practically reproduced by the two surfaces constructed, although the shape of the theoretical distributions are wider than the experimental one. However, both O and O_2 species composed the experimental hot beam. However, there are some differences with the experimental conditions because in the experiment the molecular beam contains O and O_2, hence a part of the incident O atoms can react to produce O_2 (ER) and also incoming O atoms can be scattered with the solid surface with O-precovered.

3.7 QCT study of two oxygen atoms and molecular oxygen interacting with graphite surface

3.7.1 Atomic oxygen QCT collision study with O-preadsorbed graphite (0001)

3.7.1.1 Computational details

A dynamical study involving the interaction of atomic oxygen over an oxygen preadsorbed graphite surface was done by means of the quasiclassical trajectory method. Several initial conditions were sampled in order to investigate state specific, thermal and hyperthermal processes. For state specific calculations initial collision energies between 0.01 eV $\leqslant E_{col} \leqslant$ 2.0 eV were used at two incident angles ($\theta_v = 0°$ and 45°), defined similarly as for atomic oxygen but using the center of mass velocity (figure 3.22). All these conditions were explored without and with surface temperature (100 K $\leqslant T_{surf} \leqslant$ 900 K). In addition, thermal initial conditions for O atom were calculated for a temperature range between 100 $\leqslant T \leqslant$ 1,100 K for $\theta_v = 0°$ and 45°. Finally, an hyperthermal initial atomic distribution, emulating experimental studies from Paci et al. (71), was also studied using a surface temperature of 503 K and $\theta_v = 45°$.

Initial gas phase oxygen position (X_O, Y_O) is randomly selected along the (1×1) unit cell meanwhile initial Z_O position is set to 7.5 Å, where the interaction with surface is negligible. The preadsorbed oxygen atom to the surface (coverage of a 50/100% of the initial sampled cell) was fixed initially at the equilibrium geometry of the minimum found for the FPLEPS surface ($X_O = 0.621$ Å, $Y_O = 0.359$Å, $Z_O = 1.385$ Å, table 3.11).

The GLO model was also used for atomic collisions over a surface with an preadsorbed atom at a given T_{surf}. In this case, the adsorbed atom is located at the adsorption minimum (i.e., its equilibrium geometry). This atom is initially (t = 0) displaced with the same coordinates (X_s, Y_s, Z_s) (equation A.8) of the surface particle to avoid any change in its potential. Then we impose to this adatom a distribution of kinetic energies, twice the value of the average kinetic energy at the thermal equilibrium (i.e., using $T = 2T_{surf}$). We observe that this adatom is correctly thermalised together with the GLO bath during the trajectory and before the arrival of the incoming atom. Thus, when the incoming atom is close enough to the adsorbed one or to the surface, the adatom is vibrating properly around its initial equilibrium position with similar average kinetic and potential energies. Thus, the X_O, Y_O, Z_O evolution along time and the total, potential and kinetic energies of the atom were plotted for several trajectories.

It can be seen in figure 3.51 that for the plotted trajectory the adsorbed atom remains around the equilibrium position and showing the usual oscillations of the kinetic and potential energies. The total energy is not constant due to the thermal bath effect.

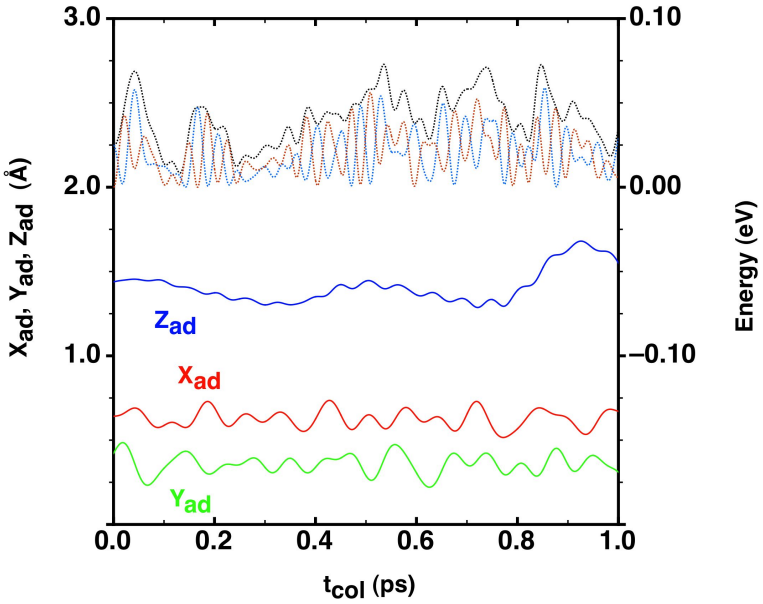

Figure 3.51: X_O, Y_O, Z_O of the adsorbed oxygen atom along time (left axis). Energies (dotted lines) are plotted (right axes) for the total (black), kinetic (blue) and potential (orange) energies.

Quasiclassical trajectories were run with *qctsurf* program, the same used as for O + graphite study.

Six possible exit channels were considered in order to classify the reactivity of the system. Adsorption and reflection of the impinging atom was considered either if the preadsorbed atom remains adsorbed to the surface or if it desorbs. The formation of the O_2 molecule was considered to give two different channels when it remains adsorbed to the surface after its formation or when it forms the gas phase molecule via an ER process. For atomic adsorption classification, the Z_O should be lower than 2.2 Å and the number of total rebounds with the surface more than 8, as was also set for the interaction of one atom with the surface. On the other hand, O atom was considered reflected if Z_O value was higher than 7.6 Å and the direction of its velocity vector pointed to the vacuum. These same conditions were considered for the O atom to be desorbed. The oxygen molecule was considered formed when the internuclear distance r was lower than 2.0 Å and dissociated when r was higher than 3.0 Å. Similarly to the atomic adsorption, to

consider the molecule adsorbed, the Z_{cm} should be smaller than 2.2 Å and the number of total rebounds with the surface more than 8.

Batches of a minimum of $N_T = 10,000$ trajectories were run at each initial condition, which leads to statistical errors lower than the 1% for the ER probability at normal incidence ($\theta_v = 0°$) and $E_{col} = 0.5$ eV.

3.7.1.2 Dynamical study

•Without surface temperature

Probabilities for each of the defined channels were calculated for state specific conditions at $\theta_v = 0°$ and 45° at several initial collision energies between 0.01 eV and 2.0 eV.

Results plotted in figure 3.52 show that the reflection of the impinging atom and the ER reaction are the two main processes observed among others, which present clearly smaller probabilities. For normal incidence (figure 3.52a) the reflection probability of the incident oxygen atom decreases when increasing initial collision energy to a more or less stationary probability at collision energies higher than 0.8 eV. On the other hand, ER probability increases with initial collision en-

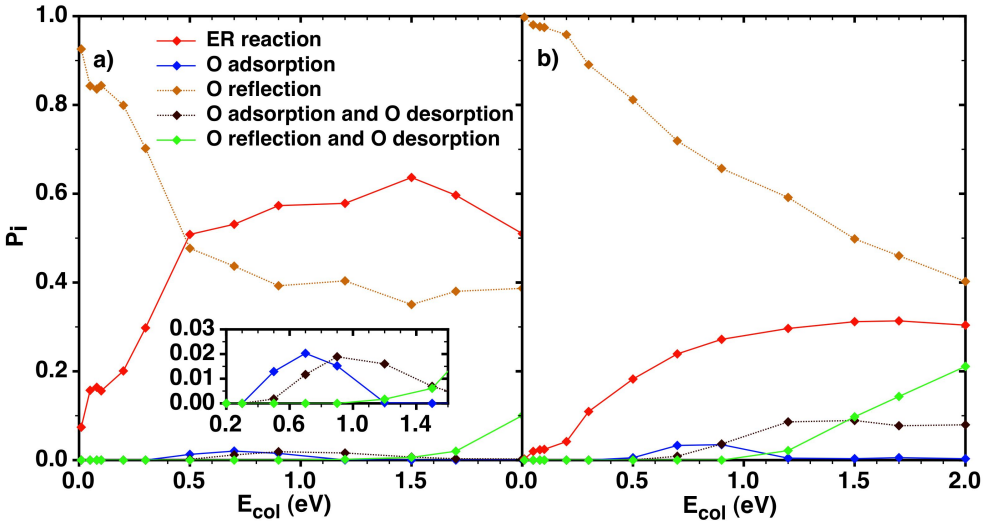

Figure 3.52: Reaction and reflection probabilities as a function of collision energy at initial a) $\theta_v = 0°$ and b) $\theta_v = 45°$ without surface temperature over an oxygen precovered graphite surface.

ergy and decreases again when $E_{col} > 1.5$ eV. This decreasing at higher collision energies is mainly due to an increase of the desorption of the preadsorbed atom.

Probably, this secondary process is getting more important at higher energies because the impinging atom will destabilize the preadsorbed one. At very low initial collision energies ER probabilities are not zero, which is seemingly contradictory with the presence of an activation barrier. Thus, as was mentioned in section 3.5.2, the calculated transition state was possibly not the lowest one for the ER process. At initial collision energies between 0.2 eV and 1.6 eV, adsorption of the impinging atom can be observed with a very low probability either producing or not the desorption of the second atom. The observed adsorption is lower than in the case of a clean graphite (0001) surface (studied in section 3.6.1.2) because now the bridge site is occupied by the preadsorbed oxygen and there are not another free bridge site inside the (1×1) unit cell.

When off normal incidence is considered, ER reaction probability decreases considerably compared with normal incidence results. The process is also observed at very low collision energies and increases with initial collision energy until an almost constant value of the probability. Desorption of the atom is considerably higher than for normal incidence probably because the kinetic energy parallel to the surface of the impinging atom is more efficient in order to interact with the preadsorbed one.

Initial position for the O impinging atom is plotted in figure 3.53 for a calculation at $\theta_v = 0°$ and $E_{col} = 0.3$ eV. It can be seen that trajectories leading to ER

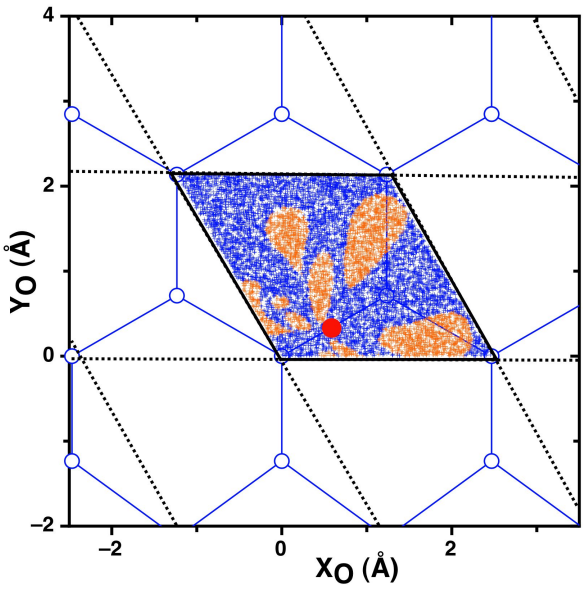

Figure 3.53: Initial X_O and Y_O position for reflected atoms (blue) and ER reaction (orange) for trajectories with normal incidence and $E_{col} = 0.3$ eV. Adsorbed atom is indicated with a red circle.

reaction generally start at positions close to the preadsorbed atom and around the areas where the interaction with surface was found more stable (figure 3.19).

The scattering angle of the reflected atom is plotted in figure 3.54a and b in order to study the effect of a preadsorbed atom. This distribution compared with the collisions over a clean surface (figure 3.28) shows that in the case of normal incidence there is a clear shift towards higher scattering angles (e.g., $\sim 60°$ for $E_{col} = 0.20$ eV). Therefore, the presence of preadsorbed oxygen atom affects the final distribution. Results obtained for off normal incidence show a maximum at around $\theta_v^{'} = 40°$, with a broader distribution compared to the one presented in figure 3.28.

The analysis of initial position of the impinging atom for normal incidence depending on the final $\theta_v^{'}$ angle is plotted in figure 3.55. It can be seen that atoms reflected at low angles are located initially far from the preadsorbed one. Thus, it can be said that the interaction of these atoms is like an interaction with a clean surface, giving a small scattering angle. On the other hand, atoms that give higher scattering angles are found close to the areas where trajectories lead to ER (white areas in figure 3.55). Consequently, these trajectories feel strongly the interaction with the preadsorbed atom and are deviated although do not react with it.

The final velocity angle distribution for O_2 molecules formed via ER reaction was also studied and plotted in figure 3.54c and d. Results show that molecules tend to leave the surface at low angles. In the case of normal incidence a peak is observed at angles around 10° - 20°, while for $\theta_v = 45°$ distribution of final velocity angle is shifted a bit at higher values (15° - 35°).

•With surface temperature

The effect of the surface temperature was added using the GLO model presented in section 2.4.1. Before the extensive QCT study, a preliminary study of the evolution of the preadsorbed oxygen atom was carried out to ensure its correct thermalization (figure 3.51).

Trajectory calculation at surface temperatures in the range of 100 - 900 K were carried out at different collision energies between 0.01 eV $\leqslant E_{col} \leqslant$ 3.0 eV for two initial incident angles ($\theta_v = 0°$ and 45°). Results are presented in figure 3.56 at three selected surface temperatures for $\theta_v = 0°$ and 45°. Comparing results for normal incidence at a low surface temperature (T_{surf} =100 K , figure 3.56a) with calculations without surface temperature, it is possible to state that general trends are kept. Most differences found involve secondary processes. The adsorption probability of the impinging atom increases when surface temperature is taken into account, possibly due to the possibility that the impinging atom exchange energy with the surface. This adsorption tends to decrease at higher temperatures. The atomic desorption is observed from high to low collision en-

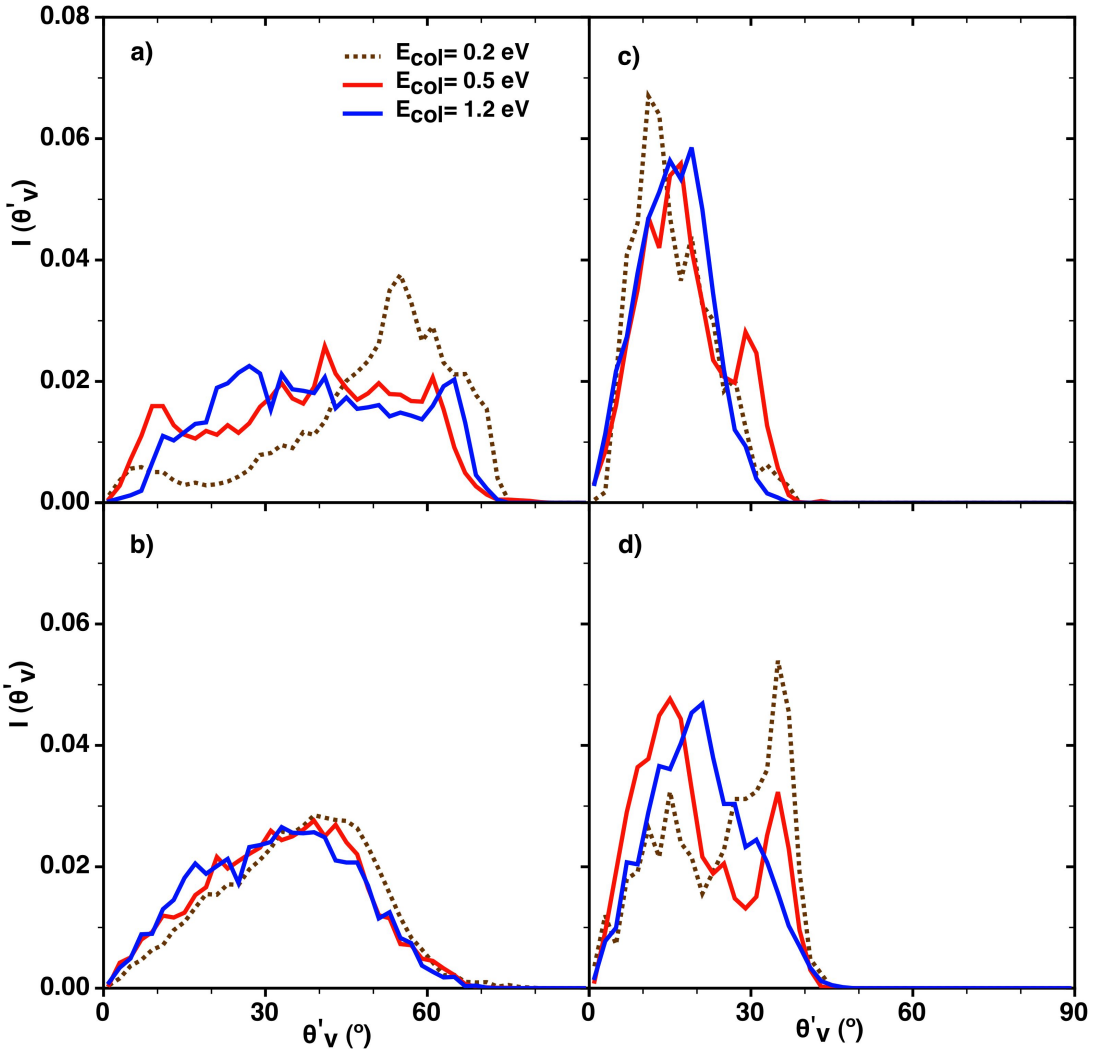

Figure 3.54: Atomic polar scattering angle distributions for $E_{col} = 0.2, 0.5, 1.2$ eV at a) $\theta_v = 0°$ and b) 45°, and molecular polar scattering angle distribution for ER formed O_2 molecules for $E_{col} = 0.2, 0.5, 1.2$ eV at c) $\theta_v = 0°$ and d) 45°.

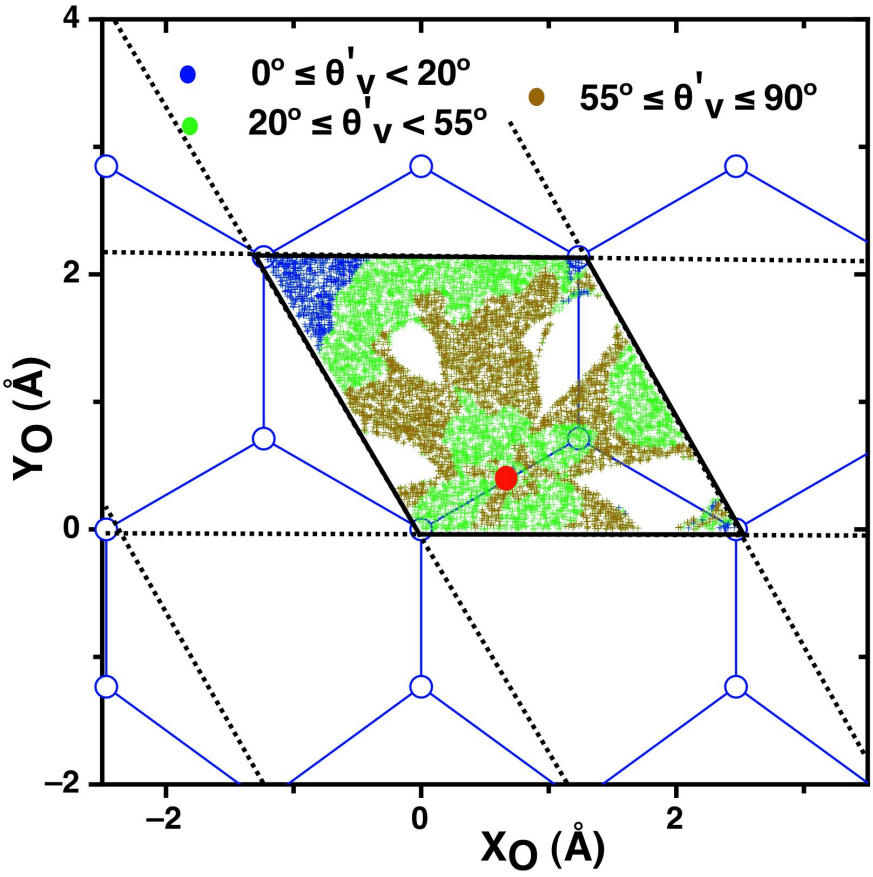

Figure 3.55: Initial X_O and Y_O position of the impinging atom for reflected trajectories with normal incidence and $E_{col} = 0.2$ eV depending on the final scattering angle observed. White areas correspond to initial positions that give place to ER reaction.

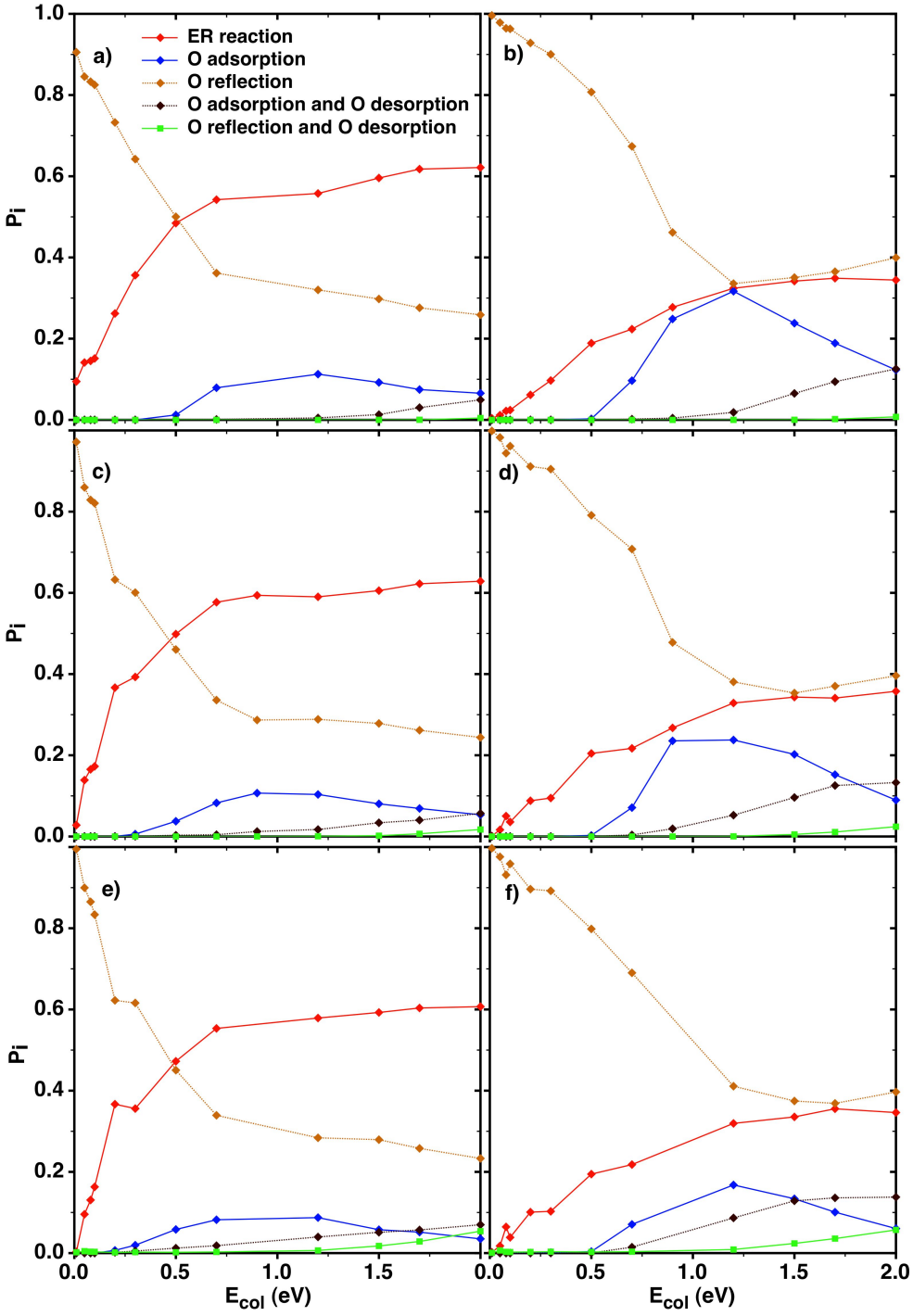

Figure 3.56: Reaction and reflection probabilities for an oxygen atom impinging a preadsorbed graphite surface as a function of collision energy at several conditions, a) $\theta_v = 0°$ and $T_{surf} = 100$ K, b) $\theta_v = 45°$ and $T_{surf} = 100$ K, c) $\theta_v = 0°$ and $T_{surf} = 500$ K, d) $\theta_v = 45°$ and $T_{surf} = 500$ K e) $\theta_v = 0°$ and $T_{surf} = 900$ K and f) $\theta_v = 45°$ and $T_{surf} = 900$ K.

ergies when the surface temperature in increased, as could be expected.

The analysis of the initial X_O and Y_O position for the impinging atom was done for a batch of trajectories at two initial collision energies ($E_{col} = 0.3$ eV and 0.7 eV). The observed features for the lower energy in figure 3.57a show a similar behaviour as when surface temperature was not taken into account. In that case,

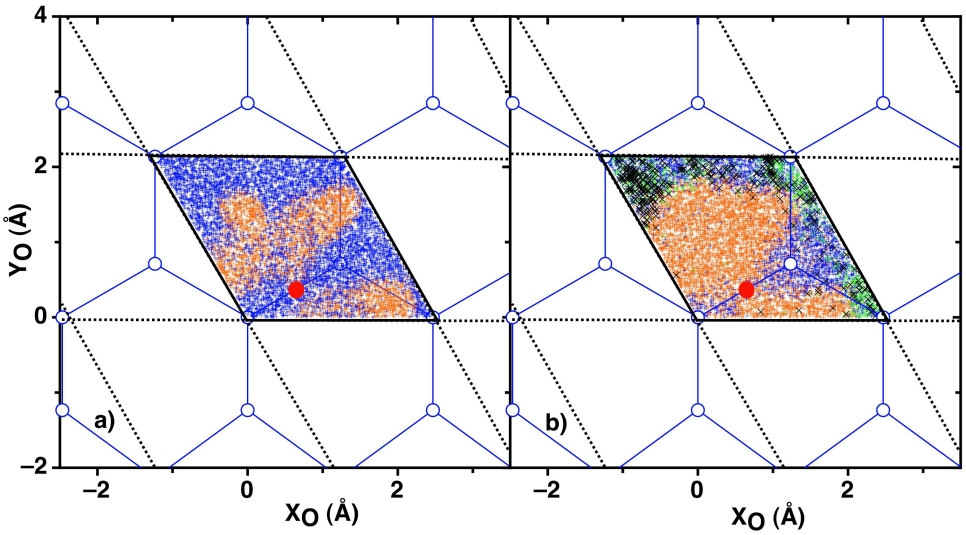

Figure 3.57: Initial X_O and Y_O position of the incoming atom for several reflected atoms (blue), ER processes (orange), O adsorption (green) or O adsorption with O desorption (black) at normal incidence ($\theta_v = 0°$) for a) $E_{col} = 0.3$ eV and b) $E_{col} = 0.7$ eV at $T_{surf} = 500$ K.

the initial position of the atom leading to ER reaction is slightly more diffused into the surface, but in general, the trajectories started on the surroundings of the preadsorbed atom allow the interaction between both oxygen atoms to form the O_2 molecule. At higher initial collision energy there are more processes that can be observed (figure 3.57b). Concerning to the ER reaction, trajectories starting at the same areas than for lower collision energy lead to formation of O_2, although trajectories starting at a longer distance of the preadsorbed atom can finally react with it due to the higher available energy. Furthermore, the initial position of trajectories producing the adsorption of the gas atom while the preadsorbed one remains on the surface, show that it is only possible when the distance to the adatom is long enough to consider the interaction almost negligible. Thus, in that case, incoming atom is behaving as if it was interacting with a clean surface. The analysis of the final position of these trajectories shows that this atom finally adsorbs at bridge sites located close to the starting position of the trajectories but in another close cells with free sites. Likewise, in trajectories where the adsorption

of O atom is observed at the same time that atom O desorbs, initial positions are found far from the preadsorbed atom as well. A final position close to the initial one for impinging atom for these trajectories suggests that the desorption of the other atom is not due to direct interaction with the impinging one. Probably the desorption is an effect of the surface temperature although small interaction at long distances with impinging atom could help the preadsorbed one to end in the gas phase.

The scattering angle of the impinging atom was analysed in order to understand the effect of the presence of a preadsorbed atom on the surface. Results are plotted in figure 3.58 for three initial collision energies (E_{col} = 0.2 eV, 0.5 eV and 1.2 eV) for the two initial incident angles ($\theta_v = 0°$ and 45°). Comparing the scattering angles for normal incidence with the results obtained for a surface without temperature the same general trend is observed for the lowest depicted initial collision energies. A peak around 50° - 60° is observed at this energy while the probability for smaller angles is much lower. On the other hand, for higher energies this behaviour is also observed, although the distribution is wider and the lower angles appear with higher intensity. This is specially clear for E_{col} = 1.2 eV where two maxima are observed, one at angles around 60° - 70° and a second one smaller at around 20°. Results for off normal incidence are comparable to the ones obtained without surface temperature. The distribution observed is very wide, although for E_{col} = 0.2 eV a maximum appears at angles around 40°. This distribution is not like the one obtained for a clean surface. The effect of increasing the temperature is not producing important changes on the distributions.

Initial positions of incoming atoms are plotted in figure 3.59 as a function of the final θ_v' scattering angle values to show how the atoms interacting closely to the preadsorbed one tend to scatter at higher angles than the atoms interacting far from it, similarly to the results without surface temperature effect.

The exchange of energy between the impinging atom and the surface was evaluated at three initial collision energies for three surface temperatures (figure 3.60). The energy exchange between the impinging atom and the surface with the preadsorbed one is in general negative, which means that the final collision energy of the reflected atom is lower than the initial one. Only when initial collision energy is very low (E_{col} = 0.2 eV) and the surface temperature high enough, the surface energy due to the temperature is able to increment the collision energy of impinging atom. This effect is higher when the surface temperature is increased. For more energetic collisions the energy is generally transferred from the atom to the surface.

The study of the scattering angle of the O_2 formed molecules via ER reaction was also analysed. Results plotted in figure 3.61 show similar behaviour to the results obtained without temperature (figure 3.54c and d). Actually, the effect of surface temperature is not noticeable.

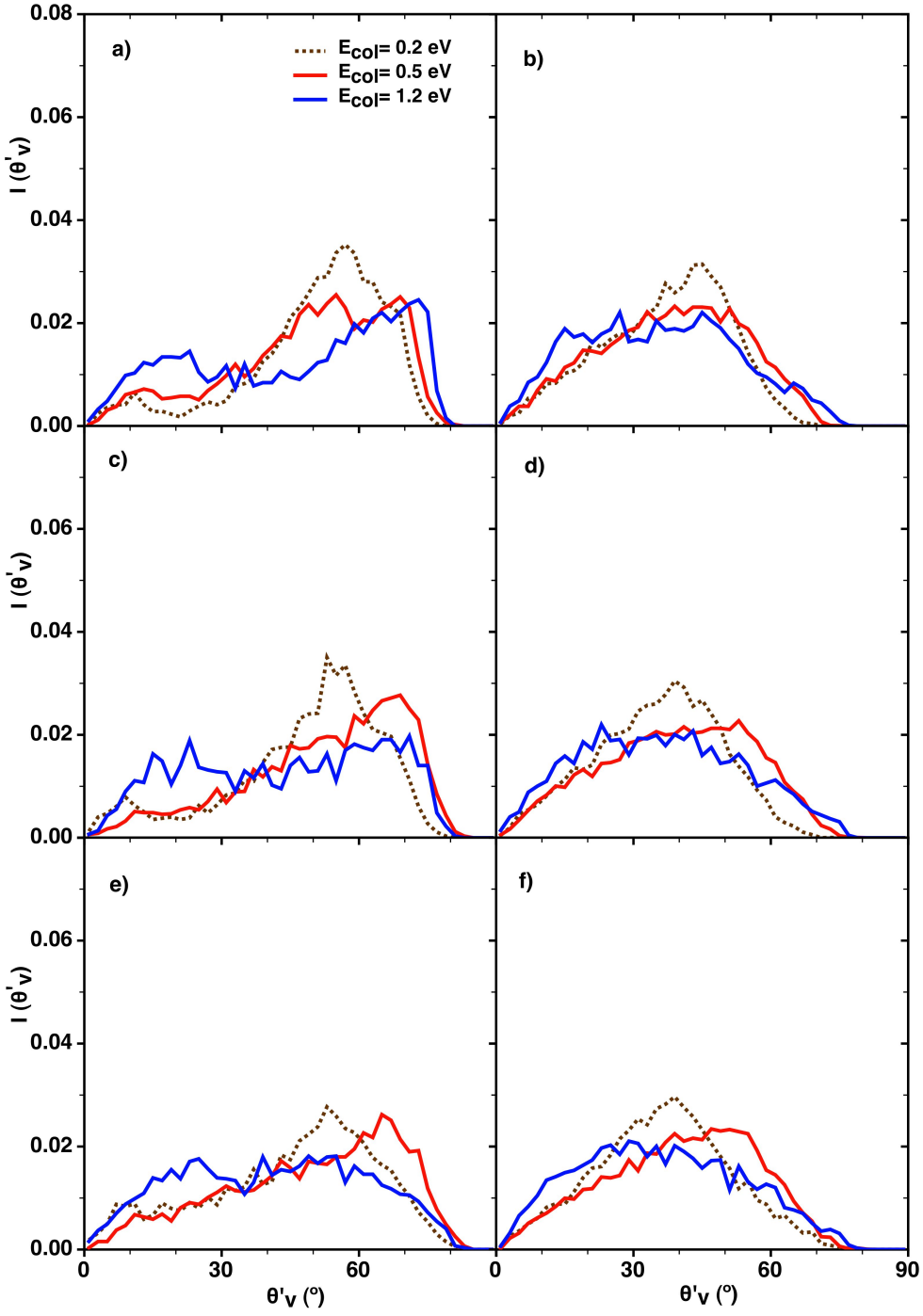

Figure 3.58: Polar scattering angle distribution for $E_{col} = 0.2, 0.5, 1.2$ eV at normal incidence (left panels) and $\theta_v = 45°$ (right panels) at a) and b) $T_{surf} = 100$ K, c) and d) $T_{surf} = 500$ K, and e) and f) $T_{surf} = 900$ K.

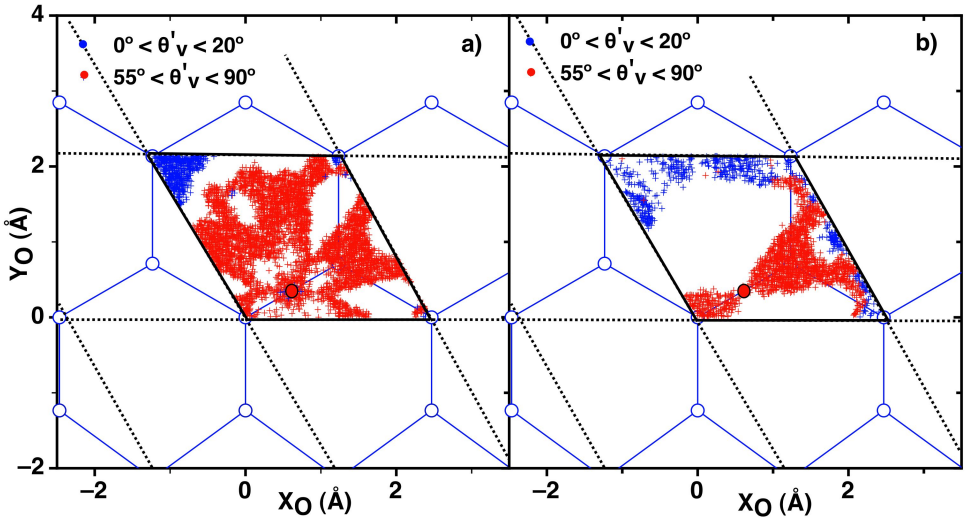

Figure 3.59: Initial X_O and Y_O position of impinging atoms of reflection trajectories with a) $E_{col} = 0.3$ eV and b) $E_{col} = 0.7$ eV, for $\theta_v = 0°$ and $T_{surf} = 500$ K depending on the final scattering angle observed.

An analysis of the internal and collision translational energy of the formed molecules via ER reaction is presented in figure 3.62 at two initial collision energies for normal incidence only at $T_{surf} = 500$ K as surface temperature effect was expected to be almost negligible. Molecules are observed with excited vibrational and rotational levels respect to the initial ones (v= 0, j= 1). Initial collision energy does not play an important role for any of the studied properties. The area for the distribution of final translational energy of the formed molecules for an initial collision of 0.2 eV and 1.2 eV is equal to the unit. Both distributions show a very similar mean value of the translational energy even when the initial collision energy is considerably different. The increase of E_{col} does not produce a significant change into the vibrational distribution although it is observed some rotational excitation, probably due to the transfer of E_{col} to the final molecular rotation. Nevertheless, as the rotational energies are much lower than the vibrational ones, this fact is not reflected into the internal energy distribution (E_{int}).

QCT reaction probabilities at thermal conditions ($T_{surf} = T$) between 300 - 1,500 K for $\theta_v = 0°$ and 45° are presented in figure 3.63. As it was observed on previous results at low initial collision energies and normal incidence (figure 3.56), the reflection of the impinging atom is the predominant process observed, with an ER reaction probability of around the 10% - 30% at the studied temperatures. The rest of the processes can be considered negligible. Only, the desorption of the preadsorbed atom together with the reflection of the impinging atom must be considered at the higher temperatures (i.e., T = 1,500 K). The increment in

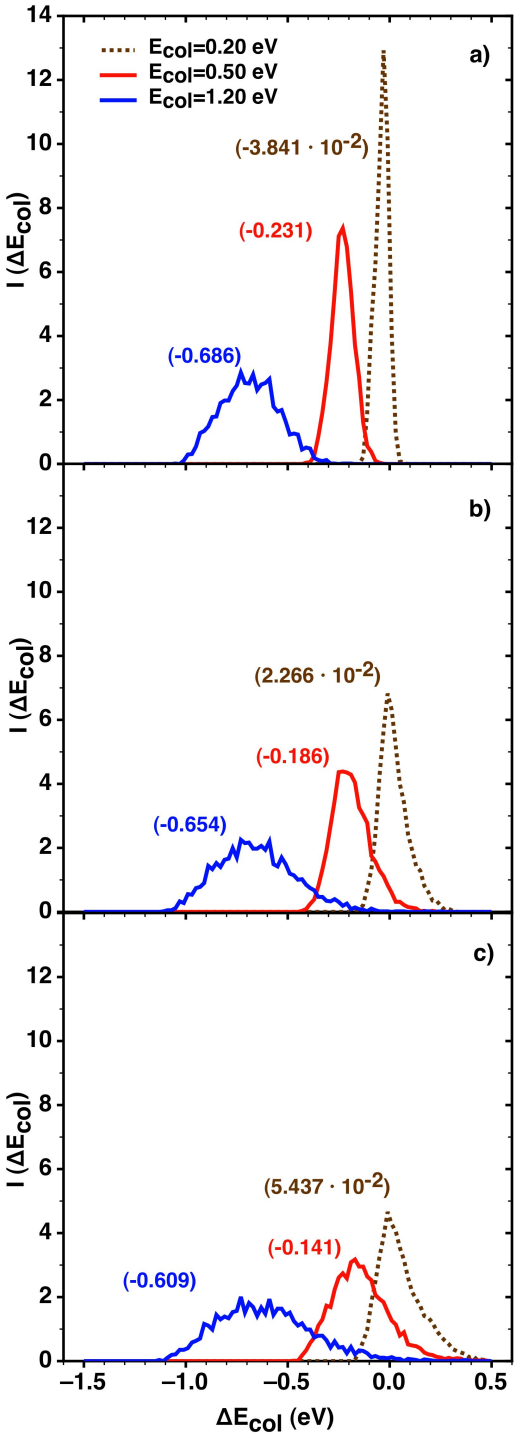

Figure 3.60: Energy exchange (ΔE_{col}) for reflection trajectories at initial $E_{col} = 0.2, 0.5$ and 1.2 eV and $\theta_v = 0°$ at a) $T_{surf} = 100$ K , b) $T_{surf} = 500$ K and c) $T_{surf} = 900$ K. Between parantheses are given the mean values ($\langle E_{col} \rangle$) in eV.

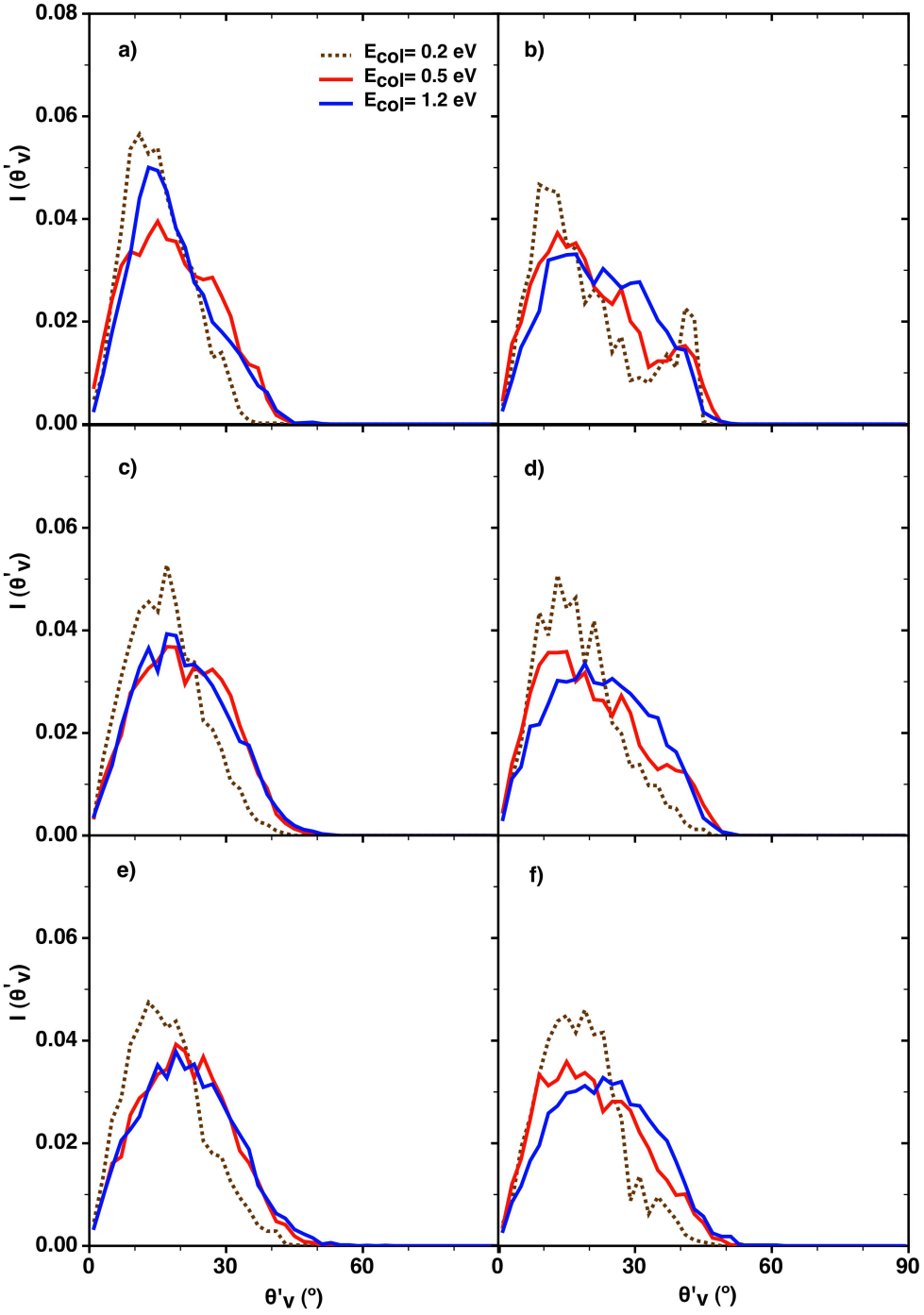

Figure 3.61: Final polar scattering angle distribution of ER formed O_2 molecules for normal incidence (left panels) and $\theta_v = 45°$ (right panels) at a) and b) $T_{surf} =$ 100 K, c) and d) $T_{surf} = 500$ K and e) and f) $T_{surf} = 900$ K.

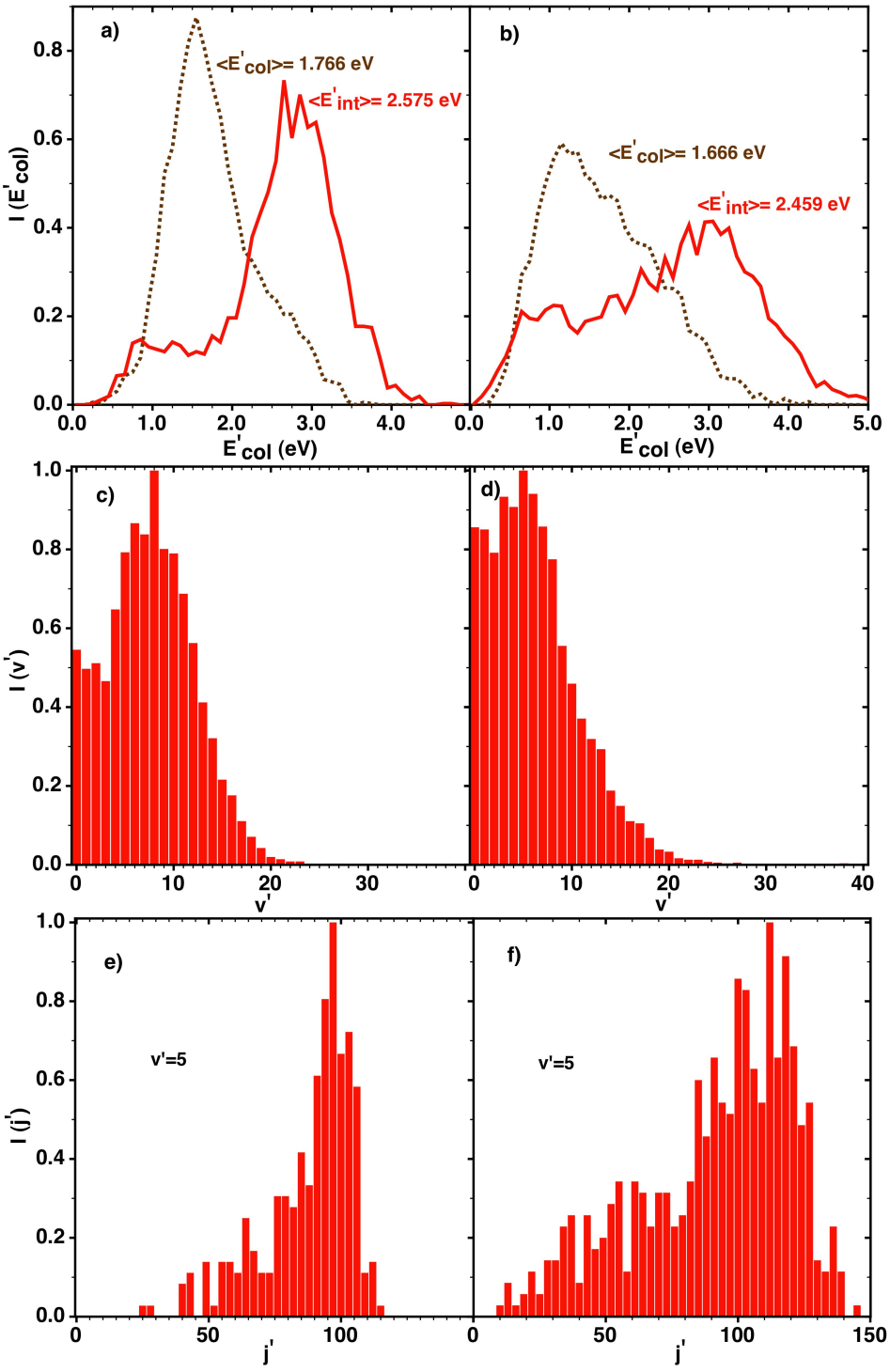

Figure 3.62: Final collision (translational) and internal energy of oxygen molecules formed via ER with normal incidence for initial a) $E_{col} = 0.2$ eV and b) 1.2 eV. Final vibrational distribution at c) $E_{col} = 0.2$ eV and d) 1.2 eV. Rotational distribution for a specific vibrational state ($v^{'} = 5$) at e) 0.2 eV and f) 1.2 eV. $T_{surf} = 500$ K.

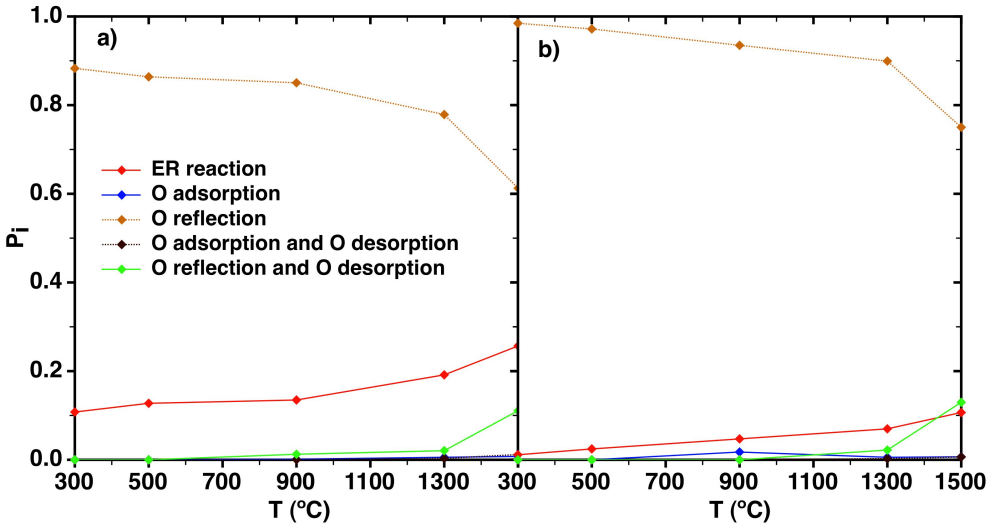

Figure 3.63: QCT reaction probabilities for the incoming oxygen atom interacting with a O precovered surface at different temperatures for initial a) $\theta_v = 0°$ and b) 45°.

desorption probability of preadsorbed atom goes together with a decrease of the process where the impinging atom reflects whereas the other remains adsorbed. Thus, it can be considered that the desorption at $T = 1,500$ K is due to the thermal surface energy, which provides to the preadsorbed atom the energy necessary to desorb and leave the surface. Off normal calculated probabilities are also consistent with the probabilities obtained at low initial collision energies.

Scattering angles of the impinging atom for the O_2 formed molecules via ER and for O desorbed atoms are plotted in figure 3.64 for thermal conditions. The scattering angles observed for normal and off normal incidence at the three temperatures plotted show similar trends that can be observed at state specific conditions (figure 3.61) for O_2 (figure 3.58) and reflected O (figure 3.61) atoms. The angular distribution for desorbed atoms appears at lower angles than for reflected atoms at both $\theta_v = 0°$ and 45° conditions.

The energy exchange between the impinging atom and the surface was analysed comparing the final collision energy of the scattered atom with its initial collision energy. In figure 3.65 it can be seen that for three plotted temperatures the mean of the increment on the energy is positive. Thus, the impinging atom is gaining translational energy, which must be given by the surface. The effect of the temperature can also be observed not only in the mean values but also on the shape of distributions, which are wider as higher is the temperature. The final energy of the formed molecules via ER was also studied by plotting the final translational and internal (vibrational and rotational) energy of the O_2 molecule

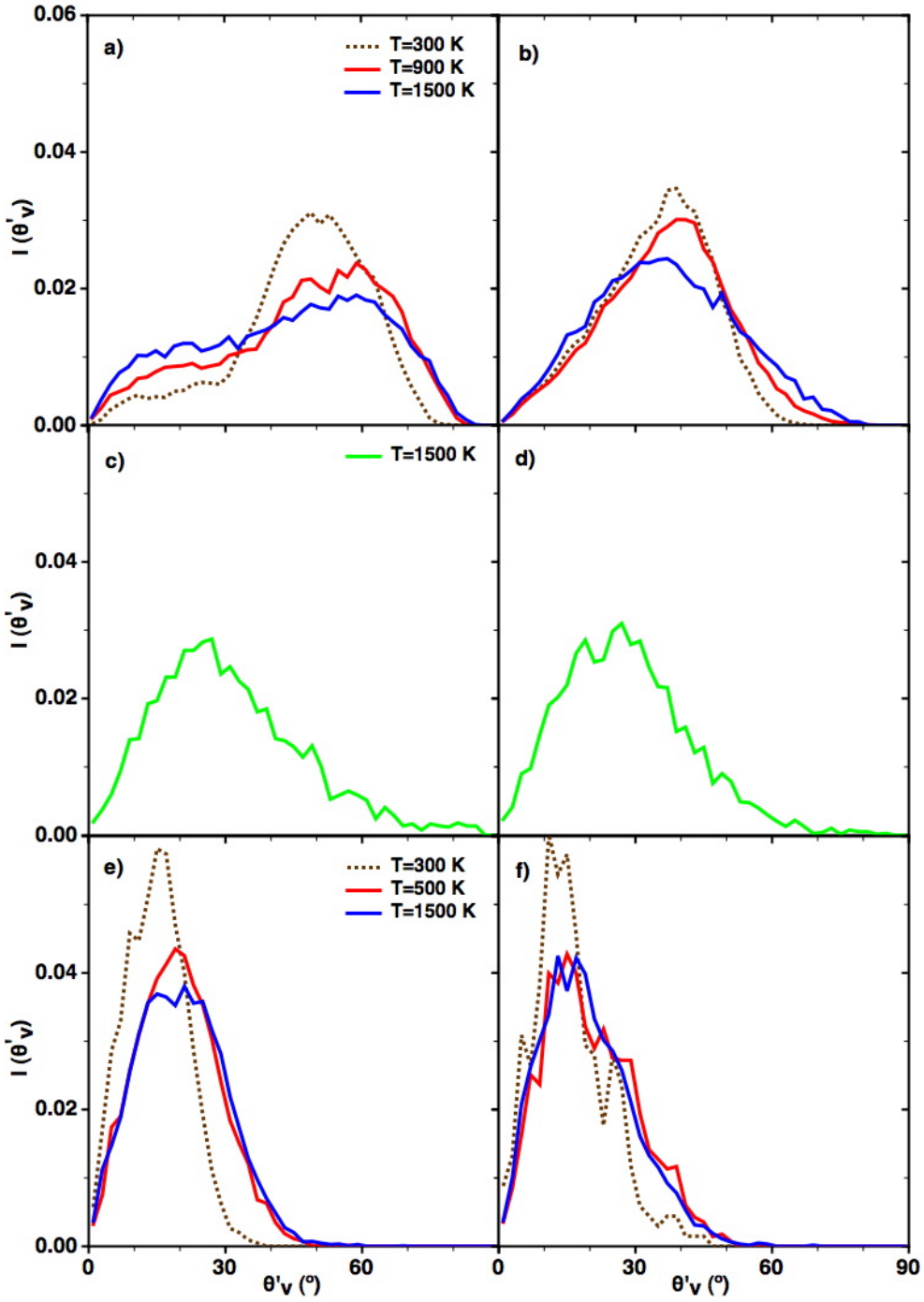

Figure 3.64: Scattering angle for reflected atomic oxygen at a) $\theta_v = 0°$ and b) $\theta_v = 45°$. Scattering angle of desorbed oxygen atoms at c) $\theta_v = 0°$ and d) $\theta_v = 45°$. Scattering angle of formed oxygen molecules via ER at e) $\theta_v = 0°$ and f) $\theta_v = 45°$.

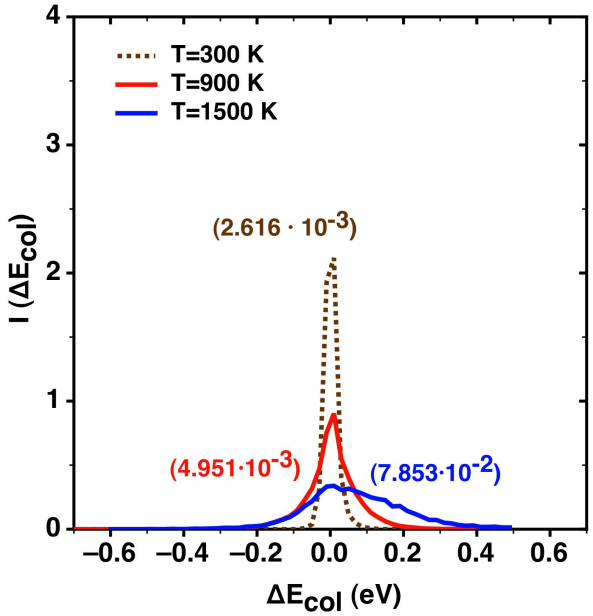

Figure 3.65: ΔE_{col} for reflected trajectories at $\theta_v = 0°$ and several temperatures. Between parentheses are given the mean values ($\langle E_{col} \rangle$) in eV.

in figure 3.66. If the mean energies for these distributions are compared at the same temperature it can be deduced that molecules are internally more excited than translationally. The increase of temperature produces a major translationally and internally excitation of O_2 molecules possibly due to the increase of the surface temperature, as the increase in the collision energy was shown that had a small effect (figure 3.62).

•Hyperthermal conditions

The effect of a preadsorbed atom on the scattering angle for state specific conditions was shown previously in this section. In order to analyse the possible effect in experimental results of Paci et al. (71), a batch of 30,000 trajectories was calculated and analysed for the experimental hyperthermal distribution of the colliding atom when T_{surf} = 503 K and θ_v=45°. The comparison with the results obtained for atomic oxygen scattered over a clean graphite surface (figures 3.67 and 3.39) shows that the presence of an oxygen preadsorbed shifts the peak of the distribution at lower angles and broadens it. (71). The experimental one resembles more the case with a clean surface possibly because the low coverage in the experimental conditions, although both QCT distributions are too broad. The O_2 molecules formed show angular distribution at much lower angles (peak

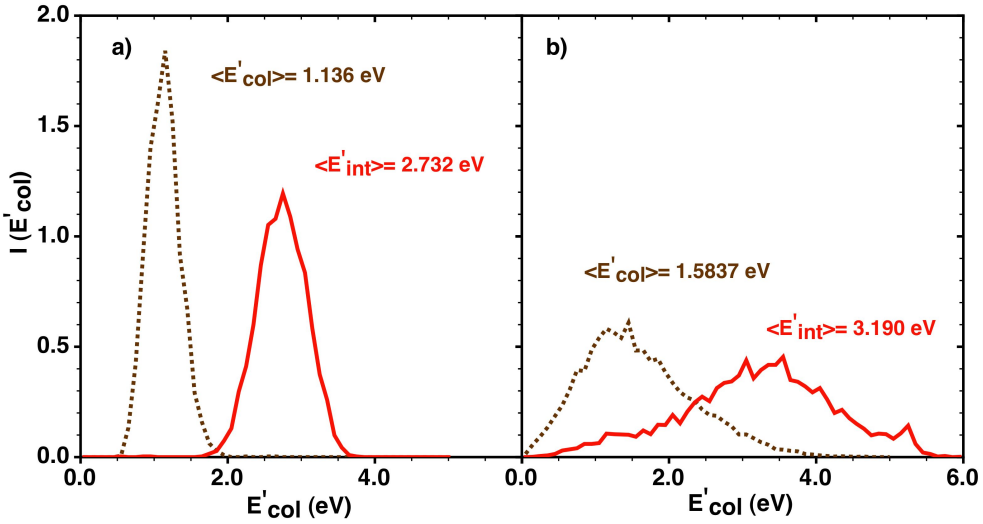

Figure 3.66: Final translational (E'_{col}) and internal (E'_{int}) energy of oxygen molecules formed via ER reaction at a) $T = 300$ K and b) $T = 1,500$ K.

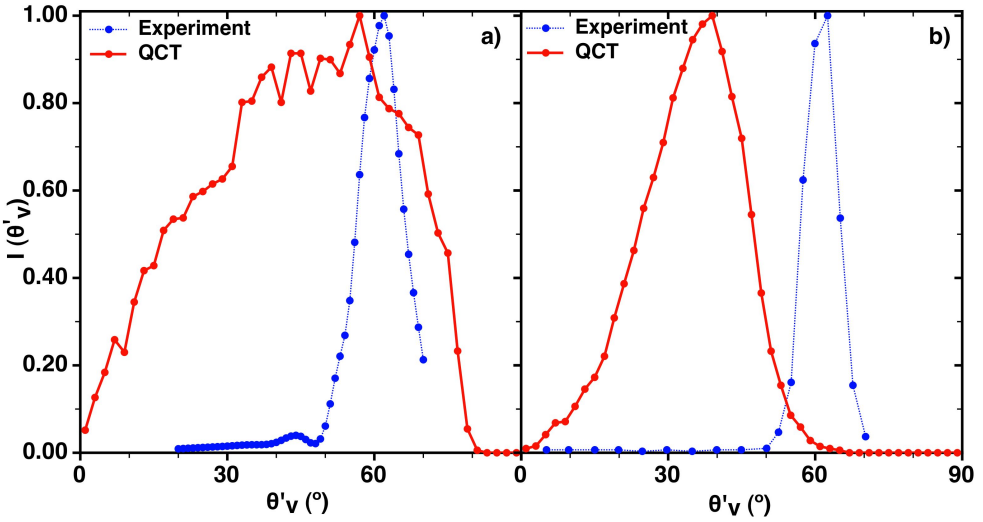

Figure 3.67: Theoretical and experimental (71) distributions of polar scattering angle of a) reflected atomic oxygen and b) ER O_2 formed molecules for a hot (hyperthermal) beam and an incident angle of $\theta_v = 45°$ and $T_{surf} = 503$ K.

at $\sim 40°$) close to the specular angle while the experimental is around 60°. Nevertheless, the experimental values correspond to an initial O_2/O flux impinging the surface and therefore measured O_2 distribution will give the two possible contributions: a) O_2 formed via ER reaction and b) initial O_2 that is scattered. In the next section the second contribution will be shown.

3.7.2 Molecular oxygen QCT collision study

3.7.2.1 Computational details

A dynamical study of the processes involving the interaction of the O_2 molecule with the graphite surface was done by means of the quasiclassical trajectory method. Several initial conditions were studied in order to investigate state specific and hyperthermal conditions. For state specific calculations initial collision energies for the center of mass of the molecule between 0.1 eV $\leqslant E_{col} \leqslant$ 2.0 eV were used for selected rovibrational levels (v=0-2, j=1,27). Initial molecular orientation angles (θ and ϕ, figure 2.1) were sampled by the standard Monte Carlo method, within intervals 0° - 180° and 0° - 360° respectively. Initial collision angles were selected at $\theta = 0°$ and 45° while the ϕ angle was randomly selected between 0° and 360°. Initial r distance was chosen between the corresponding inner (r_-) and outer (r_+) turning points of each O_2 (v, j) internal level. Only odd j initial levels were chosen for $O_2(X^3\sum_g^-)$ molecule because even rotational levels are unpopulated due to the nuclear spin of O^{16} is zero (119). These conditions were explored with and without surface temperature (100 $\leqslant T_{surf} \leqslant$ 900 K). Finally, an hyperthermal initial distribution emulating experimental studies from Paci et al. (71) was also studied using a surface temperature of 503 K.

Initial position of the molecule center of mass X_{cm} and Y_{cm} is randomly selected in the (1×1) unit cell, and Z_{cm} was set at 7.5 Å, where the interaction with surface is negligible. Quasiclassical trajectories were run with *qctsurf* code as previous studies.

Five possible exit channels were considered to classify the reactivity of the system: molecular adsorption, molecular reflection and molecular dissociation producing several gas or adsorbed atoms ($O_{(g)} + O_{(g)}$, $O_{ad} + O_{(g)}$, $O_{(g)} + O_{ad}$). The O_2 molecule was considered to be formed when r is lower than 2.0 Å and dissociated over 3.0 Å. The maximum adsorption distance from surface for both atoms and molecule is set at 2.2 Å for both Z_O and Z_{cm}. With more than 8 rebounds with the surface. The minimum distance for reflection was set at 7.6 Å and the direction of the velocity vector should be pointed to the vacuum.

Batches of a minimum of $N_T = 10,000$ trajectories were run at each condition. Statistical errors were very low as all computed trajectories at all conditions lead only to molecular reflection.

3.7.2.2 Dynamical study

•Without surface temperature

Batches of quasiclassical trajectories were run for state specific conditions where the initial internal molecular state was fixed (v = 0 - 2, j = 1 - 27) as the initial collision energy for the center of mass of the molecule between 0.1 eV $\leqslant E_{col} \leqslant$ 2.0 eV at initial $\theta_v = 0°$ and 45° when surface temperature is not taken into account. From all possible processes only molecular reflection is observed at all studied conditions. Thus, the effect of the initial translational energy and the internal vibrational and rotational energy on the scattering angle (θ_v') of the molecules is plotted in figure 3.68. Molecular scattering angles for normal incidence ($\theta_v = 0°$) are observed at low values around 10° and 20° while for off normal incidence the scattering angles have a peak at around $\theta_v' = 45°$. The influence of the initial collision rotational or vibrational energy on the final angle is negligible as can be observed in the plotted results.

The analysis of the final molecular internal and translational energies reveals that no excitation of the vibrational modes is observed. Certain loss of translational energy is observed while the rotational motion increases for all studied cases. The final state of the molecule will be discussed below, when surface temperature is taken into account.

•With surface temperature

The effect of surface temperature in the molecular scattering angle distribution and final internal state of the molecule is analysed. The polar scattering angle distribution is plotted for normal incidence at two surface temperatures in figure 3.69 for several initial collision energies and vibrational and rotational states. Scattering angles observed for normal incidence at initial internal state of (v=0, j=1) are small (figure 3.69a and b). In general, a peak is observed at around 10° (a bit shifted for higher E_{col}) although distributions are wide and some molecules can be observed at a scattering angles close to 60°. Surface temperature and vibrational or rotational excitation practically do not affect these distributions.

Figure 3.70 presents the calculations for off normal incidence. Again the behaviour respect the surface temperature and (v, j) increment is the same and negligible. The main difference is the shift of the maximum at higher angles, although the peaks are a bit higher than the specular value (e.g., 50° at low collision energies or 60° at higher ones).

The different types of energy exchange during the molecular collision (internal, translational and total energy) are plotted at three initial collision energies ($v = 0$, $j = 1$) and normal incidence at two surface temperatures (T_{surf} = 100 K and 900 K) in figure 3.71. In general, collision energy is lost during the interaction process although at higher temperatures some intensity of the distribution can

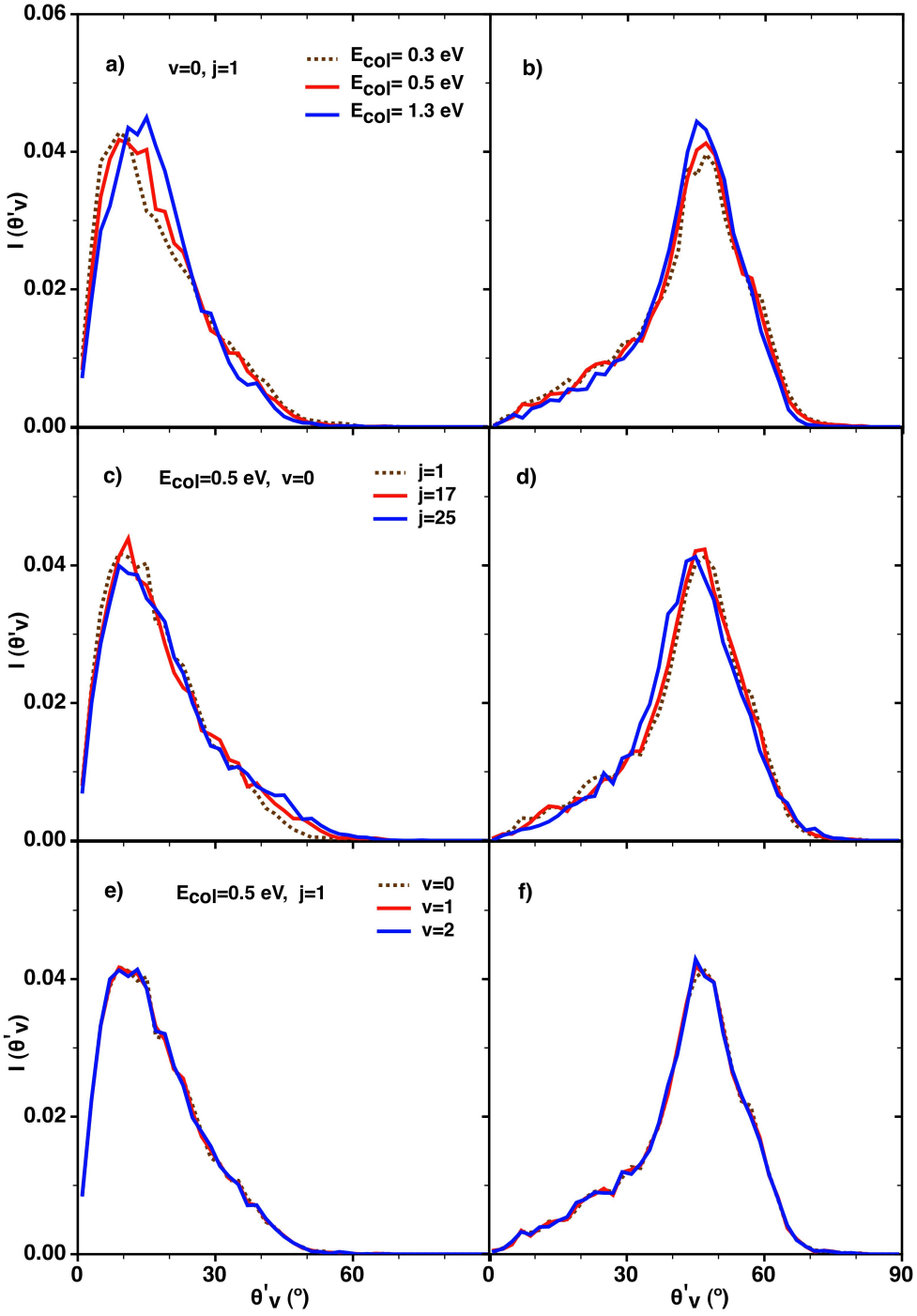

Figure 3.68: Polar scattering angle distributions for O_2 collisions with normal incidence (left panels) and $\theta_v = 45°$ (right panels) at different initial conditions.

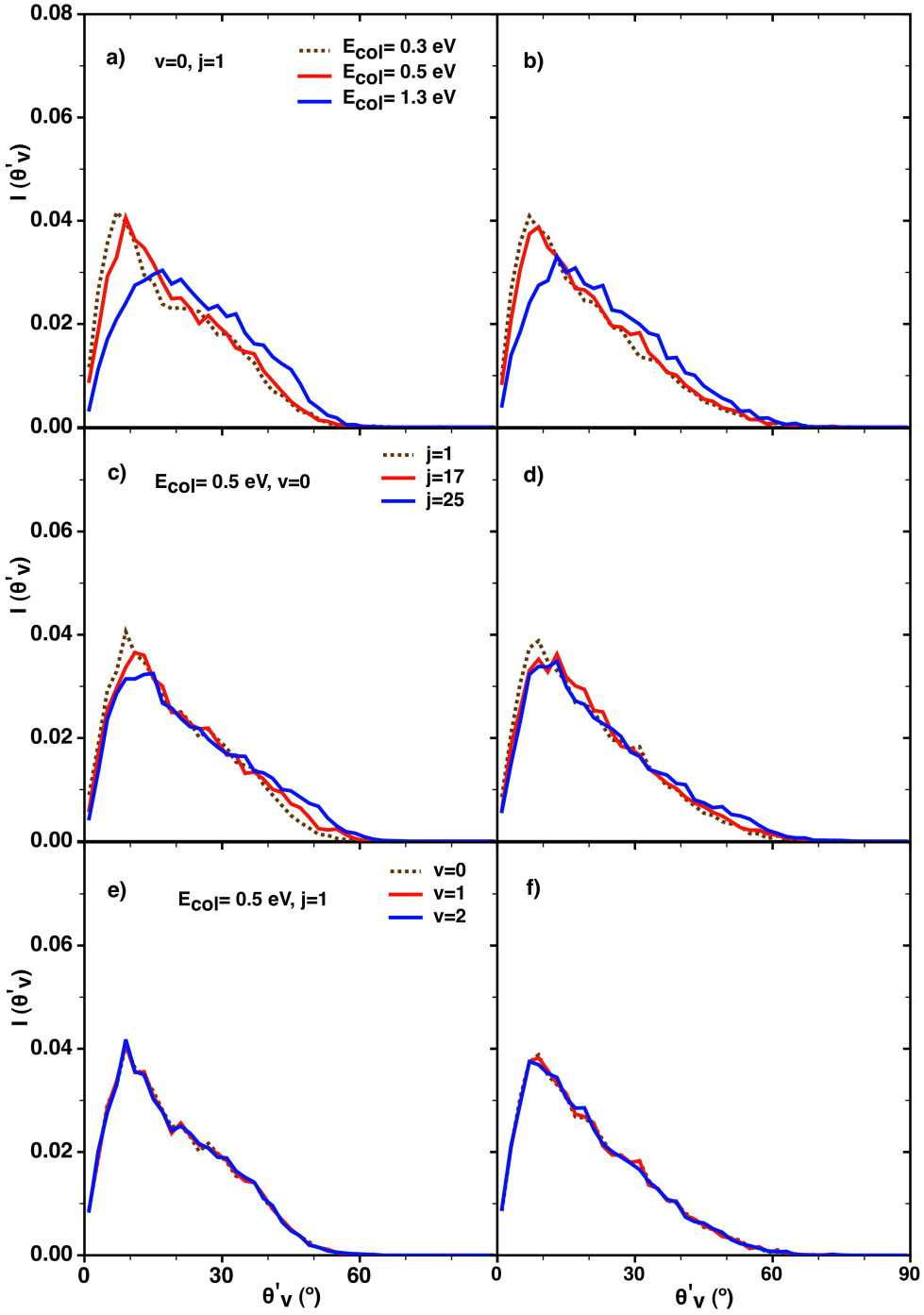

Figure 3.69: Polar scattering angle distributions for O_2 collisions with normal incidence at T_{surf}= 100 K (left panels) and 900K (right panels) at different initial conditions.

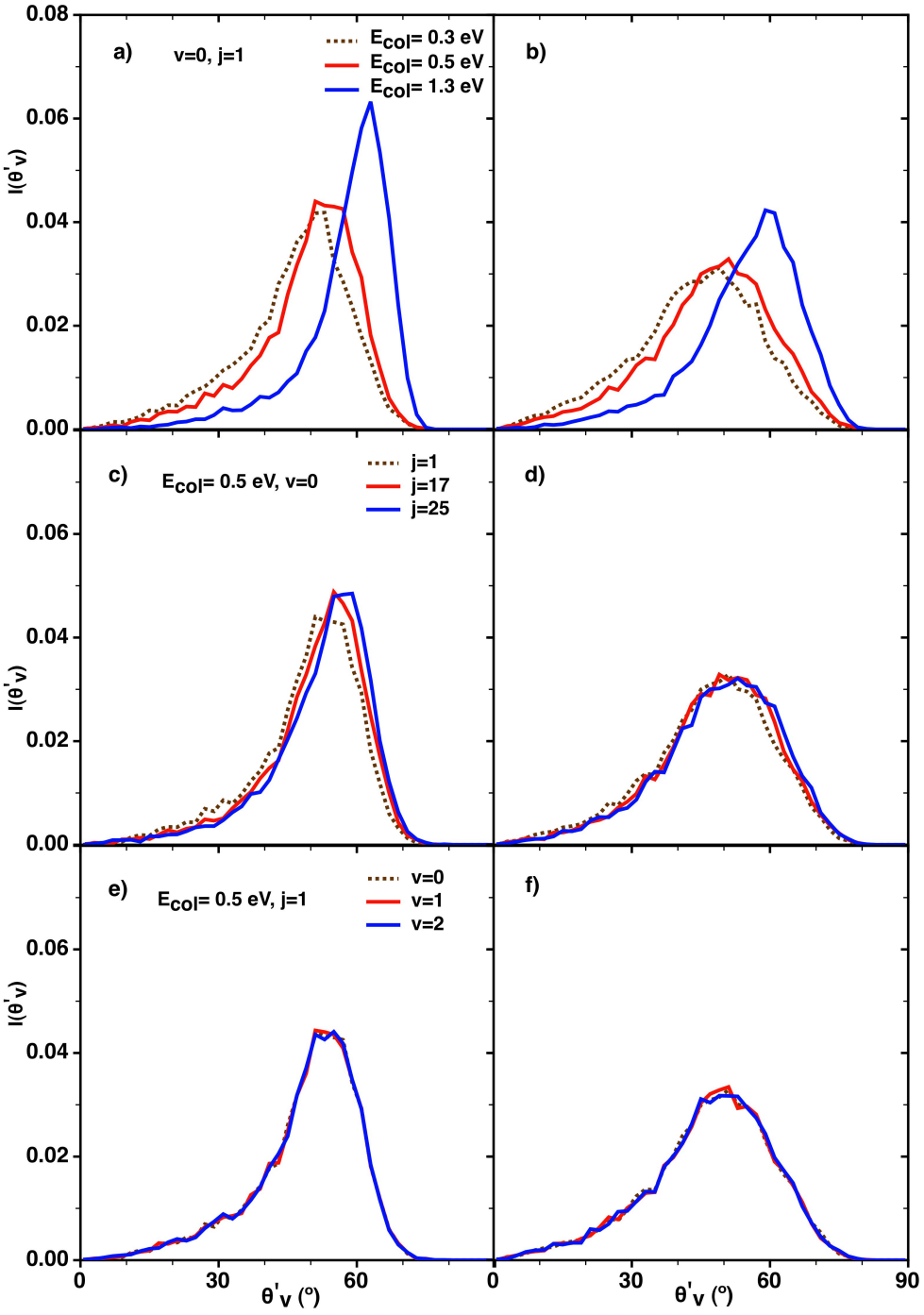

Figure 3.70: Polar scattering angle distributions for O_2 collisions with off normal incidence at T_{surf}= 100 K (left panels) and 900K (right panels) at different initial conditions.

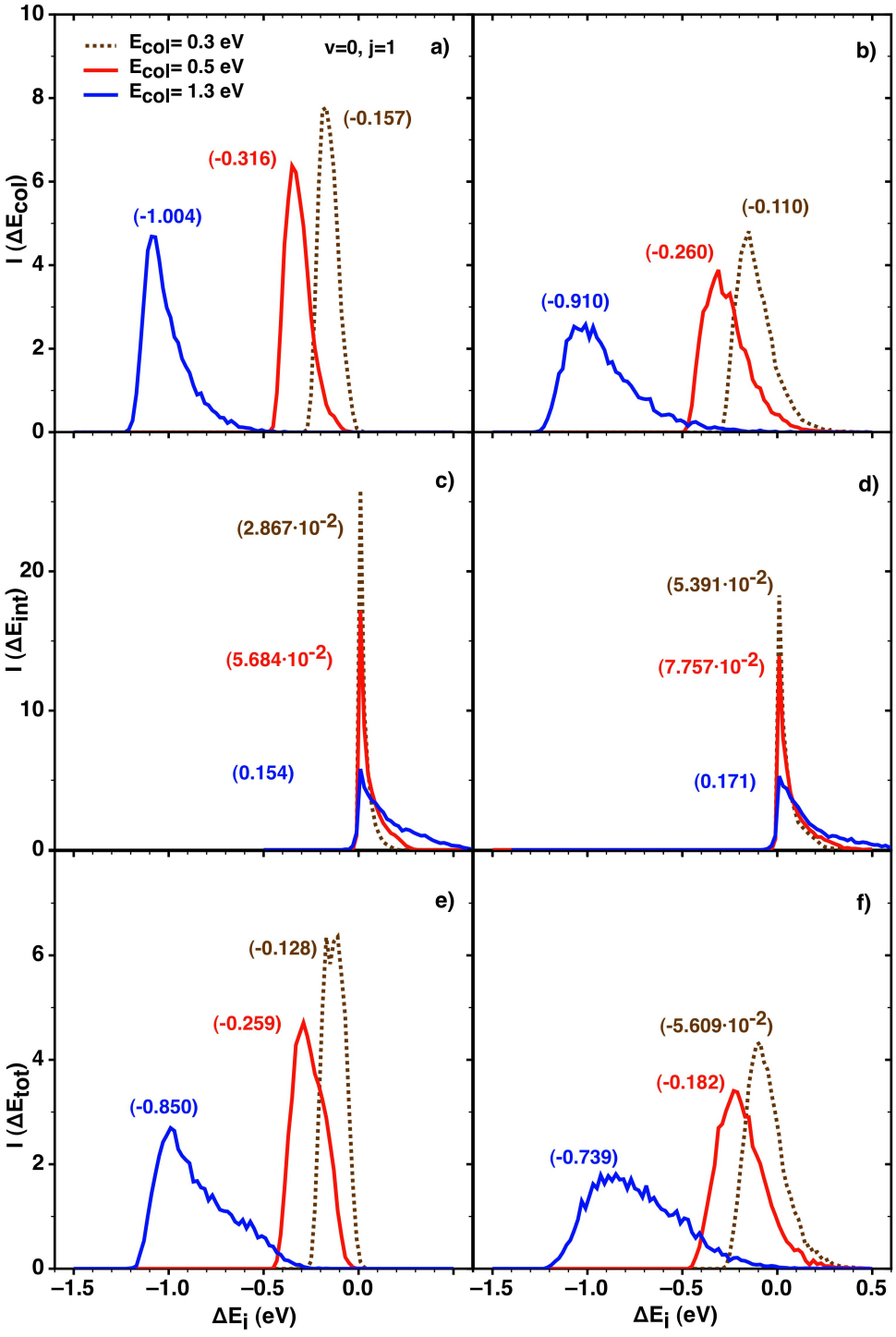

Figure 3.71: Energy exchange for reflected trajectories with normal incidence at T_{surf} = 100 K (left panels) and 900K (right panels) at different initial conditions. With a), b) E_{col}, c), d) ΔE_{int} and e), f) ΔE_{tot}.

be observed at positive values. Some of the initial collision energy is going to the excitation of internal states as can be seen in the positive values of the internal energy exchange. This increment is slightly higher when the surface temperature is increased. Nevertheless, the excitation of internal states of the molecule is not gaining all the collision energy lost during the trajectory. Thus, as it can be seen in the total energy exchange distributions, a big part of the energy is transferred to the surface. Only at the higher temperatures explored, and at lower collision energies a small intensity is observed at positive values of total energy, showing a transference of energy from the surface to the molecule.

•Calculations for experimental conditions

To complete the simulation of experimental result of Paci et al. (71), the polar scattering angle distribution of the oxygen molecule for an hyperthermal initial collision energy distribution of the molecule is analysed. For that purpose, batches of 30,000 trajectories were run for an initial incident angle of $\theta_v = 45°$. Surface temperature was set to $T_{surf} = 503$ K as in the experimental conditions. The initial internal state of the oxygen molecule was fixed to v=0 and j=1 as the effect in the scattering angle due to the initial vibrational and rotational state is negligible. The results are presented in figure 3.72 along with the experimental distribution of molecular scattering angles. The theoretical results obtained show

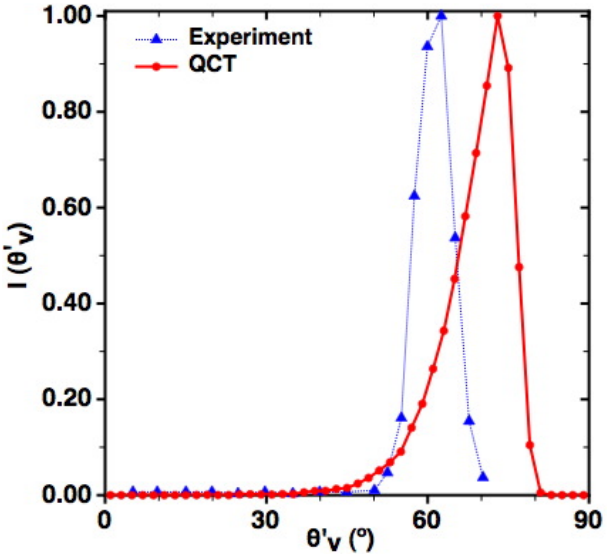

Figure 3.72: Theoretical and experimental (71) distributions of polar scattering angle of reflected molecular oxygen for a hot (hyperthermal) beam and an incident angle of $\theta_v = 45°$ and $T_{surf} = 503$ K.

a narrow distribution as it is also observed in the experimental ones, although the peak is displaced ∼10° at higher scattering angles than the obtained in the experiment. As was mentioned before, the scattered molecules observed in the experiment could come from the molecular scattering of the initial O_2 molecules of the beam and from the O_2 formed molecules via ER. The latter case produces a wider distribution peaked at much lower scattering angles (figure 3.67b). In order to have an idea of the theoretical profile that could be obtained for the scattering angles when considering both processes, a ponderate mixture of the results presented here and in section 3.7.1.2 was done and is plotted in figure 3.73. The mixture of both populations is averaged to the total intensity expected from

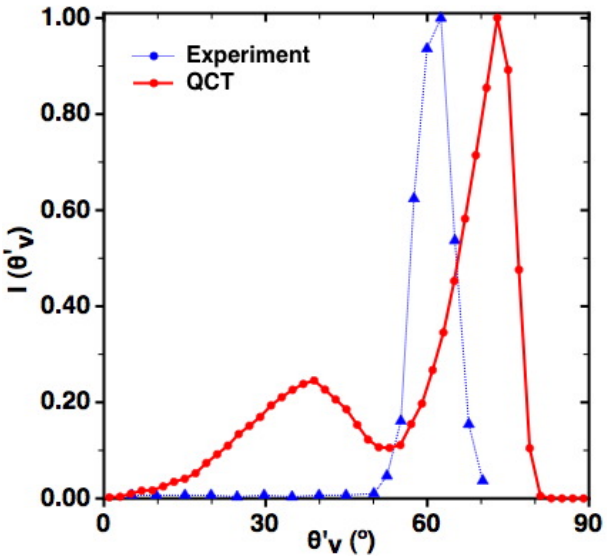

Figure 3.73: Theoretical and experimental (71) distributions of polar scattering angle of reflected molecular oxygen and ER O_2 formed molecules for a hot (hyperthermal) beam and an incident angle of $\theta_v = 45°$ and $T_{surf} = 503$ K.

each of the processes giving O_2. As the initial composition of the experimental beam flux is formed by a ratio of 0.48 for O_2/O and the computed probability of ER reaction at experimental conditions is 43.1%, the scattered O_2 will have a contribution with a factor of two compared with the O_2 formed via ER reaction. Thus, the total area of the distribution will be formed by a contribution of the scattered O_2 twice the contribution of the formed O_2 via ER. The peak of the final distribution and the experimental one are normalised to the unit. The distribution for the theoretical calculations is not consistent with the experimental one for this estimation of both competing processes. In the former, two peaks are observed, each one of them corresponds clearly to one of the processes producing the O_2 (i.e., ER reaction and O_2 scattering), while the experimental shows a single

peak. However, the coverage of the surface is probably much higher in simulations than in the experimental conditions, as in the experiment the surface is heated and low surface coverage is expected. Thus, in the theoretical distribution the peak observed for the ER contribution is quite important. This result suggests that probably in the experiment the ER reaction will not be as important as supposed.

As the initial collision energies are high enough for the dissociation of the O_2 molecule, reaction probabilities were analysed. Dissociation probability was lower than a 0.1% even if initial collision energies were in general higher than 9 eV. In order to understand the low dissociation probability, the increment of the translational, internal and total energy was plotted for O_2 molecules and presented in figure 3.74. The distribution of final vibrational states of the scattered molecules is also plotted. The increase of total energy in the scattering process is negative,

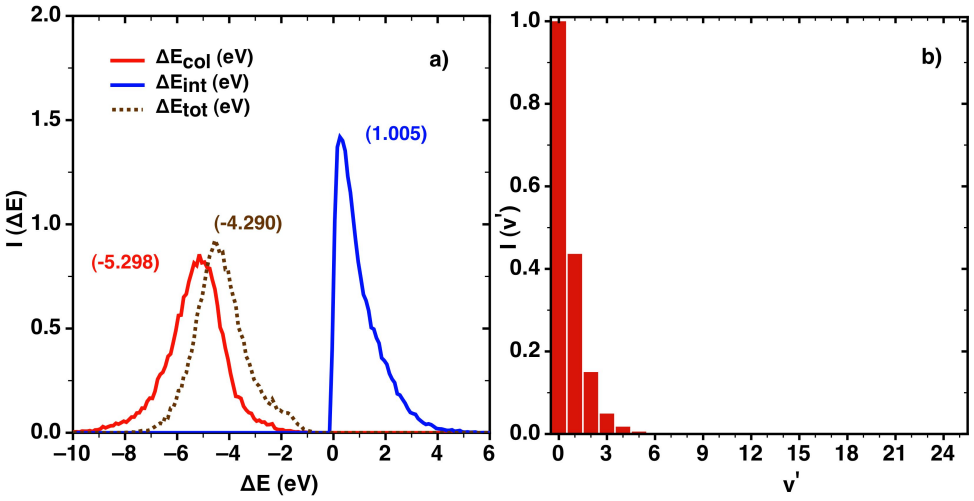

Figure 3.74: a) Energy exchange (internal, translational and total) for hyperthermal (experimental) initial beam of oxygen molecules at $T_{surf} = 503$ K, $\theta_v = 45°$ and b) final v' state for the corresponding scattered molecules.

which means that the molecule is losing part of its initial energy. In addition, internal energy is increasing considerably as it can be observed in the figure, where the distribution arise until a value of 4.0 eV. The analysis of the vibrational final modes shows that the internal energy gained by the molecule is not converted to enough vibrational energy for the molecule to become dissociated.

Some molecular oxygen beam scattering experiments from Oh et al. (72) were also simulated. In this experiment, the initial θ_v angle for the incident oxygen molecules were varied between 10° and 60° and the scattered molecules were detected only in the direction where the condition $\theta_v + \theta_v' = 90°$ was accomplished.

Several surface temperatures from 150 to 500 K and initial collision energies from 0.291 to 0.614 eV were studied. Thus, calculations where run for each specific surface temperature and initial collision energy, choosing randomly $10^\circ \leqslant \theta_v \leqslant 70^\circ$. For each set of initial collision angles within intervals of one degree, the number of trajectories, where the scattering angle fulfils the restriction above mentioned was referred to the total of initial trajectories in the set. The representation of the intensities at each given final scattering angle for several initial collision energies and surface temperatures are plotted in figures 3.75 and 3.76.

Distributions presented show good agreement with experimental results obtained by Oh et al. (72) for both peak position and full width at half maximum (fwhm). The peak position dependence with initial collision energy (figure 3.77) is smaller than the experimental one. However, if the scale of the graph is considered, differences are very small. The differences found for the fwhm are also very small although in the experiment the distributions observed are slightly narrower.

In the published work by Oh et al. (72), it is suggested from the results, that the translational energy of the molecules is reduced by the collision with the graphite surface. This fact was already studied above in this text with similar results. It is said that the energy loss becomes smaller at higher surface temperatures which was also deduced from the results presented previously in this section. The amount of energy loss is calculated at the specific conditions, where the distribution peaks are found. Thus, for each E_{col} and T_{surf} the initial angle that leads to the distribution peak is found using the experimental restrictions ($\theta_v + \theta_v^{'} = 90^\circ$). Results are listed in table 3.18 together with the theoretical results obtained in the bibliography by means of the Hard Cube Model (HCM (120)). Although the loss of energy calculated by the HCM is always higher than the calculated in this work, the tendency with temperature and initial collision energy is in agreement and the difference found between both is not higher than a 15%.

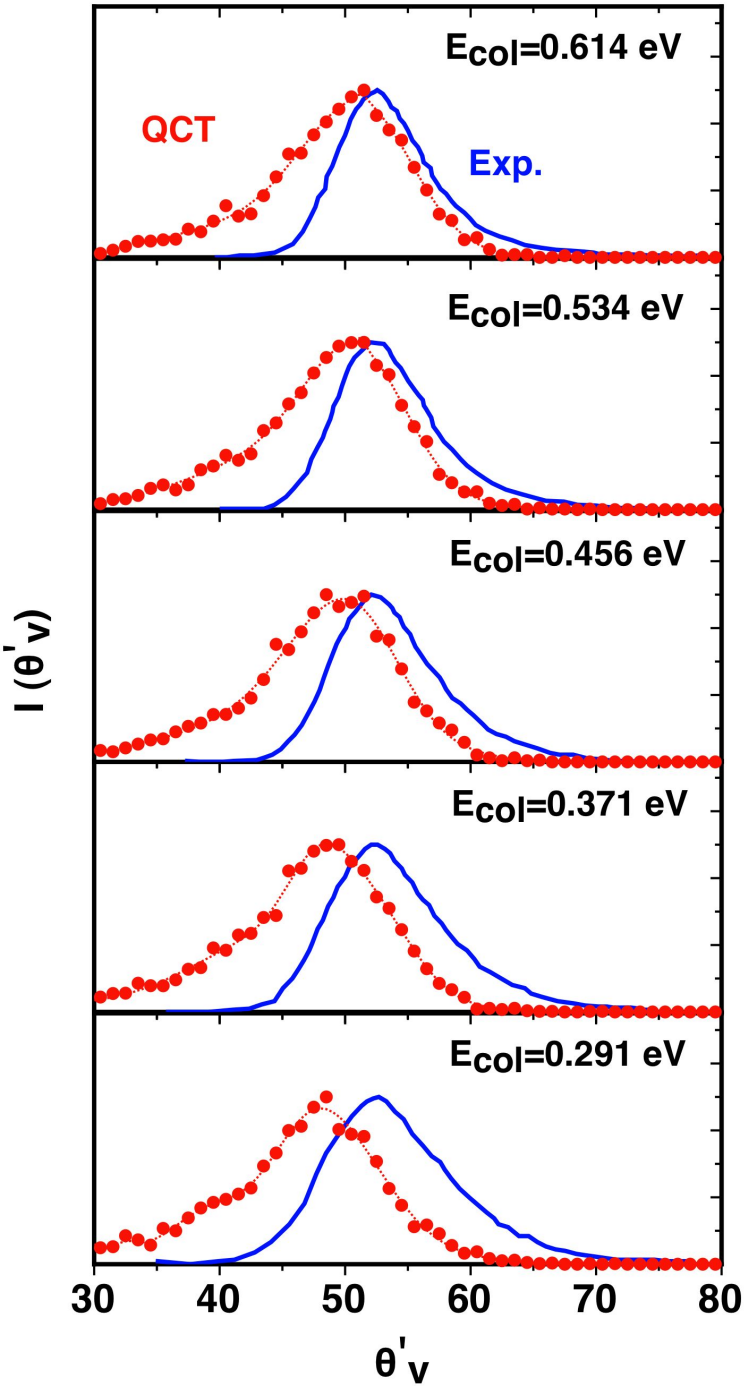

Figure 3.75: Incident energy dependence of the angular intensity distribution of oxygen molecules scattered from the graphite surface; comparison of theoretical QCT calculations (red) with experimental (blue) results (72) at different collision energies, T_{surf}= 150 K and $10^\circ \leqslant \theta_v \leqslant 70^\circ$.

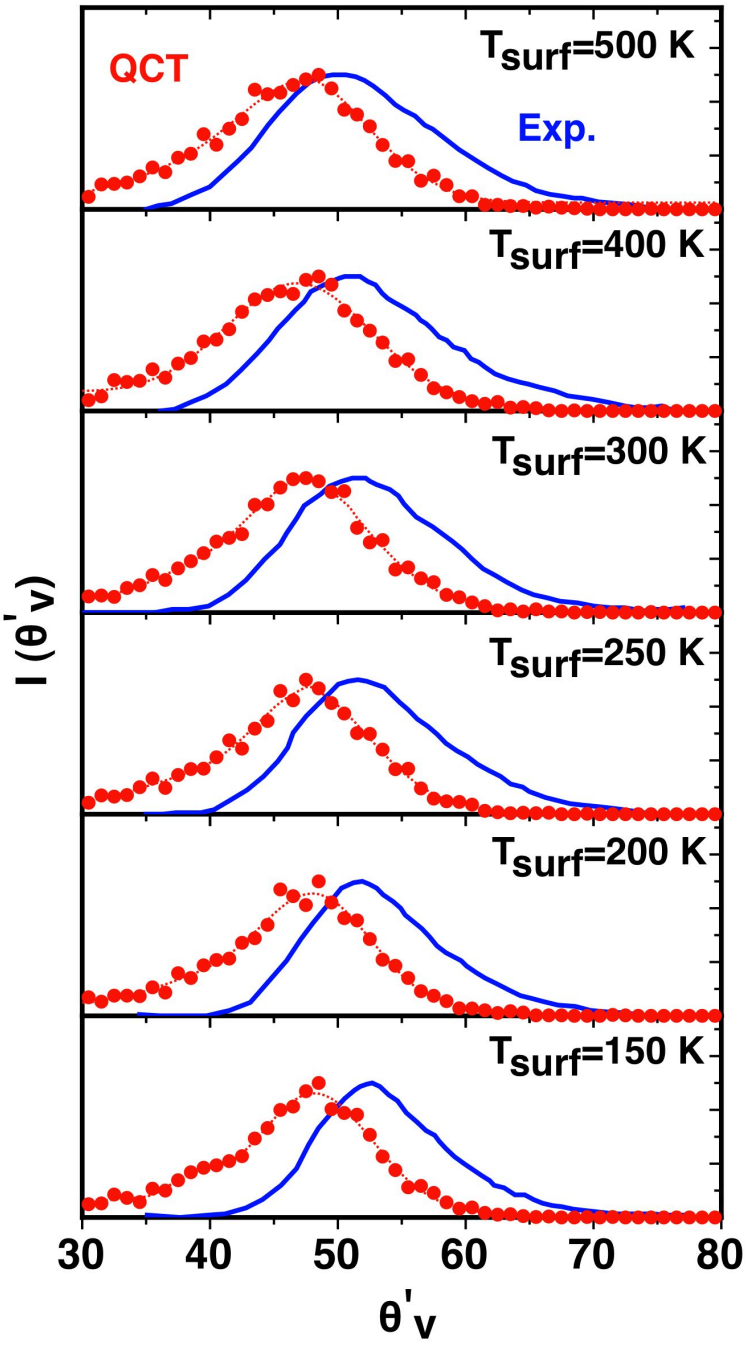

Figure 3.76: Incident energy dependence of the angular intensity distribution of oxygen molecules scattered from the graphite surface; comparison of theoretical QCT calculations (red) with experimental (blue) results (72) at different T_{surf}, E_{col}= 0.291 eV and $10^\circ \leqslant \theta_v \leqslant 70^\circ$.

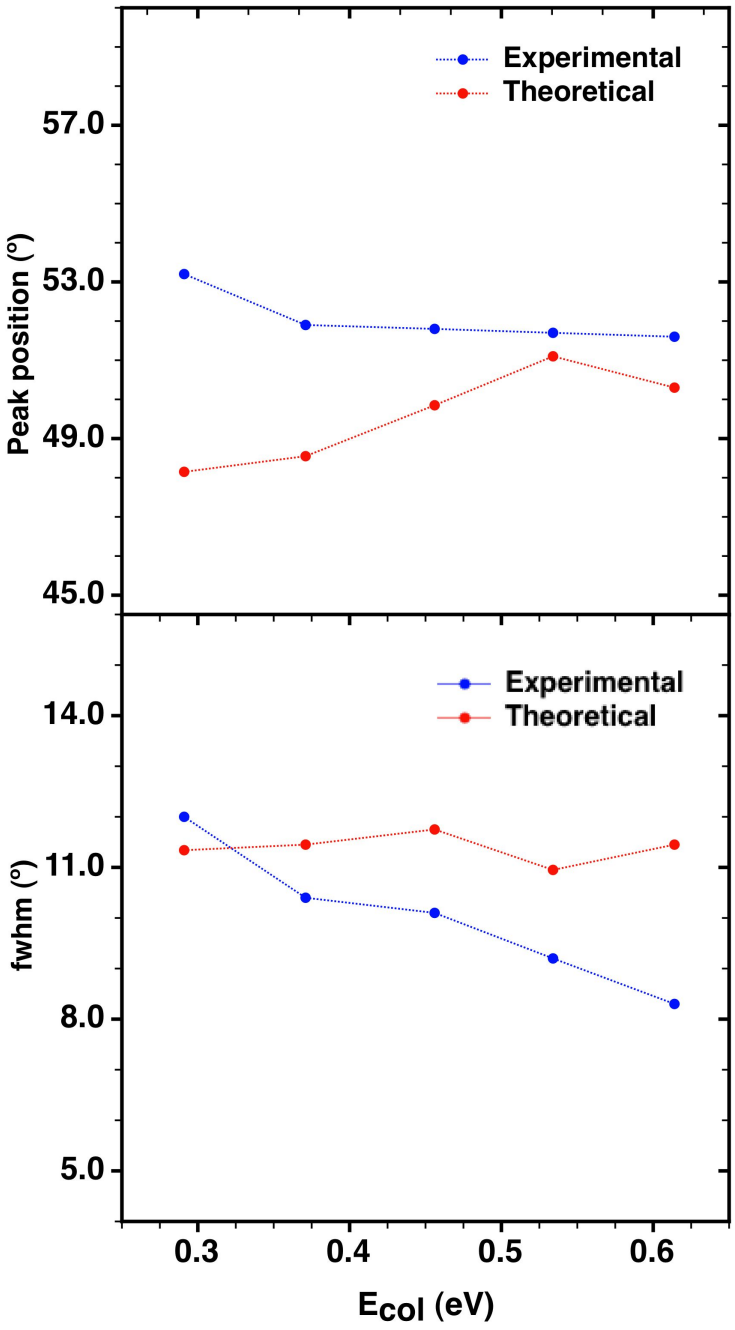

Figure 3.77: Collision energy dependence of the peak and fwhm of the angular intensity distribution of oxygen molecules scattered from the graphite surface; comparison of theoretical QCT (red) calculations with experimental results (blue) at $T_{surf} = 150$ K, $10° \leqslant \theta_v \leqslant 70°$.

Table 3.18: Energy loss results for studied conditions of temperature and initial collision energy for results (HCM) obtained in bibliography (72) (marked by *) and calculated ones in this work.

	T_{surf} (K)	E_{col} (eV)	$\theta_v^*(^\circ)$ [a]	$\theta_v^{'*}(^\circ)$	ΔE^* (%)	$\theta_v(^\circ)$	$\theta_v^{'}(^\circ)$ [a]	ΔE [b] (%)
E_{col} fixed	150	0.291	37.6	52.4	-41	42	48	-27.9
	200	0.291	38.1	51.9	-39	42	48	-27.4
	250	0.291	38.4	51.6	-37	42	48	-27.4
	300	0.291	38.6	51.4	-36	42	48	-26.7
	400	0.291	39.2	50.8	-34	43	47	-25.1
	500	0.291	40.0	50.0	-30	43	47	-19.7
T_{surf} fixed	150	0.291	37.6	52.4	-41	42	48	-27.9
	150	0.371	37.7	52.3	-40	41	49	-32.1
	150	0.456	37.7	52.3	-40	40	50	-37.6
	150	0.534	37.6	52.4	-41	39	51	-39.9
	150	0.614	37.6	52.4	-41	40	50	-39.9

[a] *this angle corresponds to the maximum of the experimental or the calculated distribution.*

[b] $\Delta E_{total}(\%) = (1 - E_{tot}^{'}/E_{tot}) \times 100.$

Chapter 4

O/O_2 mixtures over β-Cristobalite (001) surface

4.1 Introduction

The interaction study of oxygen over a β-cristobalite (001) surface was started previously in our research group. Potential energy surfaces (PES) were constructed for the description of the interaction of one oxygen atom with a clean surface, for one oxygen with an O precovered surface and for the molecular collision over a clean surface. In this chapter the results for state specific dynamical QCT calculations for the Eley-Rideal (ER) reaction and O_2 collisions with the surface, using the previously constructed PES, are presented. However, in order to facilitate the comprehension, a small introduction to the DFT treatment as long as some details of the PES construction (i.e., ER reaction and O_2 collision processes) are given.

Some further thermal dynamical calculations of the atomic and molecular collisions over the β-cristobalite surface are used to determine reaction rate constants for several elementary heterogeneous processes occurring over the surface. Finally, this information is used for constructing a microkinetic model (121); the aim of which is to obtain an overall idea of the global effect of the different elementary processes taking place over the surface at the same time and thus evaluate theoretically the γ_O and β_O coefficients, which are really important for CFD simulations.

4.1.1 Preliminary results of oxygen interaction with β-cristobalite

For the interaction of oxygen over β-cristobalite DFT calculations were carried out by Arasa et al. (97). The calculations are based on the generalised gradient correction (GGA) functional Perdew-Wang 91 (PW91 (75, 76)) and the electron-ion interaction was described by using the projector-augmented-wave (PAW) technique (81, 82).

They found almost degenerate stability among the several polymorphs of the β-cristobalite (i.e.,$P2_13$, $F\bar{4}d2$, $F3dm$, ...), although $Fdd2$ was slightly more stable than others. Its 3D structure is presented in figure 4.1.

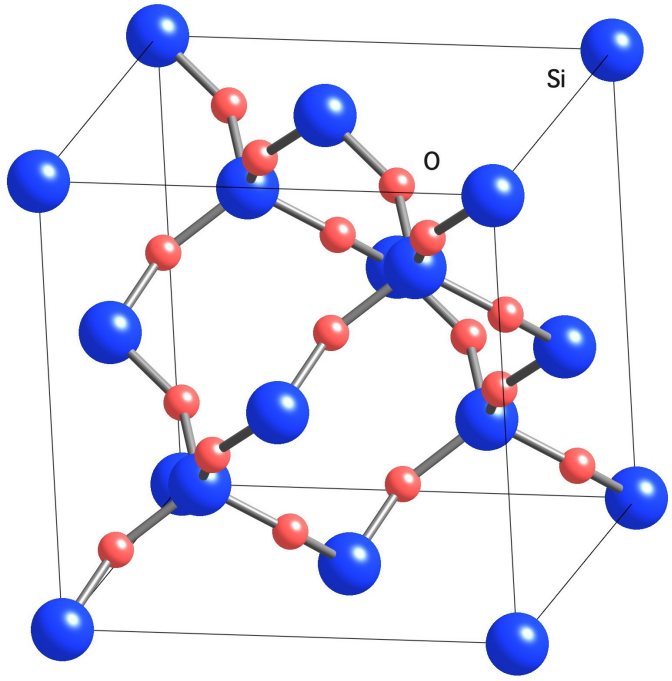

Figure 4.1: 3D view of the cubic β-cristobalite (Fdd2) unit cell.

DFT study showed that Si-finished slab model was the most stable and it was used for the PES construction. A summary of the atomic adsorption results for Si-finished β-cristobalite (001) surface over several sites (figure 4.2) is presented in figure 4.3. The data show several minima although only B1 and T1 are true minima (i.e., all the frequencies are positive). The adsorption energy for the most stable minimum (T1) is of -4.75 eV, although the analysis of the PES constructed for the system (122) allows the location of a slightly more stable minima ($T1''$, $T1'$) (table 4.1) very close to the T1 with an adsorption energy of -5.27 eV and -7.10 eV, respectively. The T1 sites are located over the outermost Si atom at a

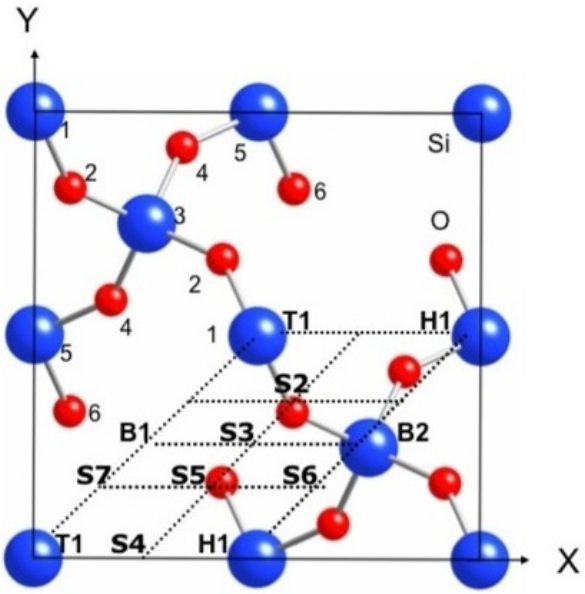

Figure 4.2: Top view of Fdd2 β-cristobalite (001) unit cell with the studied sites. Numbers indicate the surface layer.

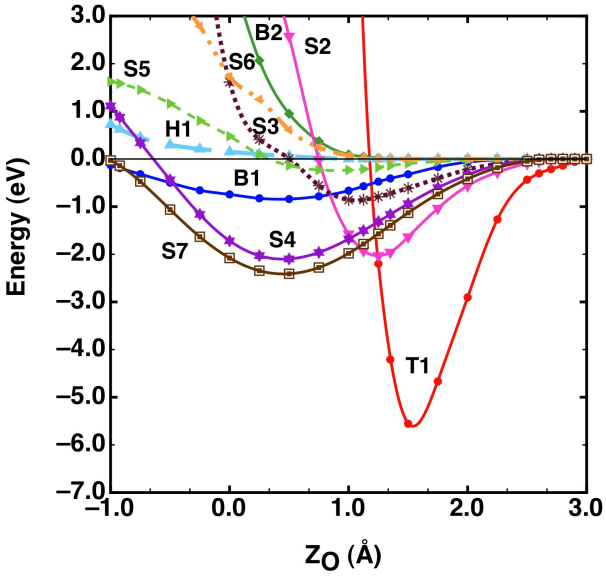

Figure 4.3: DFT potential energy for an O atom over different sites of a frozen β-cristobalite (001) surface as a function of Z_O distance to the surface (122). Lines are used to guide the eye.

Table 4.1: Relative energies of the main stationary points for the interpolated O_2/β-cristobalite PES.

	Energy (eV) [a]	d_{SiO} or d_{OO} (Å) [b]
O_{ad} (T1) + $O_{(g)}$	-4.75	1.527
O_{ad} (T1$''$) + $O_{(g)}$	-5.27	1.576
O_{ad} (T1$'$) + $O_{(g)}$	-7.10	1.551
$O_{2(ad)}$ + slab	-8.87	1.803
$O_{2(g)}$ + slab	-6.11	1.221

[a] *Zero of energies at $2O_{(g)}$ + β-cristobalite slab.*

[b] *More information on O_{ad} minima can be found in (97, 122).*

Z_O distance of 1.527 Å. The T1$'$/T1$''$ sites are placed between the T1 and B1 sites and they describe an absorption since the oxygen atom tends to penetrate into de surface ($Z_O < 0$).

4.1.2 Some details of the PES for the two oxygen interaction with β-cristobalite

The PES for the ground electronic state of the O_2/β-cristobalite interaction system was constructed with the aim of studying the ER reaction between an incoming oxygen atom from the gas phase and a preadsorbed one, as well as for the molecular collision. The general expression is (101),

$$V\Big(X_{O_A}, Y_{O_A}, Z_{O_A}, X_{O_B}, Y_{O_B}, Z_{O_B}, \{R_{ij}\}\Big) = V^{slab}\Big(\{R_{ij}\}\Big) + \\ + V^{O_A-slab}\Big(X_{O_A}, Y_{O_A}, Z_{O_A}, \{R_{ij}\}\Big) + V^{O_B-slab}\Big(X_{O_B}, Y_{O_B}, Z_{O_B}, \{R_{ij}\}\Big) + \\ + V^{O_A-O_B}\Big(X_{O_A}, Y_{O_A}, Z_{O_A}, X_{O_B}, Y_{O_B}, Z_{O_B}, \{R_{ij}\}\Big) \quad (4.1)$$

which depends on the Cartesian coordinates of both oxygen atoms over the unit cell and on all internuclear distances $\{R_{ij}\}$ (i.e., Si-Si, O-O and Si-O) of the silica slab. The first term of the PES (V^{slab}) is the potential that describes the interaction among the atoms inside the slab. It is an empirical potential (123) derived for silica and silicate systems, which was also previously used in our research group for the atomic oxygen interaction with β-cristobalite (122). The two equivalent V^{O_i-slab} terms were obtained (101) by using the corrugation-reducing procedure

(CRP) interpolation method (11) over a large grid (X_O, Y_O, Z_O) of DFT points (spin-polarized GGA-PW91 calculations) calculated over the square (1×1) 2D unit cell (figure 4.2). The $V^{O_A-O_B}$ term was derived by means of a 6D CRP interpolation using a grid of O_2 DFT points over the unit cell of β-cristobalite at its equilibrium geometry. In particular, DFT energies were calculated for both, perpendicular ($\theta = 0°$) and parallel ($\theta = 90°$) O_2 configurations, at several O-O distances (r) and Z_{cm} values of its center of mass from the outermost Si atom of the β-cristobalite slab.

Figures 4.4a and 4.4b present contour plots of this PES for one oxygen preadsorbed (O_{ad}) on a T1 site for fixed Z_O values of the incoming oxygen atom, keeping the slab fixed at its equilibrium geometry. Incoming O atom tends to

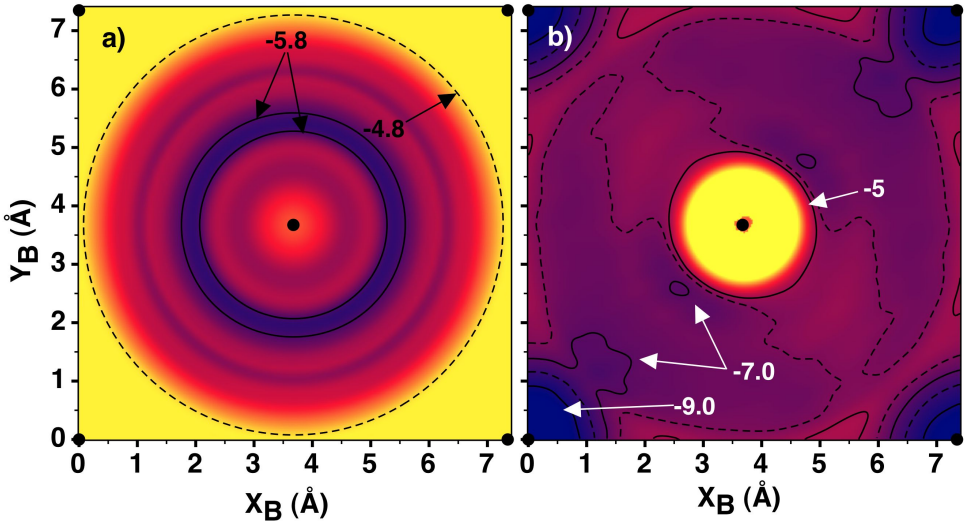

Figure 4.4: CRP PES contour plots for an O (atom A) preadsorbed on top central Si (T1 site) and the second one (O atom B) at several positions over the frozen β-cristobalite (001) surface: a) $X_A = Y_A = 3.674$ Å, Z_A= 1.560 Å and Z_B= 3.0 Å and b) $X_A = Y_A = 3.674$ Å, Z_A= 1.560 Å and Z_B= 1.560 Å. The energy difference between contour lines is 1.0 eV, with the zero of energy at $2O_{(g)}$+β-cristobalite slab. The Si atoms of the first layer of the (1×1) unit cell are shown by small black circles.

become closer to O_{ad} and to the outermost Si atoms, especially along the positive slope diagonal of the unit cell (figure 4.4b) due to the absence of O in the second layer along this diagonal. This behaviour is similar to the one observed for clean surface (122). Figure 4.5 shows contour plots for fixed X_O and Y_O positions of one adsorbed oxygen atom over a Si atom and the other one close to that (i.e., between two Si atoms) for different Z_O values. The observed stability at low

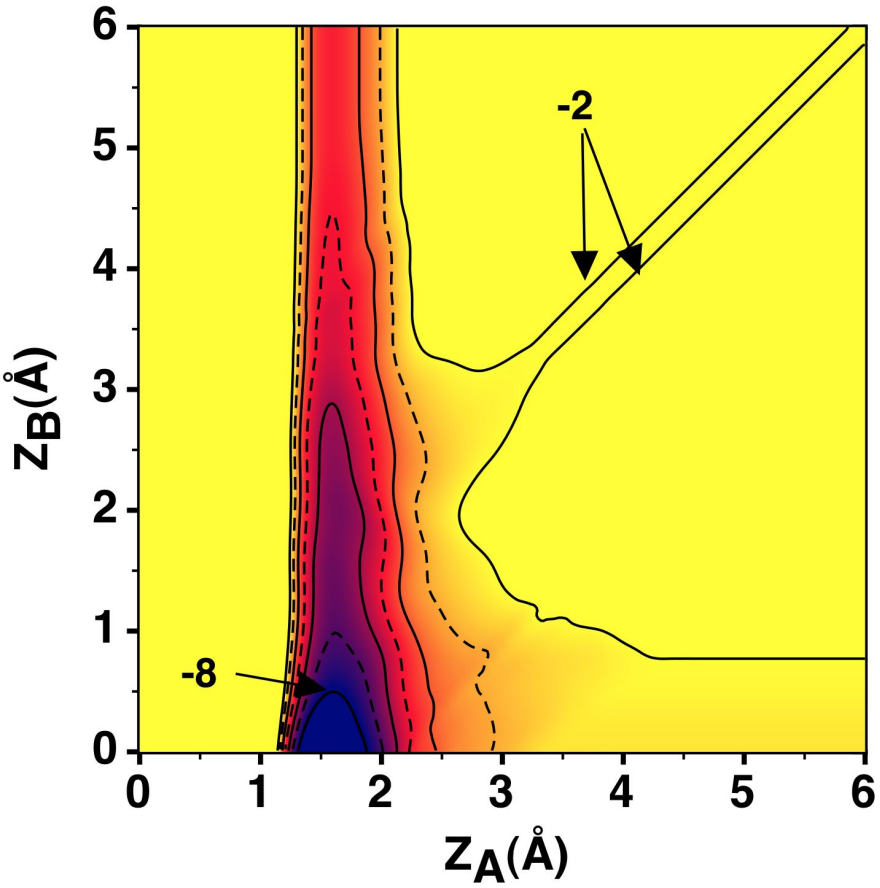

Figure 4.5: CRP PES contour plots for an O (atom A) adsorbed on top central Si (T1 site) $X_A = Y_A$= 3.674 Å and the second one (O atom B) at $X_B = Y_B$= 5.0 Å for several Z_A and Z_B positions. The energy difference between contours is 1.0 eV, with the zero of energy at $2O_{(g)}$+β-cristobalite slab.

Z_O values is in agreement with the existence of a $O_{2(ad)}$ minimum and with the favourable atomic adsorption/absorption into the β-cristobalite structure through the T1' minimum.

The relaxation of slab geometry stabilizes even more the stationary points of the PES. For instance, the energy of O_{ad} + O_{ad} minimum over two T1 sites changes to -11.03 eV, a value 0.39 eV more stable than that obtained for equilibrium rigid slab geometry. Moreover, one of Si atoms involved is shifted in Z_O from 0 to 0.314 Å, indicating that the slab reconstruction could be important during some collision processes. The contribution of V^{slab} modifies slightly the energetics of ER and LH reactions (e.g., $\Delta E_{ER} = -1.36$ eV and $\Delta E_{LH} = 4.92$ eV for O_{ad} over T1 sites).

The present CRP PES allows the calculation of energies for molecular configurations with $Z_{cm} \geqslant 0$ Å and $r \geqslant 0.5$ Å and for atomic configurations with $Z_O \geqslant$ -1 Å, due to the range of DFT data calculated. Hence, diffusion of O_2 inside the slab cannot be studied without extra modifications on the current PES.

Figure 4.6a presents a countour plot (r, Z_{cm}) of this PES for O_2 over a Si (T1 site), which shows the existence of an energy barrier for molecular dissociation. In fact, the final slab relaxation reduces significantly this initial energy barrier of 1.43 eV for rigid slab in the global PES as the dynamical study will show. Direct DFT calculations show that this barrier is located at r=1.237 Å, Z_{cm}=2.759 Å with an energy barrier of about 0.69 eV, which connects with a molecular adsorption minimum at -3.16 eV (energy respect $O_{2(g)}$ + slab asymptote); this is a true minimum (i.e., all harmonic frequencies are positive) with an equilibrium geometry equal to $X_{cm} = X_{Si}$, $Y_{cm} = Y_{Si}$, $Z_{cm} = 1.423$ Å, $r = 1.639$ Å, $\theta = 90°$, $\phi = 55.8°$ (ϕ angle is zero when O_2 molecule lays in the X direction with $\theta \neq 0°$). The DFT minimum energy path (MEP) changes from triplet state for $O_{2(g)}$ to a single state for the adsorbed molecule $O_{2(ad)}$. The two dangling bonds of the Si atom favour the minimum because in this way a first layer Si atom can achieve the silica stable SiO_4 tetrahedral unit configuration. The CRP PES reproduces as well this non-magnetic peroxo species as can be seen in figure 4.6a at Z_{cm}=1.401 Å and r=1.283 Å, E=-5.59 eV, although another local minimum is found. Nevertheless, these strong distorted structures will not be common in the dynamical study at low or medium energies. It is well known that semiconductor surfaces present a strong rearrangement after adsorption due to the covalent bonding of the substrate. In the case of silica, O or O_2 can penetrate inside the slab (absorption) and produce several kinds of stable structures (124, 125).

Figures 4.6b and 4.6c show that the dissociation of O_2 will be much less favorable (i,e., higher energy barriers) for another sites over the unit cell, specially between Si atoms located on the negative slope diagonal the unit cell due to the existence of O atoms in the second layer (steric effects). The approaching of the O_2 molecule to the slab between two Si edge atoms of the unit cell (H1 site) does not present almost interaction and will facilitate the diffusion or penetration of

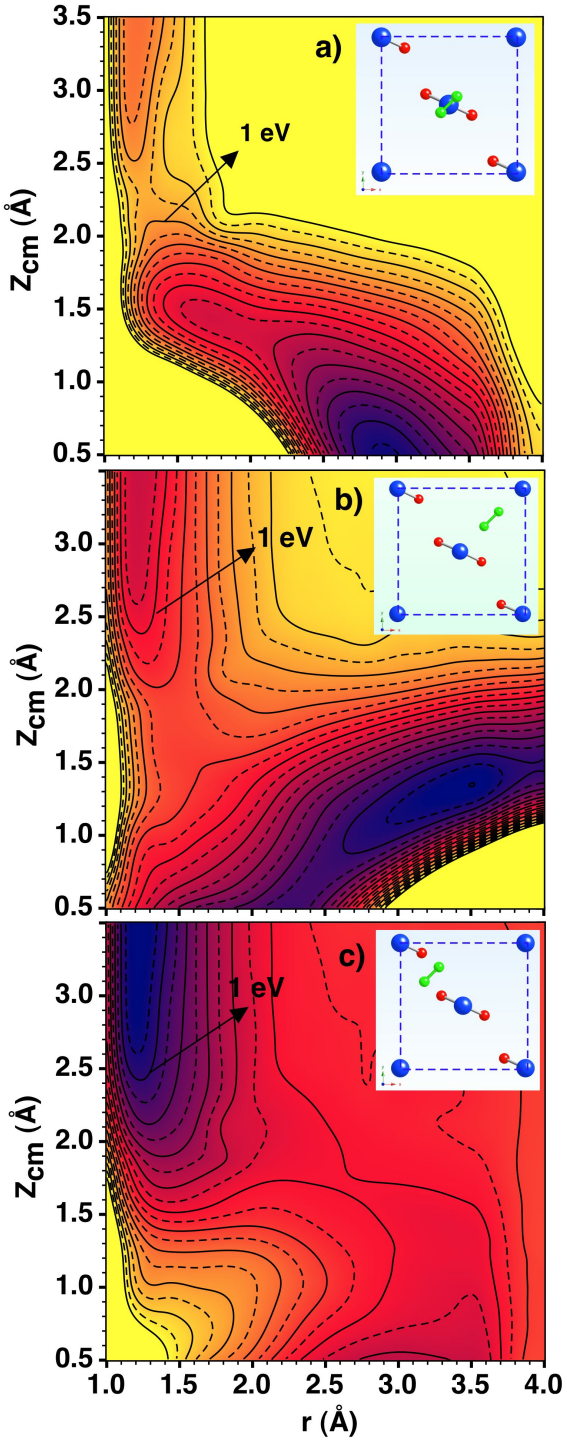

Figure 4.6: CRP PES contour plots for the O_2 molecule center of mass over three different sites of the unit cell for a molecular configuration at $\theta = 90°$ and $\phi = 45°$, with rigid slab at the equilibrium geometry. Contour spacing every 0.5 eV with the zero of energy at $O_{2(g)}$+slab asymptote. In the inset figure a representation of the O_2 position over the slab is depicted.

O_2 into the silica slab. Contour plots for O_2 configurations parallel to the surface at different ϕ angles and also for perpendicular approaching are more repulsive, confirming the high anisotropy of the PES.

The dissociation of O_2 molecule can produce two oxygen atoms that can get strongly adsorbed mainly over the Si atom (T1 and T1$'$ sites), as described in (101). This reaction channel (O_{ad}+O_{ad}) will be exothermic in comparison with reaction channels that produce one or two gas atoms (i.e., $O_{(g)}$+O_{ad} or $O_{(g)}$+$O_{(g)}$) that require an amount of energy to be produced, due to the strong adsorption energy of atomic oxygen over Si (i.e., for $O_{(g)}$+O_{ad} channel the endothermicity will be around 0.8 - 1 eV depending on the final geometry of the atomic adsorption). In the case of O penetration into the silica slab (i.e., absorption) the reaction channel becomes exothermic (101).

4.2 Atomic oxygen QCT collision study with O-preadsorbed β-cristobalite

4.2.1 Computational details

A dynamical study of atomic gas oxygen colliding with oxygen precovered β-cristobalite (001) surface is carried out by means of the QCT method (126). The silica slab includes a total of 104 atoms distributed into 9-layers for a (2×2) square surface unit cell with a cell parameter of 7.348 Å. The slab temperature (T_{surf} = 100 - 1,500 K) was controlled by means of a Generalised Langevin Oscillator (GLO) model (34, 126). The corresponding random and friction forces were applied only to the atoms of the bottom Si layer, which are also forced to oscillate around their bulk equilibrium positions (by using extra "springs") to avoid a global translation of the slab. We checked that the empirical slab vibrated with an average slab energy corresponding to the selected temperature ($\langle E_{slab} \rangle = 3Nk_BT_{surf}$). The generalised friction and the fluctuating forces were balanced, according to the second fluctuation-dissipation theorem. Thus, the proper temperature is reasonably maintained in the primary zone (i.e., the lattice atoms that can interact directly with colliding O atom).

This colliding oxygen atom is located initially at a distance of 6.0 Å from the surface (where no interaction is observed) and its aiming point (X_O, Y_O) is determined by a random uniform sampling only on an 1×1 unit cell. Preadsorbed O atom was located over the central Si atom (T1 site) at an initial Z_O of around 1.5 Å (adsorption minimum geometry). This atom was quickly thermalised at the selected slab temperature before the arrival of the incoming O atom. We checked as well that only at high temperatures (e.g., 1,000 K) this preadsorbed atom on T1 is able to evolve into T1$'$ (penetration into the slab) for collision

times longer than about 2 ps. Therefore, this initial geometry for O_{ad} seems to be appropriate enough for studying of all the processes derived from $O_{(g)} + O_{ad}$ collisions within the time scale considered (i.e., atomic reflection, atomic sticking and O_2 formation via ER reaction).

The colliding atom kinetic energy (E_{col}) range explored was 0.05 - 4.0 eV. The corresponding velocity angles θ_v and ϕ_v (figure 2.1) were fixed (θ_v =0° and θ_v =45°) and sampled by an uniform random sampling in the interval ($0° \leqslant \phi_v \leqslant 360°$), respectively.

Hamilton's equations were integrated by using a modified Beeman algorithm with a fixed step of $1{\cdot}10^{-4}$ ps, which permits an energy conservation of $10^{-4} - 10^{-5}$ eV in absence of the GLO bath. Two kind of calculations were considered: quasithermal ($T = T_{O(g)} = T_{surf}$; θ_v) and state specific (E_{col}, T_{surf}, θ_v). Batches of 3,000 - 25,000 trajectories were integrated for the different initial conditions, which ensured statistical errors below 1% for the reaction probabilities of the main channels. Trajectories were integrated up to a maximum time of 2 ps. Some tests at longer times (e.g., 5 ps) were also made to check the convergence of reaction probabilities. Nevertheless, some trajectories end at shorter collision times due to the before mentioned PES limitations, although the final probabilities are even so quite well converged.

Several main processes can occur: atomic reflection, atomic sticking, and O_2 formation (i.e., Eley-Rideal reaction). The molecules that become retained by the slab at least during the integration time were differentiated ($O_{2(ad)}$). In spite of these adsorbed molecules could finally desorb or produce two adsorbed or gas atoms at a much longer time scale, the PES topology seems to prevent a possible significant increase of the ER probability for longer collision times. In the present study we do not separate between atomic (or molecular) adsorption and absorption (penetration) processes as in an earlier paper (122), but this is practically irrelevant for the main goal of the present work, the ER reaction dynamics study.

The reaction channels are classified by analysing r, Z_O, $Z_{O'}$ and Z_{cm} values and the corresponding $v_{R,Z}$ components of both atoms (122) and molecule. For instance, the ER channel was achieved when Z_{cm} was much larger the 5 - 6 Å, the r distance was not far from the O_2 equilibrium distance (i.e., $r < 1.9$ Å) and $v_{Z_{cm}} > 0$. It was verified that once the integration is finished (usually in 2 ps) and the trajectory is classified, an extra integration time does not affect the trajectory classification. In case of discrepancy the trajectory was integrated more steps until a converged classification. This criterion was especially useful for channels involving finally adsorbed species.

The final internal state (v', j') for $O_{2(g)}$ was assigned rounding up or down rotational angular momentum j' to the nearest integer (quasiclassical approach) and by means of the radial action variable semiclassical method for the vibrational quantum number (v') (127). In spite of O_2 molecule presents only odd rotational

levels at its fundamental electronic state, this was not taken into account for final $j^{'}$ truncation due to the high closeness of the rotational levels and because it was necessary to use bins of at least $5j^{'}$ consecutive values to reduce the statistical errors in the final distributions.

4.2.2 Dynamical study

Figure 4.7a shows QCT probabilities for atomic sticking, atomic reflection, $O_{2(ad)}$ formation and ER reaction for normal incidence considering a surface temperature of 1,100 K (128, 129). Atomic sticking (adsorption/absorption) is the main process and its probability increases as translational energy does, in agreement with the O collisions over a clean β-cristobalite surface (122) (figure 4.7). $O_{2(ad)}$ formation is the second channel in importance and decreases with the augment of translational energy. Atomic reflection is lower than 10% and ER reaction is almost negligible in comparison with the other channels. Atomic desorption channels (i.e., involving O_{ad}) are practically forbidden in these conditions. The ER process, is completely absent at 300 K but its contribution is significant at 1,100 K, becoming more important for the lowest collision energies (see inset in figure 4.7a).

Off normal incidence enhances strongly the atomic sticking (figure 4.7b) diminishing as a consequence the $O_{2(ad)}$ formation. The atomic sticking probability does not present a clear normal nor total energy scaling (130) dependence with E_{col}, possibly due to the high corrugation of the surface that could favour the total energy scaling. Moreover, the competition between the different elementary processes can modify the final sticking probability, which would not occur for atomic collisions over a clean surface.

The atomic reflection for off normal incidence is now a little larger for all collision energies when compared with normal incidence. Figure 4.8 shows more clearly the effect of the incident angle on the different probabilities, revealing This reveals that the comparison between experimental and theoretical results should take into account an averaging over this angle (θ_v), specially for O sticking and $O_{2(ad)}$ formation. For ER reaction or O reflection processes this effect is smaller although it is observed that O collisions with small θ_v angles enhance the ER process (e.g., probability changes from $1.33{\cdot}10^{-3}$ at 0° to 0 at 60° for 1 eV of collision energy and 1,100 K of surface temperature) and decrease the reflection more significantly as shows figure 4.8.

The energy distributions of the O_2 molecules produced in ER reaction were also analysed. Nevertheless, its low reaction probabilities imply that the statistical uncertainties will be larger in comparison with another reaction channels (e.g., $O_{2(ad)}$ formation). Thus, figure 4.9 shows the translational, vibrational and rotational distributions for normal incidence and reactants at 1,000 K. Molecules are translationally hot, with an average $E_{col}^{'}$ equal to 0.84 eV, much larger than if

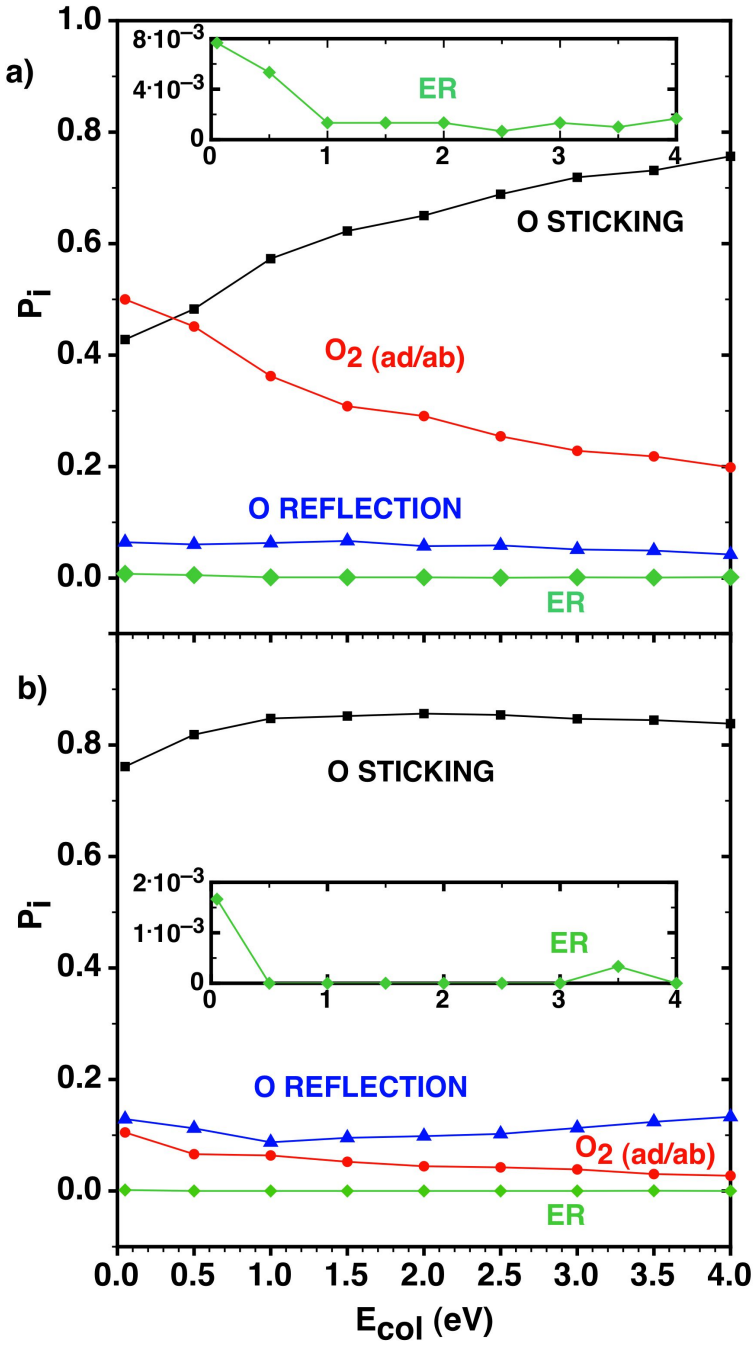

Figure 4.7: Sticking, reflection, $O_{2(ad/ab)}$ formation and ER probabilities for O collisions over an O-precovered β-cristobalite (001) surface at several collision energies and T_{surf} 1,100 K for a) $\theta_v = 0°$ and b) $\theta_v = 45°$. The inset figures amplify the ER reaction probabilities.

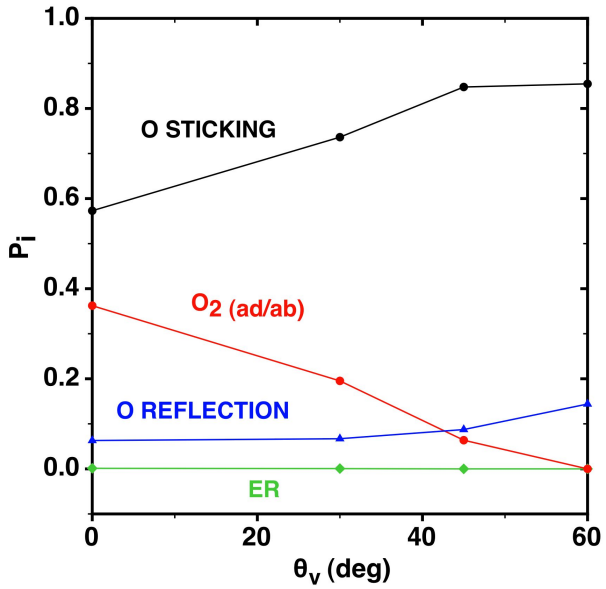

Figure 4.8: Sticking, reflection, $O_2(ad/ab)$ formation and ER probabilities for O collisions with an O-precovered β-cristobalite (001) surface at several incident angles for $E_{col} = 1$ eV and $T_{surf} = 1,100$ K.

products remained at the same temperature as the reactants (at 1,000 K the average energy would be 0.13 eV). The new O_2 molecules are also internally excited (figures 4.9b and 4.9c), much more than the corresponding thermal distributions at 1000 K, which would present a maximum in $j^{'} = 15$ and an important population of only the first vibrational levels ($v^{'} = 0$, 1, 2) with 0.9055, 0.0852 and 0.0083 values, respectively. The average internal energy of O_2 for these initial conditions is 0.67 eV, consequently indicating a much less vibrational and rotational excitation (e.g., $\langle E_{vib} \rangle = 0.27$ eV, $\langle E_{rot} \rangle = 0.42$ eV) compared with the translational one. The slab energy changes linked with its temperature distribution quite enough (the average slab energy was equal to 26.87±1.75 eV at 1,000 K) to explain the energy that finally goes into the O_2 product molecules.

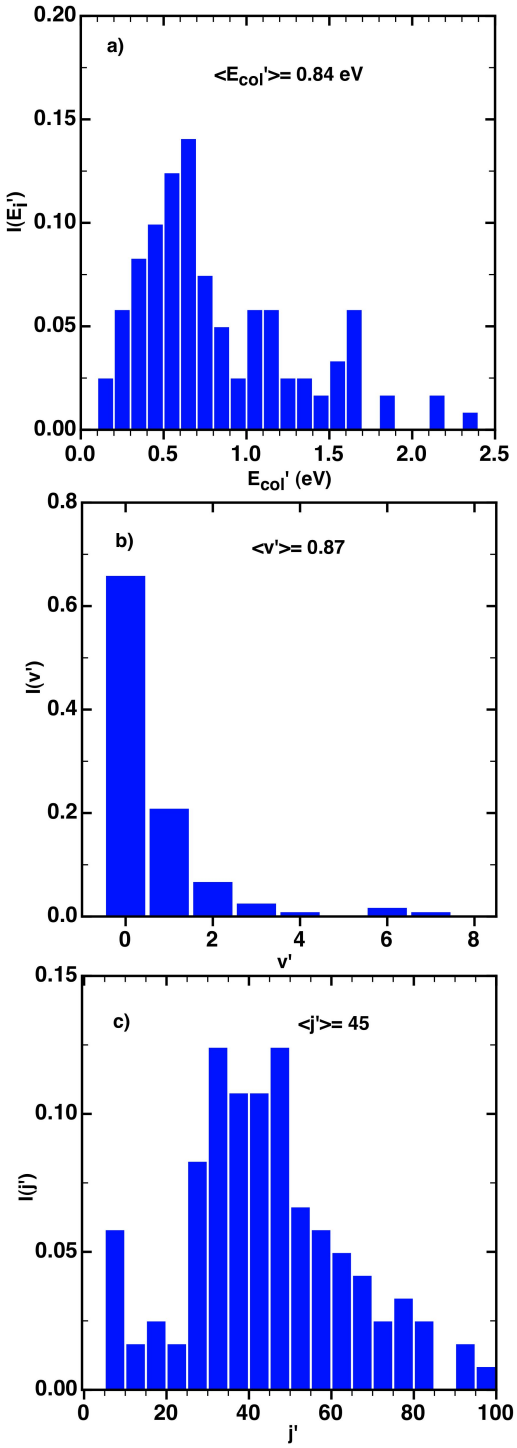

Figure 4.9: a) final translational ($E_{col}^{'}$), b) vibrational ($v^{'}$) and c) rotational ($j^{'}$) distributions of the O_2 molecules formed by the ER reaction at the following initial conditions: $\theta_v = 0°$ and $T_{surf} = 1{,}000$ K. Only 121 trajectories over a total of 25,000 trajectories produced this reaction channel. Average values are indicated inside the figures. Bins of $5j^{'}$ values were used for rotational distribution, summing over all $v^{'}$.

4.3 Molecular oxygen QCT collision study with β-cristobalite

4.3.1 Computational details

The incoming O_2 molecule was located initially at 4.5 Å from the surface where the interaction is negligible. The starting (X_{cm}, Y_{cm}) point was determined by a random uniform sampling of the square (1×1) unit cell (figure 4.2). Moreover, trajectories were also calculated for collisions over the centered Si atom of the unit cell ($X_{cm} = X_{Si} = 3.674$ Å, $Y_{cm} = Y_{Si} = 3.674$ Å) to study much better the effect of the initial conditions on the molecular dissociation. The initial molecular orientation angles (ϕ, θ, in figure 2.1) were sampled by using the standard Monte Carlo method, whithin the intervals 0° - 180° and 0° - 360°, respectively. The molecule is prepared at a selected rovibrational level within the range of v= 0 - 5 and j= 1 - 33, and translates respect the slab with a given kinetic center of mass energy (E_{col}). This energy was in the range 0.15 eV - 3.0 eV with a $T_{surf} = 300$ K.

Two sets of independent calculations were carried out for two incident angles ($\theta_v = 0°$ and 45°). The initial r distance was chosen between the corresponding inner (r_-) and outer (r_+) turning points of every O_2 (v,j) internal levels. Thus, a Monte Carlo sampling method is used for internal coordinates (r, θ, ϕ) and linear momenta (p_r, p_θ, p_ϕ) selection for a fixed total energy and rotational angular momentum $\left(L^2 = j(j+1)\right.$ in atomic units$\left.\right)$ of the molecule. Hence, the angle η, defining the orientation of $\vec{L}$ vector, was randomly selected within 0° and 360°. As in the previous case, only odd j initial levels were chosen for $O_2(X^3\Sigma_g^-)$ molecule because even rotational levels are forbidden since the nuclear spin of O^{16} is zero.

Hamilton's equations were integrated using a modified Beeman algorithm with a fixed step of 0.1 fs. Energy was conserved withing 10^{-3} - 10^{-4} eV in absence of thermal bath. Batches of at least 5,000 trajectories were integrated for each initial condition, which ensures a correct sampling of the random collision parameters and small statistical errors in the probabilities of main processes (i.e.,$< 1\%$). The major part of trajectories ended up at short collision times (< 0.5 ps), depending on both E_{col} and the particular process. Each trajectory can be classified as one of the following processes or channels:

1. $O_{ad} + O_{ad}$
2. $O_{2(ad/ab)}$
3. $O_{2(g)}$
4. $O_{(g)} + O_{ad}$

5. $O_{ad} + O_{(g)}$

6. $O_{(g)} + O_{(g)}$

Channel 3 corresponds to molecular reflection, channel 2 to molecular adsorption/absorption (hereafter sticking) and the other channels (i.e., 1 + 4 + 5 + 6) imply the molecular dissociation. Once the distances and velocity criteria were achieved, trajectories were integrated during a number of additional steps (e.g. 10 - 50 steps) to verify that the classification was converged. Only an insignificant part of the trajectories were stopped before this accurate classification due to some PES limitations (i.e., geometries with $Z_O < -1.0$ Å, $Z_{cm} < 0$ or $r < 0.5$ Å (Z=0 for first layer of Si atoms), where the PES is not defined). The distinction between adsorbed and absorbed atoms were not taken into account (i.e., $O_{ad} \equiv O_{ab}$) because the interest is centered on the molecular dissociation, although atoms will be mainly absorbed as it was shown in a previous work (122) (e.g., > 90%).

4.3.2 Dynamical study

Batches of trajectories were calculated for state specific conditions for a given surface temperature (128, 129). The different channel probabilities for O_2 ($v = 0, j = 1$) at two incident angles at T_{surf}= 300 K are plotted in figure 4.10. Molecular reflection is the main channel and its probability decreases rapidly as the collision energy increments, favoring thus the molecular sticking. This behaviour was also observed for O sticking over the same silica surface (122) and it is at variance to the usual prediction done with simple models for gas-surface collisions (e.g., hard cube model (120)). These models predict a decrease of trapping probabilities as the energy grows. The analysis of atom sticking revealed that the positive slope dependence with E_{col} was mostly caused by the predominant absorption processes, while the less important adsorption processes showed almost no variation with E_{col}. Moreover, the incident angle dependence points out that normal incidence produces higher sticking probabilities than off normal incidence (figure 4.10b) and according to this, the reverse behaviour is obtained for reflection probabilities. This can be explained taking into account that absorption is enhanced by normal collisions over open areas of the unit cell (i.e., regions between Si corner atoms mainly B1 and H sites, figure 4.2) where energy interaction is very low. The large anisotropy of the PES produces that off normal molecular collisions deviate before reaching these regions and explore more repulsive zones, increasing as a consequence the reflected collisions. An analysis of the energy scaling of the molecular sticking probabilities at several incident angles ($\theta_v = 0°, 15°, 30°$ and $45°$) show that they fall on a line (figure 4.11) when are plotted as a funcion of the perpendicular component of the translational energy, pointing out a normal energy scaling in spite of the great surface corrugation. It

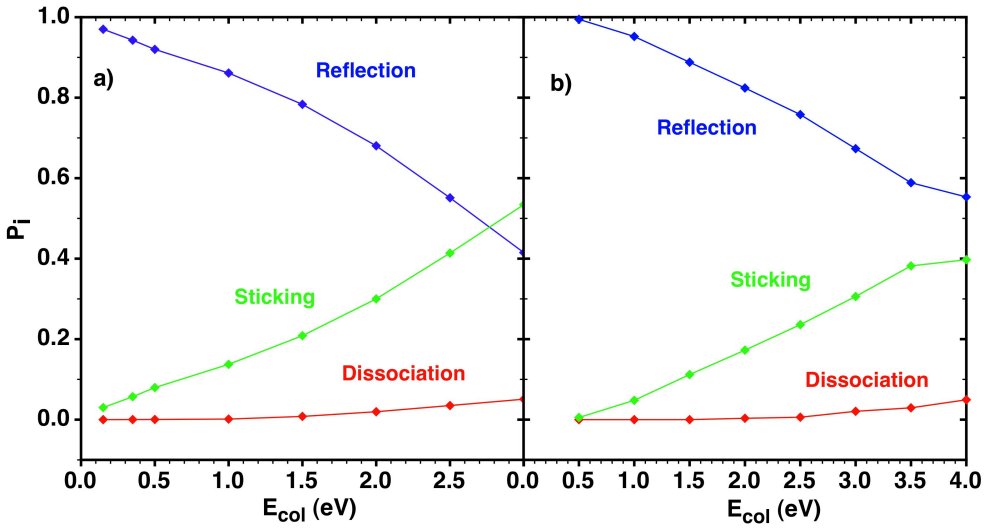

Figure 4.10: Sticking, reflection and dissociation probabilities for O_2 ($v = 0, j = 1$) collisions at several collision energies at $T_{surf} = 300$ K and at a) $\theta_v = 0°$ and b) $\theta_v = 45°$.

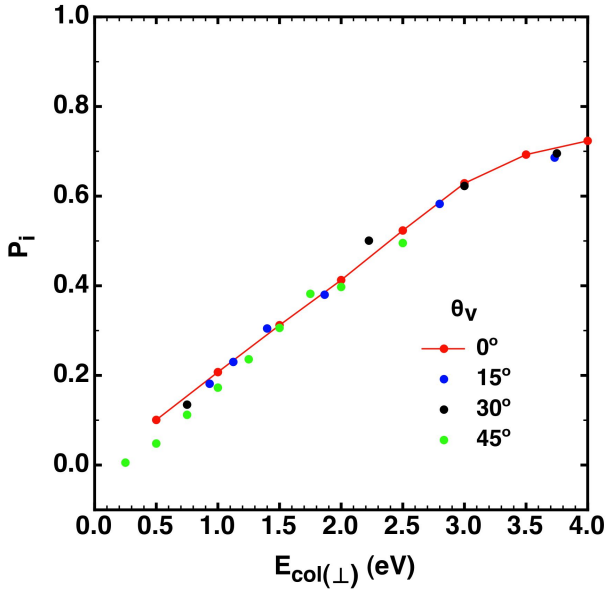

Figure 4.11: Sticking probabilities for O_2 (v=0, j=1) collisions as a function of the perpendicular collision energy at several incident angles (θ_v) and T_{surf}= 300 K.

is interesting to note that a less corrugated surface as graphite does not present the same behaviour (see section 3.6.1.2) The vibrational and rotational energies of the molecule and the rather unusual type of trapping (i.e., huge absorption) could justify this atypical effect.

Molecular dissociation processes become opened at very high collision energies (e.g., 1.0 and 2.0 eV for $\theta_v = 0°$ and 45°, respectively), which means that this is an activated reaction. To clarify much better the effect of the internal molecular state (v, j) and E_{col} on the dissociation processes along with their microscopic mechanisms, a set of trajectories were calculated for normal incidence considering the collision of the O_2 molecule over the central cell silicon atom. It is expected a large increase of molecular dissociation in agreement with the topology of the PES. If figure 4.12 is compared with figure 4.10a, the key role of Si atoms concerning to the molecular dissociation is demonstrated. In this case (figure 4.12),

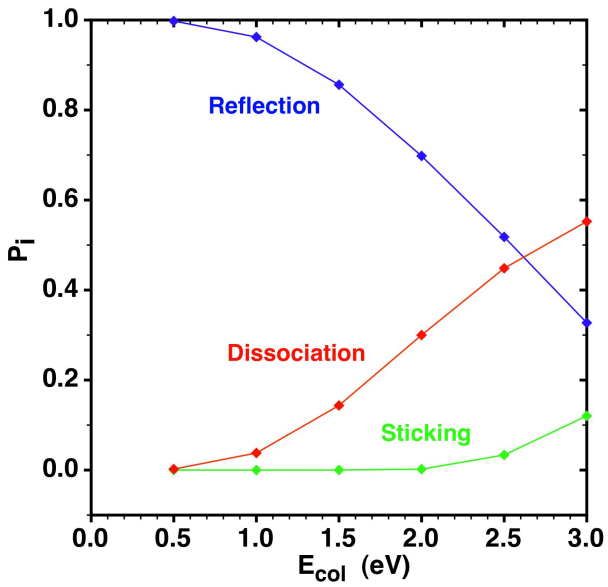

Figure 4.12: Sticking, reflection and dissociation probabilities for O_2 ($v = 0, j = 1$) collisions with the outermost Si atom of the surface for normal incidence as a function of the collision energy at $T_{surf} = 300$ K.

sticking is negligible as O_2 cannot be absorbed over the Si atom and molecular dissociation becomes much more important. Only at very high energies O_2 internuclear distance is high enough for becoming adsorbed to the Si atom. The final O adsorbed atoms are located close to the Si atom, along the positive slope diagonal of the unit cell, which is more attractive for O and O_2 than other regions of the cell. For instance, O atoms coming from dissociate molecules (channel 1) get stuck along this diagonal at different side respect the Si atoms, in agreement

with previous atomic study (122).

The O_2 vibrational excitation enhances slightly the molecular dissociation (figure 4.13a). For instance, dissociation probability increases from 14.3% to 16.1%

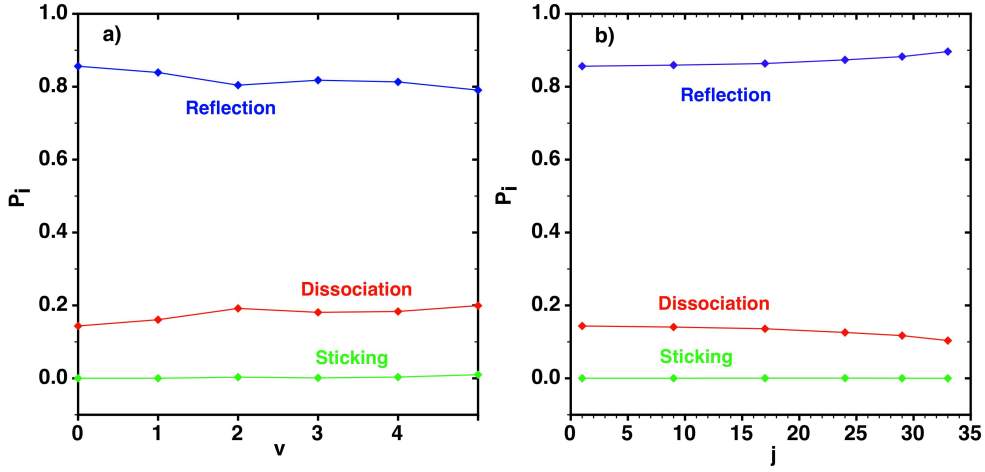

Figure 4.13: Sticking, reflection and dissociation probabilities for O_2 (v, j) collisions with the outermost Si atom of the surface for normal incidence and T_{surf}= 300 K at a) different vibrational levels for j=1 and E_{col} = 1.5 eV and b) different rotational levels for v=0 and E_{col} = 1.5 eV.

for $v = 0$ to 1, respectively. This fact implies an augment of about 0.20 eV in vibrational energy. Therefore, it seems that the efficiency (i.e., $\Delta P/\Delta E$) of vibrational energy is smaller than the translational energy to promote the molecular dissociation. The O_2 rotational excitation (figure 4.13b) produces a small but obvious decrease in dissociation probability (e.g., 14.4%, 10.4% for j=1 and j=33, respectively). This effect can be rationalised due to the high anisotropy of the PES respect the ϕ angle. This occurs specially once the energy barrier is overcome along the MEP for dissociation. This is because the PES becomes much more attractive (i.e., two adsorbed atoms, molecular adsorption,...), mainly around 45°.

The energy (internal and translational) and angular scattering distributions of O_2 reflected molecules were also studied. Final translational energy distributions (E'_{col}) are slightly colder than the initial ones (e.g., a narrow distribution with $\langle E'_{col}\rangle$ = 0.87 eV for E_{col} = 1.0 eV and v=0, j=1, θ_v = 0° and T_{surf}=300 K is obtained). Final vibrational distributions (v') are like the initial ones (e.g., $\langle v'\rangle = 0$ for almost all scattered molecules for initial O_2(v=0, $j = 1$) at E_{col} = 1.0 eV, θ_v = 0° and T_{surf} = 300 K). Only a noteworthy final rotational excitation is observed in reflected molecules ($\langle j'\rangle$=21 for the same before mentioned initial conditions). The polar scattering angle (θ'_v) presents broad distributions in the

range 110° - 180° with an average values of $\langle\theta_v^{'}\rangle$ = 154° for the same initial conditions.

For off normal incidence, the average scattering angle diminished to 136° due to the rather elastic character of these collisions. The final azimuthal angular scattering distributions ($\phi_v^{'}$) show a symmetric distribution between 0° and 360°, with alternating minima and maxima (see figure 4.14a). This can be explained by the topology of the reflection of O_2 molecules over the symmetrical unit cell. Thus, figure 4.14b shows the distribution of the initial center of mass position over the unit cell of the molecules that finally were scattered at E_{col}=1.0 eV, v=0, j=1, θ_v = 0° and T_{surf}= 300 K, corresponding approximately to the maxima of figure 4.14a. It was checked that the distribution over the cell is almost identical

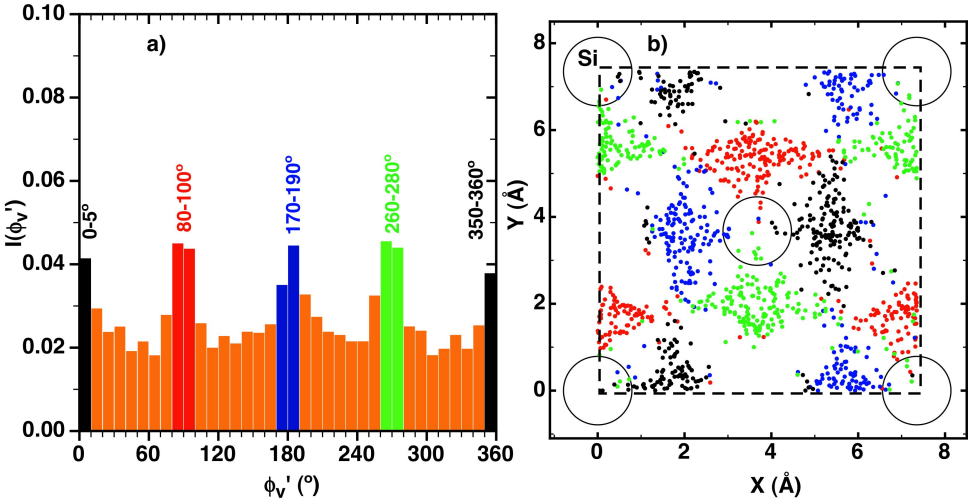

Figure 4.14: Azimuthal angular scattering distribution and the corresponding initial center of mass position of the scattered O_2 molecules for E_{col}= 1.0 eV, v=0, j=1, θ_v=0° and T_{surf}= 300 K.

to the distribution for the closest approach distance (Z_{min}) of the molecule to the surface. Therefore, scattered molecules are mainly deviated in X_O and Y_O direction (i.e., azimuthal angles) in which there are not Si atoms (which promote the dissociation) because the energy interaction is much lower. The azimuthal angles of $0° \equiv 360°, 90°, 180°$ and 270° correspond to the direction toward the cell open areas (H1 and B1 sites). Regions with minima of the azimuthal angular distributions (figure 4.14a) show as well, a consistent behaviour departing now the scattered molecules toward the diagonal directions (i.e., $45°, 135°, 225°$ and 315°).

4.4 Thermal atomic and molecular QCT collision studies

QCT dynamic studies of atomic and molecular oxygen colliding with a clean and O-preadsorbed β-cristobalite (001) surface were also carried out at thermal conditions. The temperature range (300 - 1,600 K) and the statistics of the calculated reaction probabilities were improved in order to construct a microkinetic model from QCT data. The interpolated CRP PES used (101), was already discussed in section 4.1.2.

For studying atomic oxygen collisions with a clean surface using the same O_2/β-cristobalite PES, the second O atom was kept at a large enough distance to the surface to avoid any interaction.

Batches of 5,000-15,000 trajectories were integrated at each temperature to ensure a reasonable good statistics for the reaction probabilities of the main channels. Different processes could be observed: atomic reflection, atomic sticking (adsorption+absorption), $O_{2(ad)}$ formation and $O_{2(g)}$ formation (i.e., ER reaction). Classification criteria for these events were presented in section 4.3.1 with more computational details of the study.

Figures 4.15, 4.16 and 4.17, summarize the reaction probabilities for quasithermal conditions from 300 to 1,600 K. Figure 4.15 presents the O collisions over a clean surface, observing a very strong sticking, which decreases as the temperature is increased.

A much lower sticking is observed in figure 4.16 for O_2 collisions over a clean surface. This behaviour is explained due to the favourable adsorption of both species (mostly for O) over several sites of the Si-terminated β-cristobalite surface, specially on top (T1 site) or very close ($T1^{'}$ site) to Si atoms (101). Molecular dissociative adsorption is not observed for this temperature range in agreement with the results presented previously that predicted that this process should be only opened at higher collision energies (e.g., $E_{col} > 1$ eV).

Figure 4.17 shows the reaction probabilities for O collisions with an O-precovered surface (O on T1/T1$^{'}$/T1$^{''}$ site, which means an atomic coverage of $\theta_O = 0.25$). The atomic sticking decreases in comparison with the clean surface probabilities as new processes, such as O_2 formation, appear. In fact, the distinction was done between the formation of the $O_{2(g)}$ via the ER reaction and the production of molecular oxygen that is strongly retained over the surface ($O_{2(ad)}$). This second reaction channel is much more probable than the first one, which is shown in the semilogarithmic scale of figure 4.17b. This trend was also observed in similar studies of atomic oxygen recombination over quartz (131) and in previous molecular dynamics simulations for O/O_2 over β-quartz (132). Here, $O_{2(ad)}$ formation was established if adsorption was longer than 5 ps, although simulations at very long times (i.e., 1.5 ns) showed important O_2 desorption, which

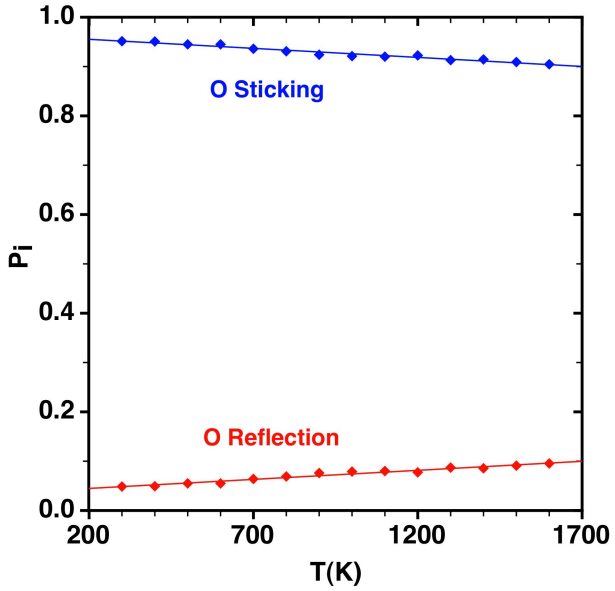

Figure 4.15: QCT reaction probabilities for normal incidence at several temperatures (300 - 1,600 K) for atomic oxygen over a clean surface. Lines show analytical fittings.

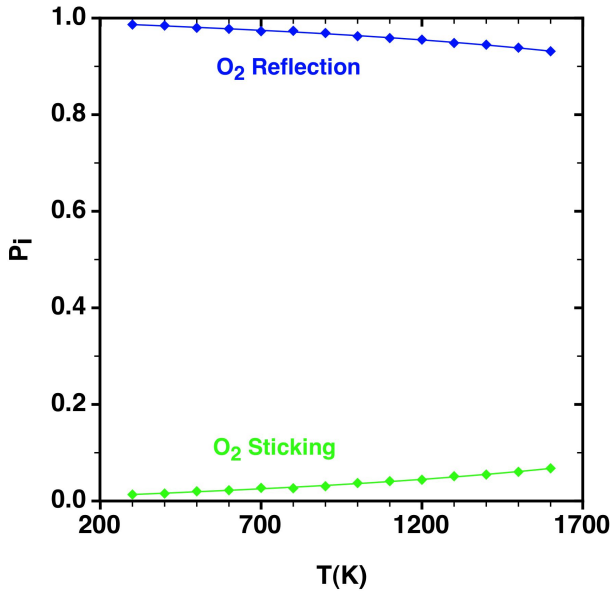

Figure 4.16: QCT reaction probabilities for O_2 collisions over a clean surface with normal incidence at several temperatures (300 - 1,600 K). Lines show analytical fits.

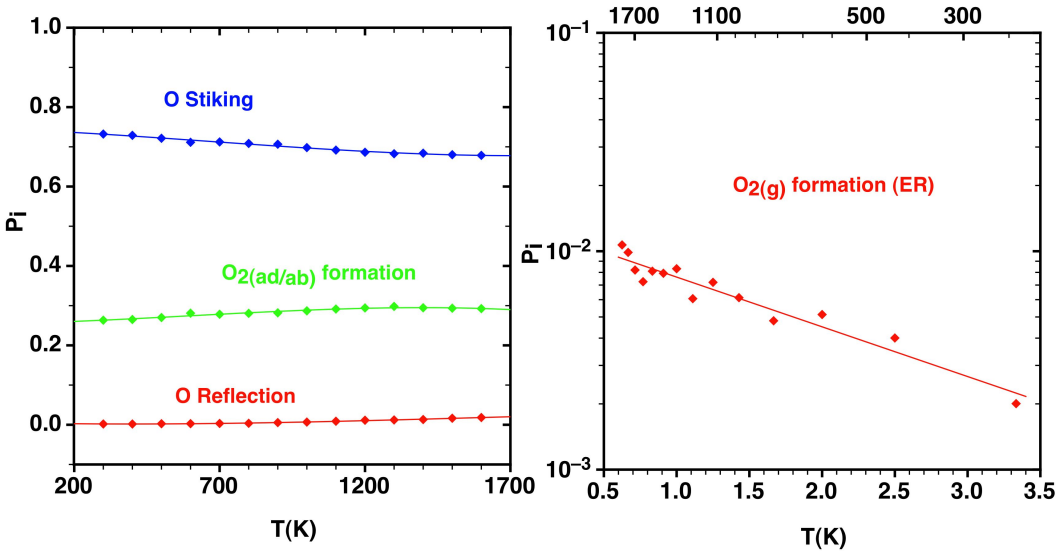

Figure 4.17: QCT reaction probabilities for normal incidence at several temperatures (300 - 1,600 K) for atomic oxygen over an O-precovered surface. Lines show analytical fits.

increases the final ER probabilities, although possibly this should be classified as molecular desorption.

4.5 Microkinetic model for O/O_2 mixtures reacting over β-cristobalite

A microkinetic model is proposed to ascertain the global effect of the main heterogeneous processes involving different O/O_2 mixtures over the β-cristobalite (001) surface at quasithermal conditions. Ten surface elementary processes were included, where i label is used for the direct processes and $-i$ for their reverse ones ($i = 1, \ldots, 5$). These are the considered processes:

chemisorption (k_1) and desorption (k_{-1}) of oxygen atoms,

$$O_{(g)} + s \underset{k_{-1}}{\overset{k_1}{\rightleftharpoons}} O_{ad} \tag{4.2}$$

molecular nondissociative adsorption (k_2) and molecular desorption (k_{-2}),

$$O_{2(g)} + 2s \underset{k_{-2}}{\overset{k_2}{\rightleftharpoons}} O_{2(ad)} \tag{4.3}$$

$O_{2(ad)}$ formation by atomic recombination (k_3) and molecular dissociative desorption (k_{-3}),

$$O_{(g)} + O_{ad} + s \underset{k_{-3}}{\overset{k_3}{\rightleftharpoons}} O_{2(ad)} \tag{4.4}$$

Eley-Rideal reaction (k_4) and molecular dissociative adsorption (k_{-4}),

$$O_{(g)} + O_{ad} \underset{k_{-4}}{\overset{k_4}{\rightleftharpoons}} O_{2(g)} + s \tag{4.5}$$

and Langmuir-Hinshelwood reaction (k_5) and molecular dissociative adsorption (k_{-5}),

$$O_{ad} + O_{ad} \underset{k_{-5}}{\overset{k_5}{\rightleftharpoons}} O_{2(g)} + 2s \tag{4.6}$$

where s indicates a free site on the surface. PES analysis shows that molecular oxygen prefers to get adsorbed in parallel configuration over a Si atom, by using the two T1′/T1″ free adjacent sites of the four available in each (1×1) unit cell. The O_2 dissociation can produce several final products (e.g., O_{ad}+O_{ad}, $O_{(g)}$ + O_{ad},...). Adsorbed (ad) or absorbed (ab) species are indicated hereafter using only the *ad* subscript, as they are not distinguished within this model. Processes are labelled as direct and reverse ones for notation compactness (i.e., k_i and k_{-i}).

The thermal rate constants for the elementary processes (1), (2), (3) and (4) were calculated from the corresponding thermal QCT reaction probabilities (P_i(T) reported in sections 4.4 and 4.3; see figures 4.15, 4.16 and 4.17) by using conveniently the following standard expressions (133),

$$k_i(T) = P_i(T)\sqrt{\frac{k_B T}{2\pi m_l}}\frac{1}{[s]_0}, \qquad i = 1,4 \qquad (m^3 \cdot s^{-1}) \tag{4.7}$$

$$k_i(T) = P_i(T)\sqrt{\frac{k_B T}{2\pi m_l}}\frac{1}{[s]_0^2}, \qquad i = 2,3 \qquad (m^5 \cdot s^{-1}) \tag{4.8}$$

where k_B is the Boltzmann constant, T is the temperature, m_l is the atomic mass (molecular mass for k_2) and $[s]_0$ is the initial surface density of free sites (i.e., 4 sites per unit cell or $7.41{\cdot}10^{18}$ sites/$\cdot$m^2 for a β-cristobalite (001) surface). The i values in the equations 4.7 and 4.8 show the elementary processes for which rate constants were calculated.

The QCT probabilities were fitted by using some polynomials for (1), (2) or (4) processes or an Arrhenius expression for ER reaction (3), which are also plotted in figures 4.15, 4.16 and 4.17. As the LH reaction was not studied by the QCT method, an estimation of its rate constant was done from the following equation (133),

$$k_5(T) = \frac{1}{\Delta}\sqrt{\frac{\pi k_B T}{2m_O}}\frac{1}{[s]_0}e^{-\Delta E_5^{0\neq}/k_B T}, \qquad (m^2 \cdot s^{-1}) \tag{4.9}$$

where Δ is the mean distance between active sites, the square root term is the mean velocity of O reacting adatoms, assuming a two-dimensional gas and $\Delta E_5^{0\neq}$ is the LH energy barrier including zero point energy, derived from the PES data (i.e., $\Delta E_5^{0\neq} \approx \Delta E_5^0 = 3.29$ eV). The rate constans for reverse processes (k_{-i}) were obtained by means of the principle of detailed balance, using the DFT reaction exo- or endothermicities of each process (ΔE_i^0, including the zero point energies, table 4.2). The spin statistical factors were not introduced into the rate constants. This assumption could be acceptable as the used adiabatic PES for all O_2/β-cristobalite processes was the same and because these factors should produce only small and similar changes into the calculated rate constants.

Figures 4.18 and 4.19 show the calculated QCT rate constants within the 400 - 2,000 K range of temperature. The great differences in the value of these rate constants will have an important influence on the global recombination kinetics of the system. It is for instance expected that LH reaction contributes much less than ER reaction to the global recombination within this model. The rate constans are finally fitted by using an Arrhenius formula within the 700 - 1,700 K range, whose parameters ($A_i, E_{a,i}$) are indicated in table 4.2 together with ΔE_i^0 values. This more restricted temperature range is selected to obtain better Arrhenius parameters to be used in the γ_O and β_O calculation; the initial T interval was too wide (400 - 2,000 K), so that significant curvature is observed at lower temperatures.

The time evolution of the surface concentration of both atomic and molecular adsorbed species resulting from the microkinetic model is given by the solution of the coupled equations

$$\begin{aligned}\frac{d[O_{ad}]}{dt} &= k_1[O][s] - k_{-1}[O_{ad}] - k_{-3}\frac{1}{3}[O][O_{ad}][s] + k_{-3}[O_{2(ad)}] - \\ &\quad -k_4[O][O_{ad}] + k_{-4}[O_2][s] - 2k_5[O_{ad}]^2 + k_{-5}\frac{1}{3}[O_2][s]^2 \end{aligned} \tag{4.10}$$

and

$$\frac{d[O_{2(ad)}]}{dt} = k_2\frac{1}{3}[O_2][s]^2 - k_{-2}[O_{2(ad)}] + k_3\frac{1}{3}[O][O_{ad}][s] - k_{-3}[O_{2(ad)}] \tag{4.11}$$

where as each $O_{2(ad)}$ uses two sites, the density of free adsorption sites at any time will be,

$$[s] = [s]_0 - [O_{ad}] - 2[O_{2(ad)}] \tag{4.12}$$

Figure 4.20 shows the available $T1'/T1''$ sites over the unit cell of the β-cristobalite (001) surface. The incoming O atom approaches preferentially the surface over Si atoms (T1 sites) but at closer distances the adsorbed atom can be tilted over the more stable $T1'/T1''$ sites as was shown in previous studies (122). Thus, every Si atom can adsorb two O atoms using its two dangling bonds.

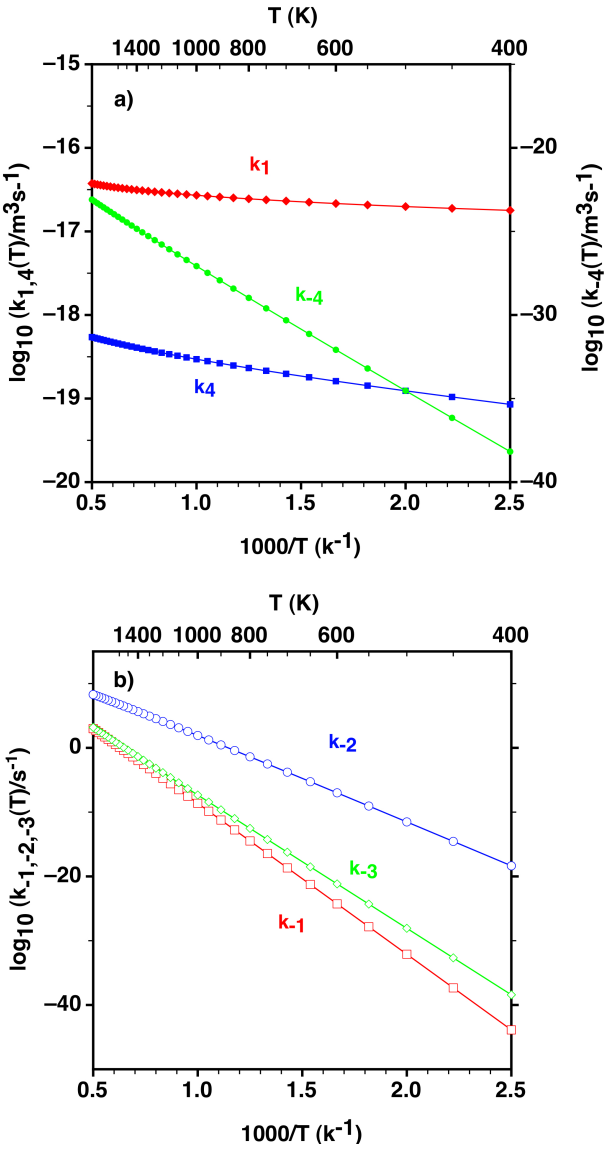

Figure 4.18: Calculated thermal rate constants (400 - 2,000 K) for different heterogeneous processes involved in the proposed microkinetic model, based on QCT data. Only rate constants with the same units can be easly compared. Points are connected with a line to guide the view.

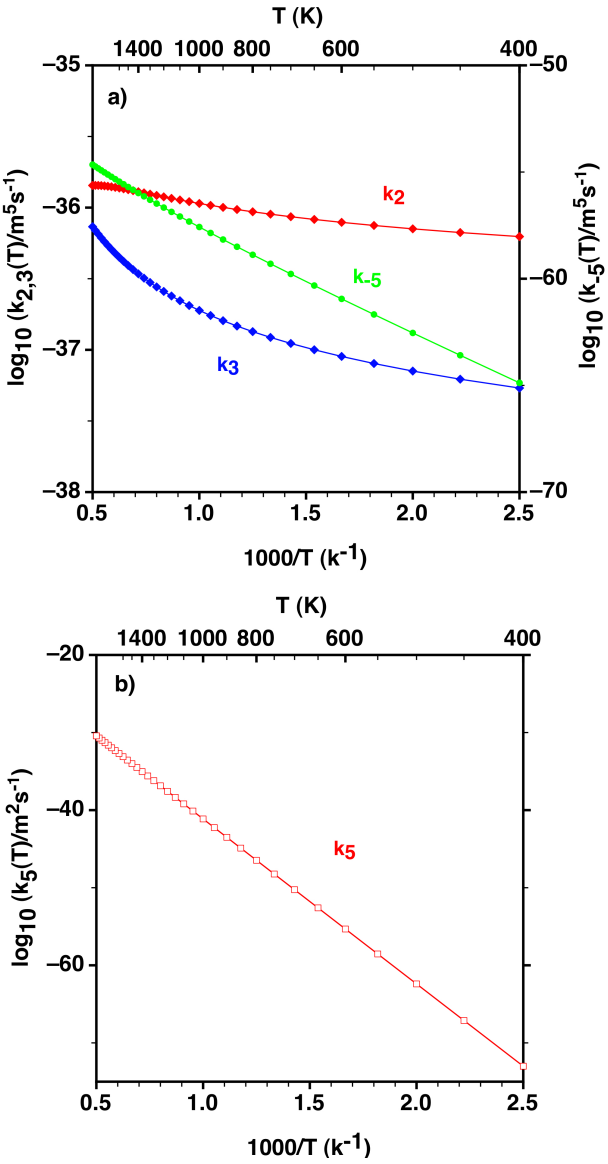

Figure 4.19: Calculated thermal rate constants (400 - 2,000 K) for different heterogeneous processes involved in the proposed microkinetic model, based on QCT data. Only rate constants with the same units can be easly compared. Points are connected with a line to guide the view.

Table 4.2: Arrhenius parameters derived from the calculated thermal rate constants using analytical $P_i(T)$ QCT probabilities within 700 - 1,700 K. ΔE_i^0 are the exo- or endothermicities energies. Q_i energies and F_i fluxes are used later for β calculations.

reaction process	A [a]	$E_{a,i}$ (eV)	ΔE_i^0 (eV) [b]	Q_i [c]	F_i ($m^{-2}s^{-1}$) [d]
1	$4.404{\cdot}10^{-17}$	0.0407	-4.65	$E_{a,-1} - E_{a,1}$	$k_1[O][s]$
-1	$5.018{\cdot}10^{14}$	4.63	4.65	$-E_{a,-1}$	$k_{-1}[O_{ad}]$
2	$1.980{\cdot}10^{-36}$	0.0518	-2.72	$\frac{1}{2}(E_{a,-2} - E_{a,2})$	$\frac{1}{3}k_2[O][s]^2$
-2	$9.730{\cdot}10^{14}$	2.60	2.72	$\frac{1}{2}(-E_{a,-2})$	$k_{-2}[O_{2(ad)}]$
3	$1.285{\cdot}10^{-36}$	0.158	-4.07	$E_{a,-3} - E_{a,3}$	$\frac{1}{3}k_3[O][O_{ad}][s]$
-3	$3.492{\cdot}10^{13}$	4.14	4.07	$-E_{a,-3}$	$k_{-3}[O_{2(ad)}]$
4	$8.686{\cdot}10^{-19}$	0.0914	-1.36	$-E_{a,4}$	$k_4[O][O_{ad}]$
-4	$4.802{\cdot}10^{-20}$	1.53	1.36	$-E_{a,-4}$	$k_{-4}[O_2][s]$
5	$1.663{\cdot}10^{-20}$	4.24	3.29	$\frac{1}{2}(-E_{a,5})$	$2k_5[O_{ad}]^2$
-5	$8.069{\cdot}10^{-53}$	1.08	-3.29	$\frac{1}{2}(-E_{a,-5})$	$\frac{1}{3}k_{-5}[O_2][s]^2$

[a] *Units are (s^{-1}, $m^3 \cdot s^{-1}$, $m^2 \cdot s^{-1}$ and $m^5 \cdot s^{-1}$) as for the rate constants (figures 4.18 and 4.19).*

[b] *Values derived from the interpolated O_2/β-cristobalite PES, including zero point energies. Atomic adsorption assumed on T1 site.*

[c] *Energies by O atom required (<0) or released (>0) to the surface for each i process.*

[d] *Partial atomic or molecular fluxes for each reaction process.*

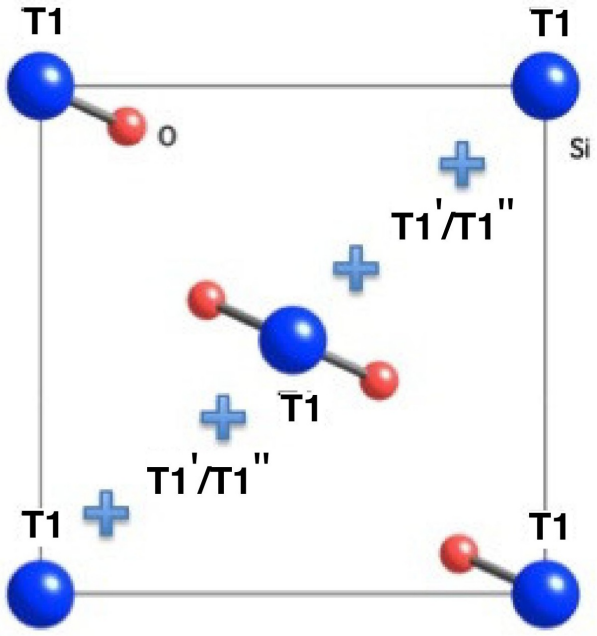

Figure 4.20: Top view of the (001) face of β-cristobalite showing the two first layers and the T1 (Si) and $T1'/T''$ (crosses) sites.

The factor 1/3 takes into account that only the nearest neighbours (i.e., two O on the same Si) will be effective for several reactions (e.g., two adjacent sites inside the unit cell, which means one of the three pair of sites, are necessary for reaction (2)). In fact, this small correction introduces some correlation between the locations of the reactants on the surface that a phenomenological kinetic approach does not take into account as compared with more accurate kinetic Monte Carlo simulations (134).

The numerical integration of these differential equations (4.10 and 4.11) for a constant flux of an O/O_2 mixture (i.e., constant P_O and P_{O_2}) impinging against the surface at a given temperature allows monitoring the evolution of atomic (θ_O) and molecular (θ_{O_2}) coverages up to final steady-state (ss) as shown in figure 4.21 at 900 K and 1,500 K for P_O= 91 Pa and P_{O_2}= 9 Pa, respectively. These partial pressures are close to the experimental ones for highly dissociated air plasma (ca. 70% - 80% (135, 136)) at total presure of 200 Pa over β-cristobalite. Two different trends are observed:

1. a final molecular coverage at temperatures lower than 1,000 K, which occurs at much longer times.

2. a final predominant and very high atomic coverage at higher temperatures.

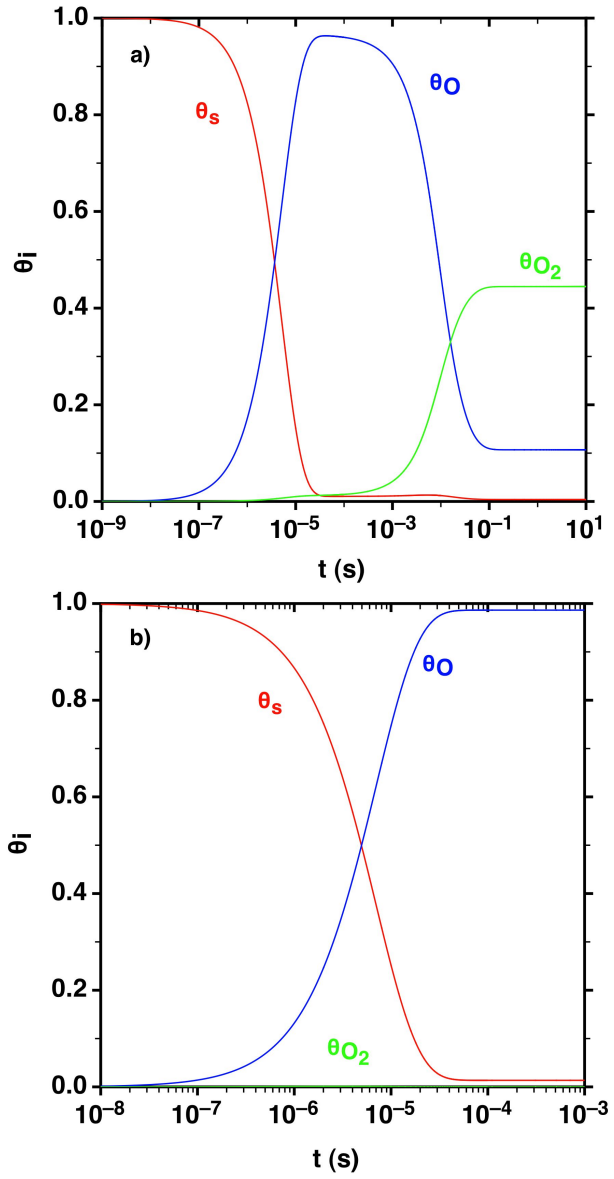

Figure 4.21: Free sites fraction and atomic and molecular surface coverage evolution for an O/O_2 mixture (91, 9 Pa) at a) 900 K and b) 1,500 K.

These overall behaviours are observed for several mixtures; however, the formation of $O_{2(ad)}$ by the competitive processes (2) and (3), which have similar rate constants (figure 4.19), increases mainly with the raise of P_{O_2} and P_O, respectively, hence alternating their influence for different initial mixtures. For pure O gas, mostly atomic coverage is observed.

The differences between both behaviours are mainly originated from the temperature dependence of both molecular desorption processes (-2) and (-3). At very high temperatures their rate constants (k_{-2}, k_{-3}) are very large (being $k_{-2} >> k_{-3}$) and only a final atomic coverage is observed (e.g., $\theta_O = 0.99$ at 1500 K, figure 4.21b), being negligible the final $O_{2(ad)}$ formation by (2) or (3) processes. At lower temperatures atomic oxygen is initially adsorbed until a suitable atomic coverage (maximum in figure 4.21a), when reaction (3) starts to produce $O_{2(ad)}$, which is not desorbed enough because both k_{-2} and k_{-3} (also with $k_{-2} >> k_{-3}$) are now much lower (e.g., coverage of 0.11 at 900 K, figure 4.21a). The calculated atomic and molecular coverages are much larger that the ones observed for graphite (0001) ($\theta < 10^{-3}$ and $\theta_{O_2} \approx 0$, section 3.4), which can be justified by the very strong atomic and molecular chemisorption on β-cristobalite.

The atomic oxygen recombination coefficient γ_O was also calculated as the ratio of the total flux of recombining oxygen atoms ($O_{(g)}$ consumption and formation) to the initial flux of impinging oxygen atoms (Z_O) over the surface once achieved the steady-state (ss) concentrations, using the following equation,

$$\gamma_O = \frac{k_1[O][s]_{ss} - k_{-1}[O_{ad}]_{ss} + k_3\frac{1}{3}[O][O_{ad}]_{ss}[s]_{ss} - k_{-3}[O_{2(ad)}]_{ss}}{Z_O} + \\ + \frac{k_4[O][O_{ad}]_{ss} - k_{-4}[O_2][s]_{ss}}{Z_O} \tag{4.13}$$

Z_O which is the number of O collisions over a surface per unit area and unit time, is given by the standard Hertz-Knudsen relation 2.176 (47) for a constant and normal flux of O/O_2 (i.e., $[O]=[O]_0$ and $[O_2]=[O_2]_0$). It was checked that the γ_O coefficient derived from O_2 balance (47, 108) leads to the same values than the ones from equation 4.13 at the final steady-state (or quasisteady-state). At lower temperatures, the surface suffers a passivation ($\gamma_O \approx 0$) due to the high O_2 coverage, which prevents any atomic recombination. Therefore, in this case the γ_O coefficient was estimated at the quasisteady-state reached at shorter times, which is comparable with experimental measurements on β-cristobalite (135). Figure 4.22 shows γ_O dependency against the inverse of the temperature, splitting this among the three main contributions: (1), (3) and (4) processes. It was observed that γ_O is almost independent on the initial mixture composition, as was verified for some initial conditions (e.g., P_O/P_{O_2}= 0.1, 1, 10 at several total pressures lower than 5,000 Pa). Atomic oxygen recombination is almost insensitive to the presence of molecular oxygen in the initial flux because of the very low rate constants of the processes (2), (-4) and (-5) involving O_2 (figures 4.18 and 4.19),

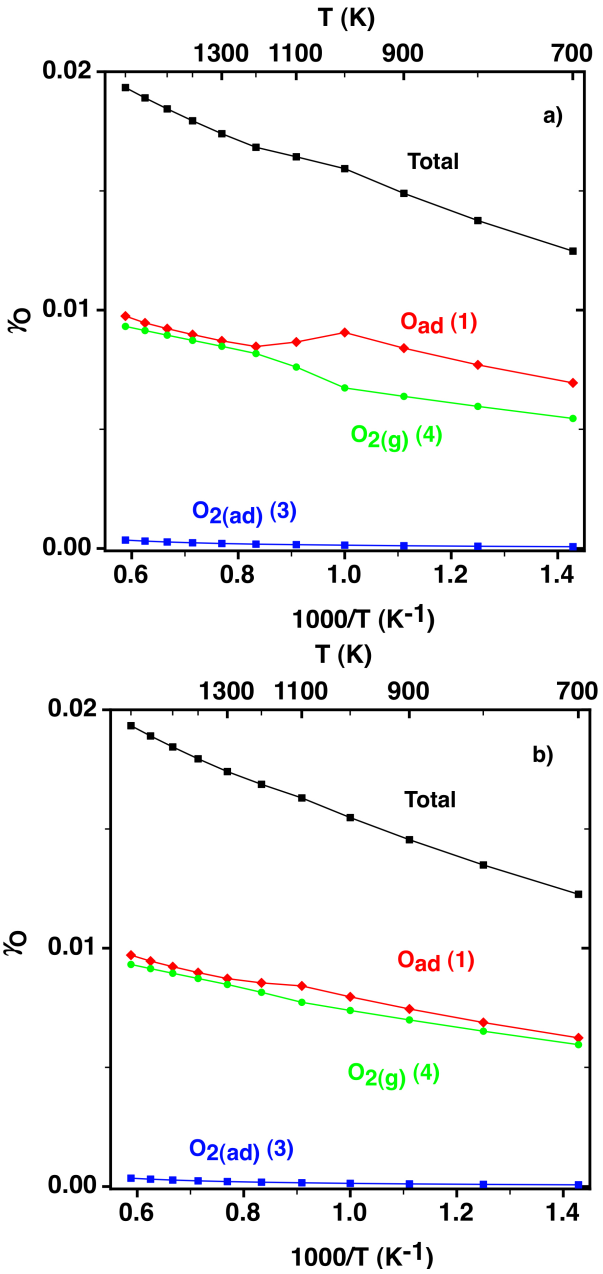

Figure 4.22: Calculated γ_O(T) coefficients as a function of the reciprocal of the temperature, showing their main contributions: a) P_O= P_{O_2} =50 Pa, b) P_O = 100 Pa, P_{O_2} = 0.

leading to negligible molecular dissociative or nondissociative adsorptions. However, at very large pressures these processes could become more important (i.e., trough the concentration effect in equation 4.13) as it was shown for O recombination over β-quartz at 100 atm (132), where for O/O_2 mixtures with partial pressures of 50 atm, the γ_O coefficient decreased with respect to pure O at 100 atm.

Small recombination coefficients are observed ($0.01 < \gamma_O < 0.02$) in the 700 - 1,700 K range, which are essentially originated from atomic adsorption and ER reaction with a similar proportion. No LH contribution is observed at all. In spite of the reaction (3) competes with ER reaction (4) with much higher reaction probabilities (figure 4.17a and 4.17b), its lower rate constants (i.e. $k_3 < k_4$; figures 4.18a and 4.19a) together with the small amount of free surface sites ($[s]_{ss}$ in figure 4.21), can justify its negligible contribution to γ_O.

These two contributions in γ_O are in agreement with previous assumptions made in similar kinetic models (137, 138). At very large pressures the LH reaction seems to gain importance for β-quartz (132), leading to larger γ_O values ($0.01 \leqslant \gamma_O \leqslant 0.35$).

Figure 4.23 compares the calculated γ_O values with recent molecular dynamics calculations on O/O_2 over β-quartz (132) along with experimental measurements on several silica surfaces (135, 139, 140, 141). The calculated coefficients increase with T following an exponential trend in agreement with the scattered experimental data. The dispersion in the experimental data may be due to several factors such as composition and structure of the silica surface (i.e., amorphous silica, several cystalline polymorphs,...), surface roughness (49, 139), gas composition (e.g., air, pure O, O/O_2 mixtures,...) or the experimental method used. The present calculated γ_O coefficients correspond to a perfect β-cristobalite (001) surface. The introduction of defects in the surface (e.g., corners, steps, O vacants,...) would modify somewhat the reactivity and consequently the calculated γ_O coefficient. In fact, the experimental measurements used a β-cristobalite surface coating (135) obtained by oxidation of sintered SiC samples at different temperatures, with possibly a polycrystalline nature, which could justify the slightly higher experimental reactivity.

In a previous work (101) it was directly compared the experimental γ_O values with QCT ER reaction probabilities, obtaining similar values although with a slope closer to the experimental one than that of the present work. The seemingly better previous results could be fortuitous because another processes (e.g., specially the atomic adsorption) should be included in a more reliable calculation of this coefficient. On the other hand, as the calculated γ_O coefficients are based on QCT reaction probabilities, some improvements on those could increase slightly the γ_O values. Thus, the inclusion of physisorbed O atoms (not only chemisorbed on $T1/T1'/T1''$ sites) in the ER study would probably increase the O_2 formation. Moreover, the integration at longer times (e.g., 2.5 - 5 ps) for re-

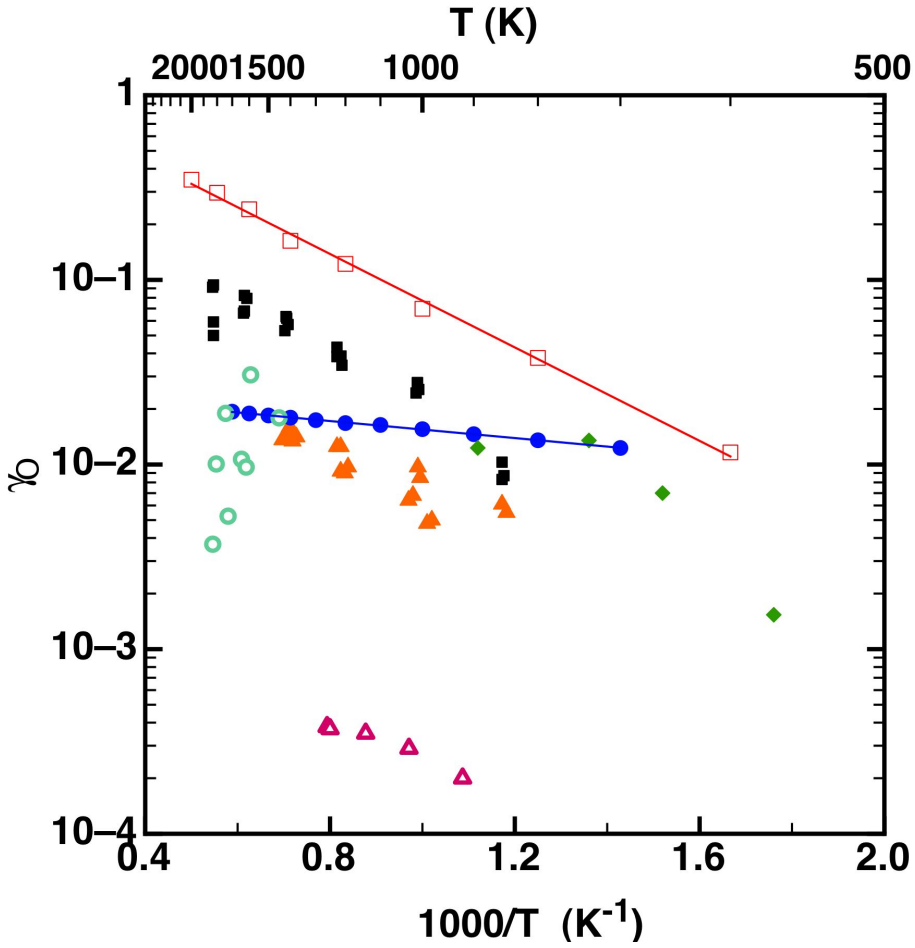

Figure 4.23: Calculated and experimental $\gamma_O(T)$ coefficients versus the reciprocal of the temperature for several silica materials. The solid lines show and Arrhenius fitting of the calculated data. Calculated γ_O: this work for O/O_2 (P_O = 91 Pa, P_{O_2} = 9 Pa) on β-cristobalite (filled circles); ReaxFF Molecular Dynamics calculation for pure O at $1{\cdot}10^6$ Pa on β-quartz (empty squares) (132). Experimental γ_O: air on β-cristobalite (filled squares) and quartz (filled triangles) at 200 Pa (135), pure O on fused quartz at 27 Pa (empty triangles) (139), O on silica (vitreosil) at P_O 1500-1600 Pa (filled diamonds) (140); γ'_O for O on RCG at P_O=133-824 Pa (empty circles) (141).

action (3), which produces adsorbed O_2 could increase the molecular desorption with following final augment of the ER contribution. For instance, simulations for β-quartz (132) were run at least for t < 5 ps, showing also a significant increase of γ_O but possibly at too long times (i.e., 1.5 ns).

Finally, although microkinetic models are commonly used to simulate the heterogeneous chemical kinetics of dissociated airflows impinging different types of surfaces (47, 108), with good agreement in comparison to available experimental data (e.g., total heat flux to the surface, γ coefficients, ...), more developed Monte Carlo simulations (e.g., N over silica (105), H over graphite (109)) could also be needed to provide a deeper microscopic understanding of these processes.

Following a similar approach as for the calculation of γ_O coefficient, the β_O coefficient can be calculated once achieved the final steady or quasisteady-state from the ratio between the total chemical energy that can be transferred to the surface and the energy that would be released if all consumed O atoms gave place to O_2(g), using the equation 2.177 modified for the particular microkinetic model used,

$$\beta = \frac{\sum_{i=-5, i\neq 0}^{+5} F_i \cdot Q_i}{Z_O \cdot \gamma \cdot (D_{O_2}/2)} \tag{4.14}$$

where D_{O_2} is the O_2 dissociation energy, F_i represents the atomic or molecular fluxes at the steady-state (table 4.2) and Q_i are the energies per O atom required or released in each process, which are derived from the expressions and activation energies listed in table 4.2. The adsorbed species (e.g., process (1)) were assumed to release all of their available energy to the surface whereas gas products (e.g., process (4)) will escape with all of their available energy (i.e., assuming a very short interaction with the surface), which would give a minimum β. This latter point is supported by previous QCT studies of the ER reaction on β-cristobalite (101), which showed that formed O_2 molecules become translationally and internally excited, taking rather some energy from the surface. Similar expressions were used in earlier studies (137) to estimate this β coefficient under several assumptions. This calculation should be considered as a first approximation to this coefficient (β_{min}) as there is not an unique choice of Q_i energies. Detailed dynamic studies on each elementary process, determining their energy fluxes with the solid, could afford a much accurate β calculation. Figure 4.24a presents β_O as a function of temperature for the same conditions as for figure 4.23, showing a value within the 0.75 - 0.80 range. There is only a very slight dependence with the temperature with a small maximum around 1,100 K, which arises from the small decrease in molecular coverage (figure 4.24b) since the desorption process (-2) becomes more important than the O_2 formation by process (3) for $T \geqslant 1,100$ K, being in these conditions β propotional to $k_i \cdot [s]/\gamma \cdot T^{1/2}$. A similar shape with almost constant β values were found for instance for N recombination over palladium and rhodium (137). β_O was also calculated for several initial O/O_2 mixtures with similar results; only for P_O=P_{O_2}=50 Pa the maximum achieved

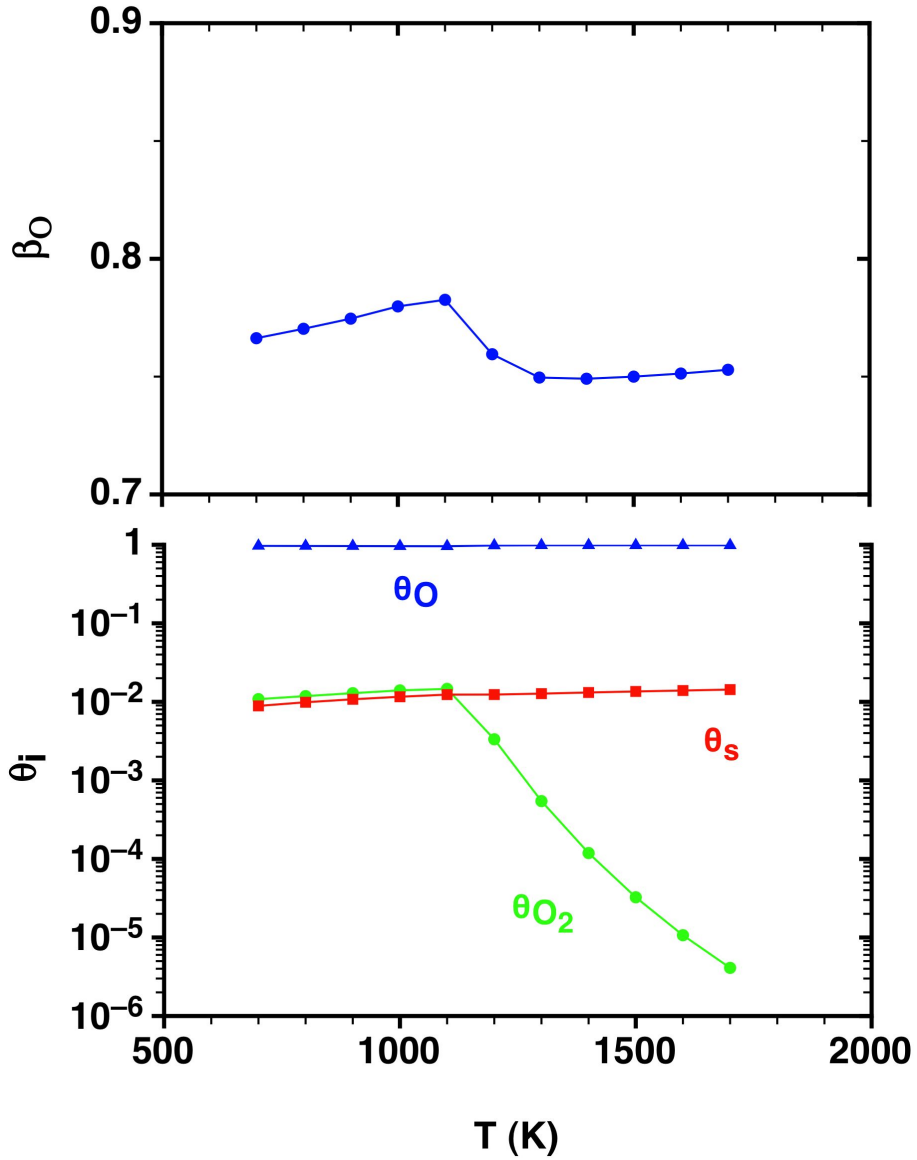

Figure 4.24: Calculated β_O(T) coefficients and surface coverage for an O/O_2 mixture (91, 9 Pa) over β-cristobalite at several temperatures.

a larger value (i.e., $\beta_O = 0.85$ at 1,000 K). The values obtained show that the common assumption that $\beta_O = 1$ and hence $\gamma_O^{'} = \gamma_O$ ($\gamma_i^{'} = \gamma_i \cdot \beta_i$) is not justified at all for O recombination over β-cristobalite. An analysis of the main contribution to β_O is shown in figure 4.25, which displays the total and the partial energy fluxes originated by the main processes. Clearly, the atomic adsorption process is largely the one producing almost the total energy released to the surface.

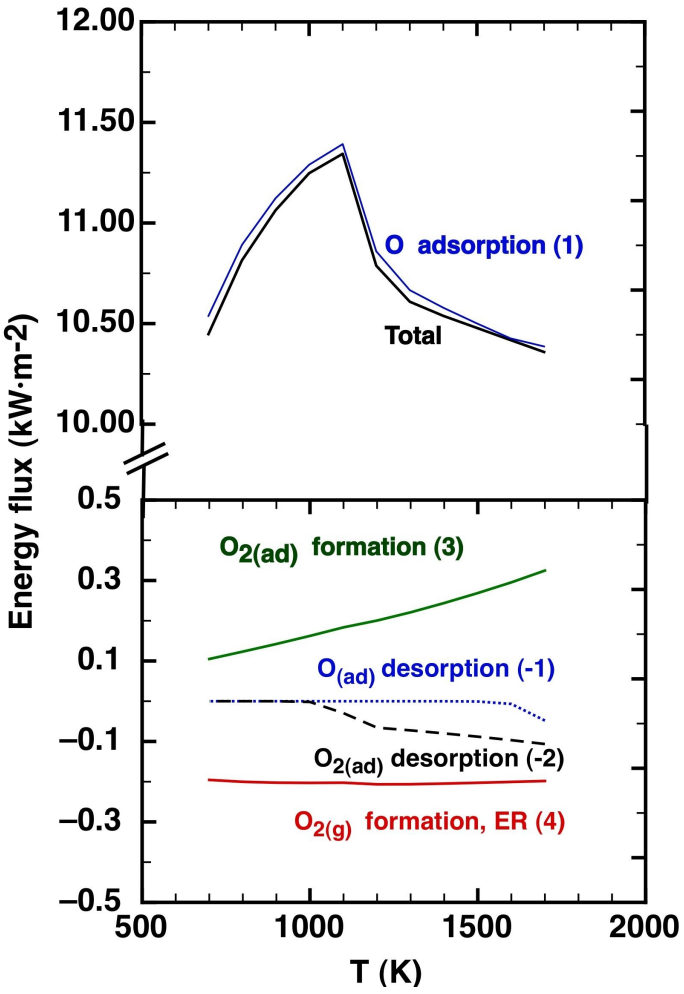

Figure 4.25: Calculated total and partial ($F_i \cdot Q_i$) energy fluxes transferred with the β-cristobalite surface for an O/O_2 mixture (91, 9 Pa) at several temperatures. The main contributions of the different processes are also shown. Be careful because the lower panel uses a much more amplified Y-axis (1 kWm^{-2}).

The only communication found (142) about some direct measurement of β_O and catalytic recombination fluxes on β-cristobalite, reports a strong decrease of

this coefficient in the interval 966 - 1,770 K at 200 Pa ($0.69 < \beta_O < 0.12$), but with a surprising almost constant energy flux (e.g., 35 ± 5 kW/m^2 for the lowest and highest β_O values) in this temperature range. The same authors presented the effective catalycity ($\gamma_O^{'}$), which decreases slightly as temperature increases (104) contrary to the common increase of $\gamma_O^{'}$ observed for several silica materials (e.g., RCG, SiO_2+B_2O_3,...(104)). The present calculations show nearly constant β_O coefficients and energy fluxes, showing however lower values (10.4 - 11.3 kW/m^2 for $P_O = 91$ Pa, $P_{O_2} = 9$ Pa) and a different behaviour particularly respect to β_O. The experimental recombination fluxes increase for more catalytic materials (SiC $\approx$ SiC+SiO_2 $\leqslant$ AlN $\leqslant$ Al_2O_3 (143)); thus sintered SiC shows a nearly constant value (25 or 35 kW/m^2 for air at 200 or 2,000 Pa, respectively) while pure alumina reaches 184 kW/m^2 at 1,400 K, decreasing to 93 kW/m^2 at 1,800 K for 2,000 Pa (143). The experimental increase of this flux as pressure rises (e.g., from 200 to 2,000 Pa) could also indicate the necessity of a better understanding of the experimental conditions in order to facilitate a more reliable comparison with current calculations. For instance, it was also observed this increase for higher oxygen pressures (e.g., a mean value of 23.5 kW/m^2 for $P = P_O = 200$ Pa). Moreover, new measurements of β_O for pure oxygen mixtures would be necessary in order to analyse if the results for air are reliable enough and to compare more properly with the present calculations.

Chapter 5

Conclusions

The aim of this work was to study the reactive processes of oxygen (atomic and molecular) over two solid surfaces as a model of the materials used in Thermal Protection Systems (TPS) and applied to spacecrafts, graphite and β-cristobalite. In this chapter there is a brief summary of the main conclusions obtained from each of the sections of the study, presented in order to give a global view of the work done.

- DFT study of O/O_2 over graphite:
  - DFT calculations of bulk graphite (e.g., lattice parameters, cohesive energy, isotropic bulk modulus, ...) and about O_2 molecule show a quite good agreement with experimental data.
  - The use of one or two layers for the slab model of graphite in the study of the elementary processes seems to be equivalent.
  - The O adsorption is mainly produced on C-C bridge sites with a considerable puckering of these carbons. This epoxide-like (COC) ring structure has also been observed in earlier theoretical and experimental studies on graphene and graphite oxides.
  - Atomic adsorption is an activated process, whose energy barrier decreases for lower coverages and under slab relaxation.
  - Atomic diffusion between two bridge sites is also an activated process, with lower energy barriers at low coverages but with higher values when slab relaxation is allowed, due to the larger adatom stabilization.
  - Atomic recombination processes via ER and LH mechanisms are also activated processes although their energy barriers decrease with coverage increment, specially for ER reaction, which will dominate the atomic recombination reaction from low to high temperatures.

  - Small molecular and atomic physisorption minima are observed, as confirmed by the inclusion of dispersion energy corrections.

- QCT study of atomic and molecular oxygen interaction with graphite:

  - Atomic reflection process is the main observed at most of the conditions studied. The chemisorption process has a collision energy threshold in close agreement with the different adsorption energy barriers of both PES and also presents always a maximum, although off normal incidence decreases its probability.
  - The atomic physisorption minimum of the MS PES enhances a high adsorption at low collision energies and large distances.
  - The inclusion of the thermal bath (surface temperature) favours the adsorption as the atom is able to release a part of its energy to the surface.
  - The polar scattering angle distributions of atomic oxygen show a maximum at low angles for normal incidence that is shifted at larger angles for off normal incidence, which is in good agreement with hyperthermal experiments (peak at $\sim 60^{\circ}$).
  - Atomic reflection along with Eley-Rideal (ER) reaction are the main processes for O colliding with an O-preadsorbed surface. Off normal incidence enhances the reflection diminishing the ER reaction.
  - O_2 molecules formed via ER reaction are internally and translationally excited as could be expected due to the ER exothermicity.
  - Molecular O_2 collisions over graphite show no dissociation. The reflected polar angle scattering distributions present a maximum, which is shifted at larger values for off normal incidence. Comparison with experimental data at different surface temperatures and collision energies show a quite good agreement.
  - The polar scattering angle distributions of scattered O_2 molecules and the O_2 formed via ER reaction show different peak positions, suggesting that ER contribution should be much less important in the experimental conditions.

- Microkinetic model for O/O_2 mixtures reacting over graphite:

  - The microkinetic model (300 - 1,000 K) based on TST data confirms a very small contribution of the LH process and predicts a very low atomic coverage ($\theta_O < 0.5\%$).

- Atomic adsorption and ER reaction are the most important processes with similar contributions at low temperatures, while at high temperatures this occurs for adsorption and desorption processes, although in this case their rates are compensated.
- These results along with the small rate constants originate very low atomic recombination coefficients ($\gamma_O < 5 \cdot 10^{-4}$).
- The increase in O partial pressure augments γ_O while the presence of molecular oxygen has no consequences.
- Temperature raise enhances γ_O values until reaching a temperature where the desorption becomes very important, hence diminishing γ_O.

• QCT study of atomic and molecular oxygen interaction with β-cristobalite:

- For the interaction of O with O-precovered β-cristobalite the atomic adsorption is the principal process, which increases with collision energy. The formation of $O_{2(ad)}$ is the second channel in importance and decreases with the augment of collision energy. O reflection and ER reaction are much less important although also significant. Off normal incidence enhances both reflection and adsorption, diminishing as a consequence the $O_{2(ad)}$ formation and ER reaction.
- The O_2 molecules produced via ER reaction at high temperatures become internally and translationally excited, while the slab becomes colder.
- The interaction of O_2 with a clean β-cristobalite surface produces molecular reflection, molecular sticking and dissociative sticking, being this latter process possible only at high collision energies. Normal incidence O_2 collisions produce higher dissociative and non-dissociative sticking than off normal collisions, because these skewed collisions favour the reflection processes. Rotational and vibrational excitation of O_2 reactant and the increase of surface temperature show small effects in all probabilities.
- Reflected molecules are rotationally hotter and a little translationally colder than the initial energy distributions.
- Dynamical results at thermal conditions show that the atomic adsorption over the clean surface is the predominant process but decreases when compared to an O-precovered surface due to the appearance of two competitive processes that produce $O_{2(ad)}$ and $O_{2(g)}$. Molecular non-dissociative adsoprtion is also observed.

• Microkinetic model for O/O_2 mixtures reaction over β-cristobalite:

  - Microkinetic model study (700 - 1,700 K) based on QCT data shows a large final molecular coverage at temperatures lower than 1,000 K, which could produce surface passivation at long times, whereas a large atomic coverage at higher temperatures is obtained.
  - The γ_O coefficient shows small values in the 700 - 1,700 K range ($0.01 < \gamma_O < 0.02$), almost independent on the initial mixture composition, being the atomic adsorption and ER their main contributions.
  - The γ_O coefficient increases with the temperature following an Arrhenius equation, with values close to the experimental ones.
  - An almost constant value for the β_O coefficient is obtained ($0.75 < \beta_O < 0.80$) within 700 - 1,700 K, indicating that the usual assumption that $\beta_O = 1$ seems to be inaccurate.
  - The atomic adsorption process is mostly the one producing the total energy relased to the surface.
  - There are some divergences of the calculated β_O respect the only set of available experimental values for air over β-cristobalite, although the agreement is much better respect the total energy flux transferred to the surface.

- Theoretical methods:
  - Construction of potential energy surfaces using an analytical FPLEPS or an interpolated MS one can produce similar PES, although MS seems to demand a stronger computational and personal effort. Moreover, FPLEPS energy first derivatives are better than MS ones.
  - Dynamic quasiclassical trajectory studies with restricted or full dimensional PES and using the GLO thermal bath are a reliable and powerful approach to deeply understand the main features of the different gas-surface processes.
  - Microkinetic models based on TST or/and QCT thermal rate constants are very useful for the overall description of several competing gas-surface processes, reporting reasonable γ and β coefficients as a function of pressures and temperatures.

Appendix A

One-dimension GLO model

For a GLO model in one dimension (figure A.1), the Hamiltonian[1] corresponding to the different oscillators (an effective linear harmonic chain for the ghost particle) can be written as

$$H = \frac{1}{2}m_s\left(\frac{dx_s}{dt}\right)^2 + \frac{1}{2}m_s\left(\frac{dx_g}{dt}\right)^2 + \frac{1}{2}m_s\omega_3^2 x_s^2 + \frac{1}{2}m_s\omega_1^2 x_g^2 + \frac{1}{2}m_s\omega_2^2\left(x_s - x_g\right)^2 \quad \text{(A.1)}$$

as for each oscillator $k_i = m_s\omega_i^2$, with the same mass. Introducing into the

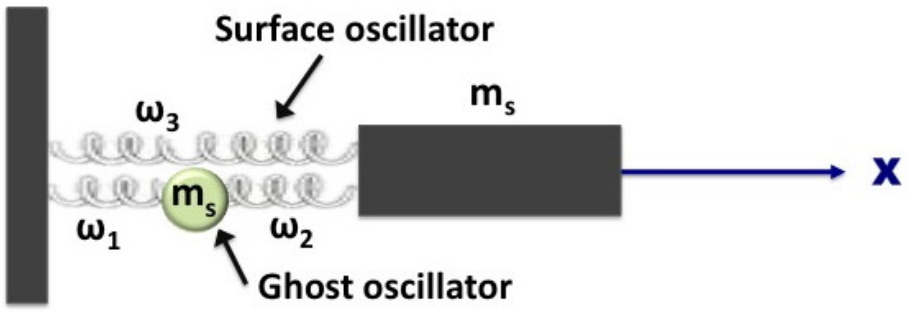

Figure A.1: Surface and ghost oscillators for one-dimensional GLO model.

[1]This appendix is written using mainly a private communication from Dr. Fabio Busnengo (Instituto de Física Rosario, CONICET and Facultad de Ciencias Exactas, Ingeniería y Agrimesura, Univ. Nacional de Rosario, Argentina)

Hamiltonian the following changes respect to the ω_i frequencies,

$$\begin{aligned} \Omega_p^2 &= \omega_2^2 + \omega_3^2 \\ \omega_0^2 &= \omega_1^2 + \omega_2^2 \\ \Lambda_0^{1/2}\omega_0 &= \omega_2^2 \end{aligned} \tag{A.2}$$

we obtain

$$H = \frac{p_{x_g}^2}{2m_s} + \frac{p_{x_s}^2}{2m_s} + \frac{1}{2}m_s\omega_0^2\left(x_g - \frac{\Lambda_0^{1/2}}{\omega_0}x_s\right)^2 + \frac{1}{2}m_s\Big(\Omega_p^2 - \Lambda_0\Big)x_s^2 \tag{A.3}$$

and defining a new variable τ,

$$\tau = x_g - \frac{\Lambda_0^{1/2}}{\omega_0}x_s \tag{A.4}$$

the Hamiltonian can be simplified even more,

$$H = \frac{p_{x_g}^2}{2m_s} + \frac{p_{x_s}^2}{2m_s} + \frac{1}{2}m_s\omega_0^2\tau^2 + \frac{1}{2}m_s\Big(\Omega_p^2 - \Lambda_0\Big)x_s^2 \tag{A.5}$$

For this Hamiltonian, the corresponding initial positions (x_s, x_g) and linear momenta (p_{x_s}, p_{x_g}) can be sampled from an 1D canonical ensemble at the surface temperature (T_{surf}) using

$$p_{x_s}(t=0) = g_1\sqrt{k_B T_{surf} m_s} \tag{A.6}$$

$$p_{x_g}(t=0) = g_2\sqrt{k_B T_{surf} m_s} \tag{A.7}$$

$$x_s(t=0) = g_3\frac{1}{\Big(\Omega_p^2 - \Lambda_0\Big)^{1/2}}\sqrt{\frac{k_B T_{surf}}{m_s}} \tag{A.8}$$

$$\tau(t=0) = g_4\frac{1}{\omega_0}\sqrt{\frac{k_B T_{surf}}{m_s}} \tag{A.9}$$

Thus, $x_g(t=0)$ can be obtained from $\tau(t=0)$,

$$x_g(t=0) = \tau(t=0) + x_s(t=0)\frac{\Lambda_0^{1/2}}{\omega_0} = \frac{1}{\omega_0}\left[g_4\sqrt{\frac{k_B T_{surf}}{m_s}} + \Lambda_0^{1/2}x_s(t=0)\right] \tag{A.10}$$

being g_i Gaussian random numbers generated with *gasdev* function.

The Hamilton equations for this system are

$$\frac{dp_{x_s}}{dt} = -\frac{\partial H}{\partial x_s}, \qquad \frac{dp_{x_g}}{dt} = -\frac{\partial H}{\partial x_g}, \qquad \frac{dx_s}{dt} = \frac{\partial H}{\partial p_{x_s}}, \qquad \frac{dx_g}{dt} = \frac{\partial H}{\partial p_{x_g}} \tag{A.11}$$

and then using equations A.1 and A.2, the following final expressions are easily derived,

$$\frac{dp_{x_s}}{dt} = -m_s\Omega_p^2 x_s + m_s\Lambda_0^{1/2}\omega_0 x_g \tag{A.12}$$

$$\frac{dp_{x_g}}{dt} = -m_s\omega_0^2 x_g + m_s\Lambda_0^{1/2}\omega_0 x_s \tag{A.13}$$

$$\frac{dx_s}{dt} = \frac{p_{x_s}}{m_s} \tag{A.14}$$

$$\frac{dx_g}{dt} = \frac{p_{x_s}}{m_s} \tag{A.15}$$

As the GLO model introduces friction and random forces into the ghost oscillator, equation A.13 has to be modified as

$$\frac{dp_{x_g}}{dt} = -m_s\omega_0^2 x_g + m_s\Lambda_0^{1/2}\omega_0 x_s - m_s\gamma_g\frac{dx_g}{dt} + f_{rand}(\Delta t) \tag{A.16}$$

For a 3D GLO model, similar expressions can be written for the y and z coordinates, using as well matrices for the different variables (e.g., $\vec{r}_g$, $\vec{r}_s$, $\hat{\omega}_0$, $\hat{\Lambda}_0^{1/2}$, $\hat{\Omega}_p$, $\hat{\gamma}_g$, ...).

Appendix B

Publications

- V. Morón, C. Arasa, R.Sayós and H.F. Busnengo, AIP Conf. Proc. **1084**, 682 (2008).
- R. Sayós, V. Morón, C. Arasa and H.F. Busnengo, in *Proceedings of the 6th European Symposium on Aerothermodynamics for Space Vehicles*, (ESA, Versailles, France, 2008). No. SP-659, Session 28, 1-7.
- C. Arasa, V. Morón, H.F. Busnengo and R. Sayós, Surface Science **603**, 2742 (2009).
- V. Morón, P. Gammallo and R. Sayós, Theoretical Chemistry Accounts **128**, 683 (2011).
- V. Morón, P. Gamallo, L. Martin-Gondre, C. Crespos, P. Larregaray and R. Sayós, Physical Chemistry Chemical Physics **13**, 17494 (2011)
- The work was also presented in several International (4 invited conferences, 2 oral communications and 7 posters) and National (4 oral communications and 2 posters) conferences.

Appendix C

Summary in catalan

C.1 Introducció

L'objectiu d'aquest treball és estudiar les reaccions químiques que tenen lloc entre les espècies en fase gas i les superfícies cristal·lines. La dinàmica dels processos que tenen lloc sobre els sistemes de protecció tèrmica (*Thermal Protection Systems*, TPS) dels vehicles espacials tenen una gran repercusió industrial i econòmica, tot i que el coneixement que es té d'aquests és més aviat escàs. Aquests TPS són els responsables de la protecció dels vehicles espacials en els quals hi pot haver molta informació experimental emmagatzemada, intrumentació científica i tecnològica important i fins i tot vides humanes. La fallida del TPS pot implicar la pèrdua de grans inversions econòmiques, de temps de treball i fins i tot pot posar en perill la vida de les persones que hi viatgen, com va passar l'any 2003 a l'accident que va patir el Columbia.

Els TPS han d'estar dissenyats per a resistir condicions extremes durant la reentrada a grans velocitats (Match 30 $\sim$ 10,208 m/s) a l'atmosfera terrestre. Durant aquesta reentrada, l'escalfament de les superfícies d'aquests vehicles es produeix a causa de la fricció i dels processos catalítics entre les superfícies i el gas present a l'atmosfera (format principalment per un 78% de N_2, 21% de O_2 i un 1% d'Ar). Les temperatures que s'assoleixen poden oscil·lar entre 500 i 1,900 K depenent de les zones del vehicle. El coeficient catalític d'aquests tipus de materials ha de ser baix per tal de minimitzar el flux d'energia tèrmica cap a la superfície. Actualment, existeix una gran varietat de materials emprats com a TPS com rajoles de sílice, carboni reforçat, nylon,...

Les simulacions computacionals de dinàmica de fluids (*computer fluid dynamics*, CFD) es duen a terme per tal de predir els aspectes més importants dels processos durant la reentrada. Aquestes simulacions requereixen de l'ús de dos coeficients per tal d'incloure els efectes catalítics de la superfície: a) el coeficient

de recombinació atòmica γ i b) el coeficient d'acomodació d'energia química β. Tot i que els valors que poden prendre aquests coeficients per definició es troben entre $0 \leqslant \gamma, \beta \leqslant 1$, la manca d'informació sobre els valors reals implica una descripció poc detallada de la contribució catalítica en els processos de reentrada.

Per tal d'ampliar el coneixement de la reentrada i específicament, dels processos catalítics que tenen lloc sobre aquests materials, la química teòrica i computacional pot tenir un paper molt important. Així, els estudis dinàmics poden donar informació microscòpica de la manera en la què tenen lloc i quin és el paper de la superfície. A més a més, la construcció de models cinètics pot donar informació sobre els coeficients γ i β per a les diferents espècies en fase gas sobre els diversos materials sòlids.

El present resum es divideix en dues grans seccions, que tracten els processos elementals de l'oxigen atòmic i molecular sobre dues superfícies sòlides. Tot i que l'oxigen és la segona espècie més abundant a l'atmosfera, la baixa energia de dissociació respecte al nitrogen suggereix que l'oxigen aquests hi tindrà un paper predominant.

A la primera part, s'estudien els processos sobre el grafit, que s'ha considerat una bona aproximació al carboni reforçat. Per a aquest sistema es duu a terme un estudi DFT de la interacció del gas amb el sòlid, s'han construït dues superfícies d'energia potential (SEP) i s'ha realitzat un model microcinètic amb els processos principals.

A la segona part, s'ha completat l'estudi dinàmic sobre la β-cristobalita emprant una SEP construïda anteriorment. Seguidament es presenta un model microcinètic realitzat a partir de la informació dinàmica obtenida anteriorment. Finalment, es presenten les conclusions principals del treball.

C.2 Estudi d' O/O_2 sobre grafit (0001)

• Introducció

Els materials fets principalment per carboni estan rebent en els darrers anys una atenció especial en la indústria espacial, degut al seu pes lleuger i gran resistència tèrmica i mecànica. Així, per exemple, el carboni reforçat s'utilitza com a sistema de protecció tèrmica, al nas del transbordador espacial (*shuttle*).

Els vehicles de baixa òrbita (Low Earth Orbit, LEO) orbiten a una distància d'uns 160 - 2,000 Km sobre la superfície de la Terra, on l'oxigen atòmic és una de les principals espècies presents. Aquest oxigen pot col·lisionar amb la superfície dels vehicles espacials a energies de translació molt elevades (al voltant de 4.5 ± 1.0 eV, degut a la gran velocitat, que pot arribar als 7.5 Km/s), produint una degradació notable del TPS (51). A més, durant la reentrada dels vols hipersònics a l'atmosfera terrestre (per exemple, el transbordador espacial), no només l'oxigen atòmic sinó que també l'oxigen molecular pot ser rellevant per tal d'entendre de forma completa la gran quantitat d'energia transferida al TPS i el comportament d'aquest sota aquestes condicions tan extremes. Per tant, un estudi en profunditat de tots els processos elementals que es poden donar sobre la superfície del TPS és essencial per a la tecnologia aeroespacial. En principi, cal considerar els processos heterogenis següents: a) adsorció atòmica ($O_{(g)} + s \rightarrow O_{ad}$), b) adsorció de l'$O_2$ dissociativa ($O_{2(g)} + 2s \rightarrow O_{ad} + O_{ad}$) i no dissociativa ($O_2 + s \rightarrow O_{2(ad)}$), c) reacció d'Eley-Rideal (ER, $O_{(g)} + O_{ad} \rightarrow O_{2(g)} + s$) d) reaccció de Langmuir-Hinshelwood (LH, $O_{ad} + O_{ad} \rightarrow O_{2(g)} + 2s$) i e) arrancament d'àtoms de carboni de la superfície de grafit per acció de l'oxigen atòmic (*etching*, $O_{(g)} + C - s \rightarrow CO_{(g)} + s$).

Existeix un gran nombre d'estudis teòrics que fan referència a la interacció d'oxigen molecular sobre grafit (53, 54, 55, 56, 57), grafè (58, 59) i nanotubs de carboni (54, 60), sense donar una panoràmica global de la reactivitat d'O/O_2 sobre les diferents superfícies. També es troben a la biliografia treballs experimentals de la interacció d'oxigen hipertèrmic, que permeten entendre la degradació d'aquest tipus de superfícies a altes energies (51, 68, 69), ja que en aquestes col·lisions es formen també molècules de CO i CO_2.

Per tal d'aprofundir en l'enteniment dels processos heterogenis que es produeixen damunt d'aquestes superfícies, es realitza un estudi d'aquests processos elementals produïts per oxigen atòmic i molecular sobre una superfíe de grafit (0001) neta a nivell DFT. Així, es caracteritzen els punts estacionaris (mínims, estats de transició, ...) per als diferents processos i per a diferents recobriments. Aquestes dades, tant energètiques com geomètriques, ens permetran obtenir les constants de velocitat associades a aquests processos mitjançant la Teoria de l'Estat de Transició (Transition State Theory, TST). Aquestes constants es fan servir simultàniament dins un modèl microcinètic, que permetrà l'estudi global dels diferents processos a unes temperatures i pressions totals i/o parcials deter-

minades de les espècies involucrades. A més a més, aquestes dades facilitaran el càlcul del coeficient de recombinació atòmica (γ_O), necessari a les simulacions CFD (52).

També es realitza un estudi de la dinàmica dels processos elementals per tal d'entendre millor el mecanisme associat, així com les distribucions angular i energètiques associades a cada un dels processos. Els resultats obtinguts es comparen amb una sèrie d'experiments (71, 72) per tal de donar explicació a les observacions experimentals i avaluar la precisió de les simulacions realitzades.

• Estudi DFT

Abans d'iniciar l'estudi de l'adsorció pròpiament dit, cal obtenir una correcta descripció de la cel·la unitat així com del *bulk* del sòlid. L'estructura del grafit consta de capes de carboni unides per febles forçes de van der Waals. A la mateixa capa, els carbonis es disposen en forma hexagonal i la cel·la unitat és del tipus romboédrica (figura C.1). Es realitza l'estudi del *bulk* del grafit amb

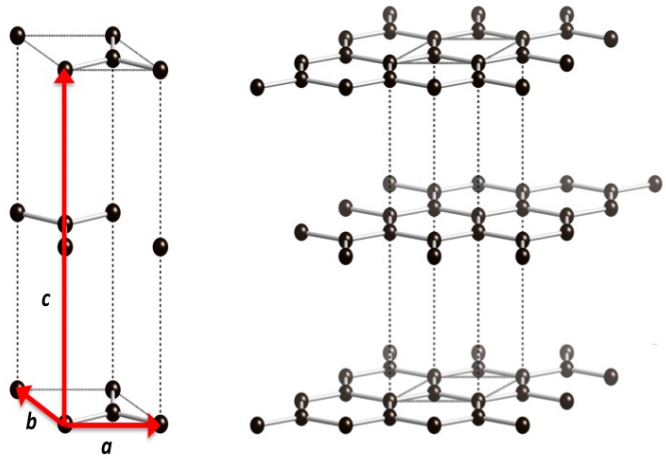

Figure C.1: Cel·la unitat del grafit amb els paràmetres a, b i c a l'esquerra. Repetició espacial de la cel·la unitat per representar el sòlid.

diferents funcionals i expressions per l'energia d'intercanvi-correlació obtenint uns paràmetres de cel·la propers als experimentals (55, 56) (taula C.1). Donat que per als càlculs realitzats amb el funcional Revised Perdew-Burke-Ernzerhof (RPBE) els resultats energètics i geomètrics són els més propers als experimentals, es farà servir aquest per a realitzar l'estudi de la interacció d' O i O_2 amb el grafit.

S'utilitza el métode d'*slab* amb dues capes de carbonis separades per un buit de més de 15 Å de separació per a l'estudi de l'adsorció atòmica de l'oxigen sobre

Table C.1: Comparació dels paràmetres calculats i experimentals per al *bulk* de grafit.

Method	$a = b$ (Å)	c (Å)	d_{C-C} (Å)	E_{coh} (eV/atom)[a]	B_{iso} (GPa)[a]	B'_{iso}
PW91	2.465	7.698	1.423	7.856	275.4	4.04
PBE	2.467	7.816	1.425	7.847	277.4	3.69
RPBE	2.467	8.022	1.425	7.516	270.3	4.29
LDA/CA[b]	2.441	6.64	–	8.903	–	–
PW91[b]	2.461	∼9.0	–	7.865	–	–
Exp.	2.456[c]	6.696[c]	1.418[c]	7.371±0.005[d]	318±11(0K)[e] 286±11(300K)[e]	13.6 (295 K)[f]

[a] *E_{coh}, B_{iso} and B'_{iso} van ser calculats emprant el valor experimental per al paràmetre c.*

[b] *Càlculs prèvis amb LDA/Ceperley-Alder and GGA/Perdew-Wang 91 i pseudopotencials ultrasoft (85).*

[c] *Valors experimentals (73).*

[d] *Valors experimentals (86) derivats de $\Delta_f H°(0\ K)$ per al procés: $C(grafit) \rightarrow C(g, ideal)$.*

[e] *Valors experimentals (87, 88) obtinguts de constants elàstiques (C_{ij}) a partir de la fórmula $B_{iso} = \frac{2}{9}(C_{11} + C_{12}) + \frac{4}{9}C_{13} + \frac{1}{9}C_{33}$, (89).*

[f] *Valor experimental(87) obtingut de la derivada de la pressió de l'equació anterior.*

tres setis (figura C.2): B, T1 i T2 amb diferents condicions de recobriment i considerant la superficie rígida o bé introduint certa relaxació de les capes de carboni (taula C.2), observant que la posició d'adsorció sobre el bridge (B) és en tots els casos la més estable. S'observa també un efecte d'estabilització important

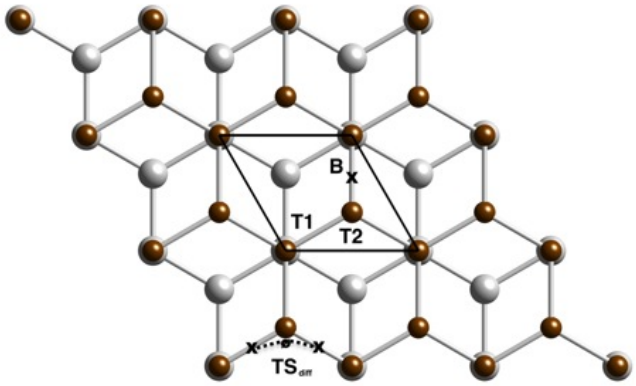

Figure C.2: Vista superior del *slab* de grafit (0001) amb dues capes de carbonis on es representen els diferents llocs d'adsorció considerats: B, T1 i T2. Els àtoms de la segona capa es representen amb una grandària major i un color més clar per facilitar la distinció dels de la primera capa. Es mostra també l'estat de transició de la difusió d' O entre dos B. Es delimita la cel·la unitat (1×1) mitjançant una línia.

amb la relaxació de la superficie. La dependència de l'energia d'adsorció amb el recobriment té comportaments inversos segons si es té en compte la relaxació de l'*slab* o no. Així, una disminució del recobriment sobre una superfície no relaxada disminueix l'estabilització, mentre que tenint en compte la relaxació l'àtom s'adsorbeix més energèticament. També s'aconsegueix el càlcul dels estats de transició dels processos elementals de l'adsorció i difusió atòmica i dels processos d'Eley-Rideal i Langmuir-Hinshelwood (taules C.3 i C.4), observant en tots els casos i als diferents recobriments estudiats processos activats. Es realitza un petit estudi de l'*etching* d'àtoms de carboni de la superfície per l'acció de l'oxigen atòmic, obtenit una barrera per al procés molt elevada ($\Delta E_0^{\neq}$= 5.362 eV) com per ser considerat rellevant a les temperatures de treball (300 - 1,500 K). El càlculs d'adsorció molecular posen de manifest molt poca tendència a l'adsorció, observant un petit mínim de fisisorció.

Table C.2: Propietats calculades per l'adsorció de l' O sobre la superfície basal de grafit (0001) sense relaxació de l'slab (a dalt) o per al bridge considerant la relaxació (a baix).

Coverage (%)[a]	Site[b]	E_{ad} (eV)	Z_O (Å)	d_{O-C} (Å)	ν_i (cm^{-1})[c] $\perp$	$\parallel$	
50/100	T1	-0.816	1.544	1.544	574.5	367.2i	374.2i
	T2	-0.811	1.509	1.509	571.0	407.6i	410.5i
	B	0.881	1.251	1.440	822.6	610.6	379.7
12.5/25	T1	0.281	1.556	1.556	542.7	89.0i	95.1i
	T2	0.308	1.554	1.554	583.2	196.1i	201.2i
	B	0.660	1.385	1.557	548.7	325.8	315.2
5.5/11.1	T1	0.0215	1.589	1.589	489.7	142.0	133.1
	T2	0.0679	1.584	1.584	526.8	151.7i	170.5i
	B	0.541	1.384	1.557	538.3	389.4	350.0

Coverage (%)	E_{ad} (eV)	Z_O (Å)[d]	Z_C (Å)[d]	d_{O-C} (Å)	d_{C-C} (Å)	ν_i (cm^{-1})[f] $\perp$	$\parallel$	
50/100	0.945	1.254	-[e]	1.437	1.432	830.7	617.8	400.7
12.5/25	1.283	1.532	0.246	1.482	1.472	652.4	411.3	337.2
5.5/11.1	1.255	1.547	0.267	1.478	1.479	655.2	438.1	337.0

*La geometria de l'*slab *va ser fixada a l'òptima calculada (d_{C-C} = 1.425 Å) derivada dels càlculs DFT sense O, fixant la distància entre capes (d_{12}) al valor experimental de 3.347 Å.*

[a] *El recobriment es calcula respecte els llocs* top *(O/C %) o els* bridge *(O/bridge %) per facilitar la comparació amb estudis previs.*

[b] *Per els llocs d'adsorció T1 i T2, només la variable Z_O es va optimitzar.*

[c] *Les freqüències harmòniques de vibració es calculen respecte l'adsorbat sobre el substrat rígid. La primera correspon a una vibració perpendicular a la superfície mentres que les altres a les vibracions paral·leles.*

[d] *z=0 per a la primera capa formada per àtoms de carboni sense incloure els àtoms de carboni just per sota de l'oxigen atacant.*

[e] *Per al recobriment més gran (50/100 %), la relaxació del carboni implica que tota la primera capa es desplaçi fins a una distància d_{12} = 3.957 Å). Per a altres recobriments la distància es manté fixa al valor experimental d_{12}= 3.347 Å.*

[f] *Freqüències vibracionals harmòniques de l'adsorbat atòmic respecte del sòlid rígid. La primera correspon a una vibració perpendicular i les altres a vibracions paral·leles sobre la superfície de grafit.*

Table C.3: Propietats calculades dels estats de transició per l'adsorció i la difusió de l' O sobre la superfí de grafit (0001).

Process and coverage[a]	$\Delta E^{\neq}$ (eV)[b]	Z_O (Å)[c]	d_{O-C} (Å)[c]		ν_i (cm^{-1})[d]		
					$\perp$	$\parallel$	
$O_g + s \rightarrow O_{ad}$ *(adsorption)*							
50/100%	0.67(0.69)	1.755	1.878	1.910	535.4i	220.2	123.4
12.5/25%	0.31(0.32)	1.874	1.940	2.090	734.1i	103.8	47.5
	0.19(0.13[e])	2.060	1.863	1.918	112.1i	266.7	171.1
5.5/11%	0.28[f]	1.848	1.981	1.981	-	-	-
$O_{ad} + s' \rightarrow O_{ad'} + s$ *(diffusion)*							
50/100%	1.43(1.49)	1.425	1.955		675.1	611.7i	306.4
12.5/25%	0.38(0.42)	1.533	1.555		549.7	188.6i	113.0
	0.73(0.70)[e]	1.718	1.421		709.6	157.3	101.7i
5.5/11.1%	0.47(0.51)	1.585	1.588		519.9	169.8	97.8i

*La geometria de l'*slab *(dues capes de C) va ser fixada a l'òptima calculada (d_{C-C} = 1.425 Å) derivada dels càlculs DFT sense O, fixant la distància entre capes (d_{12}) al valor experimental de 3.347 Å.*

[a] s o s' corresponen als llocs d'adsorció tipus bridge sobre l'enllaç C-C.

[b] Les barreres energètiques estan referides respecte els reactants (tenint en compte l'energia de punt zero entre parèntesi).

[c] L'estat de transició per a l'adsorció es troba pràcticament sobre l'enllaç C-C i per a la difusió entre dos àtoms de carboni no adjacents (figura C.2).

[c] Les freqüències harmòniques de vibració es calculen respecte l'adsorbat sobre el substrat rígid. La primera correspon a una vibració perpendicular a la superfície mentres que les altres a les vibracions paral·leles.

[e] En aquest cas, els carbonis directament enllaçats amb l' O es van permetre relaxar en totes les direccions (Z_C= 0.314 i 0.297 Å per el TS d'adsorció i difusió, respectivament).

[f] L'estat de transició es va derivar aproximadament de l'encreuament entre les corbes singlet i triplet.

Table C.4: Propietats calculades dels estats de transició per als processos amb O tipus Eley-Rideal i Langmuir-Hinshelwood sobre la superfície basal de grafit (0001).

Process and coverage[a]	$\Delta E^{\neq}$	Z_O		d_{O-C}		d_{O-O}	ν_i (cm^{-1})					
	(eV)[b]	(Å)[c]		d_a, d_b^c(Å)		(Å)	$\perp$	$\parallel$				
O(g) + O_{ad} → O_2+s *(ER reaction)*												
50/100%	1.11 (1.06)	1.525	3.235	1.685	1.682	1.711	962.4i	246.7	339.7	152.8	124.2	63.5
12.5/25%	0.10 (0.076)	1.499	3.492	1.647	1.672	2.024	527.9i	209.5	301.8	268.4	87.7i	33.9
O_{ad} + O_{ad} → $O_{2(g)}$+s *(LH reaction)*												
50/100%	1.91 (1.87)	1.569	1.570	1.609	1.610	1.736	611.6i	496.8	397.4	330.0	256.2	196.0
11.1/22.2%	1.28[e]	1.600	1.600	1.625	1.622	1.774	–					

*La geometria de l'*slab *(dues capes de C) va ser fixada a l'òptima calculada (d_{C-C}=1.425 Å), derivada dels càlculs DFT sense O, fixant la distància entre capes (d_{12}) al valor experimental de 3.347 Å.*

[a] *s or s′ corresponen als llocs d'adsorciò tipus bridge sobre l'enllaç C-C . Per a la reacció LH els recobriments es doblen respecte l'ER o l'adsorció, utilitzant la mateixa cel·la unitat.*

[b] *Les barreres energètiques estan referides respecte els reactants (tenint en compte l'energia de punt zero entre parèntesi).*

[c] *Per l'estat de transició de la reacció LH l'angle dihedre <OCCO és 24.7° per a un recobriment del 25/50% i 16.8° per a 11.1/22.2%.*

[d] *Les freqüències harmòniques de vibració es calculen respecte l'adsorbat sobre el substrat rígid. Aproximadament, les dues primeres corresponen a la vibració perpendicular i la resta a les paral·leles per a l'ER. En el cas de LH, la freqüència imaginària presenta una barreja de moviments paral·lels i perpendiculars.*

[e] *El TS es va derivar aproximadament d'una xarxa de punts.*

• **Model microcinètic**

A partir de les dades DFT calculades prèviament (energies i freqüències de vibració), es calculen les funcions de partició a través de la teoría de l'estat de transició que s'utilitzen per al càlcul de les constants de velocitat de cadascun dels processos elementals (figura C.3) a diferents temperatures.

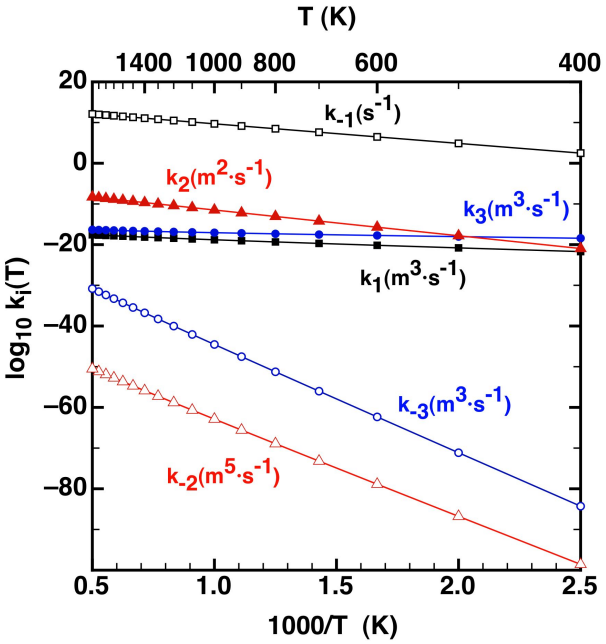

Figure C.3: Constants de velocitat tèrmiques a nivell TST calculades per als diferents processos heterogenis introduïts al model microcinètic proposat, basades en dades DFT per a un recobriment del 12.5/25% (11.1/22.2% per a la reacció LH). Únicament les constants amb les mateixes unitats (definides al gràfic) es poden comparar directament. Els punts estan connectats amb una línia per guiar la vista.

El model permet estudiar l'evolució del recobriment de la superfície al llarg del temps fins a l'estat estacionari (figura C.4), donant així una primera idea de l'efecte dels diversos processos elementals sobre la superfície. A més a més, també ens permet fer una estimació del recobriment atòmic i del coeficient γ_O a diferents condicions de temperatura i composició inicial del sistema (figura C.5).

S'observa un recobriment final petit a totes les condicions estudiades de pressió i temperatura, observant un màxim d'adsorció per a temperatures entre 400 i 500 K, segons la composició inicial del sistema. El coeficient de recombinació γ_O presenta un comportament molt similar al recobriment. L'adsorció i el procés d'ER són els que presenten una contribució més elevada al coefficient (γ_O) a

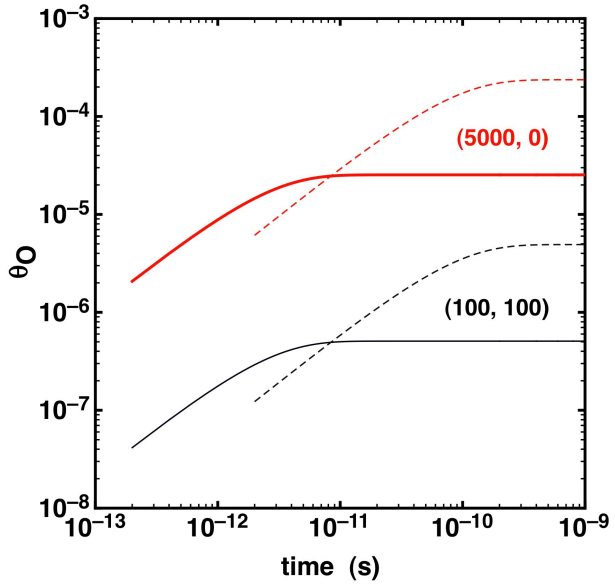

Figure C.4: Evolució al llarg del temps del recobriment atòmic per dues composicions inicials de O/O_2: (100, 100 Pa) i (5000, 0 Pa) a 700 K (línia de punts) i 900 K (línia contínua).

temperatures baixes, mentres que a temperatures més elevades l'adsorció i la desorció atòmica són els processos predominants.

• Estudi QCT de la interacció d'un àtom d'oxigen amb grafit

S'ha realitzat un estudi dinàmic mitjançant el mètode de trajectòries quasiclàssiques de la interacció d'un àtom d'oxigen sobre una superfície de grafit. Per a això, s'han construït dues superfícies d'energia potencial, una d'analítica mitjançant el mètode *Flexible Periodic London-Eyring-Polayi-Sato* (20, 21, 22) (FPLEPS) i una interpolada mitjançant una adaptació del mètode *Modified Shepard* (27, 28, 29, 30)(MS). S'ha fet la caracterització d'ambdues SEPs, observant un comportament molt similar tot i que la superfície MS es capaç de reproduir el mínim de fisisorció a distàncies de la superfície pròximes als 2 - 3 Å. No obstant això, queden ben descrits els trets observats a l'estudi DFT de l'adsorció atòmica. A la figura C.6 es mostren corbes energètiques en funció de Z_O sobre els setis més importants, mostrant petites diferències per a les dues SEP. És més important veure les diferències sobre els setis com es mostren a la figura C.7.

Es calculen les probabilitats de adsorció i reflexió atòmiques sense tenir o tenint en compte la temperatura de la superfície amb les dues SEP a incidència normal i no normal ($\theta_v = 45°$). Els resultats obtinguts sense tenir en compte

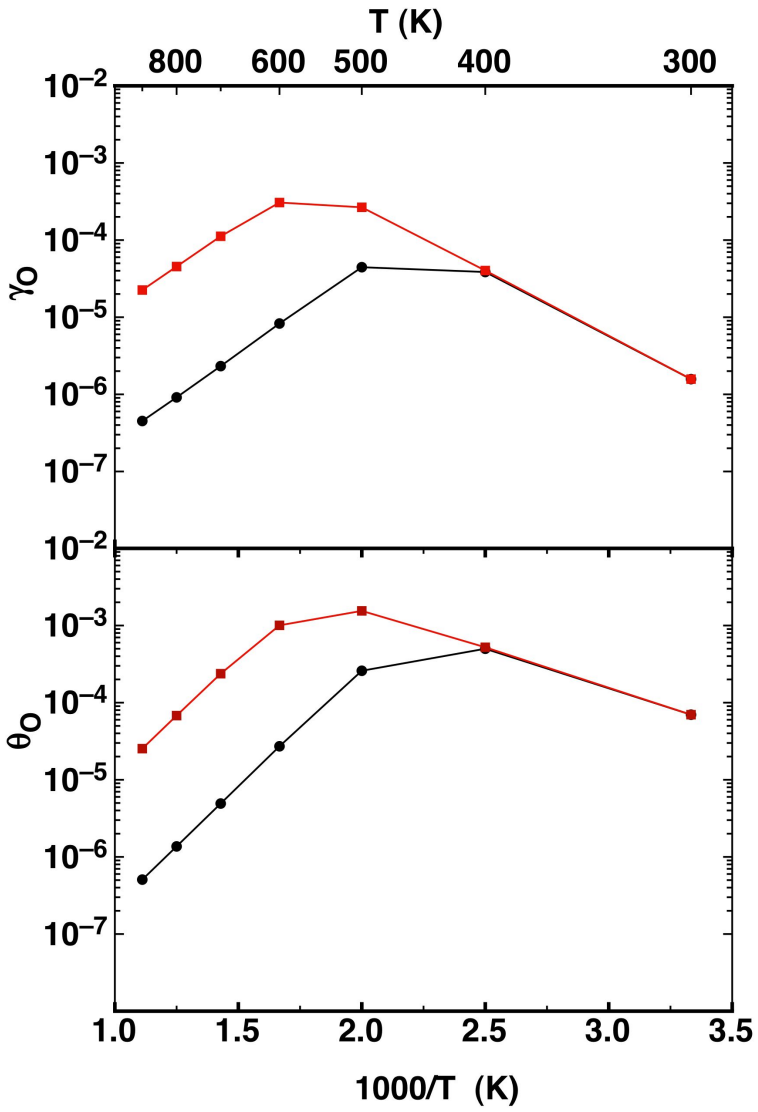

Figure C.5: Recobriment atòmic i coeficient γ_O depenent de la temperatura per a dues composicions inicials d' O/O_2: (100, 100 Pa) amb cercles negres i (5,000, 0 Pa) quadrats vermells.

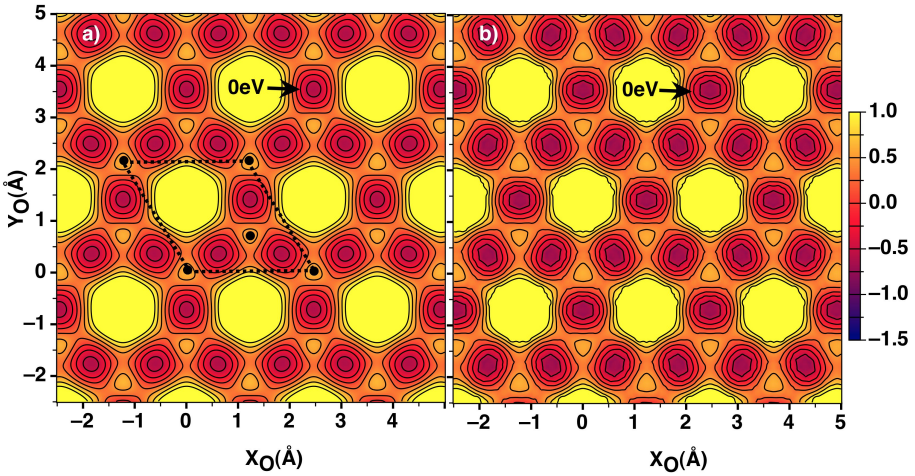

Figure C.6: Corbes d'energia per a una Z_O =1.3 Å fixada per a a) FPLEPS i b) MS.

la temperatura de la superfície i incloent-la són similars (figura C.8), tot i que les probabilitats d'adsorció són en general més altes quan l'àtom i la superfície són capaços d'intercanviar energia, tal com passa en el cas d'afegir l'efecte de la temperatura. En tot cas s'observa que generalment la reflexió és més important que l'adsorció. Les probabilitats d'adsorció són més altes per a incidència normal que per θ_v= 45°. També s'observa un petit increment de l'adsorció a temperatures més baixes. Els resultats obtinguts amb les dues SEP són comparables exceptuant a energies de col·lisió baixes, on el mínim de fisisorció descrit a la SEP MS provoca un augment en l'adsorció que no s'observa sobre la superfície FPLEPS (figura C.8).

S'han analitzat també els angles de dispersió atòmica ($\theta_v^{'}$) sense tenir o tenint en compte l'efecte de la temperatura (figura C.9) amb les dues SEP. A energies baixes, s'observen angles de dispersió propers a 10° i 45° per a incidència normal i θ_v = 45°, respectivament, mentres que a energies més elevades (E_{col} = 1.3 eV) la distribució observada es més ampla.

En el cas de tenir en compte la temperatura de la superfície, l'intercanvi energètic entre l'àtom incident i l'*slab* és possible. S'analitza doncs la distribució de la variació de l'energia cinètica a l'inici i al final de les trajectòries de reflexió a diferents condicions inicials (E_{col} = 0.25, 0.5 i 1.3 eV amb T_{surf}= 300 i 900 K, figura C.10). S'observa un comportament similar per a les dues SEP utilitzades. En general, la transferència d'energia es produeix de l'àtom cap a l'*slab* provocant una disminució en la energía cinètica final de l'àtom, tot i que a les energíes més baixes hi ha una certa quantitat de trajectòries on l'àtom l'ha vist incrementada, efecte que es fa més important en augmentar la temperatura de la superfície.

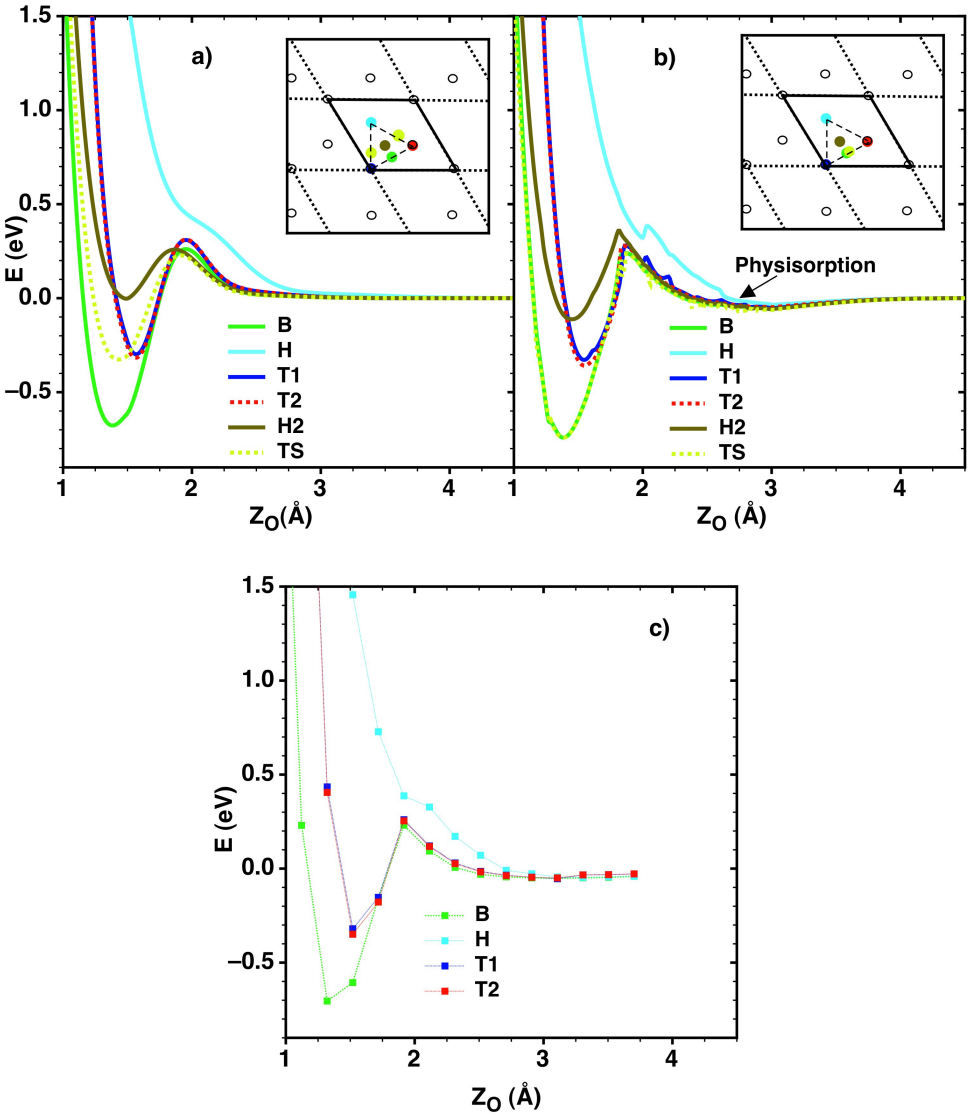

Figure C.7: Interacció de l'oxigen a diferents distàncies de la superfície sobre diferents *sites* (X_O i Y_O fixades) per a) FPLEPS, b) MS and c) dades DFT. Les corbes anomenades TS es calculen sobre els valors de X_O i Y_O on es troba la barrera d'adsorció mínima.

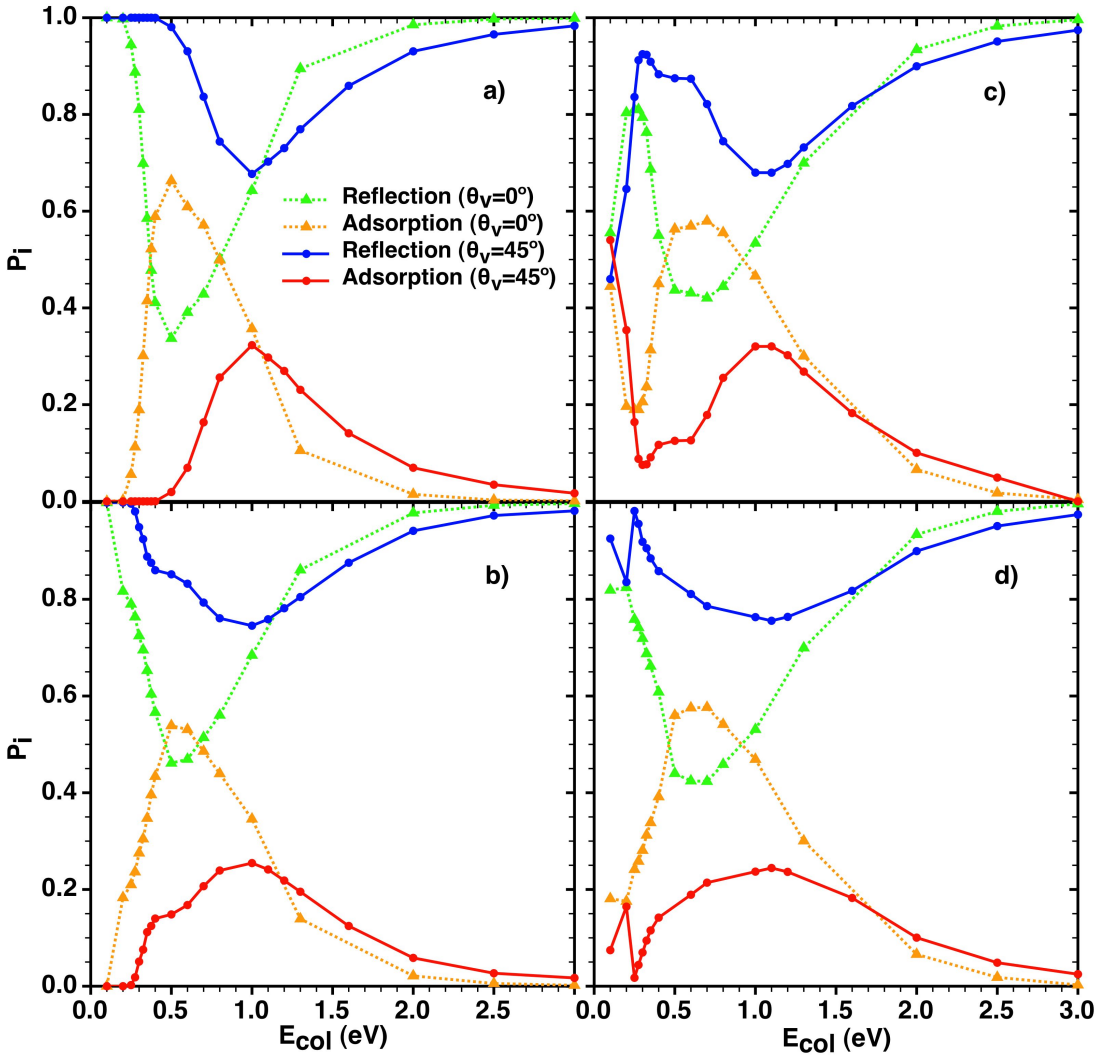

Figure C.8: Probabilitats de reacció per a la interacció d'un àtom d'oxigen a T_{surf} = 300 K (a dalt) i 900 K (a baix) per a) i b) FPLEPS i c) i d) MS i per a dos angles d'incidència (θ_v =0° i 45°).

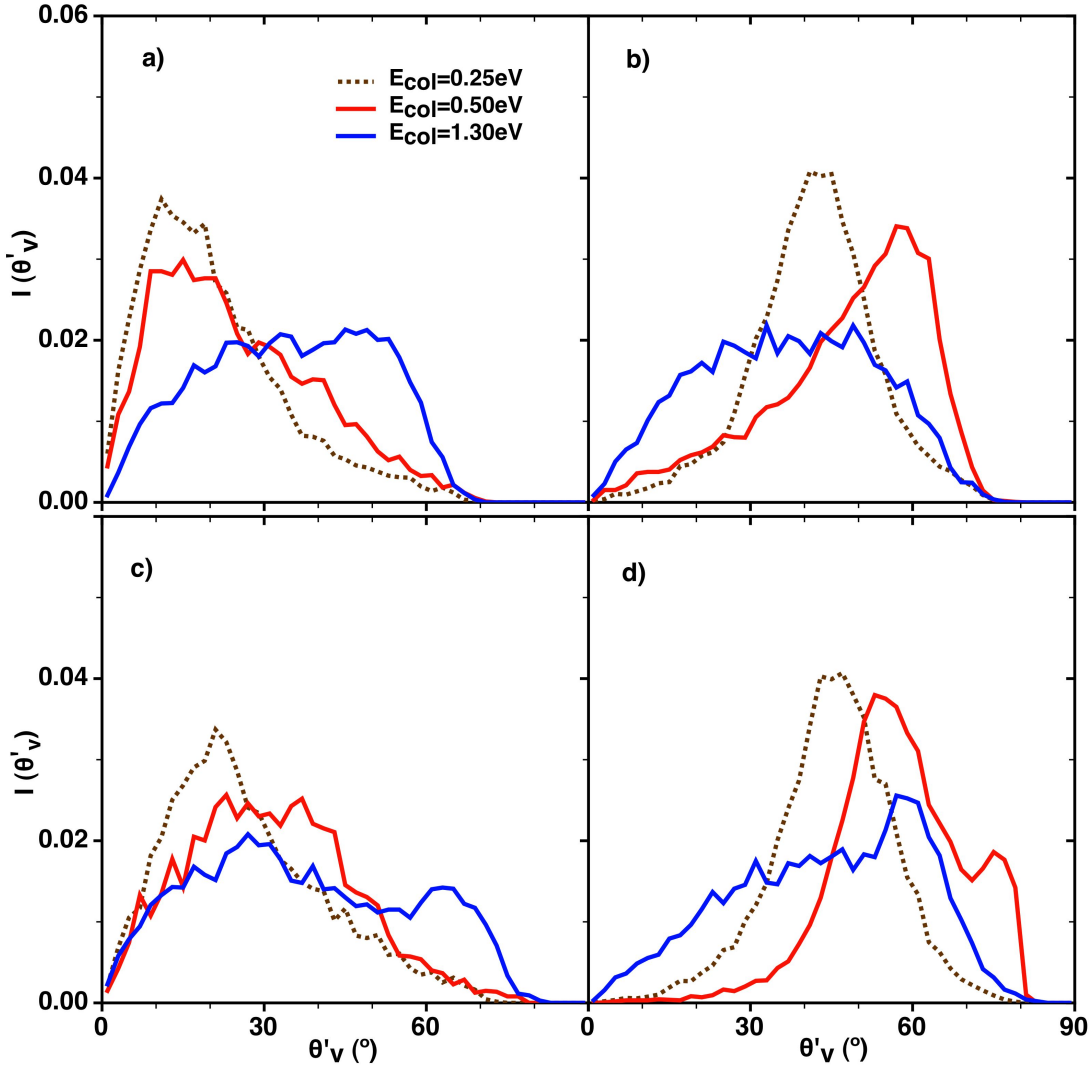

Figure C.9: Distribució dels angles de dispersió a T_{surf} =900 K per a FPLEPS (esquerra) i MS (dreta) a a) i c) $\theta_v = 0°$ i b i d) $\theta_v = 45°$.

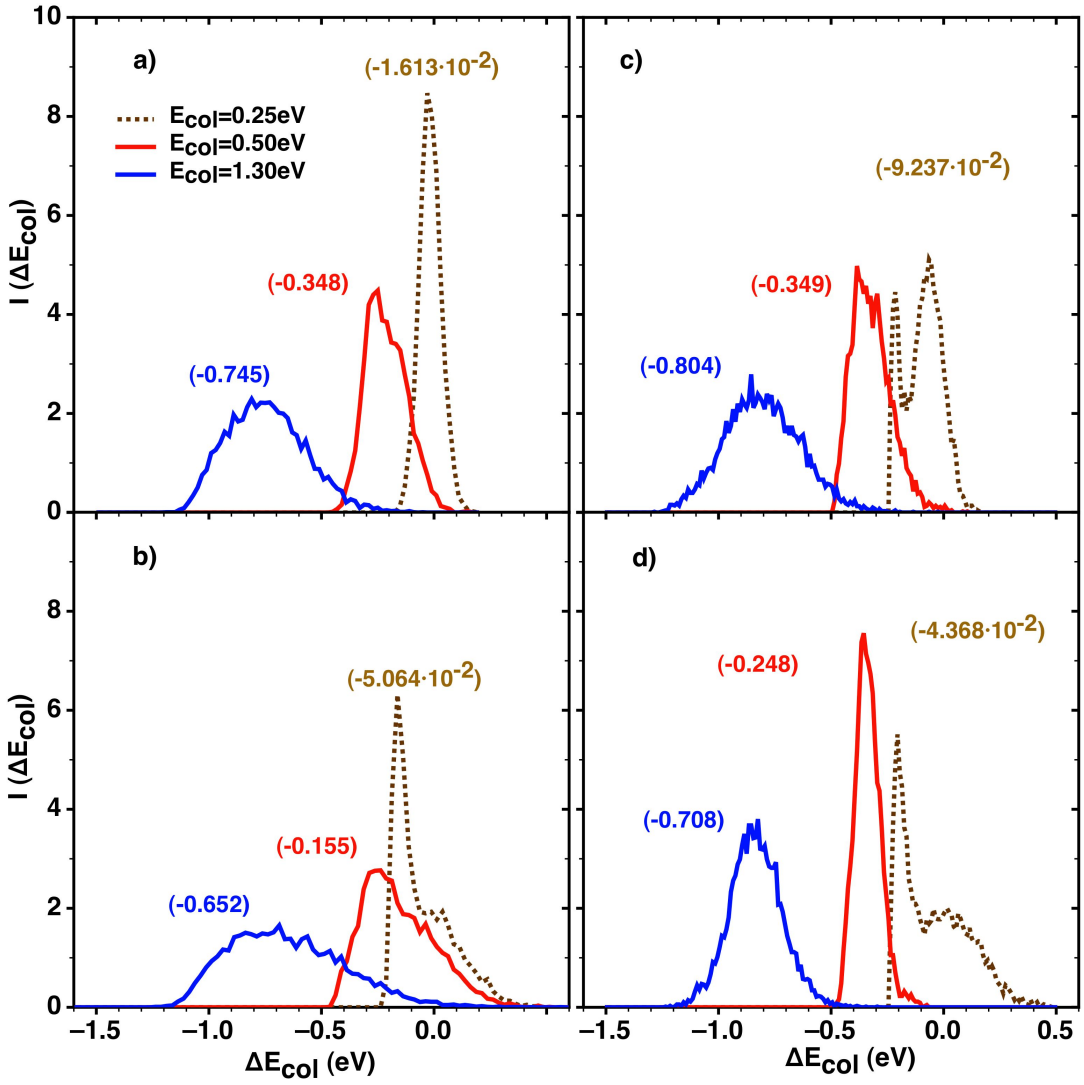

Figure C.10: Intercanvi d'energia de col·lisió (ΔE_{col}) dels àtoms dispersats per a $\theta_v = 0°$ a T_{surf} =300 K (a dalt) i 900 K (a baix) per a) i b) FPLEPS i c) i d) MS.

Finalment, es realitzen una sèrie de càlculs quasitèrmics, on $T_{surf} = T_O = T$ a dos angles d'incidència inicial ($\theta_v = 0°$ i $45°$). Les energies de col·lisió inicials dels àtoms a l'intèrval de temperatures estudiat (300 - 1,500 K) són baixes. Així doncs, les probabilitats d'adsorció i anglesde dispersió observats són similars als estudiats per al cas estat específic a energies inicials baixes. De la mateixa manera que en els resultats previs, s'obtenen comportaments molt similars amb les dues SEP, exceptuant la fisisorció que s'observa sobre la superfície MS degut al mínim descrit en aquesta (figura C.7), i que no apareix en el cas de la FPLEPS.

• Estudi QCT de la interacció de dos àtoms d'oxigen amb grafit

Per a l'estudi de la dinàmica de la interacció de dos atoms d'oxigen sobre la superfície de grafit es construeix una SEP analítica amb el mètode FPLEPS. Aquesta superfície és vàlida tant per a l'estudi de la interacció d'un àtom d'oxigen sobre una superfície de grafit precoberta d'oxigen com per a la interacció de l'oxigen molecular. A la figura C.11 es mostren dos grafics amb corbes d'energia per a diferents Z_{O_A} i Z_{O_B} dels àtoms d'oxigen fixats sobre dos *sites* B consecutius i per als dos oxigens sobre el mateix seti B. Es representen també amb dos punts

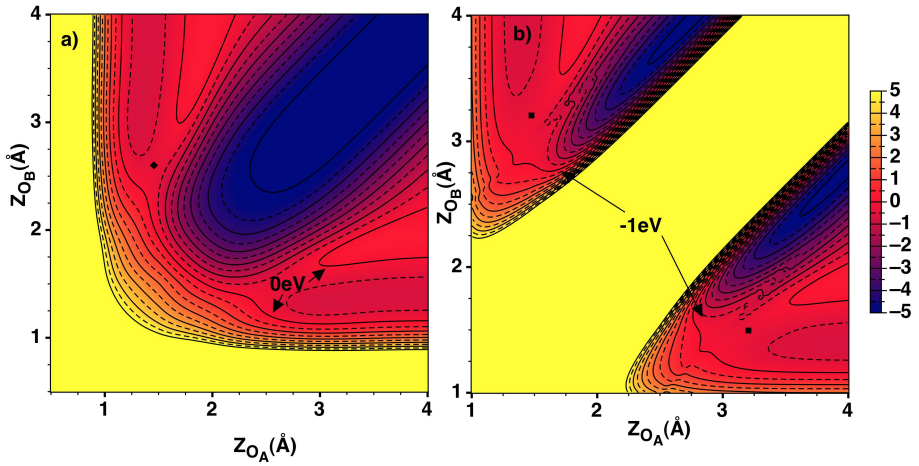

Figure C.11: Corbes d'energia per a X_{O_A}, Y_{O_A} i X_{O_B}, Y_{O_B} fixades a) sobre dos posicions B consecutives a una distància de 1.214 Å i b) tots dos àtoms sobre el mateix B (configuració perpendicular). El TS aproximat per la reacció ER s'indica amb un quadrat negre. La separació energètica entre línies és de 0.5 eV.

negres els possibles estats de transició per a una reacció d'Eley-Rideal. A la figura C.12 es presenten dos grafics amb els contorns d'energia per a dos possibles processos de dissociació molecular sobre la superfície, observant un procés molt endotèrmic ($\sim$ 4 eV) amb una barrera elevada ($\sim$ 5.7 eV).

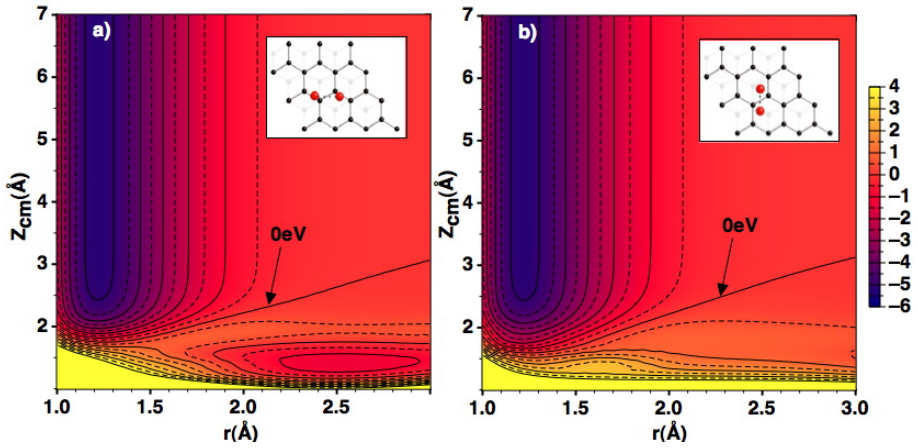

Figure C.12: Corbes d'energia per a X_{cm}=0.627 Å, Y_{cm} =0.362 Å a diverses Z_{cm} i r per a) $\phi = 0°$ i b) $\phi = 90°$ i $\theta = 90°$. La separació energètica entre línies és de 0.5 eV. El zero d'energies correspon a $O_{(g)} + O_{(g)} + slab$.

L'estudi dinàmic considerant la interacció d'un àtom en fase gas sobre una superfície precoberta d' O es realitza a diferents energies de col·lisió inicials sobre un *slab* de grafit sense i amb l'efecte de la temperatura. Els resultats obtinguts en ambdós casos són similars. Es presenta a la figura C.13 les probabilitats dels diferents processos possibles per a incidència normal i $\theta_v = 45°$ a T_{surf} =500 K. S'observa una fracció important de reacció ER i de reflexió atòmica. Els processos d'adsorció no són tant importants excepte a certes energies per a incidència no normal. L'anàlisi dels angles de dispersió de l'àtom incident mostren un efecte important de l'àtom preadsorbit a la superfície per a una incidència normal. En aquests casos s'observa un pic a la distribució proper als 50° - 60° front als 10° observats sobre la superfície neta. Per a $\theta_v = 45°$ no s'observa cap efecte important. De la mateixa manera, l'intercanvi d'energia de l'àtom incident amb la superfície no es veu notablement afectat per la presència de l'àtom preadsorbit.

L'anàlisi de les molècules d'O_2 formades via ER mostren angles de sortida propers als 10° - 20° independentment de θ_v. Pel que fa a l'energia rotacional i vibracional és pràcticament independent d' E_{col}.

A l'estudi de la interacció de l'oxigen molecular amb el grafit no es posa de manifest la dissociació de la molècula a les energies estudiades degut a l'elevada energia de dissociació. En aquest cas s'ha estudiat l'angle de dispersió a dos angles d'incidència ($\theta_v = 0°$ i 45°), a diferents condicions inicials de T_{surf}, v i j, sense observar diferències substancials a les distribucions resultants. Només cal destacar cert desplaçament del pic a angles lleugerament superiors per a les distribucions d'incidència no normal tenint en compte la temperatura de la superfície a mesura que augmenta E_{col} (figura C.14). A la figura C.14 es mostren les distribucions

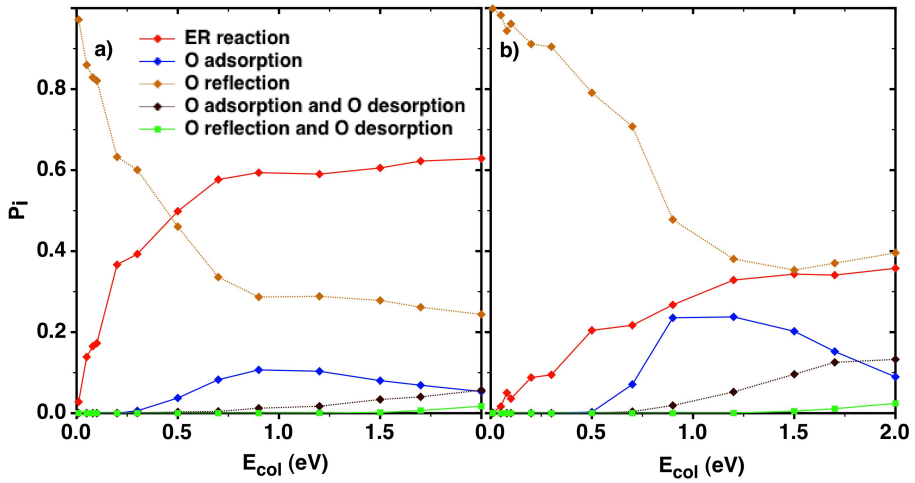

Figure C.13: Probabilitats de reacció per a la interacció d'un àtom d'oxigen a T_{surf} =500 K sobre una superfície precoberta d'oxigen a) $\theta_v = 0°$ b) $\theta_v = 45°$.

resultants per a una de les condicions estudiades observant angles de dispersió propers a 10° - 20° per a incidència normal i d'uns 45° - 60° per a $\theta_v = 45°$.

L'anàlisi de l'energia cinètica, vibracional i rotacional de les molècules després del procés de dispersió, reflecteix una pèrdua important d'energia cinètica que no es tradueix en un increment significatiu ni de l'energia vibracional ni rotacional.

• Comparació amb dades experimentals

S'han realitzat una sèrie de càlculs per tal de simular les condicions experimentals de Paci et al. (71) i Oh et al. (72).

En el primer dels casos (71) es presenten experiments de dispersió sobre la superfície de grafit (highly oriented pyrolytic graphite, HOPG) amb un feix d'àtoms i molècules d'oxigen amb una distribució hipertèrmica. La temperatura de la superfície durant l'experiment es va fixar a 503 K. Per a simular la dispersió atòmica es tenen en compte els resultats obtinguts per a la interacció d'un àtom d'oxigen sobre una superfície neta i sobre una superfície precoberta d'àtoms d'oxigen. Els resultats obtinguts (figura C.15) mostren unes distribucions dels angles de dispersió més amples que les observades experimentalment, tot i que el màxim observat és molt pròxim a l'experimental. En aquestes condicions, l'efecte del recobriment (és a dir, que el gas interaccioni amb una superfície precoberta d'oxigen) és practicament negligible respecte els resultats d'interacció sobre una superfície neta.

En el cas de la dispersió de la molècula d'oxigen sobre el grafit cal tenir en compte la contribució de dos processos sobre el senyal observat experimentalment.

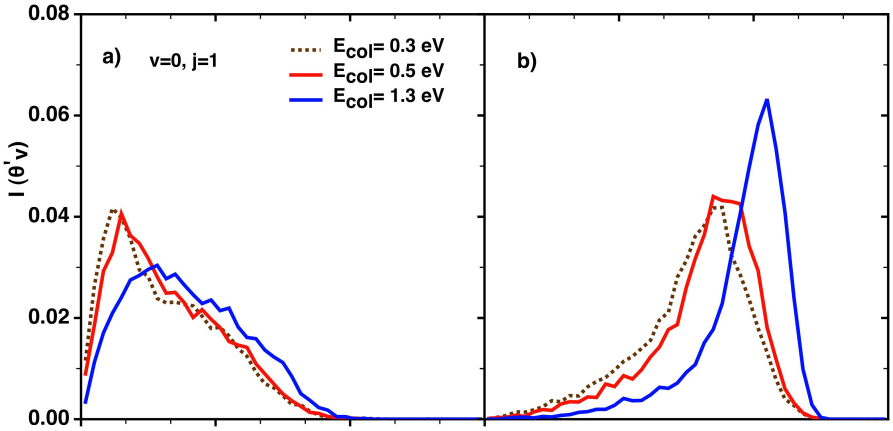

Figure C.14: Distribució dels angles de dispersió molecular a T_{surf} =300 K per a) $\theta_v = 0°$ i b) $\theta_v = 45°$.

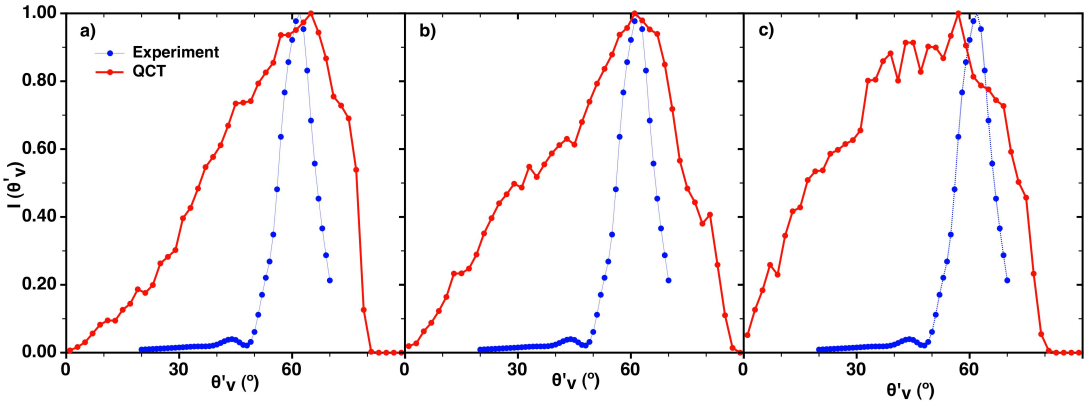

Figure C.15: Comparació entre la distribució teòrica i experimental (71) dels angles de dispersió de l'oxigen atòmic per a una distribució inicial hipertèrmica amb $\theta_v = 45°$ i a una T_{surf} =503 K per a) superfície neta amb la SEP FPLEPS, b) superfície neta amb SEP MS i c) superfície precoberta d'oxigen amb SEP FPLEPS.

El primer es tracta de la dispersió de la molècula incident, i el segon, de la formació de molècules d'oxigen a partir del procés d'Eley-Rideal. Donada la proporció O/O_2 del feix i tenint en compte la probabilitat de reacció calculada en aquestes condicions per a la reacció d'ER, s'estableix una ponderació de la contribució de cadascun dels dos processos a la distribució final (figura C.16). Dels dos pics

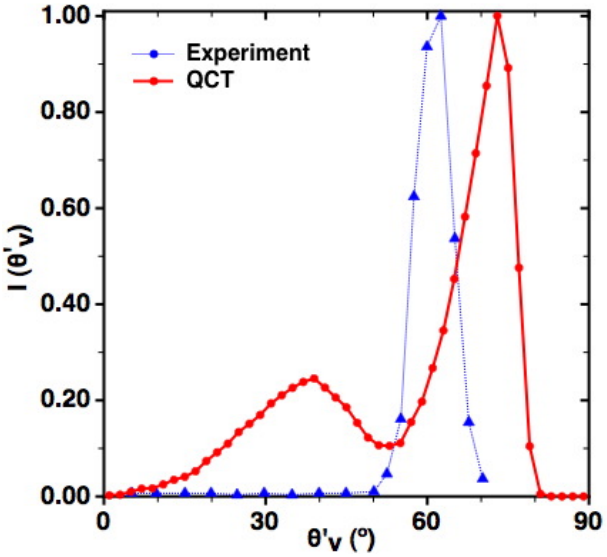

Figure C.16: Distribucions teòriques i experimentals (71) de l'angle de dispersió molecular per a un feix hipertèrmic a un angle incident de $\theta_v = 45°$, a una T_{surf} =503 K.

teòrics que s'observen, cadascun prové d'un dels dos processos esmentats. El que s'observa a angles més petits es produeix per la formació de molècules d'O_2 via ER, mentre que el d'angles més elevats es degut a la dispersió d'O_2. Comparant la distribució teòrica amb l'experimental es pot entendre que probablament el procés d'ER no sigui important en els experiments realitzats.

D'altra banda la simulació dels experiments de dispersió d'O_2 duts a terme per Oh et al. (72) dóna resultats molt similars als experimentals (figura C.17). Els experiments es realitzen a angles d'incidència entre 10° i 60° mesurant la intensitat d'O_2 dispersada a un angle θ_v' que compleix la condició $\theta_v + \theta_v' = 90°$.

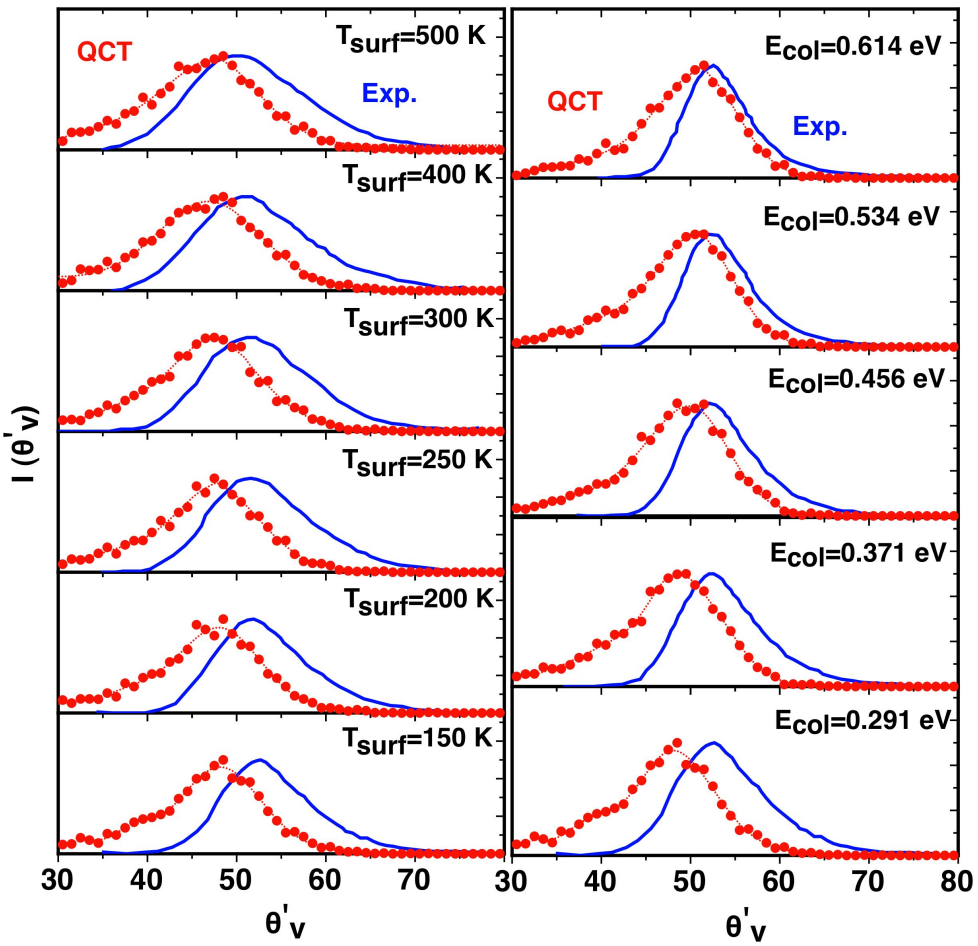

Figure C.17: Comparació entre resultats teòrics (vermell) i experimentals (blau) (72) de la intensitat angular dedispersió molecular segons la temperatura de la superfície per a E_{col} =0.291 eV (esquerra) i les energies de col·lisió per a T_{surf} =150 K (dreta). L'angle inicial varia de $10° \leqslant \theta_v \leqslant 70°$.

C.3 Estudi d' O/O_2 sobre β-cristobalita (001)

• Estudi QCT amb dos àtoms d'oxigen

S'ha realitzat un estudi dinàmic de la interacció de dos àtoms d'oxigen amb una superfície de β-cristobalita emprant una SEP prèviament construïda (122) emprant dades DFT (97, 101) i fent servir el mètode Corrugation Reducing Procedure.

Per al cas de l'estudi d'un àtom d'oxigen en fase gas interaccionant amb una superfície de β-cristobalita precoberta d'oxigen amb incidència normal s'observen dos processos principals: l'adsorció/absorció atòmica, i la formació d'O_2, què romanen adsorbides/absorbides a la superfície. La formació d'$O_{2(ad)}$ disminueix amb l'augment de la energía de col·lisió. En el cas d'una incidència de 45° s'observa principalment l'adsorció/absorció de l'oxigen atòmic, i amb molta menys incidència la reflexió i la formació de molècules d'$O_{2(ad)}$ sobre la superfície.

La dinàmica realitzada sobre la β-cristobalita amb la molècula d'O_2 gas presenta probabilitats de dissociació baixes a les energies i angles d'incidència estudiats (0.1 eV $\leqslant E_{col} \leqslant$ 3.0 eV per $\theta_v = 0°$, 15°, 30° i 45°). Les probabilitats de reflexió i adsorció/absorció moleculars són pràcticament complementàries. Així, mentres que la reflexió disminueix des d'un valor de pràcticament el 100% a energies baixes fins a un 40% a $E_{col} = 3.0$ eV l'adsorció presenta un comportament totalment invers. Per estudiar amb més detall el procés de dissociació molecular, s'han realitzat una sèrie de càlculs amb la posició inicial de la molècula sobre el lloc on més dissociació es produeix (sobre els àtoms de silici). Així s'observa un augment de la probabilitat de dissociació en augmentar E_{col}, mentres que es troba un efecte negligible de l'estat vibracional i rotacional inicial de la molècula.

• Model microcinètic

S'ha implementat un model microcinètic on s'ha pres sota consideració els processos anteriorment estudiats a més de tenir en compte els processos d'adsorció/absorció atòmica. Les constants de velocitats necessàries per a l'estudi s'obtenen a partir de càlculs QCT amb condicions tèrmiques en l'intèrval de 300 K -1,600 K per a tots els processos, obtenint valors molt diferents per a cadascun d'ells (figura C.18), cosa que impicarà una forta influència en la cinètica global.

La integració de les equacions diferencials per a un flux constant de O/O_2 a una temperatura donada permet observar l'evolució del recobriment de O i O_2 al llarg del temps fins que s'assoleix l'estat estacionari. Els resultats obtinguts per a una composició de P_O= 91 Pa i P_{O_2}= 9 Pa, pròxima a les dades experimentals a 900 K i 1,500 K per un plasma d'aire a un pressió total de 200 Pa, mostren dues característiques generals: un recobriment molecular a temperatures per sota de 1,000 K a temps llargs i un recobriment atòmic predominant a temperatures més

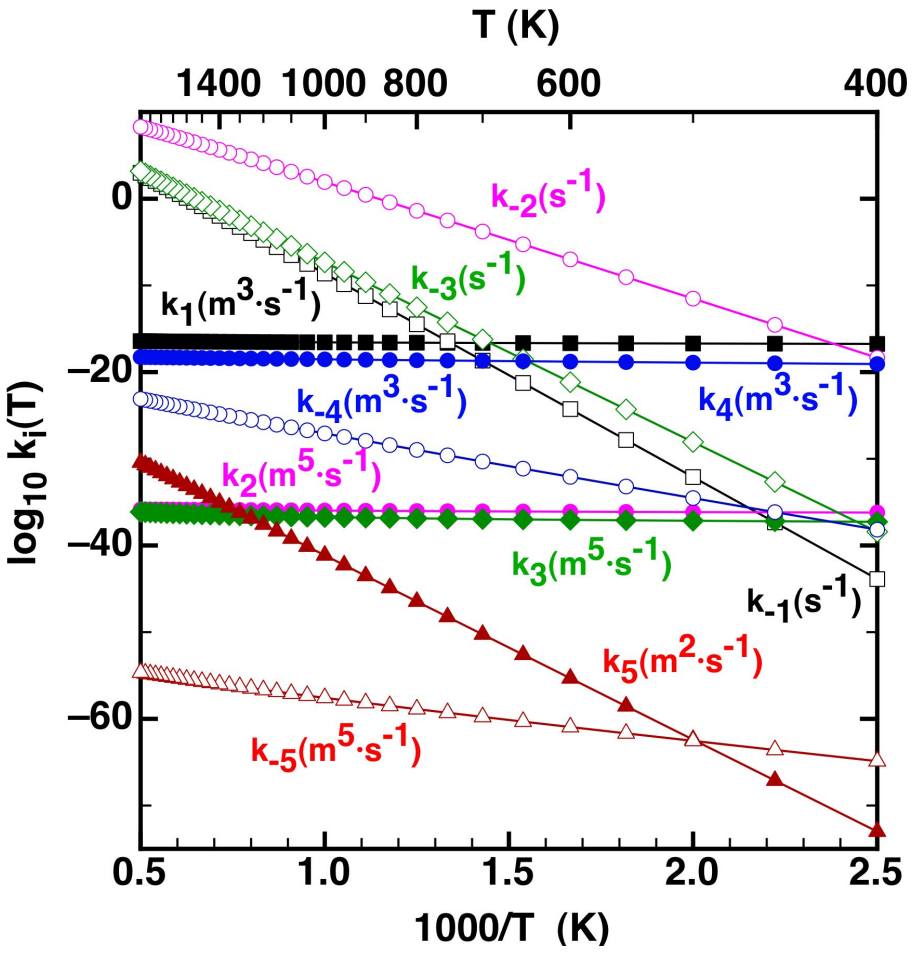

Figure C.18: Calculated thermal rate constants (400 - 2,000 K) for different heterogeneous processes involved in the proposed microkinetic model, based on QCT data. Only rate constants with the same units can be easily compared. Points are connected with a line to guide the view.

elevades.

S'ha realitzat una estimació del coeficient γ_O a diferents temperatures i de la contribució de cadascun dels processos al valor total (figura C.19a) a diferents condicions inicials per a diferents pressions parcials d'oxigen atòmic i molecular. Els valors calculats per a γ_O es comparen amb resultats teòrics i experimentals

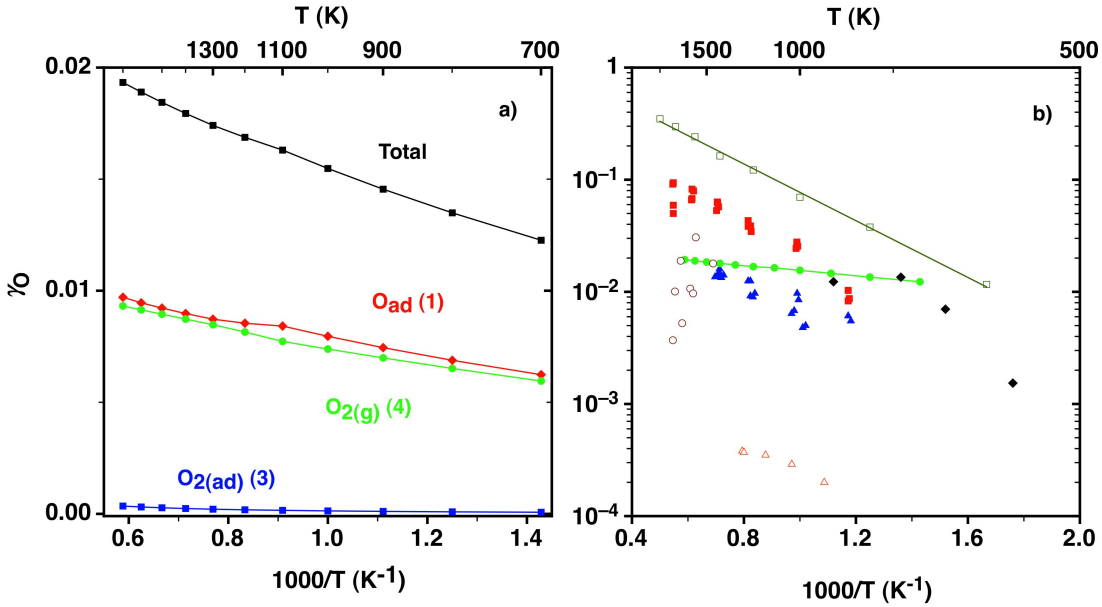

Figure C.19: a) Valors del γ_O calculats i les seves contribucions en funció de l'invers de la temperatura per P_O =100 Pa and P_{O_2} = 0 Pa. b) Comparació del γ_O calculat (cercles verds) a P_O =91 Pa, P_{O_2} =9 Pa sobre β-cristobalita; resultats de dinàmica molecular de ReaxFF per a O pur a $1{\cdot}10^{+6}$ Pa sobre β-quarz (quadres buits) (132). γ_O experimental d'aire sobre β-cristobalita (quadres vermells) i quarz (triangles blaus) a 200 Pa (135). Oxigen pur sobre quarz fos a 27 Pa (triangles buits) (139), O sobre silica (vitreosil) a P_O =1500-1600 Pa (rombes negres) (140) i $\gamma_O^{'}$ sobre RCG amb P_O =133 - 824 Pa (cercles buits)(141).

(132, 135, 137, 138, 139, 140) obtinguts a diferents condicions experimentals sobre diversos sòlids (figura C.19b) obtenint resultats comparables. Les diferències observades respecte els experiments podrien venir donades principalment pel fet de treballar amb O/O_2 en comptes d' amb aire dissociat i amb un model de sòlid cristal·lí ideal de β-cristobalita que difereix del material experimental de tipus policristal·lí.

De forma similar es realitza una estimació del coeficient β_O a partir dels fluxes atòmics calculats a través del model. Els valors obtinguts a les diferents temperatures varien lleugerament entre 0.7 i 0.8, cosa que suggereix que estan lluny de

prendre els valors assumits a les simulacions computacionals CFD. A la figura C.20 es representen les diferents contribucions al flux total d'energía transferides a la superfície. S'observa com la major part del flux a la superfície ve donat pel procès d'adsorció atòmica.

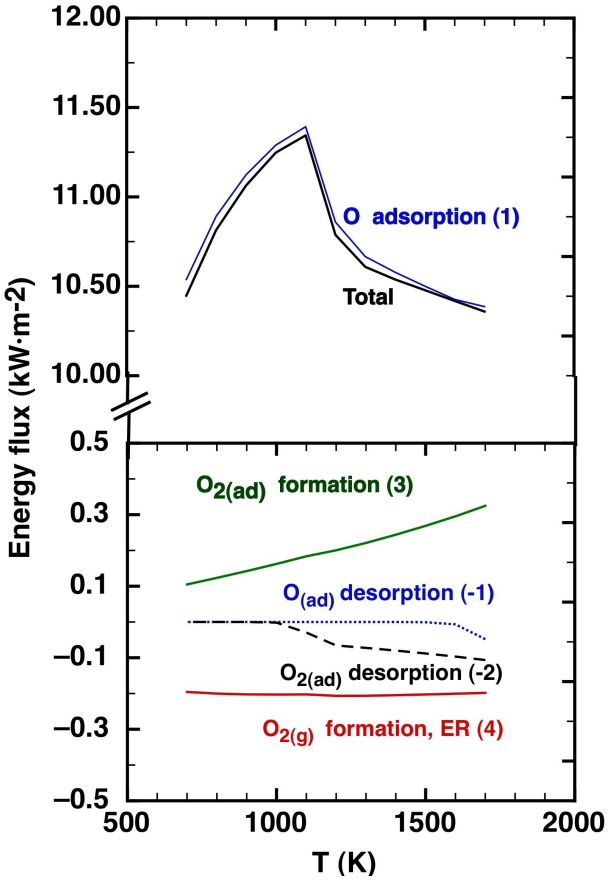

Figure C.20: Fluxes d'energia parcials i totals transferits a la superfície de β-cristobalita per a una barreja de O/O_2 (91, 9 Pa) a diverses temperatures. Es representen les contribucions dels processos principals. Atenció amb l'escala amplificada sobre l'eix Y per a la gràfica inferior (1 kWm^{-2}).

C.4 Conclusions

Tot seguit es presenta un breu resum de les conclusions principals obtingudes per a cadascun dels estudis realitzats:

- Estudi DFT de l'O/O_2 sobre grafit:
  - Els càlculs DFT del *bulk* (paràmetres de cel·la, energia de cohesió,...) i de la molècula d'O_2 mostren un bon acord amb les dades experimentals.
  - El model d'*slab* d'una o dues capes de carboni produeix resultats similars.
  - L'adsorció atòmica es produeix principalment sobre un enllaç C-C, donant lloc a una relaxació important de la superfície. La estructura tipus epoxi formada s'ha observat previament en estudis teòrics i experimentals.
  - L'adsorció atòmica és un procés activat on la barrera disminueix a mesura que disminueix el recobriment i al deixar relaxar l'*slab*.
  - La difusió atòmica també és un procés activat amb barreres menors per a recobriments baixos, però major al tenir en compte la relaxació de l'*slab*.
  - La recombinació atòmica via els mecanismes ER o LH, presenten barreres tot i que aquestes disminueixen amb un augment del recobriment, especialment per a l'ER, que dominarà la recombinació des de baixes a altes temperatures.
  - S'observa un mínim de fisisorció tant en el cas atòmic com en el molecular, confirmats a l'afegir les correccions de l'energia de dispersió.
- Estudi QCT atòmic i molecular de l'oxigen sobre el grafit:
  - El procés més important observat és la reflexió atòmica. La quimisorció s'observa a partir d'un valor llindar per a l'energia de col·lisió d'acord amb les diferents barreres d'adsorció observades en ambdues SEP, i presenta un màxim, tot i que l'incidència no normal en disminueix la probabilitat.
  - El mínim de fisisorció a la SEP MS provoca un augment de l'adsorció a energies de col·lisió baixes i a distàncies de la superfície altes.
  - El fet d'afegir un bany tèrmic (temperatura de la superfície) afavoreix l'adsorció ja que l'àtom es capaç de cedir part de la seva energia.
  - Les distribucions de l'angle de dispersió per a l'oxigen atòmic mostra un màxim a angles petits per a incidència normal, desplaçat a valors més elevats per a incidència no normal, en perfecte acord amb els experiments hiperèrmics (màxim a $\sim 60°$).

  - La reflexió atòmica i la reacció ER són els processos principals quan un O col·lisiona amb una superfície precoberta d' O. La incidència no normal augmenta la reflexió disminuint com a conseqüència l'ER.
  - Les molecules d'O_2 formades via ER presenten excitació interna i translacional com caldria esperar degut a la gran exotermicitat de la reacció.
  - La col·lisió molecular sobre el grafit no presenta dissociació. Les distribucions dels angles de dispersió presenten màxims que es desplaçen gradualment a valors més grans al augmentar l'angle d'incidència. La comparació amb resultats experimentals a diferents temperatures i energies de col·lisió és bona.
  - Les distribucions d'angles de dispersió de l'O_2 amb els de l'O_2 format via ER presenten pics ben diferenciats, suggerint que la contribució d'aquest segon procés és menys important a les condicions experimentals donades.

- Model microcinètic d'O/O_2 reaccionant sobre el grafit:
  - El model microcinètic (300 - 1,000 K) basat en dades TST confirma una contribució molt petita del procés LH i prediu un recobriment atòmic molt baix ($\theta_O < 0.5\%$).
  - L'adsorció atòmica i la reacció ER són els processos més importants amb contribucions similars a temperatures baixes, mentre que a temperatures més elevades són l'adsorció i desorció atòmiques, tot i que en aquest cas les velocitats de reacció es veuen compensades.
  - Aquests resultats juntament amb les petites constants de velocitat, originen coeficients de recombinatió atòmica molt baixos ($\gamma_O < 5 \cdot 10^{-4}$).
  - Un increment de la pressió parcial de l'O produeix un augment de γ_O mentres que la presència d'O_2 no té conseqüències destacables.
  - Un increment de la temperatura incrementa γ_O fins que s'arriba a una temperatura límit on la desorció esdevé molt important, produint així una disminució de γ_O.

- Estudi QCT atòmic i molecular de l'oxigen sobre la β-cristobalita:
  - L'estudi dinàmic presenta l'adsorció atòmica com el procés principal de la interacció d'O amb una superfície de β-cristobalita precoberta d'O. La formació d'$O_{2(ad)}$ és el segon procés en importància i disminueix a l'incrementar l'energia de col·lisió. La reflexió atòmica i el procés ER són menys importants però també significatius. La incidència no

normal augmenta les probabilitats de reflexió i adsorció, disminuint així la formació d'$O_{2(ad)}$ via la reacció ER.

- Les molècules d'O_2 formades via la reacció ER a temperatures elevades esdevenen excitades internament i translacionalment mentres la superfície es refreda.
- La interacció d'O_2 sobre una superfície de β-cristobalita neta produeix reflexió i adsorció molecular i dissociació de la molècula; aquest últim procés només és possible a energies de col·lisió altes. La incidència normal produeix probabilitats d'adsorció dissociativa i no dissociativa més elevades que col·lisions a incidència no normal. L'increment de l'estat vibracional i rotacional de la molècula i de a temperatura de la superfície mostren efectes negligibles a les probabilitats.
- Les molècules reflexades s'obtenen excitades rotacionalment i amb una energia translacional lleugerament inferior que l'inicial.
- Els resultats de dinàmica a condicions quasitèrmiques mostren que l'adsorció atòmica sobre la superfície neta és predominant tot i que disminueix si es compara amb la probabilitat a l'interaccionar amb una superfície precoberta d' O, degut a l'aparició de dos processos competitius que produeixen $O_{2(ad)}$ i $O_{2(g)}$. L'adsorció molecular no dissociativa també s'observa.

- Model microcinètic d'O/O_2 reaccionant sobre la β-cristobalita:
  - El model microcinètic (700 - 1,700 K) basat en dades QCT mostra un recobriment molecular elevat a temperatures inferiors als 1,000 K, cosa que podria produir la pasivació de la superfície a temps llargs, mentres que s'observa un recobriment atòmic elevat a temperatures més elevades.
  - El coeficient γ_O mostra valors molt petits ($0.01 < \gamma_O < 0.02$) a les temperatures estudiades (700 - 1,700 K), pràcticament independent de la composició inicial de la mescla d'O/O_2, siguent l'adsorció atòmica i el procés ER les contribucions més considerables.
  - El coeficient γ_O augmenta amb la temperatura seguint un comportament d'Arrhenius, amb valors pròxims als experimentals.
  - S'observa un valor pràcticament constant del coeficient β_O ($0.75 < \beta_O < 0.80$) dins de l'intèrval de temperatures de 700 - 1,700 K, indicant que la suposició de que $\beta_O = 1$ no és del tot acurada.
  - El procés d'adsorció atòmica és el principal causant del total de la energia transferida a la superfície.

  - S'observen algunes divergències al comparar amb els valors experimentals de β_O d'aire sobre β-cristobalita, tot i que el fluxe d'energia transferit a la superfície està en acord amb les observacions experimentals.

- Mètodes teòrics:

  - La construcció de superfícies d'energia potencial, analítiques (FPLEPS) o interpolades (MS) produeixen resultats similars, encara que el mètode MS requereix un esforç computacional i personal més elevat. A més a més, les primeres derivades FPLES són millors que les MS.
  - Els estudis dinàmics amb trajectòries quasiclàssiques amb una superfície 6D o amb totes les dimensions, emprant el bany tèrmic GLO, són útils i fiables a l'hora d'entendre les característiques principals dels diferents processos gas-superfície.
  - Els models microcinètics basats en les constants tèrmiques de velocitat, TST o QCT, són molt útils per a descriure la globalitat dels processos competitius gas-superfície, proporcionant coeficients γ i β prou raonables en funció de les temperatures i les pressions.

Bibliography

[1] M. Springborg, *Density-Functional Theory of Atoms and Molecules* (John Wiley and Sons, New York, 1997).

[2] R. Parr, *Density-Functional Theory of Atoms and Molecules* (Clarendon Press, Oxford, 1989).

[3] M. Solà and J. M. Ugalde, in *Theoretical and computational chemistry: Foundations, methods and techniques*, edited by J. Andrés and J. Bertran (Universitat Jaume I, Castelló, 2007).

[4] S. Vosko, L. Wilk, and M. Nusair, Canadian Journal of Chemistry **58**, 1200 (1980).

[5] J. M. Bowman, J. S. Bittman, and L. B. Harding, The Journal of Chemical Physics **85**, 911 (1986).

[6] L. M. Raff, M. Malshe, M. Hagan, D. I. Doughan, M. G. Rockley, and R. Komanduri, The Journal of Chemical Physics **122**, 084104 (2005).

[7] T. Hollebeek, T. Ho, and H. Rabitz, Annual Review of Physical Chemistry **50**, 537 (1999).

[8] S. Lorenz, M. Scheffler, and A. Gross, Physical Review B (Condensed Matter and Materials Physics) **73**, 115431 (2006).

[9] Y. Guo, A. Kawano, D. L. Thompson, A. F. Wagner, and M. Minkoff, The Journal of Chemical Physics **121**, 5091 (2004).

[10] G. G. Maisuradze, D. L. Thompson, A. F. Wagner, and M. Minkoff, The Journal of Chemical Physics **119**, 10002 (2003).

[11] H. F. Busnengo, A. Salin, and W. Dong, The Journal of Chemical Physics **112**, 7641 (2000).

[12] S. Lorenz, A. Gross, and M. Scheffler, Chemical Physics Letters **395**, 210 (2004).

[13] S. Chapman, M. Dupuis, and S. Green, Chemical Physics **78**, 93 (1983).

[14] F. London, Zeitschrift fur Electrochemie **35**, 552 (1926).

[15] H. Eyring and P. H, Zeitschrift fur Physicalische Chemie-Abteilung B-Chemie der Elementarprozesse Aufbau der Materie **12**, 279 (1931).

[16] S. Sato, The Journal of Chemical Physics **23**, 2465 (1955).

[17] M. Karplus and R. Sharma, The Journal of Chemical Physics **43**, 3259 (1965).

[18] J. McCreery and G. Wolken, The Journal of Chemical Physics **63**, 2340 (1975).

[19] J. McCreery and G. Wolken, The Journal of Chemical Physics **64**, 2551 (1977).

[20] L. Martin-Gondre, C. Crespos, P. Larregaray, J. Rayez, B. van Ootegem, and D. Conte, The Journal of Chemical Physics **132**, (2010).

[21] L. Martin-Gondre, C. Crespos, P. Larregaray, J. Rayez, D. Conte, and B. van Ootegem, Chemical Physics **367**, 136 (2010).

[22] L. Martin-Gondre, C. Crespos, P. Larregaray, J. C. Rayez, B. van Ootegem, and D. Conte, Chemical Physics Letters **471**, 136 (2009).

[23] G. Volpilhac, H. Busnengo, W. Dong, and A. Salin, Surface Science **544**, 329 (2003).

[24] P. Rivière, H. Busnengo, and F. Martín, The Journal of Chemical Physics **121**, 751 (2004).

[25] M. Johnston, *Computational Chemistry* (Elsevier Science, New York, 1988).

[26] W. Vetterling, W. Press, S. Teukolsky, and B. Flannery, *Numerical Recipes in Fortran 77* (Cambridge University, Cambridge, 1992).

[27] M. A. Collins, Theoretical Chemistry Accounts **108**, 313 (2002).

[28] R. P. A. Bettens and M. A. Collins, The Journal of Chemical Physics **111**, 816 (1999).

[29] C. Crespos, M. Collins, E. Pijper, and G. Kroes, Chemical Physics Letters **376**, 566 (2003).

[30] C. Crespos, M. Collins, E. Pijper, and G. Kroes, The Journal of Chemical Physics **120**, 2392 (2004).

[31] H. Goldstein, *Mecanica Clásica* (Reverté, Barcelona, 1998).

[32] D. Beeman, The Journal of Computational Physics **20**, 130 (1976).

[33] K. Binder and D. Heermann, *Monte Carlo Simulation in Statistical Physics: an Introduction* (Springer, Berlin, 1998).

[34] J. Tully, The Journal of Chemical Physics **73**, 1975 (1980).

[35] J. C. Polanyi and R. J. Wolf, The Journal of Chemical Physics **82**, 1555 (1985).

[36] H. F. Busnengo, M. A. Di Césare, W. Dong, and A. Salin, Physical Review B **72**, 125411 (2005).

[37] H. Busnengo, W. Dong, and A. Salin, Physical Review Letters **93**, 236103 (2004).

[38] S. Adelman and J. Doll, The Journal of Chemical Physics **64**, 2375 (1976).

[39] J. Tully, G. Gilmer, and M. Shugard, The Journal of Chemical Physics **7**, 1630 (1979).

[40] G. Armand and J. Manson, Surface Science **80**, 532 (1979).

[41] N. Levine, *Química Cuántica* (Pearson Educación, New York, 2001).

[42] N. Levine, *Molecular Spectroscopy* (John Wiley Sons, New York, 1975).

[43] M. D. Pattengill, in *Atom-Molecule Collision Theory*, edited by R. Bernstein (Plenum Press, New York, 1984).

[44] S. Glasstone, K. Laider, and H. Eyring, *Theory of Rate Processes* (McGraw-Hill, New York, 1941).

[45] I. Smith, *Kinetics and Dynamics of Elementary Gas Reactions* (Butterworths, London, 1980).

[46] K. Laidler, *Chemical Kinetics* (Harper Row, New York, 1987).

[47] M. Barbato, S. Reggiani, C. Bruno, and J. Muylaert, Journal of Thermophysics and Heat Transfer **14**, 412 (2000).

[48] V. Kovalev and A. Kolesnikov, Fluid Dynamics **40**, 669 (2005).

[49] J. Thoemel, E. Cosson, and O. Chazot, in *Proceedings of the 6th European Symposium on Aerothermodynamics for Space Vehicles* (ESA, Versailles, France, 2008), No. SP-659, session 18, 1-14.

[50] C. Scott, in *Advances in Hypersonics*, edited by J. Bertin, J. Periaux, and J. Ballman (Birkhäuser, Boston, 1992), Vol. 2.

[51] T. Ngo, E. Snyder, W. Tong, R. Williams, and M. Anderson, Surface Science **314**, L8217 (1994).

[52] *Molecular physics and hypersonic flows*, edited by M. Capitelli (Kluwer Academic Publishers, Dordrecht, 1996), Vol. 482.

[53] D. Lamoen and B. Persson, Journal of Chemical Physics **108**, 3332 (1998).

[54] D. Sorescu, K. Jordan, and P. Avouris, Journal of Physical Chemistry B **105**, 11227 (2001).

[55] A. Incze, A. Pasturel, and C. Chatillon, Applied Surface Science **177**, 226 (2001).

[56] A. Incze, A. Pasturel, and C. Chatillon, Surface Science **537**, 55 (2003).

[57] Y. Xu and J. Li, Chemical Physics Letters **400**, 406 (2004).

[58] J. Ito, J. Nakamura, and A. Natori, Journal of Applied Physics **103**, 1 (2008).

[59] Z. Xu and K. Xue, Nanotechnology **21**, 045704 (2010).

[60] X. Zhu, S. Lee, Y. Lee, and T. Frauenheim, Physical Review Letters **85**, 2757 (2000).

[61] S. Walch, Chemical Physics Letters **374**, 501 (2003).

[62] H. Ulbricht, R. Zacharia, N. Cindir, and T. Hertel, Carbon **44**, 2931 (2006).

[63] A. Tkatchenko and M. Scheffler, Physical Review Letters **102**, 073005 (2009).

[64] H. Ulbricht, G. Moos, and T. Hertel, Physical Review B **66**, 075404 (2002).

[65] H. Ulbricht, G. Moos, and T. Hertel, Surface Science **532**, 852 (2003).

[66] M. Barber, E. Evans, and J. Thomas, Chemical Physics Letters **3**, 423 (18).

[67] S. Kelemen and H. Freund, Carbon **23**, 619 (1985).

[68] H. Kinoshita, M. Umeno, M. Tagawa, and N. Ohmae, Surface Science **440**, 49 (1999).

[69] K. Nicholson, T. Minton, and S. Sibener, Journal of Physical Chemistry B **109**, 8476 (2005).

[70] V. Morón, P. Gamalo, and R. Sayós, Theoretical Chemistry Accounts **128**, 683 (2011).

[71] J. T. Paci, H. P. Upadhyaya, J. Zhang, G. C. Schatz, and T. K. Minton, The Journal of Physical Chemistry A **113**, 4677 (2009).

[72] J. Oh, T. Kondo, K. Arakawa, Y. Saito, W. Hayes, J. Manson, and J. Nakamura, The Journal of Physical Chemistry A **115**, 7089 (2011).

[73] R. W. G. Wyckoff, *Crystal Structures* (Interscience, New York, 1965).

[74] X. Sha and B. Jackson, Surface Science **496**, 318 (2002).

[75] J. Perdew, J. Chevary, S. Vosko, K. Jackson, M. Pederson, D. Singh, and C. Fiolhais, Physical Review B **46**, 6671 (1992).

[76] J. Perdew and Y. Wang, Physical Review B **45**, 13224 (1992).

[77] G. Kresse and J. Hafner, Physical Review B **47**, 558 (1993).

[78] G. Kresse and J. Hafner, Physical Review B **48**, 13115 (1993).

[79] G. Kresse and J. Furthmüller, Computational Material Science **6**, 15 (1996).

[80] G. Kresse and J. Furthmüller, Physical Review B **54**, 11169 (1996).

[81] P. Blöchl, Physical Review B **50**, 17953 (1994).

[82] G. Kresse and D. Joubert, Physical Review B **59**, 1758 (1999).

[83] J. Perdew, K. Burke, and M. Ernzerhof, Physical Review Letters **77**, 3865 (1996).

[84] B. Hammer, L. Hansen, and J. Nørskov, Physical Review B **59**, 7413 (1999).

[85] M. Hasegawa and K. Nishidate, Physical Review B **70**, 205431 (2004).

[86] M. W. Chase, *NIST JANAF Thermochemical Tables* (American Institure of Physics, New York, 1998).

[87] W. B. Gauster and I. J. Fritz, Journal of Applied Physics **45**, 3309 (1974).

[88] O. L. Blakslee, D. G. Proctor, E. J. Seldin, G. B. Spence, and T. Weng, Journal of Applied Physics **41**, 3373 (1970).

[89] H. J. F. Jansen and A. J. Freeman, Physical Review B **35**, 8207 (1987).

[90] F. Birch, Physical Review **71**, 809 (1947).

[91] K. Eunja and C. Changfeng, Physics Letters A **326**, 442 (2004).

[92] A. Lerf, H. He, and M. Forster, Journal of Physical Chemistry B **102**, 4477 (1998).

[93] T. Szabo, O. Berkesi, P. Forgo, K. Josepovits, Y. Sanakis, D. Petridis, and I. Dekany, Chemistry of Materials **18**, 2740 (2006).

[94] J. Paci, T. Belytschko, and G. Schatz, Journal of Physical Chemistry C **111**, 18099 (2007).

[95] S. Casolo, O. Lovvik, and R. Martinazzo, Journal of Chemical Physics **130**, 054704 (2009).

[96] S. Grimme, Journal of Computational Chemistry **27**, 1787 (2006).

[97] C. Arasa, P. Gamallo, and R. Sayós, Journal of Physical Chemistry B **109**, 14954 (2005).

[98] P. Gamallo and R. Sayós, Physical Chemistry Chemical Physics **9**, 5112 (2007).

[99] G. Henkelman, B. Uberuaga, and H. Jonsson, The Journal of Chemical Physics **113**, 9901 (2000).

[100] G. Henkelman and H. Jónsson, The Journal of Chemical Physics **113**, 9978 (2000).

[101] C. Arasa, V. Morón, H. Busnengo, and R. Sayós, Surface Science **603**, 2742 (2009).

[102] P. Cen and R. Yang, Carbon **22**, 186 (2005).

[103] M. Balat-Pichelin, L. Bedra, O. Gerasimova, and P. Boubert, Chemical Physics **340**, 217 (2007).

[104] L. Bedra and M. Balat-Pichelin, Aerospace Science and Thecnology **9**, 318 (2005).

[105] V. Guerra and J. Loureiro, Plasma Sources Science and Technology **13**, 85 (2004).

[106] A. Savvatimskiy, Carbon **43**, 1115 (2005).

[107] J. Hahn, Carbon **43**, 1506 (2005).

[108] V. Guerra, IEEE Transaction on Plasma Science **35**, 1397 (2007).

[109] H. Cuppen and L. Hornekaer, Journal of Chemical Physics **128**, 174707 (2008).

[110] M. Abramowitz and I. Stegun, *Handbook of Mathematical Functions With Formulas, Graphs and Mathematical Tables* (United States Department of Commerce and National Bureau of Standards, Washington, 1964).

[111] G. Groenenboom and I. Struniewicz, Journal of Chemical Physics **113**, 9562 (2000).

[112] K. Huber and G. Herzberg, *Constants of diatomic molecules* (Van Nostrand Reinhold Company, New York, 1979).

[113] A. Albinet, J. P. Biberian, and M. Bienfait, Physical Review B **3**, 2015 (1971).

[114] L. Lang, S. Doyen Lang, A. Charlier, and M. F. Charher, Physical Review B **49**, 5672 (1994).

[115] D. Singh and Y. P. Varshni, Physical Review B **24**, 4340 (1981).

[116] G. Boato, P. Cantini, C. Salvo, R. Tatarek, and S. Terreni, Surface Science **114**, 485 (1982).

[117] L. DeLouise, Chemical Physics Letters **180**, 149 (1991).

[118] M. McMaster, S. Schroeder, and R. Madix, Surface Science **297**, 253 (1993).

[119] G. Herzberg, *Molecular Spectra and Molecular Structure* (Krieger, Malabar, Florida, 1989), Vol. I.

[120] R. Logan and R. Stickney, Journal of Chemical Physics **44**, 195 (1966).

[121] V. Morón, P. Gamallo, L. Martin-Gondre, C. Crespos, P. Larregaray, and R. Sayós, Physical Chemistry Chemical Physics **13**, 17494 (2011).

[122] C. Arasa, H. Busnengo, A. Salin, and R. Sayós, Surface Science **602**, 975 (2008).

[123] A. Rosenthal and S. Garofalini, Journal of the Chemical Ceramic Society **70**, 821 (1987).

[124] D. Hamann, Physical Review Letters **81**, 3447 (1998).

[125] Y. Kim and K. Chang, Physical Review Letters **86**, 1773 (2001).

[126] G. Billing, *Dynamics of Molecule Surface Interaction* (John Wiley Sons, New York, 1987).

[127] D. Truhlar and J. Muckermann, in *Atom-Molecule Collision Theory*, edited by R. Berstein (Plenum Press, New York, 1984).

[128] R. Sayós, V. Morón, C. Arasa, and H. Busnengo, in *Proceedings of the 6th European Symposium on Aerothermodynamics for Space Vehicles* (ESA, Versailles, France, 2008), No. SP-659, session 28, 1-7.

[129] V. Morón, C. Arasa, R. Sayós, and H. Busnengo, AIP conference proceedings **1084**, 682 (2008).

[130] A. Gross, *Theoretical Surface Science. A Microscopic Perspective* (Springer-Verlag, Berlin, 2003).

[131] L. Bedra, M. Rutigliano, M. Balat-Pichelin, and M. Cacciatore, Langmuir **22**, 7208 (2006).

[132] P. Norman and T. Schwartztentruber, AIAA **4320**, 1 (2010).

[133] F. Nasuti, M. Barbato, and C. Bruno, Journal of Thermophysics and Heat Transfer **10**, 131 (1996).

[134] B. Temel, H. Meskine, K. Reuter, M. Scheffler, and H. Metiu, The Journal of Chemical Physics **126**, 204711 (2007).

[135] M. Balat-Pichelin, J. Badie, R. Berjoan, and P. Boubert, Chemical Physics **291**, 181 (2003).

[136] M. Balat-Pichelin and A. Vesel, Chemical Physics **327**, 112 (2006).

[137] B. Halpern and D. Rosner, Journal of the Chemical Society Faraday Transactions I **74**, 1883 (1978).

[138] S. Sepka, Y. Chen, and M. J, Journal of Thermophysics and Heat Transfer **14**, 45 (2000).

[139] Y. Kim and M. Boudart, Langmuir **7**, 2999 (1991).

[140] J. Greaves and J. Linnett, Transactions of the Faraday Society **55**, 1355 (1959).

[141] P. Kolodziej and D. Stewart, AIAA **87**, 1637 (1987).

[142] M. Balat-Pichelin, V. Kovalev, A. Kolesnikov, and A. Krupnow, AIP conference proceedings **762**, 1347 (2005).

[143] M. Balat-Pichelin, M. Czerniak, and J. Badie, Applied Surface Science **120**, 225 (1997).